

Advancing Treatment Accuracy of Accelerated Partial Breast Irradiation

by

Ghada Aldosary

A thesis submitted to the Faculty of Graduate and Postdoctoral Affairs in partial fulfillment of the requirements for the degree of

Doctor of Philosophy

in

Physics

(Specialization in Medical Physics)

Ottawa-Carleton Institute of Physics
Department of Physics
Carleton University
Ottawa, Ontario, Canada

Dedication

In memory of my grandmother, Al-Jawhara bint Mubarak bin Hethab (May Allah grant her the highest Firdous), who did not have a chance to go to school but encouraged me to earn the highest degrees.

For my husband, Mohammed and our daughters, Jana and Aya.

*And,
for our brave patients,
may this educational pursuit help me better serve you.*

Abstract

Accelerated partial breast irradiation (APBI) has been clinically demonstrated as a new and advantageous breast radiotherapy treatment. Contrary to standard-of-care whole breast radiotherapy (WBRT), APBI focuses radiation to the tumour bed with a small surrounding margin. To ensure successful treatment outcomes, these precise treatment techniques require a higher level of treatment accuracy than WBRT. The purpose of this thesis is to inform and advance treatment accuracy of external beam APBI. This is achieved through two main approaches.

First, 3D printing was utilized to construct phantoms for assessing image fidelity and measuring geometric distortions on multiple radiological imaging modalities used in target delineation during high-precision radiotherapy treatment planning. The proof of concept was demonstrated using a small version of the phantom and with co-registered helical computed tomography (CT), cone beam computed tomography (CBCT), and magnetic resonance imaging (MRI) image sets, which are routinely employed during target delineation of certain cranial diseases for high-precision, high-accuracy radiotherapy. The second part of this work was motivated by the fact that MRI offers excellent soft tissue visualization, which can be particularly advantageous for APBI. In MRI, the breast is positioned at the lateral parts of the imaging field-of-view where geometric distortion increases. Methods demonstrated for the cranial site were further developed to construct a modular, large 3D printed phantom to characterize image geometric distortion for the breast site. MRI geometric distortion was measured on image sets acquired with MRI

sequences often utilized for clinical breast imaging. Results showed that errors arising from geometric distortions can be sufficiently significant to consider in margins for APBI.

Second, a novel, realistic, deformable breast phantom was developed for multi-modality imaging, radiation absorption measurements, surgical simulation, and radiotherapy applications. The phantom's properties were optimized to match human breast tissues'. Mechanical properties were validated through mechanical and shear-wave ultrasound elastography testing. Radiation absorption characteristics were determined through empirical calculations, experimental measurements, treatment planning system calculations, and EGSnrc Monte Carlo simulations. Surgical simulation validation was confirmed by surgeons. Finally, a set of breast phantoms were produced and used to simulate various oncoplastic breast surgery (OBS) techniques and investigate consequences related to adjuvant radiotherapy treatment planning. This study provided new insight on how OBS causes extensive breast tissue deformation and relocation, affects the tumour bed, results in surgical clip displacement, and ultimately showed how OBS can impact patient eligibility for APBI.

Acknowledgements

First and foremost, I would like to thank Allah Almighty for his endless blessings, guidance, and mercy. For no matter the effort, struggle, or feat, He paves the best way. “Yudabir al’amr wahu Allateef Alkhabeer”.

I would like to extend my sincere gratitude to my supervisors, Dr. Eric Vandervoort and Dr. Claire Foottit. They have provided me with thoughtful guidance, valuable input, and space to grow as a medical physicist. They were generous with their knowledge, expertise, and time. They always encouraged me to pursue my own ideas and patiently humoured my curiosity. They were kind, patient mentors, and provided immense support as I balanced course work, research, work commitments, solo parenting, *and* as we navigated a global pandemic. I am truly fortunate to have been able to work with them, and for the enlightening discussions and fun along the way!

I would like to thank my supervisory committee, Dr. Tong Xu (Carleton University) and Dr. Ladan Arissian (The University of Ottawa), my external examiner, Dr. Wendy Smith (University of Calgary), and internal examiner, Dr. Pascal Fallavollita (The University of Ottawa) for their valuable input and time.

I am honoured to be a full scholarship recipient, and I am indebted to my funding institution and employer, King Abdulaziz Medical City-MNGHA in Riyadh, Saudi Arabia, and especially Dr. Abdulrahman Al Hadab for his mentorship and relentless support over the years. I would like to thank the Saudi Arabian Cultural Bureau in Canada, and especially Dr. Muhsen Mohammed for his guidance, assistance, and for never failing to lift my spirit during trying times.

Many thanks to Ms. Doris Vieira, Ms. Kirsten Berry, and Ms. Temi Gouti for assisting me with my administrative matters. Thanks to members of the Carleton Laboratory for Radiotherapy Physics; Ms. Ericka Venturina, Dr. Sara Kashi, Dr. Ming Liu, Dr. Chris Dydula, Dr. Mathew Efseaff, and Iymad Mansour. I would like to address a

special thank you to Dr. Joanna Cygler and Dr. Dave Rogers, they are true inspirations and role models, and have welcomed me with heartwarming kindness and support.

I was fortunate to have the opportunity to work with many wonderful people at The Ottawa Hospital (TOH). Special thanks to Dr. Jason Belec, who I worked closely with on the breast phantom prototype development and oncoplastic breast surgery studies. His guidance and feedback were integral to these projects, and I cannot thank him enough for everything. Special thanks to Dr. Janos Szanto, who conceived the idea of characterizing multi-modality image geometric distortion for CyberKnife treatment planning. I very much enjoyed working with him and learning from him. I would also like to thank the dedicated radiation oncologists at TOH, Dr. Jean-Michel Caudrelier and Dr. Lynn Chang, and surgeons, Dr. Tabitha Tse and Dr. Angel Arnaout for all their time, feedback, and valuable contributions to our research. I have enjoyed working with a multi-disciplinary team, and I am grateful for the valuable insight gained. I would like to express my sincere appreciation to Mr. Bernie Lavigne and Mr. Ron Romain for their attentiveness, meticulousness, and timeliness in constructing phantom parts. Without them, it would not have been possible to achieve all my experimental goals. Thank you to Mr. William Lee (TOH) and Mr. Stephen Karwaski (The Ottawa Civic Hospital) for their help with imaging scans, Mr. Paul Nichols (TOH) for showing me how to make phantom molds, Dr. Adnan Sheikh, Dr. Waleed Althobaity and Eng. Olivier Miguel for providing access to the TOH 3D Printing Lab. Many thanks to Dr. Miller MacPherson, for his moral support and for financially supporting conference visits and research material procurement. Thank you to Ms. Cathy Rose, Dr. Lesley Buckley, Dr. Katie Lekx-Toniolo, Mr. Andrew Richardson, Mr. Chris Lambert, and Mr. Steve Andrusyk for assisting with logistical aspects of my research. I'd also like to express my sincere gratitude to Dr. Malcolm McEwen for his support and for providing access to the Co-60 irradiator at the NRC, and Mr. Brad Downton for assisting with those measurements. And, many thanks to Dr. Catriona Cyrnyj and Dr. Linda McLean, for taking interest in my research and for providing me with access to their research laboratory equipment.

My educational journey spanned cities (space!) and time, and I am so incredibly grateful for all my family and friends across the world. My utmost sincere love and appreciation are for my beautiful family: my mother Salwa, my father Battal, my siblings Buthainah, Mohammed, Abdullah, and Naif, my parents-in-law, Ayesha and Fahim, and family-in-law, Shamayel, Shaza, Omar, Aamer, Hamooz, Mimi, Hamoudi, Rayanu, and Neemo. Without their moral support, confidence and endless prayers, none of this would have been possible. I am so grateful for my Ottawa family, Nuzhat Auntie, Khaled Uncle and Zawaar for opening their home to me, Jana, and Mohammed. I will forever be in gratitude, and they will forever be in my prayers. Thank you to my friends for their support over the years; Anan, Arwa, Anwaar, Amani, Banaf, Fatimah B., Fatimah Z., Hamed, Hawra, Iqbal, Ibtisam, Kara, Kathleen, Marija, Mirvat, Nadia, Saad, Sumaya, and Wesam. And thank you to my four-legged friends, who have filled my days with joy and helped me clear my mind: Affie (our cat) and Gracie, Holly, and Jax (my equine friends).

Last but not least, I would not be where I am today without my beloved husband, Mohammed and our daughter, Jana. No words can describe my gratitude for them and their place in my heart. This journey has come with many sacrifices and challenges. With them, I have found my way and perseverance, through them, my hope, and for them, my strength. To Mohammed, my best friend: thank you for your endless patience, your unwavering love and support, and for always believing in me. Thank you for appreciating the scientific pursuit, and for making me laugh when it goes awry! To Jana, my smart, kind, beautiful daughter: You may not know it yet, but you have been my driving force, my true joy, my greatest treasure. Thank you for being you. Inshallah one day, as you carve your own path, I will be there to support and love you as you do for me.

Statement of Originality

The author confirms that she is the sole author of this dissertation enclosed herein and that it consists of the author's research during her doctoral program at Carleton University. The content of this thesis was reviewed and accepted by the thesis supervisors, Dr. Eric Vandervoort and Dr. Claire Foottit, who are clinical physicists at The Ottawa Hospital Cancer Centre, where most of this thesis work was conducted.

Dr. Eric Vandervoort and Dr. Claire Foottit were involved in all aspects of this thesis work, including but not limited to, revising the author's written work, reviewing proposed phantom designs and experimental methodology, conducting experiments, and reviewing results of experiments, empirical calculations, treatment planning system calculations, and Monte Carlo simulations. All data acquisition and analyses were conducted by the author, except for magnetic resonance imaging (MRI) scans which were performed with Dr. Claire Foottit, and the final experiments performed during the COVID-19 pandemic, which were conducted with Dr. Eric Vandervoort and Dr. Claire Foottit. The author also worked with Dr. Eric Vandervoort to develop the MATLAB scripts used for analyzing X-ray and MRI based images. All other software analysis techniques and in-house scripts were developed by the author.

The research projects enclosed in this thesis have been presented at conferences and seminars, as well as published as manuscripts and conference abstracts. Details of which, along with the author's contributions, are provided below:

Peer-reviewed manuscripts (The author's name is highlighted in bold):

- I. **Aldosary, G.**, Belec J., Foottit, C., Vandervoort, E. *Dosimetric Considerations for Moldable Silicone Composites Used in Radiotherapy Applications*. Journal of Applied Clinical Medical Physics. Accepted (Publication in progress). This paper encompasses the work presented in Chapter 5. The author's contributions include, but were not limited to, preparation of the phantoms used and research materials, experimental design, mathematical calculations, treatment planning system calculations, Monte Carlo simulations, conducting experiments, and preparation of the manuscript.
- II. **Aldosary G**, Caudrelier JM, Arnaout A, Chang L, Tse T, Foottit C, Song J, Belec J, Vandervoort E. *Can we rely on surgical clips placed during oncoplastic breast surgery to accurately delineate the tumour bed for targeted breast radiotherapy?* Breast Cancer Research and Treatment. 2021 Apr;186(2):343-352. doi: 10.1007/s10549-020-06086-3. Epub 2021 Jan 23. PMID: 33484375. The author's contributions include, but were not limited to, preparation of the breast phantoms and other research materials, experimental design, acquiring CT images, treatment planning system calculations and analysis, treatment planning system contouring (of the true tumour beds), preparing in-house scripts for image analysis, additional software analysis, and preparation of the manuscript.
- III. **Aldosary, G.**, Tse, T., Arnaout, A., Caudrelier, J-M., Czernyj, C., Romain, R., McLean, L., Foottit, C., Vandervoort, E., Belec, J. 2020. *Radiological, dosimetric and mechanical properties of a deformable breast phantom for radiation therapy*

- and surgical applications.* Biomedical Physics and Engineering Express. 6 035028. The author's contributions include, but were not limited to, testing and validating the breast phantom prototype by optimizing the phantom recipe, preparing research materials, mechanical testing and data analysis, multi-modality imaging and image analysis, and preparation of the manuscript.
- IV. **Aldosary, G.**, Szanto, J., Holmes, O., Lavigne, B., Althobaity, W., Sheikh, A., Foottit, C., Vandervoort, E. 2020. *Geometric inaccuracy and co-registration errors for CT, DynaCT and MRI images used in robotic stereotactic radiosurgery treatment planning.* Physica Medica, 69, pp. 212-222. The author's contributions include, but were not limited to, experimental design, optimizing 3D printing design and prototypes, preparation of additional research materials, multi-modality image acquisition and analysis, analyzing images through the specified treatment planning system, preparing in-house scripts for image analysis, and preparation of the manuscript.
- V. Song, J., Tang, T., Caudrelier, J-M, Belec, J., Chan, J., Lacasse, P., **Aldosary, G.**, Nair, V. 2020. *Dose-sparing effect of deep inspiration breath hold technique on coronary artery and left ventricle segments in treatment of breast cancer.* Radiotherapy and Oncology. 154: pp 101-109. The author contributed to this work by extracting clinical patient data, reporting metrics of interest, and reviewing the prepared manuscript.

Conference abstracts (The author's name is highlighted in bold, and the Asterix indicates the presenting author):

- I. **Aldosary, G.***, Caudrelier, J-M, Tse, T., Arnaout, A., Foottit, C., Belec, J., Vandervoort, V. *Can oncoplastic breast surgery impact radiotherapy treatment planning?* The Ottawa Hospital Research Institute Research Day. November 17-18, 2021. Abstract P-6. PhD Student Oral Poster Competition Winner.
- II. **Aldosary, G.***, Belec, J., Foottit, C., Vandervoort, V. *Dosimetric considerations of moldable silicones for radiotherapy boluses and phantoms.* AAPM Annual Scientific Meeting. July 25-29, 2021 (Virtual). ePoster July 25, 2021; 323099; 57404.
- III. **Aldosary, G.***, Caudrelier, J-M, Tse, T., Arnaout, A., Foottit, C., Belec, J., Vandervoort, V. *Investigation of tumor bed delineation accuracy for targeted breast radiation therapy following oncoplastic breast surgery.* AAPM|COMP Joint Scientific Meeting. July 12-16, 2020 (Virtual). Therapy Scientific Session: Treatment Planning and Delivery Techniques. Abstract 04.
- IV. **Aldosary, G.***, Szanto, J., Althobaity, W., Sheikh, A., Holmes, O., Foottit, C., Vandervoort, V. *Measurement of multimodality image geometric inaccuracies and co-registration errors for robotic stereotactic radiosurgery treatment planning with a 3D printed phantom.* ICRM, Riyadh, 2020, February 9-13. 3D Printing Session, Abstract 02.
- V. **Aldosary, G.***, Tse, T., Lee, W., Alotaibi, T., Foottit, C., Caudrelier, J-M., Vandervoort, E., Belec, J. *Radiological and dosimetric characterization of a*

customizable breast phantom for radiotherapy and surgical applications. AAPM Annual Scientific Meeting, July 12-15, 2019, San Antonio, Texas. ePoster # WE-C1030-GePD-F6-5. Published Abstract: Med. Phys. 46(6), e450-e450 (2019).

- VI. **Aldosary, G.***, Tse, T., Arnaout, A., Caudrelier, J-M., Romain, R., Lavigne, B., Song, J., Vandervoort, E., and Belec., J. *Are post oncoplasty surgical clips a reliable radiographic surrogate of breast tumor bed locations? A phantom based study.* CARO Annual Scientific Meeting, Oct 2-5, 2019, Halifax, Canada. Meeting abstract # 164. Published Abstract: Radiotherapy & Oncology 139, Suppl. 1, S70-S71 (2019).
- VII. **Aldosary, G., Tse, T.***, Arnaout, A., Caudrelier, J-M., Foottit, C., Vandervoort, E., Belec, J. *A cost efficient, realistic breast phantom for oncoplastic breast surgery training.* Canadian Surgery Forum, Sep 5-7, 2019, Montreal, Canada. Abstract CAGS-31. Published Abstract: Canadian Journal of Surgery Vol 62 (4 Suppl 2) August 2019.
- VIII. Miksys, N., Lekx-Toniolo, K., **Aldosary, G.**, Buckley, L.*., La Russa, D., MacPherson, M. and Vandervoort, E. *Site preparation, acceptance and commissioning of the GammaPod Accelerated Partial Breast Irradiation System.* Scientific Session 6: Special Techniques, Abstract 03. COMP Annual Scientific Meeting, Sep 24-27, 2019, Kelowna, Canada. Published Abstract: Medical Physics. 46(11), 5400-5400. (2019).
- IX. Song, J.*., Belec, J., Caudrelier, J-M., Lacasse, P., **Aldosary, G.** and Nair, V. *Dose-sparing effect of deep inspiration breath hold technique on coronary artery and left ventricle segments.* CARO Annual Scientific Meeting, Oct 2-5, 2019, Halifax,

- Canada. Meeting Abstract # 118. Published Abstract: Radiotherapy & Oncology, 139, Supplement 1, S51-S52 (2019).
- X. Song, J.* , Belec, J., Caudrelier, J-M., Lacasse, P., **Aldosary, G.** and Nair, V. *Dose-sparing effect of deep inspiration breath hold technique (DIBH) on coronary artery segments.* ASTRO ASM, Chicago, 2019 September 15-18. Meeting abstract # 3661. Published Abstract: International Journal of Radiation Oncology Biology Physics 105(1), e712-e712 (2019).
- XI. **Aldosary, G.***, Szanto, J., Holmes, O., Foottit, C., Vandervoort, E., *Assessing collective errors in image registration and geometric accuracy of CT, MRI and 3D angiography images for radiosurgery planning with the CyberKnife Software.* CARO-COMP-CAMRT Joint Scientific Meeting, Sep 12-15, 2018, Montreal, Canada. Poster Abstract 367.

Seminar presentations (The author's name is highlighted in bold, and the Asterix indicates the presenting author):

- I. **Aldosary, G.***, Foottit, C., Vandervoort, E. *The reliability of surgical clips for defining radiotherapy treatment targets following oncoplastic breast surgery.* Presented at The Ottawa Medical Physics Institute (OMPI) Seminar, February 25th, 2021.
- II. **Aldosary, G.***, Foottit, C., Vandervoort, E. *Development and characterization of a realistic breast phantom for medical physics applications.* Presented at The Ottawa-Carleton Institute of Physics (OCIP) Seminar, December 22nd, 2020.

- III.** **Aldosary, G.** *Are post-oncoplastic surgical clips reliable radiographic surrogates of breast tumour bed locations for adjuvant radiotherapy?.* Presented at the Radiation Medicine Rounds, The Ottawa Hospital Cancer Centre, September 30th, 2020.
- IV.** **Aldosary, G.***, Foottit, C., Vandervoort, E. *Evaluation of MRI geometric inaccuracy for MRI-based treatment planning on GammaPod.* Presented at The Ottawa Medical Physics Institute (OMPI) Seminar, January 17th, 2019.

Table of Contents

Dedication.....	1
Abstract	i
Acknowledgements	iii
Statement of Originality.....	vi
Table of Contents.....	xiii
List of Tables.....	xvii
List of Figures	xxiii
List of Abbreviations and Symbols	xxxvi
Chapter 1: Introduction.....	1
1.1 Breast cancer	1
1.1.1 Incidence and prognosis	1
1.1.2 Breast cancer treatment.....	2
1.2 Overview of standard external beam breast adjuvant radiotherapy	8
1.2.1 Patient setup, immobilization devices, and CT simulation.....	11
1.2.2 Target definition, dose prescription, and treatment planning	12
1.2.3 Treatment setup and verification	14
1.3 Advancements in external beam breast radiotherapy	17
1.3.1 Respiratory motion management.....	17
1.3.2 The use of magnetic resonance imaging.....	21
1.3.3 Technological advancements in radiotherapy delivery	25
1.3.4 Accelerated partial breast irradiation.....	26
1.4 The use of phantoms in medical physics applications	32
1.5 Thesis motivation	36
1.6 Thesis overview	37

Chapter 2: Geometric Distortions and Image Co-Registration Errors of Radiological Images Used in Robotic Stereotactic Radiosurgery	40
2.1 Introduction.....	40
2.2 Materials and methods	44
2.2.1 Phantoms and definitions of points of interests (POI's).....	45
2.2.2 Imaging setup, modalities, and characteristics	50
2.2.3 Image analysis and measurement of POI positions	56
2.3 Results	63
2.3.1 CNR comparison	63
2.3.2 Target registration errors for treatment planning CT's with varying imaging protocols	67
2.3.3 Target registration errors (TRE's) for different imaging modalities	69
2.4 Discussion	71
2.5 Conclusions.....	77
Chapter 3: Measurement of MRI Geometric Distortion for Breast Radiotherapy Treatment Planning.....	80
3.1 Introduction.....	80
3.2 Materials and methods	83
3.2.1 Phantom design.....	83
3.2.2 Imaging setup and protocols	86
3.2.3 Image analysis techniques	89
3.3 Results	93
3.3.1 CT imaging	93
3.3.2 MR imaging	97
3.4 Discussion	106
3.5 Conclusions.....	110

Chapter 4: Development and Characterization of a Deformable, Realistic Breast Phantom for Surgical, Radiotherapy Planning, and Dosimetric Applications.....112

4.1	Introduction.....	112
4.2	Materials and Methods.....	115
4.2.1	Breast phantom fabrication.....	115
4.2.2	Validation through surgical simulation	123
4.2.3	Characterization of mechanical properties	124
4.2.4	Characterization of radiological properties	127
4.3	Results	132
4.3.1	Validation through surgical simulation	132
4.3.2	Characterization of mechanical properties	133
4.3.3	Characterization of radiological properties	137
4.4	Discussion	140
4.5	Conclusions.....	145

Chapter 5: Dosimetric Considerations of Moldable Silicones for Radiotherapy Bolus and Phantom Applications147

5.1	Introduction.....	147
5.2	Materials and Methods.....	152
5.2.1	Description of phantoms.....	154
5.2.2	Experimental setup	156
5.2.3	CT imaging and TPS calculations	162
5.2.4	Monte Carlo simulations.....	164
5.3	Results	165
5.3.1	Dosimetric quantities of silicone	165
5.3.2	Experimental and TPS calculations	166
5.3.3	Monte Carlo simulations.....	173

5.4	Discussion	175
5.5	Conclusions.....	181
Chapter 6: The Reliability of Surgical Clips as Radiographic Surrogates of Tumour Beds Following Oncoplastic Breast Surgery	183	
6.1	Introduction.....	183
6.2	Materials and Methods.....	186
6.2.1	Breast phantom preparation.....	187
6.2.2	Preoperative planning, surgical simulation, and CT imaging.....	190
6.2.3	Image handling and contouring	193
6.2.4	Comparison metrics	195
6.3	Results	196
6.4	Discussion	205
6.5	Conclusions.....	210
Chapter 7: Conclusions and Future Work.....	211	
7.1	Summary and conclusions	211
7.2	Future work	216
7.2.1	Optimization of MRI protocols for APBI.....	217
7.2.2	Further applications of the realistic breast phantom.....	218
7.3	Outlook.....	219
Appendices	221	
Appendix A . Example of an Inadequate Imaging Protocol on DynaCT for Stereotactic Radiosurgery Treatment Planning.....	222	
Appendix B . Summary of 3D Printing Technologies Used in Medical Applications	224	
References	227	

List of Tables

Table 1.1 A summary of the oncoplastic breast surgery (OBS) classification system proposed by Arnaout <i>et al.</i> [10], in which OBS techniques are classified depending on their level of complexity (I, II, or III in increasing order).....	7
Table 1.2 Summary of respiratory motion management strategies used in radiotherapy [44]. This table includes the general concept behind each strategy, various sub-types, defines which step of the radiotherapy process the strategy is implemented (a diagram showing the full radiotherapy process is provided in Figure 1.3), and highlights some workflow considerations, as well as the applicability of each strategy to breast radiotherapy	19
Table 1.3 A summary of select randomized controlled APBI trials (administered as adjuvant radiotherapy after BCS). Trials utilizing external beam radiotherapy techniques are highlighted in bold text. The control arms for all these trials were WBRT techniques.	
<i>Abbreviations:</i> APBI= accelerated partial breast irradiation, BCS= breast conserving surgery, EB= external beam, CRT= conformal radiotherapy, IMRT= intensity modulated radiotherapy, WBRT= whole breast radiotherapy, IORT= intraoperative radiotherapy, MIB= Mammosite interstitial brachytherapy, HDR= high dose rate brachytherapy, PDR= pulsed dose rate brachytherapy, IBTR= ipsilateral breast tumour recurrence, QOL= quality of life.	29
Table 2.1 Imaging modalities, scan parameters and phantoms included in this study. Scan parameters were chosen based on the department's standard imaging protocols for stereotactic radiosurgery planning using CyberKnife®. For DynaCT: $\Delta\theta$ is the angular	

range of the data acquisition arc for the DynaCT cone beam system, and t is the rotation time. Abbreviations: TPCT= treatment planning CT, dCTA= helical CT imaging system used for angiography, DynaCTA= DynaCT imaging system used for angiography, TR= repetition time, TE= echo time, FA= flip angle, T1w= T1 weighting, T2w= T2 weighting.

.....52

Table 2.2 Scan parameter changes for image sets acquired with CT using the head phantom with the Ball-Cube II (Cube A). Scan No. 1 is taken as the reference image for this phantom only. A reference image set of the rod phantom (Cube B) was also acquired, and image sets of the 3D printed phantom lattice (Cube C) were also required under all the setup conditions listed below.....55

Table 2.3 Relative CNR values of original and filtered (post image inversion) CT and MR image sets of phantom Cube C (i.e., the 3D lattice phantom). Calculated CNR values are normalized to the original readings obtained from the non-filtered CT. Negative values indicate that the signal intensity in the ROI within the lattice structure was low compared to the contrast medium. Example image slices corresponding to these image sets are shown in Figure 2.8.64

Table 3.1 Details of the phantom setups and imaging parameters and phantom setups used for the reference CT image (image series number 1), as well as scans used to test the robustness of the phantom design, 3D printing quality, and image analysis method applied in this study.....87

Table 3.2 Details of the phantom setups and MR imaging pulse sequences used to measure system and sequence-dependent geometric distortions.....88

Table 3.3 A summary of the maximum and mean geometric radial distortion errors (r) for different phantom setups and different CT imaging protocols.....	95
Table 3.4 A summary of the maximum and mean geometric radial distortion errors (r) for different phantom setups and different MR pulse sequences. The pairwise maximum and mean differences in r for each image sequence, and under the same setup, but with opposing phase encoding readout directions are also compared.....	102
Table 4.1 The manufacturer reported [214] mechanical properties of Ecoflex™ silicone products (Smooth-On Inc., PA, USA) used for initial testing while constructing a realistic breast phantom.....	117
Table 4.2 Different types of Ecoflex® silicone materials tested for fabricating various breast phantom prototypes and their components (the epidermis, parenchyma, and the chest wall). Additive materials were also used to reinforce the epidermis (using mesh fabric), or to increase the elasticity and softness of the breast parenchyma (such as the Slacker® silicone mutator or silicone oil). The final breast phantom prototype is based on prototype number 8.....	119
Table 4.3 The ultimate tensile strength and strain on rupture as measured for the phantom parenchyma and skin, measured pig fat, and human skin (as reported in literature [223]).	
.....	137
Table 4.4 Measured SNR and CNR for the phantom parenchyma and surgical clips on various imaging modalities (CT, MRI, and US). Imaging protocols can be found in Section 4.2.4.C.1. CNR is calculated between surgical clips and phantom parenchyma. Note that SNR and CNR involving surgical clips were not calculated on MRI images due to their lack of signal	139

Table 4.5 A comparison of the measured T ₁ and T ₂ relaxation times for the breast phantom parenchyma to those of published values for silicone breast implants and patient breast fat.	139
Table 5.1 Stoichiometric data and fractional weight of each element found in different media of interest used in this study. Each element is listed with its atomic number (Z), provided in brackets.	154
Table 5.2 Physical quantities related to radiation attenuation and absorption, as reported for generic silicone, and compared to common materials used in radiotherapy dosimetry (namely, Solid Water and Water).	166
Table 5.3 Uncertainty budget of dose value readings of the Markus IC measurements in both photon (Co-60 and 6 MV) and electron (6 MeV and 15 MeV) beams.	167
Table 5.4 Uncertainty budget of net optical density readings obtained with EBT3 film for photon and electron beams. Note that Co-60 photon beams and 15 MeV electron beams were performed using one piece of film only, whereas 6 MV photon beams and 6 MeV electron beams were performed using four pieces of film which resulted in a reduced overall uncertainty.	168
Table 5.5 DSW – SWMS – SW and DSW – SWMS – MS values at 100 SAD and variable depths, in a Co-60 photon beam from experimental measurements and MC simulations (DOSXYZnrc). Note that MC simulations were performed for a generic form of silicone, therefore the same simulation output data is provided for both types of silicone (E10 and E50).	170
Table 5.6 DSW – SWMS – SW and DSW – SWMS – MS values at 100 cm SAD and two depths, in a 6 MV photon beam from experimental measurements, TPS-CC	

calculations (using Collapsed Cone Convolution Algorithm), TPS-MC (using Monaco's MC Calculation Algorithm) and MC simulations (DOSXYZnrc). Note that MC simulations and TPS calculations were performed for a generic form of silicone, therefore the same resulting output data is provided for both types of silicone (E10 and E50).....171

Table 5.7 **DSW – SWMS – SW** and **DSW – SWMS – MS** values at 100 cm SAD and 1.5 cm depth, in a 6 MeV and 15 MeV electron beams from experimental measurements and TPS-MC (using Monaco's MC Calculation Algorithm). Note that TPS calculations were performed for a generic form of silicone, therefore the same calculation data is provided for both types of silicone (E10 and E50).....172

Table 6.1 Details of each phantom case and the corresponding OBS technique used. The distance from the nipple and depth of the tumours were measured on projection radiographs generated from CT images. The breast, tumour, and specimen volumes (extracted tissue) were derived from CT images. The number of surgical clips and surgical staples used were counted prior to surgical closure and verified on CT images.

.....189

Table 6.2 The ranges of tumour bed (TB) contour structure volumes, before and after applying expansion margins, as well as the ranges of under-contoured volumes (*i.e.*, TB_{True} volumes that were not included in radiation oncologists TB_{RO1} and TB_{RO2} contours) and over-contoured volumes (*i.e.*, “healthy” breast volumes that were included in radiation oncologists TB_{RO1} and TB_{RO2} contours). Note: all radiation oncologists’ contours are taken in comparison with TB_{True}.....201

Table 6.3 Comparison of the Dice Similarity Coefficient (DSC) of contour structure volumes for each OBS technique. The radiation oncologists’ contours are relative to

TB_{True} . The Difficulty Score for each case was provided by RO₁. Abbreviations: IPRM= inferior pedicle reduction mammoplasty, SMRM= superior medial reduction mammoplasty, and SMPVRM= superior medial pedicle vertical reduction mammoplasty.

.....202

List of Figures

Figure 1.1 Comparison of breast tissue excision volumes and excision patterns for different types of breast conserving surgeries (BCS) and a mastectomy. Diagrams are reprinted with permission from Patient Resources LLC. © 2021 Patient Resources LLC. 3

Figure 1.2 Example oncoplastic breast surgery techniques according to the original tumour or tumours' location(s), which are shown as a black dot(s). This figure is reproduced with permission from Figure 12 in the manuscript published by MG Berry *et al.* "Oncoplastic breast surgery: A review and systematic approach. *Journal of Plastic, Reconstructive & Aesthetic Surgery*. 2010; 63, 1233-1243. Copyright Elsevier (2010)"...6

Figure 1.3 A diagram showing steps of the radiotherapy treatment process. Steps specific to radiotherapy are highlighted in blue, and those that precede or follow radiotherapy are in grey. These steps are informed by clinical protocols, which are identified in white boxes. This diagram is modified from the original Figure 1 in the report by International Atomic Energy Agency. Commissioning, and quality assurance of computerized planning systems for radiation treatment of cancer, Technical Reports Series No. 430, IAEA, Vienna (2004).....10

Figure 1.4 An example patient plan for a left-sided breast radiotherapy treatment in a supine position with the ipsilateral arm elevated. The treatment volume (ipsilateral breast) and nearby radiosensitive organs are shown in orthogonal CT views: (a) axial, (c) coronal, and (d) sagittal. The tumour bed and associated planning target volume (PTV), which will receive sequential additional "tumour bed boost" radiation, are also displayed in the sagittal view (d). Beam directions are indicated with respect to the 3D body view in (b), where the green block is the treatment couch. The prescribed radiation to the entire

breast volume is shown along axial, coronal, and sagittal views as the rainbow colour wash, with the orange/yellow colours displaying the relative 100% prescription dose volume.....14

Figure 1.5 Examples of supine and prone setups and associated immobilization devices shown at CT simulation and delivery for breast radiotherapy. (a) An example immobilization device (the Access™ Supine Breast Board, Qfix, Avondale, PA, USA). (b) A patient positioned for left-sided breast radiotherapy CT simulation. (c) Another patient positioned with this device for treatment on a linac. Note that the patient shown in (b) underwent adjuvant radiotherapy after a mastectomy, whereas in (c), the patient's breast is intact after a lumpectomy. (d) and (e), a prone setup immobilization device (the Bionix Prone Breast System, Bionix, Toledo, Ohio, USA). (f) A patient undergoing CT simulation for right-sided breast radiotherapy. Figure shown in (a) was adapted from www.qfix.com, and all other images are courtesy of Mr. Steve Andrusyk, RTT (The Ottawa Hospital General Campus Cancer Centre).16

Figure 1.6 An example of breast patient prone setup positioning challenges in MRI imaging. Here, three scenarios are presented. (A) The lack of space for a posteriorly placed receiver coil can cause a cutoff of the body contour and reduced signal-to-noise ratio (SNR). (B) A more ideal setup in which there is space to include the receiver coil and allow the breast to hang freely. (C) An attempt to place a posterior receiver coil for a prone positioned patient causes the breast to touch the tabletop (couch) and deform. This figure is reproduced with permission from Figure 2 in the manuscript by Groot Koerkamp ML *et al.* “Optimizing MR-guided radiotherapy for breast cancer patients. *Frontiers in Oncology*. 2020:1107”.25

Figure 2.1 Top: Accuray's E2E anthropomorphic head phantom, with the commercial phantom insert (Cube A) in place. Bottom: The three investigated phantom insert cubes assessed in this study. All inserts have identical external dimensions, but with different designs. On the left is the commercial phantom containing gold fiducials and copper markers, the middle is the rod phantom (Cube B), and on the right is the 3D printed lattice phantom in the acrylic housing (Cube C)	48
Figure 2.2 Multiple views of the rod phantom's (Cube B) 3D computer-aided design (CAD) drawing. The acrylic rods (filled with air) were placed orthogonally and on different levels in the cube. The inter-rod space was filled with MR contrast.....	49
Figure 2.3 Multiple views of the 3D printed phantom's (Cube C) CAD drawing. The lattice is shown without the external acrylic housing, which was filled with contrast solution for MR imaging and provided an additional thickness of 10.00 mm on each cube side.....	50
Figure 2.4 The registration box (shown on a CT image) used to define the volume of interest for image co-registration is shown on the left. The magenta circles show the gold fiducials as found by MultiPlan's Auto Centre algorithm. The smaller high density objects are the copper markers.	57
Figure 2.5 Two axial MR image slices from different positions along the longitudinal direction of phantom Cube B (the rod phantom). The white circles highlight the same rod shown on an axial slice showing a region of interest where clear distinction of the rod is found (left side image), and on another axial slice showing a region of interest where MRI artifacts cause two adjacent orthogonal rods to appear connected, thus biasing the calculated centre of mass for that rod on that axial slice (right side image).	59

Figure 2.6 An illustration of the effect of convolution on a reference CT image slice. (a) An axial image from the raw data shown in pixel representation (physical dimensions= 53.00 x 53.00 x 53.00 mm³), (b) the 3D cross-like convolution filter, shown with voxels set to one as red. (c) The resulting convolved image. (d) The convolved image after a threshold is applied, where the threshold is based upon the maximum value in spherical regions of interest (ROIs) around the expected lattice intersection points. The centroid inside the thresholded data inside each spherical ROI is determined using data after the step shown in (d). The ROIs used for the CNR analysis are also shown in (a) and (c), where the black circles show the signal region, and the magenta circles show the background regions.60

Figure 2.7 Representative images of the CyberKnife head phantom with different Cube inserts: (a) a reference TPCT of Cube A, (b) DynaCT of Cube A, (c) reference TPCT of Cube C, and (d) DynaCT of Cube C. Image slices from the CT system used for angiography are not shown due to their similarity to the reference TPCT.....65

Figure 2.8 Example axial image slices of phantom Cube C from co-registered image sets; (a) a reference TPCT (in air), (b) a low contrast TPCT (in MRI contrast solution), (c) a T1w MRI, and (d) a T2w MRI. Images shown are from the same z slice on co-registered image sets. The measured relative CNR for these image slices are provided in Table 2.3.

.....66

Figure 2.9 Measured mean target registration errors (TRE's) for Cubes A and C with the treatment planning CTs (Philips Big Bore scanner) acquired using variable imaging parameters. Results for Cube A (Accuray's commercial phantom) are shown using MultiPlan and MATLAB, for two cases: when the gold fiducials are taken as the points

of interest (top figure), and when the copper markers are taken as the points of interest (middle figure). In comparison, the mean TRE's using the 3D printed lattice phantom are shown in the lower figure. The error bars represent one standard deviation of the mean TRE value determined for that respective image set.....68

Figure 2.10 Measured mean target registration errors (TRE's) for different imaging modalities as given by Cube A (with both gold (Au) fiducials and copper (Cu) markers), Cube B (rod phantom) and Cube C (3D printed lattice). TPCT refers to the CT simulator (Philips Big Bore) used as the reference scanner. The CT (Toshiba Aquilon) and DynaCT (Siemens Artis Q) scanners are those used for dCTA and DynaCTA, respectively. Results from MultiPlan are shown in black, and those from MATLAB are in blue. The error bars represent one standard deviation of the mean TRE value determined for that respective image set.....70

Figure 3.1 (a) Design of the large 3D printed lattice cube phantom with measurements showing the cube's dimensions, the inter-lattice line distance (10.0 mm), and the lattice line thickness (3.0 mm). (b) A top view of the 3D printed phantom inside the custom built PMMA housing with the lid on. In this photo, the phantom was setup for CT imaging with the lattice in air. The leveling platform is indicated by the red arrow. (c) A front view of the phantom, with the lattice submerged in MR contrast. (d) An image of the phantom's centre setup in alignment with the MR scanner's isocentre.85

Figure 3.2 4 Image slices from CT scans of the 3D printed phantom in the phantom housing. Images are shown along orthogonal slice directions (axial, coronal, and sagittal) and the physical directions with respect to the phantom are shown for orientation purposes. CT scans were taken with different parameters and setups, details of which are

listed in Table 3.1. Displayed CT image slices were acquired at the same axial slice with
image window= 600 and image level= 40.....94

Figure 3.3 The magnitude of radial geometric distortion errors (r) for images of the 3D
printed phantom acquired with the CT scanner shown as a function of radial distance
from the scanner isocentre. The radial geometric distortion error represents the difference
between the radial position of a particular POI compared with its radial position on the
reference CT scan, which was acquired in air, with slice thickness (t) of 0.5 mm, 120
kVp, and 350 mAs. The dashed black lines show the magnitude of the slice thickness in
mm for each scan used and are provided for visual comparison purposes only.96

Figure 3.4 MR images of the 3D printed phantom in the phantom housing filled with MR
contrast when the phantom was positioned at the scanner isocentre. The image series are
presented in reformatted orthogonal views (axial, coronal, and sagittal) through the centre
of the phantom for comparison. The physical directions with respect to the phantom are
shown for orientation. MR sequence details are listed in Table 3.2, and phase encoding
direction is indicated in parenthesis. Displayed MR image slices were captured at the
same imaging position, and with image window= 663 and image level= 370 for T1w
VIBE and T1w TSE sequences, and image window= 350 and image level= 200 for T2w
SPACE sequences.98

Figure 3.5 MR images of the 3D printed phantom in the phantom housing filled with MR
contrast when the phantom was shifted by 150 mm towards patient's right with respect to
the centre of the scanner isocentre. The image series are presented in reformatted
orthogonal views (axial, coronal, and sagittal) through the centre of the phantom for
comparison. The physical directions with respect to the phantom are shown for

orientation. MR sequence details are listed in Table 3.2, and phase encoding direction is indicated in parenthesis. Displayed MR image slices were captured at the same imaging position, and with image window= 663 and image level= 370 for T1w VIBE and T1w TSE sequences, and image window= 350 and image level= 200 for T2w SPACE sequences.....99

Figure 3.6 MR images of the 3D printed phantom in the phantom housing filled with MR contrast when the phantom was shifted by 150 mm towards patient's left with respect to the centre of the scanner isocentre. The image series are presented in reformatted orthogonal views (axial, coronal, and sagittal) through the centre of the phantom for comparison. The physical directions with respect to the phantom are shown for orientation. MR sequence details are listed in Table 3.2 and phase encoding direction is indicated in parenthesis. Displayed MR image slices were captured at the same imaging position, and with image window= 663 and image level= 370 for T1w VIBE and T1w TSE sequences, and image window= 350 and image level= 200 for T2w SPACE sequences.....100

Figure 3.7 The magnitudes of the radial distortion errors (r) shown as a function of the radial distance from the isocentre when the phantom cube was centered in the scanner bore. The radial distance includes the x, y, and z coordinates of each POI. Each subfigure shows the effect of a particular MR imaging sequence, as well as the phase encoding readout direction. The mean radial geometric error (r_{avg}) and the total number of POIs (n) included in the analysis are provided for each image set. The dashed black lines show the magnitude of the slice thickness in mm for each MR sequence used and are provided for visual comparison purposes only.....103

Figure 3.8 The magnitudes of the radial distortion errors (r) shown as a function of the radial distance from the scanner isocentre when the phantom cube was shifted 150 mm to the right from the scanner isocentre (as viewed from the foot of the couch). The radial distance includes the x, y, and z coordinates of each POI. Each subfigure shows the effect of a particular MR imaging sequence, as well as the phase encoding readout direction. The mean radial geometric error (r_{avg}) and the total number of POIs (n) included in the analysis are provided for each image set. The dashed black lines show the magnitude of the slice thickness in mm for each MR sequence used and are provided for visual comparison purposes only. 104

Figure 3.9 The magnitudes of the radial distortion errors (r) shown as a function of the radial distance from the scanner isocentre when the phantom cube was shifted 150 mm to the left from the scanner isocentre (as viewed from the foot of the couch). The radial distance includes the x, y, and z coordinates of each POI. Each subfigure shows the effect of a particular MR imaging sequence, as well as the phase encoding readout direction. The mean radial geometric error (r_{avg}) and the total number of POIs (n) included in the analysis are provided for each image set. The dashed black lines show the magnitude of the slice thickness in mm for each MR sequence used and are provided for visual comparison purposes only. 105

Figure 4.1 A step-by-step illustration of the breast phantom fabrication process. (a) The breast inverse mold being shaped from the breast attachment of an anthropomorphic body phantom, (b) The mold and phantom parenchyma with the marble tumour suspended in the desired position by a string. (c) The setup for adding the chest wall layer. (d) The phantom after adding the mesh fabric. (e) The final phantom after adding the epidermis,

areola, and nipple components. (f) A phantom marked for pre-op incision planning using an oncoplastic breast surgery crescent incision approach.....122

Figure 4.2 The setup for ultimate tensile strength measurements. (a) A photo of the BioTester's measurement plane with the sample suspended in place by the two biaxial claw attachments. (b) Sequential images of the phantom skin being tested at four different time points ($t=0$ s, 0.8, 2.4 and 4.8 s, corresponding to $F=0$, 561, 1923, and 309 mN, respectively). The sample's cross-sectional area along the testing plane was approximately $5 \times 5 \text{ mm}^2$125

Figure 4.3 Elasticity measurements for the different breast phantom prototypes tested. For reference, the material composition of each breast phantom components from Table 4.2 are repeated in this figure. Measurements were conducted using shear wave US elastography only.....135

Figure 4.4 Elasticity measurements for the final breast phantom prototype's components (parenchyma and epidermis) and pig fat, at various sample temperatures. Measurements were conducted using shear wave US elastography as well as mechanical testing. The reported range of patient data for breast fat and parenchyma acquired using shear wave US elastography [222] is shown between the dashed lines to contrast with the elastography measurements obtained.....136

Figure 4.5 The breast phantom as appearing on a) a CT axial view (window= 600, level=400), b) an ultrasound planar view (window=250, level=130), c) MRI T1w (window= 650, level= 300) and d) T2w (window= 800, level= 300) sagittal views. Breast components are identified as 1- epidermis layer, 2- parenchyma, 3-nipple, 4- areola, 5- chest wall, 6- surgical clips. Note that MRI and CT views are not taken along the same

axial slice to show different components. Images were acquired after the tumour was resected and surgical clips were placed. Surgical clips appear as a signal loss on MRI. 138

Figure 5.1 The molding process for the silicone slabs included using a custom-built acrylic open faced cuboid container, which had an optional Markus IC dummy insert that can be added at the base to form a slot for IC placement. The molded E10 and E50 silicone slabs are shown on the right-hand image. Slabs were wrapped in a thin cellophane plastic to prevent accumulation of dust.....156

Figure 5.2 Pictoral representations of the experimental setups used for each beam type. Photon beams were measured at depths of 1.5 cm and 5.0 cm: setups (1), (2), (3), (4), (5), and (6) as shown in (a) and (b). Electron beams were measured using 1.5 cm depth slabs: setups (1), (2), and (3) as shown in (a). IC measurements were conducted in the lower MS slabs that were made to fit the IC flush against its surface. The measurement points (at the interfaces) are identified with the “x” marker in the illustrations shown in (a) and (b) and evaluated dose ratios are shown in grey boxes. Measurements are compared to Monaco TPS calculations for 6 MV and to EGSnrc Monte Carlo simulations for Co-60 and 6 MV at the same depths. An example of one of the setups used for measurements in the Co-60 beam is provided in (c), in which the acrylic mold was used as a frame (the base was removed) to maintain the silicone slabs in an upright position for a lateral beam orientation. An example of one of the setups used for measurements in the 6 MV beam, using the Markus IC, is provided in (d). Measurements for 6 MeV and 15 MeV electron beams were conducted with a 10 x 10 cm² electron applicator in a similar setup to that shown in (d)......158

Figure 5.3 MC (DOSXYZnrc) simulation results showing relative dose values around the interface of two phantom slabs when different configurations of material placements were used: top and bottom phantoms slabs are Solid Water (SW-SW), the top slab is molded silicone and the bottom slab is solid water (MS-SW), or the top and bottom slabs are molded silicone (MS-MS). Results are shown using a Co-60 photon beam with a 1.5 cm top phantom slab thickness (a) and a 5.0 cm top phantom slab thickness (b), as well as for a 6 MV photon beam with a top phantom slab thickness of 1.5 cm (c), and a top phantom slab thickness of 5.0 cm (d). In all cases, the dose is presented relative to the dose at 100 cm SAD for the SW-SW setup at each respective depth and beam energy.

The field size and SAD for all simulations were $10 \times 10 \text{ cm}^2$, and 100 cm, respectively, and all simulations yielded values with uncertainties below 0.3%. Dose ratios from film measurements made with silicone E10 and E50 types are also shown for comparison..174

Figure 6.1 An example breast phantom (case 2) adhered to an acrylic plate (shown on the right). The BBs that were used to identify each phantom on the CT image are shown in the upper right corner of the plate (in this example, two were used). Prior to imaging each phantom, a reference frame was attached to the acrylic plate, as shown on the right. The reference frame had three additional BBs (one anterior and two lateral) that were used for setup laser alignment and to co-register multiple CTs of the same phantom.....188

Figure 6.2 The six breast phantoms used to simulate oncoplastic breast surgery with intended surgical incision lines indicated by the pen markings. This planning process is similar to what occurs during preparation of patients for a surgery, however, this type of photo/ diagram is usually not provided in a patient's post-operative note following oncoplastic breast surgery. *Abbreviations:* IPRM= inferior pedicle reduction

mammoplasty, SMRM= superior medial reduction mammoplasty, and SMPVRM= superior medial pedicle vertical reduction mammoplasty.....191

Figure 6.3 An example case (case 3, with a racquet OBS technique) shown during different phases and with the corresponding CTs. Step 1: CT1 is acquired prior to beginning surgery. Step 2: CT2 is acquired after the tumour was resected. Step 3: CT3 is acquired after OBS was performed and surgical closure was complete. Step 4: A copy of CT3 is generated, and a homogenous override of the relative electron density is applied to mask all features except the surgical clips. All steps show the breast phantom along the same CT slice.192

Figure 6.4 Surgical clip displacements measured on CT for each breast phantom case. Each clip displacement is shown separately along the three CT axis directions (a, b, and c), and the average and standard deviations of 3D displacement for all clips in each case (d). The displacements were calculated by comparing the final position of each surgical clip after oncoplastic breast surgery closure, with that to the initial clip position as found just after tumour excision. *Abbreviations:* IPRM= inferior pedicle reduction mammoplasty, SMRM= superior medial reduction mammoplasty, and SMPVRM= superior medial pedicle vertical reduction mammoplasty.....199

Figure 6.5 (a) A visual comparison of 3D rendered TBs for the same phantom case (case 3, racquet technique), before (CT2) and after OBS closure (CT3). CT image slices of a breast phantom with homogenous parenchyma density after OBS (case 2, inferior pedicle reduction mammoplasty) are shown on (b), (d) and (e).200

Figure 6.6 Comparison of the 3D distances between RO contours against each other (Intra-RO and Inter-RO). As well as differences between TB_{True} and RO contours

(without and with expansion margins). The HD_{max}, HD_{95%}, and HD_{avg} values are provided for each OBS technique as shown on the abscissa. *Abbreviations:* IPRM= inferior pedicle reduction mammoplasty, SMRM= superior medial reduction mammoplasty, and SMPVRM= superior medial pedicle vertical reduction mammoplasty.204

List of Abbreviations and Symbols

2D: two-dimensional

3D: three-dimensional

4DCT: four-dimensional computed tomography

$\left(\frac{\bar{L}}{\rho}\right)_{water}^{med}$: relative mean mass restricted stopping power ratio for a medium compared

with water

$\left(\frac{\bar{\mu}}{\rho}\right)_{water}^{med}$: relative mean mass energy-absorption coefficient ratio for a medium compared

with water

$(\frac{\mu}{\rho})$: photon mass attenuation coefficient

$(\frac{s_{col}}{\rho})$: electronic (collisional) mass collisional stopping power

ρ : mass density (in g/cm³)

ABC: active-breathing control

APBI: accelerated partial breast irradiation

AVM: arterio-venous malformation

BB: ball bearing

BCS: breast conserving surgery

BCT: breast conserving therapy

BID: bis in die (*Latin*), meaning two times a day

CC: Collapsed cone convolution

CBCT: cone beam computed tomography

CNR: contrast-to-noise ratio

CRT: conformal radiotherapy

CT: computed tomography

CTV: clinical-target-volume

cSt: centistoke

dCTA: dynamic computed tomography angiography

DIBH: deep inspiration breath hold

DSC: dice similarity coefficient

DynaCTA: DynaCT angiography

E10: Ecoflex™ 00-10 moldable silicone (Smooth-On Inc., PA, USA)

E2E: end-to-end

E50: Ecoflex™ 00-50 moldable silicone (Smooth-On Inc., PA, USA)

EB: external beam

EB-APBI: external beam accelerated partial breast irradiation

EBRT: external beam radiotherapy

ED: electron density

FA: flip angle

FIESTA: Fast Imaging Employed Steady-state Acquisition (MRI sequence)

FOV: field-of-view

GTV: gross-target-volume

HD: Hausdorff Distance

HD_{95%}: 95th percentile Hausdorff Distance

HD_{avg}: average Hausdroff Distance

HD_{max}: maximum Hausdorff Distance

HDR: high dose rate

HU: Hounsfield Unit

IBRT: ipsilateral breast tumour recurrence

IC: ionization chamber

IGRT: image guided radiotherapy

IMRT: intensity modulated radiotherapy

IORT: intraoperative radiotherapy

IPRM: inferior pedicle reduction mammoplasty

kV: Kilovolt

kPa: Kilopascal

MC: Monte Carlo

MeV: Mega-electron volt

MIB: Mammosite interstitial brachytherapy

MLC: multi-leaf collimator

MRgRT: magnetic resonance guided radiotherapy

MPa: Megapascal

MRI: magnetic resonance imaging

MS: moldable silicone

MU: monitor unit

MV: Megavolt

OAR: organ at risk

OBS: oncoplastic breast surgery

PBI: partial breast irradiation

PDR: pulsed dose rate

PET: positron emission tomography

PMMA: poly-methyl methacrylate

POI: point of interest

PTV: planning-target-volume

QA: quality assurance

QOL: quality-of-life

RED: relative electron density

RO: radiation oncologist

ROI: region of interest

SAD: source-to-axis distance

SMPVRM: superior medial pedicle vertical reduction mammoplasty

SMRM: superior medial reduction mammoplasty

SNR: signal-to-noise ratio

SPGR: Spoiled Gradient Recalled acquisition in the steady-state (MRI sequence)

SRS: stereotactic radiosurgery

SSD: source-to-surface distance

SW: Solid Water

T₁: spin-lattice relaxation time

T1a: breast tumour that is > 1 mm but ≤ 5 mm

T1b: breast tumour that is > 5 mm but ≤ 10 mm

T2b: breast tumour that is > 20 mm but ≤ 50 mm and has spread to 1 to 3 axillary lymph nodes, or is > 50 mm but has not spread to axillary lymph nodes

T_2 : spin-spin relaxation time

TB_{RO} : the tumour bed contoured by a radiation oncologist

TB_{True} : the true tumour bed

TE: echo time

TI: inversion time

TR: recovery time

TPS: treatment planning system

US: ultrasound

UTS: ultimate tensile strength

VMAT: volumetric modulated arc therapy

WBRT: whole breast radiotherapy

Z: atomic number

Z_{eff} : effective atomic number

Chapter 1: Introduction

This chapter begins by providing a broad overview on breast cancer, breast cancer treatment with emphasis on surgery and adjuvant radiotherapy, and the overall role of radiotherapy in the management of breast cancer. Standard-of-care external beam adjuvant radiotherapy is then discussed, and key advancements in external beam breast radiotherapy are highlighted. This chapter concludes by defining the motivation of this thesis and providing an overview of the thesis structure.

1.1 Breast cancer

1.1.1 Incidence and prognosis

It is estimated that one out of two Canadians will be diagnosed with cancer over their lifetime [1,2]. For women in Canada, breast cancer is the most commonly diagnosed cancer and the leading cause of cancer-related death [1,2]. Cancer screening programs play an important role in the early detection of breast cancer, and so most women are diagnosed with early-stage breast cancer, which is usually defined as Stages T1a, T1b, or T2b, with the tumour size ≤ 5 cm, and less than 3 lymph nodes involved [3]. For these cases, high 5-year survival rates of 93-100% are achievable [2].

1.1.2 Breast cancer treatment

Treatments of breast cancer often include combinations of breast surgery, endocrine therapy, adjuvant systemic (chemotherapy), and adjuvant radiotherapy. Due to the early detection of breast cancer, improvements in surgical techniques, new systemic options, and advances in the understanding of the disease pathology [3], outcomes for breast cancer treatment have significantly improved over the past few decades.

Breast Conserving Surgery:

Surgical approaches fall into two broad categories; breast mastectomy or breast conserving surgery (BCS), as illustrated in Figure 1.1. Breast mastectomies vary, and can include a radical mastectomy, which entails removal of the breast pectoral muscles with axillary lymph node dissection; modified radical mastectomy, where the entire breast is removed to the level of the pectoralis minor muscle with axillary lymph node dissection; total mastectomy, where the entire breast is removed to the level of the pectoralis muscle but no lymph nodes are dissected; skin sparing mastectomy, in which breast skin is preserved to enhance reconstructive cosmetic procedures, such as breast implants or expanders, and finally; total skin sparing mastectomy, where the skin and nipple areolar complex are preserved for further cosmetic reconstruction as well [4].

BCS techniques aim to preserve as much breast tissue as possible. BCS techniques include (in order of decreasing tissue removed): quadrantectomy; where a quadrant of the

breast is removed; wide excision, where a surgical specimen is resected to include the tumour bed and a large surrounding margin; and a lumpectomy (local excision), where a surgical margin is resected to include the tumour bed and a small surrounding margin [3].

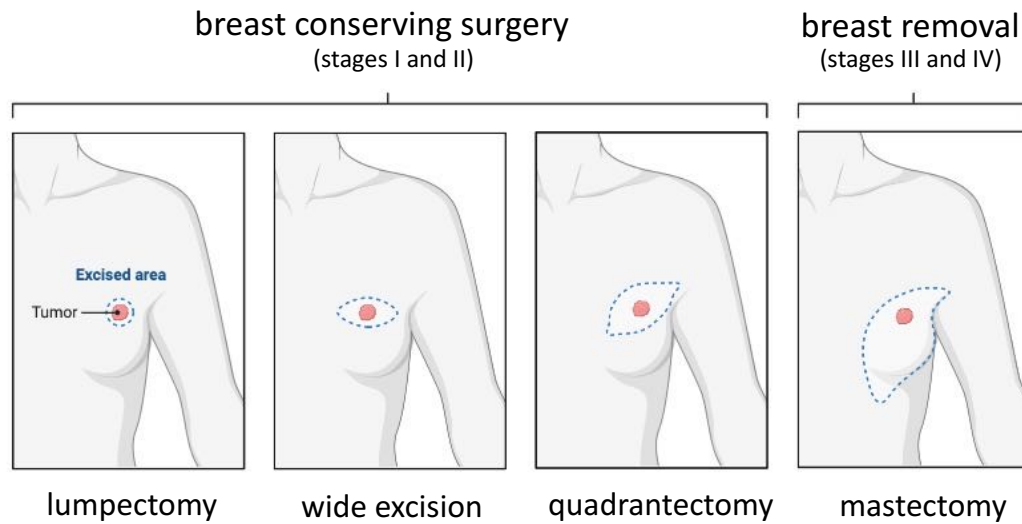


Figure 1.1 Comparison of breast tissue excision volumes and excision patterns for different types of breast conserving surgeries (BCS) and a mastectomy. Diagrams are reprinted with permission from Patient Resources LLC. © 2021 Patient Resources LLC.

Breast Conserving Therapy:

Breast conserving therapy (BCT), which includes conventional BCS (see diagrams in Figure 1.1) and adjuvant radiotherapy, is a well-established alternative to mastectomy for early-stage breast cancer. It is now offered as standard-of-care, as several large randomized trials worldwide have demonstrated that BCT and mastectomy are comparable in achieving locoregional tumour control [5–8]. An overview of standard-of-care external beam adjuvant breast radiotherapy is provided in Section 1.2.

Oncoplastic Breast Surgery:

For many decades, BCS has been the main surgical treatment for breast cancer. As mentioned previously, BCS is based on the principle of complete removal of cancer tissue with adequate surrounding margins while maintaining the natural breast shape. In many cases; however, the amount of excised breast tissue can be a limiting factor and so simultaneously achieving both goals can be challenging. For these cases, where it is imperative to remove cancer tissue, conventional BCS can subsequently result in poor cosmetic results.

In the past few years, oncoplastic breast surgery (OBS) has emerged as one of the new standards of care for BCS [9–12]. OBS differs from BCS, by offering wide tumour excision with improved cosmesis. In fact, the philosophy of OBS holds that “whenever surgery is performed on the breast, consideration of both cancer and esthetics must be critical components of the breast cancer treatment” [13]. This dual advantage has increased OBS’ popularity amongst breast cancer surgeons. To achieve better cosmesis, OBS integrates plastic surgery techniques during tumour excision, offering effective oncological surgeries with immediate reshaping of breasts.

Unlike with simple, conventional BCS approaches (see Figure 1.1), OBS can be performed through many different plastic surgery techniques that vary in complexity. Although an updated comprehensive atlas of these techniques is yet to be published, Figure 1.2. demonstrates some examples. In general, OBS techniques are based on two

main methods: 1- volume-displacement techniques, which uses dermoglandular displacement, rotation, and redistribution of breast tissue into the tumour cavity; and, 2-volume-replacement techniques, which compensates volume loss after tumour resection by using breast implant reconstruction or an autologous flap [14]. For the purpose of standardization of practices and surgical training in Canada, Arnaout *et al.* [10] proposed to classify OBS techniques based upon their associated levels of complexity. This classification is based on three levels as summarized in Table 1.1. The proposed system has been modified from the original European bi-level classification system which was initially introduced by Clough *et al.* [12].

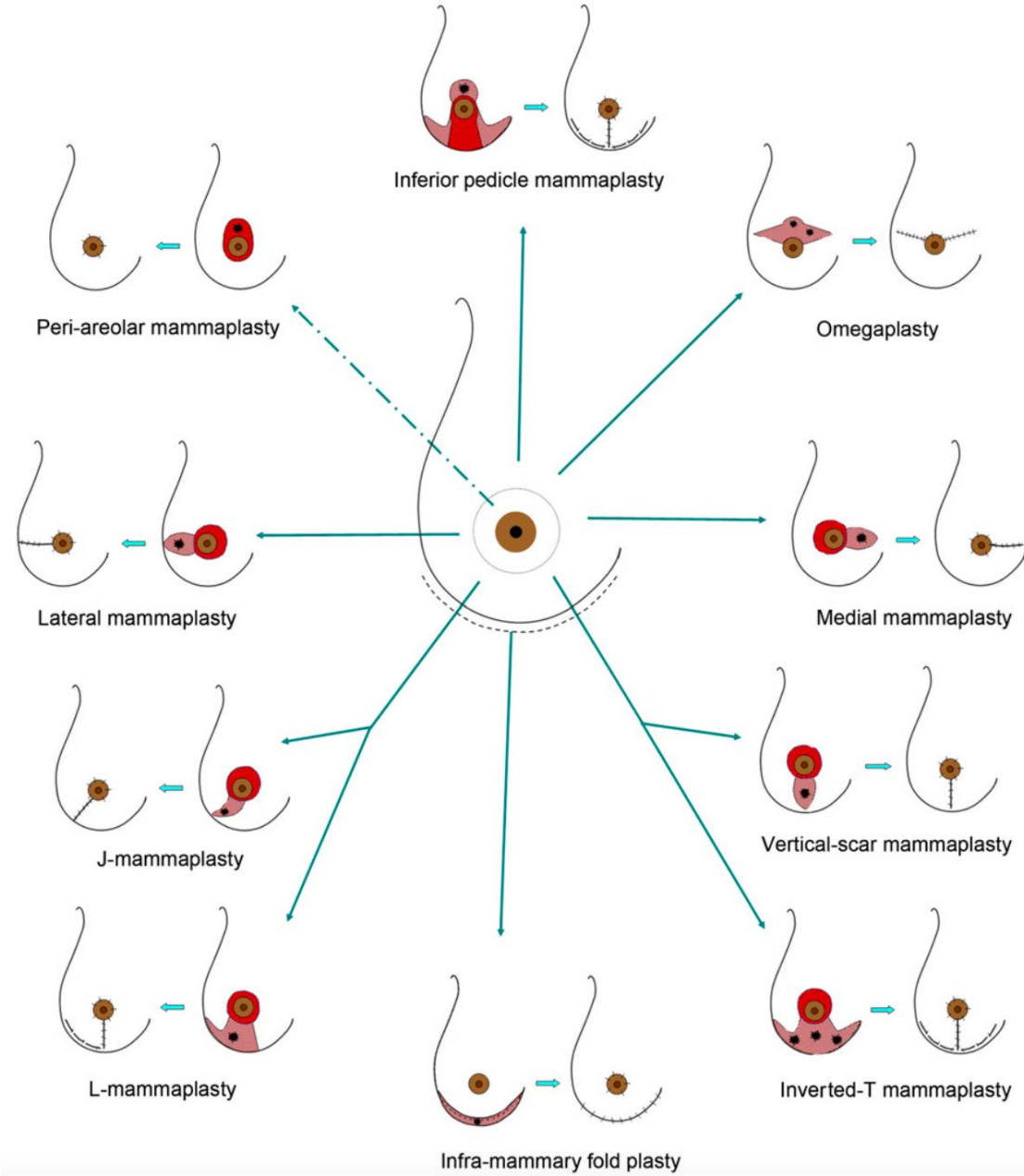


Figure 1.2 Example oncoplastic breast surgery techniques according to the original tumour or tumours' location(s), which are shown as a black dot(s). This figure is reproduced with permission from Figure 12 in the manuscript published by MG Berry *et al.* "Oncoplastic breast surgery: A review and systematic approach. *Journal of Plastic, Reconstructive & Aesthetic Surgery*. 2010; 63, 1233-1243. Copyright Elsevier (2010)".

Table 1.1 A summary of the oncoplastic breast surgery (OBS) classification system proposed by Arnaout *et al.* [10], in which OBS techniques are classified depending on their level of complexity (I, II, or III in increasing order).

<i>Level</i>	<i>Indication</i>	<i>Description of surgical components</i>	<i>Example technique names</i>	<i>Excised breast volume (%)</i>
I	Simple tumour resection	Dual plane undermining, nipple undermining, and glandular advancement.	Simple lumpectomy defect closure without skin resection	< 15
II	Tumour is in a cosmetically sensitive location	Glandular rotations, nipple recentralization, de-epithelialization to preserve blood supply to breast parenchyma and the nipple-areolar complex, and purposeful skin resection.	Crescent, racquet, batwing, or V or J mammoplasty	15 to 25
III	Large breasts requiring large resection margins for tumours > 5 cm.	Use of glandular pedicles and large displacements and rotations of residual breast tissue to fill tumour cavity defects and maintain blood supply to the nipple-areolar complex. May also perform a contralateral breast symmetry procedure of similar technique to improve overall cosmesis.	Vertical mammoplasty, wise-pattern reduction mammoplasty	25 to 60

OBS and its surgical implications on adjuvant radiotherapy will be discussed further in Chapter 6. For now, the next section focuses on standard-of-care external beam adjuvant breast radiotherapy following conventional BCS.

1.2 Overview of standard external beam breast adjuvant radiotherapy

“And so, without the blaring of trumpets or the beating of drums, X-ray therapy was born. The very first application of the X-ray for therapeutic purposes was made upon Ms. Rose Lee’s cancerous left breast, by myself”—Emil Grubbe, 1933 [15].

On January 29th, 1896, only a year after Wilhelm Rontgen discovered X-rays, radiation was used by Emil Grubbe and Dr. R. Ludlam in Chicago to treat a patient with advanced breast cancer [15]. The first ever breast radiotherapy treatment was delivered with low energy X-rays. Since then, clinical evidence and radiotherapy technology have evolved to provide safer and more effective treatments. Today, radiotherapy plays an important role in breast cancer treatment, and whole breast radiotherapy (WBRT) is indicated for all patients after BCS [16].

As with any planned external beam radiotherapy treatment, there are several steps required in the breast radiotherapy process (see Figure 1.3 for a summary of the radiotherapy process). The treatment aim is to direct radiation to the breast and any local lymph nodes while sparing nearby healthy organs-at-risk (OARs) such as the neighbouring heart, lungs, and contralateral breast. To achieve this, visualization of the treatment volume is necessary.

By the end of the 20th century, breast cancer radiotherapy techniques were based on 2D planning, where radiotherapy parameters were determined using a radiographic X-ray

simulator or a patient contour wire [17]. The intended radiotherapy dose was prescribed to a point along the central axis close to the centre of the breast. The central axis depth, radiation source-to-patient surface distance, and other treatment parameters were all determined at the time of simulation. Planar radiographic films acquired during simulation were often compared with port films during treatment [17]. Nowadays, the first technical step in the radiotherapy treatment process (see Figure 1.3), called treatment simulation, entails acquiring 3D images of the patient's treatment anatomy. Adopting computed tomography (CT) imaging in the simulation process has provided better insight on breast tissue anatomy, facilitated better dose distribution uniformity, and allowed measures to be taken to reduce radiation dose to OARs [18]. A brief description of the CT simulation step, as well as subsequent steps in the radiotherapy process are provided in the subsections below.

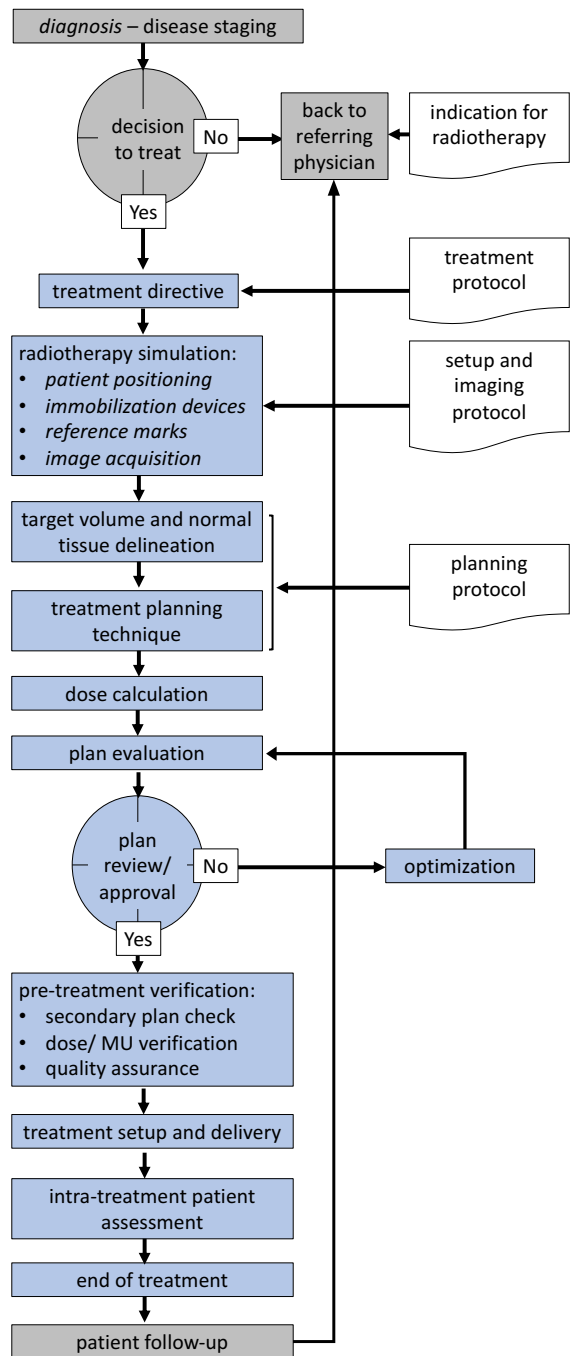


Figure 1.3 A diagram showing steps of the radiotherapy treatment process. Steps specific to radiotherapy are highlighted in blue, and those that precede or follow radiotherapy are in grey. These steps are informed by clinical protocols, which are identified in white boxes. This diagram is modified from the original Figure 1 in the report by International Atomic Energy Agency. Commissioning, and quality assurance of computerized planning systems for radiation treatment of cancer, Technical Reports Series No. 430, IAEA, Vienna (2004).

1.2.1 Patient setup, immobilization devices, and CT simulation

CT simulation for breast radiotherapy involves positioning the patient in the treatment setup with the appropriate immobilization devices, such as the breast board in breast radiotherapy, as shown in Figures 1.4 and 1.5. The patient is then aligned to reference orthogonal lasers, and the patient's skin is marked with tattoos. Radio-opaque markers are often used to determine clinical boundaries, such as the medial, lateral, superior, and inferior borders of the breast, and a radio-opaque wire is placed on the lumpectomy scar. A CT image of the patient is then acquired.

Patients receiving adjuvant breast radiotherapy are usually treated in a supine position, although prone [19] or decubitus [20] positions have also been adopted. For supine treatments, the patient is positioned on a breast board and depending on whether the right or left breast is being treated, the ipsilateral arm is usually elevated above the head. It can also be advantageous to have both arms elevated, with the hands clasped together [21]. Additionally, depending on the radiotherapy centre, the patient's head may be turned away from the involved side; however, it is more common, and can be advantageous [21], to maintain a symmetrical position by keeping the head straight.

It has been reported that for patients with large, pendulous breasts a supine setup may result in more severe acute dermatitis and negative cosmesis [22]. As an alternative for these subset of patients, breast radiotherapy in the prone position can improve radiation-related toxicities [19,23]. These techniques require patients to lay in the prone position on

a breast board with an opening that accommodates the breast, such that the breast is left to hang freely and away from the chest wall (refer to Figure 1.5). Advantages include improved dose homogeneity, and reduced radiation dose to nearby OARs such as the lung and heart [24–26]. Disadvantages include potential inadequate coverage to involved low-level axillary lymph nodes [27], regional lymph nodes [28], or very medial or lateral lesions [29]. Patient position reproducibility plays an important role in successful radiotherapy treatments, and a patient’s ability to tolerate a prone setup is also an important factor to consider when deciding which setup to use.

1.2.2 Target definition, dose prescription, and treatment planning

In standard adjuvant WBRT, the goal is to treat all glandular breast tissue and spare the underlying muscle, rib cage, overlying skin or excision/ surgical scar, and nearby OARs (refer to Figure 1.4 for an example patient plan). In addition to the breast, locoregional lymph nodes (mainly, the supraclavicular nodes, infraclavicular nodes, internal mammary nodes, and axillary nodes) may also be treated. Depending on the breast size, comorbidity, and chemotherapy agents delivered, a total dose of 45 Gy or 50 Gy, with 1.8 Gy/ fraction or 2 Gy/ fraction, respectively, is delivered to the target volume over 25 fractions [30]. This is achieved by using two to four high-energy photon beams, with two opposing beams aimed tangentially, parallel to the line of the chest wall, and towards the breast, as shown in Figure 1.5(c). Radiation is generally delivered using a standard medical linear accelerator (linac) operating with 4 to 20 MV accelerating potentials.

In the case of BCT, a supplemental dose of radiation, referred to as a boost, may be delivered to the tumour bed when indicated [31–34]. With the aid of surgical clips and a visible seroma on CT, the tumour bed is usually delineated by a clinician and is expanded with a margin of 5.0 to 15.0 mm to form a clinical-target-volume (CTV). The CTV is then cropped from the skin and ribs (usually by 5.0 mm), and an additional planning-target-volume (PTV) margin is added to account for institution-specific margins related to setup and treatment uncertainties. In these cases, the tumour bed PTV dose prescription is usually delivered as 10 to 16 Gy in 2 Gy per fraction [31,35]. High-energy electron beams, with energies ranging from 9 MeV to 12 MeV, are the most frequently used radiation type for delivering boost dose for a superficial tumour bed [36]. Delivering the prescribed boost for superficial targets or in the presence of an irregular lumpectomy scar can be challenging. In these cases, the use of a tissue equivalent material (bolus) to increase surface dose, and compensate for irregular tissue can achieve the desired dosimetric goals [37,38].

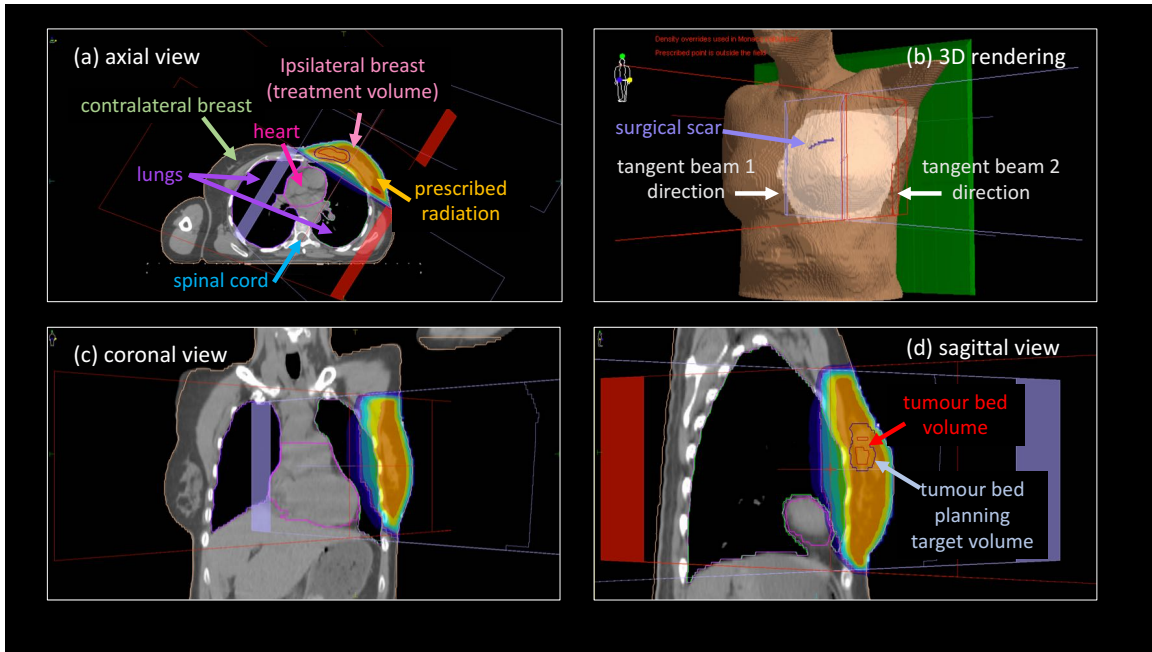


Figure 1.4 An example patient plan for a left-sided breast radiotherapy treatment in a supine position with the ipsilateral arm elevated. The treatment volume (ipsilateral breast) and nearby radiosensitive organs are shown in orthogonal CT views: (a) axial, (c) coronal, and (d) sagittal. The tumour bed and associated planning target volume (PTV), which will receive sequential additional “tumour bed boost” radiation, are also displayed in the sagittal view (d). Beam directions are indicated with respect to the 3D body view in (b), where the green block is the treatment couch. The prescribed radiation to the entire breast volume is shown along axial, coronal, and sagittal views as the rainbow colour wash, with the orange/yellow colours displaying the relative 100% prescription dose volume.

1.2.3 Treatment setup and verification

On the day of treatment, breast cancer patients receiving standard adjuvant radiotherapy are positioned on the treatment linac couch in the same position (supine or prone) and with the same immobilization devices used during CT simulation, which were described in Section 1.2.1. Figure 1.5 provides examples of various immobilization devices

and contrasts the difference between a supine versus prone treatment on a linac. To facilitate reproducible and accurate patient setups, modern linacs are equipped with in-room image guidance systems. Typical installations include a kV X-ray tube orthogonal to the central axis of the treatment beam and electronic imaging detector which allow kV portal images and cone-beam CT (CBCT) images to be acquired, and an electronic imaging detector parallel to the central axis of the treatment beam which allows MV portal images to be acquired. Using these systems, image-guided radiotherapy (IGRT) [39] is routinely employed to verify the patient's treatment position prior to treatment. For standard (3D conformal) breast radiotherapy techniques, commonly implemented IGRT protocols involve two X-ray images (MV or kV) with medial and lateral views. If more advanced radiotherapy techniques, such as respiratory management strategies or volumetric modulated arc therapy (VMAT) are used (see upcoming discussions in Section 1.3.1 and Section 1.3.3, respectively), then fluoroscopic imaging can be used to verify respiratory motion extent in 4D, and CBCT may also be used to verify the patient's anatomy in 3D for VMAT delivery. Additional options for IGRT may also be advantageous for advanced breast radiotherapy techniques [40].

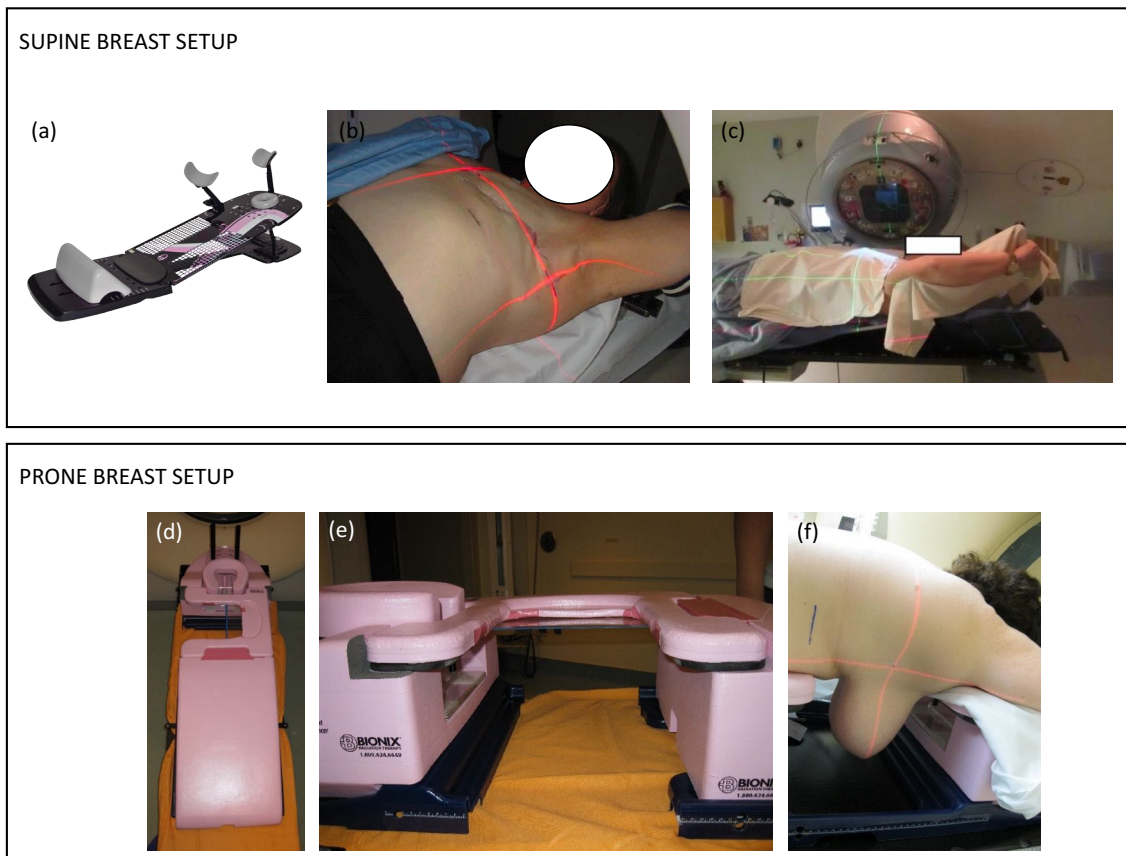


Figure 1.5 Examples of supine and prone setups and associated immobilization devices shown at CT simulation and delivery for breast radiotherapy. (a) An example immobilization device (the Access™ Supine Breast Board, Qfix, Avondale, PA, USA). (b) A patient positioned for left-sided breast radiotherapy CT simulation. (c) Another patient positioned with this device for treatment on a linac. Note that the patient shown in (b) underwent adjuvant radiotherapy after a mastectomy, whereas in (c), the patient's breast is intact after a lumpectomy. (d) and (e), a prone setup immobilization device (the Bionix Prone Breast System, Bionix, Toledo, Ohio, USA). (f) A patient undergoing CT simulation for right-sided breast radiotherapy. Figure shown in (a) was adapted from www.qfix.com, and all other images are courtesy of Mr. Steve Andrusyk, RTT (The Ottawa Hospital General Campus Cancer Centre).

1.3 Advancements in external beam breast radiotherapy

Standard adjuvant radiotherapy breast treatments are carefully planned to minimize radiation to nearby OARs [41]. With favourable long-term survival rates, breast cancer patients are expected to live longer. Consequently, long-term follow up studies have been possible and have shown that these patients can experience late toxicities [42,43]. Furthermore, with improved long-term survival, efforts have intensified to improve patients' quality-of-life (QOL). Over the last two decades, there have been significant advances in external beam breast radiotherapy, which have aided in reducing risks related to radiation induced cardiac toxicity and radiation induced pneumonitis. These efforts have been facilitated by several key technological and clinical advances and are briefly discussed below.

1.3.1 Respiratory motion management

Intrafraction motion in radiotherapy has been an issue of special interest. This type of motion can be caused by respiratory motion, cardiac motion, skeletal muscular motion, and gastrointestinal system motion. Pertinent to breast radiotherapy are respiratory and cardiac motions, which are involuntary motions that can influence target coverage.

There are now several respiratory motion management strategies available to mitigate this issue [44]. A summary of these strategies and their demonstrated applicability to breast radiotherapy is provided in Table 1.1. Generally, for the breast site, respiratory

motion can be eliminated with breath-holding strategies [45], reduced using gating [46], reduced using abdominal compression [47], or accounted for by modifying the linac multi-leaf collimator (MLC) sequence or treatment planning and delivery process (*e.g.*, tumour-tracking) [48].

As previously mentioned, cardiac and lung irradiation and associated potential subsequent toxicities are of concern, particularly in left-sided breast radiotherapy [42,43]. This motivated utilizing different respiratory motion management strategies to minimize cardiac irradiation. For example, Lu *et al.* [49] demonstrated that deep inspiration breath hold (DIBH) is an effective strategy for reducing irradiated cardiac volumes. Several other studies have also reported on the advantages of DIBH on cardiac structure sparing, while others have reported variable dosimetric effects on lung dose [50–53]. Respiratory gating has also been investigated for breast radiotherapy, and has shown advantages compared with free breathing (standard) techniques [46]. Compared with gating; however, DIBH has been shown to be more advantageous in reducing predicted cardiac mortality rates [46], with the reported rates being 4.8% with standard free breathing compared to 0.5% with gating and only 0.1% with DIBH [54]. Furthermore, compared with WBRT with tangential fields, the use of respiratory motion management can be advantageous for advanced radiotherapy techniques, such as those discussed in Section 1.3.3 and Section 1.3.4

Table 1.2 Summary of respiratory motion management strategies used in radiotherapy [44]. This table includes the general concept behind each strategy, various sub-types, defines which step of the radiotherapy process the strategy is implemented (a diagram showing the full radiotherapy process is provided in Figure 1.3), and highlights some workflow considerations, as well as the applicability of each strategy to breast radiotherapy.

<i>Strategy</i>	<i>General concept</i>	<i>Sub-types</i>	<i>Radiotherapy process step implementation</i>	<i>Workflow considerations</i>	<i>Published use in breast radiotherapy</i>
Motion-encompassing	CT scans average a tumour's motion in a composite image	- Slow CT scanning - Inhalation and exhalation breath hold CTs - 4DCT (prospective or retrospective)	Simulation	- Prospective 4DCT provides less information on respiratory motion and less imaging dose to the patient - Retrospective 4DCT provides more information on all phases of respiration but more imaging dose to the patient	[55,56]
Respiratory gating	Radiation delivery is activated during a certain user-selected portion of the respiratory cycle	- Gating using an external respiratory signal - Gating using an internal fiducial marker	Treatment	- Requires internal or external marker tracking system - Duty cycle can be very low (the time the beam is on compared to the total treatment time)	[46,54]

Table 1.1 continued...

<i>Strategy</i>	<i>General concept</i>	<i>Sub-types</i>	<i>Radiotherapy process step implementation</i>	<i>Workflow considerations</i>	<i>Published use in breast radiotherapy</i>
Breath-hold	Manual gating which can be monitored using markers or performed by relying on the patient to hold their breath reproducibly (usually at deep inspiration)	- Deep inspiration breath hold (DIBH) - Active-breathing control (ABC) - Self-held breath hold with or without respiratory monitoring	Simulation and treatment	- Patient eligibility and tolerance must be established prior to simulation	[45,46,50,52,53,57]
Forced shallow breathing with abdominal compression	Patient's abdomen is compressed by a paddle which limits their breathing amplitude	--	Simulation and treatment	- Relatively uncomfortable	[47]
Real-time tumour-tracking	Offered by Cyberknife's Synchrony System™, where the robotic arm continuously updates beam direction following tracks the tumour motion during treatment delivery	--	Treatment	- Requires implanted fiducials - Can be a long treatment	[48,58]

1.3.2 The use of magnetic resonance imaging

Radiotherapy target delineation and treatment planning is performed on a CT simulation image; however, target delineation on CT images can be challenging due to limited soft tissue contrast on these images. Several studies have shown how target delineation on CT images can cause variability among breast tumour beds delineated by radiation oncologists [59–61]. Compared with CT, magnetic resonance imaging (MRI) provides excellent soft tissue contrast [62–64] and has been shown to provide better target visualization for many anatomical sites [65,66], including breast radiotherapy target delineation [67,68]. This is greatly advantageous as improved tissue visualization can directly relate to improved treatment quality due to better targeting accuracy and reduction in OAR-related toxicities [69].

Over the past years, MR-guided radiotherapy (MRgRT) has been an active area of research and clinical implementation. MRgRT can refer to the use of MRI in the radiotherapy simulation process followed by treatment on a conventional linac, or treatment on a hybrid machine (e.g., Elekta Unity® MR-linac, Stockholm, Sweden, or the ViewRay MRIdian® MR-linac, Oakwood Village, Ohio). While the basic underlying physics is the same in both techniques, for the purpose of this thesis, discussion will be limited to MRI in the radiotherapy planning process (*i.e.*, MRI simulation) and its associated challenges.

Incorporating MRI in the simulation process presents obvious advantages which have also been recognized by vendors and have motivated the development of auxiliary equipment to facilitate integrating MRI into the radiotherapy treatment planning process. These equipment include; flat tabletops, MRI compatible immobilization devices, and external reference lasers to aid in patient setup [70]. Nevertheless, there are several challenges that must also be considered, some of which are particularly important for breast radiotherapy [66,68]:

Geometric accuracy: Accurate target delineation and radiotherapy treatment planning require high quality radiographic images with high geometric fidelity that preserve spatial information. In MRI, geometric distortion is caused by incorrect spatial mapping of signal data and is a well-known issue. Geometric distortion will be discussed further in Chapter 2 and Chapter 3.

Patient setup: MRI scanners have a smaller bore size than CT scanners' (60-70 cm vs. 80-90 cm). For supine setups, this can limit breast patient positioning in terms of arm inclination [71]. For prone setups, this can reduce the usable scan field-of-view (FOV) for the area of interest because the patient will be displaced from the centre of the scanner's bore causing a cutoff or deformation of the body contour. Additionally, for prone setups, the smaller bore size can limit the space needed for a breast to hang freely without being in contact with the table top surface [68], an example of this in "bad" and "good" breast radiotherapy simulation setups are shown in Figure 1.5.

Image quality: It is possible to obtain high-quality images for breast radiotherapy with proper selection of suitable MRI imaging parameters and optimal placement of receiver coils [72]. Another challenge for this anatomical site; however, is related to the relatively longer image acquisition time for MRI compared with CT [66]. This results in respiratory and cardiac motion which could cause significant image artifacts. There are several strategies to mitigate this effect, such as imaging with prone positioning [73], coaching patients to maintain shallow breathing [72], choosing a right-left phase encoding direction for MRI scans [74], using 3D sequences [75], and motion artifact correction methods [76].

Image coregistration: In radiotherapy treatment planning, MRI images are often considered secondary image sets, and are coregistered to CT images (the primary image set). This process involves the use of a coregistration algorithm to transform the secondary image set to the primary image set. Image coregistration algorithms vary [77], and must be properly understood and validated to eliminate any errors arising from this process which may impact image fidelity. Commissioning and validating image coregistration algorithms for the breast, being a deformable organ, can be challenging. Image coregistration is discussed further in Chapter 2.

Target delineation/ contouring: Surgical clips are often placed to guide radiation oncologists during tumour bed delineation in adjuvant breast radiotherapy planning. GEC ESTRO provides recommended guidelines [78] for target delineation of boost or accelerated partial breast irradiation (APBI, defined in Section 1.3.4). They recommend that target delineation must include both visible seroma and surgical clips. While MRI

provides better visualization of the seroma, surgical clips lead to signal voids on MRI, which is another challenge [79]. Furthermore, the value of target delineation on MRI has been disputed depending on whether pre- or post-operative MRI scans were available in addition to a postoperative planning CT [80–83]. Nevertheless, a recent study by Al-Hammadi *et al.* [84] demonstrated that MRI reduced variability in target delineation amongst radiation oncologists when surgical clips were not used to demarcate the tumour bed. Though not yet considered standard-of-care, MRI simulation has shown promising results in the neoadjuvant breast radiotherapy setting for *in situ* tumours [85].

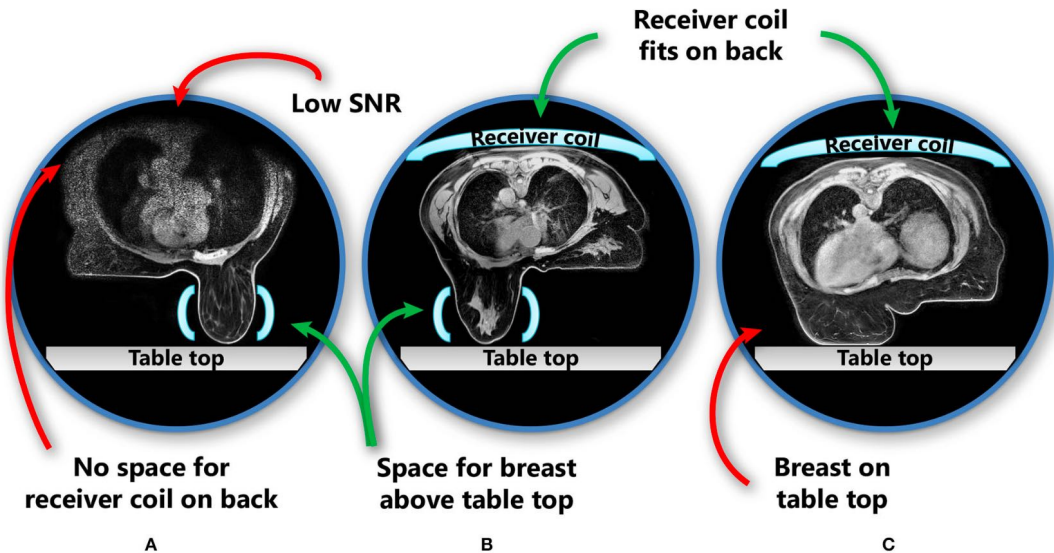


Figure 1.6 An example of breast patient prone setup positioning challenges in MRI imaging. Here, three scenarios are presented. (A) The lack of space for a posteriorly placed receiver coil can cause a cutoff of the body contour and reduced signal-to-noise ratio (SNR). (B) A more ideal setup in which there is space to include the receiver coil and allow the breast to hang freely. (C) An attempt to place a posterior receiver coil for a prone positioned patient causes the breast to touch the tabletop (couch) and deform. This figure is reproduced with permission from Figure 2 in the manuscript by Groot Koerkamp ML *et al.* “Optimizing MR-guided radiotherapy for breast cancer patients. *Frontiers in Oncology*. 2020;11:107”.

1.3.3 Technological advancements in radiotherapy delivery

External beam radiotherapy has evolved from a limited number of rectangular fields to highly modulated and conformal dose deliveries. In the case of adjuvant breast radiotherapy, this has led to the reduction in lung and cardiac toxicities. For example, intensity modulated radiotherapy (IMRT), whether delivered on a conventional linac [86] or TomoTherapy® (Accuray, Sunnyvale, California, United States), has been demonstrated to be useful for left-sided breast with regional nodal radiotherapy [87]. For non-WBRT

techniques, beam delivery flexibilities offered by robotic stereotactic radiosurgery (CyberKnife®, Accuray, Sunnyvale, California, United States) [48,58,88] and a new dedicated breast radiotherapy unit (GammaPod®, Xcision, Maryland, Baltimore, United States)[89] have also been shown to be useful for tumour bed irradiation.

1.3.4 Accelerated partial breast irradiation

Although BCT presents many advantages, many women still opt for mastectomy instead of BCS with adjuvant radiotherapy [90–92]. Furthermore, 15% to 30% of patients who undergo BCS do not follow up with adjuvant radiotherapy [93–95]. The reasons relate to logistical issues due to an inability to commit to 5-6 weeklong treatment courses [96], residential distance from radiotherapy centres, lack of transportation, lack of mobility, or lack of patient support [94,97,98].

To address these treatment barriers, hypofractionated treatment regimens offer a reduced total treatment period by increasing the dose per treatment fraction. Instead of treating with WBRT of 50 Gy in 25 fractions (2 Gy/ fraction), these treatments offer WBRT of 42.5 Gy in 16 fractions (2.66 Gy/ fraction) with demonstrated equivalency in tumour control and cosmetic outcome [99,100]. While the latter regimen provides shorter treatment times, in both cases, the whole breast is irradiated tissue.

It has been reported that 75% of local tumour reoccurrences occur at or near the tumour bed site [101] and that tumours rarely recur in other areas of the ipsilateral

breast [102]. This evidence has led to debate in the need to irradiate the entire breast during adjuvant radiotherapy for certain groups of patients, as this may cause unnecessary toxicity. As an alternative treatment technique, APBI has the potential of reducing irradiated tissue volumes and sparing more normal tissue including the ipsilateral normal breast tissue [103,104] and cardiac and lung volumes [43,92,105].

APBI is a radiotherapy approach that focuses radiation to the tumour bed plus a surrounding 1 to 2 cm margin. It is a hypofractionated regimen, meaning that the dose per fraction is greater than 2 Gy, and is usually delivered in 3 to 5 weeks. It is a treatment option as a form of BCT for eligible patients with early-stage, low-risk breast cancer [106]. There are different treatment modalities available for APBI, including brachytherapy (multi-catheter interstitial or balloon catheter), intraoperative radiotherapy (IORT), and external beam APBI (EB-APBI) [92]. Each modality differs in radiation delivery method, level of invasiveness, radiation oncologist's proficiency and training, and treatment time duration.

Historically, although considered relatively invasive, multi-catheter interstitial brachytherapy has been widely utilized and is associated with long-term follow-up data [92,96,107]. On the other hand, EB-APBI is considered as the least invasive APBI treatment modality. Other advantages of EB-APBI include that it is delivered using widely available technology (*i.e.*, linacs). In terms of treatment technique, EB-APBI can be delivered with either three to five beam 3D conformal radiotherapy (CRT) or IMRT non-coplanar beams [92]. In addition, EB-APBI provides better dose homogeneity compared

with brachytherapy, eliminates the need for anesthesia and potential infections, and relies less on treatment planning expertise, meaning that cross-centre patient outcomes can be easily compared [92,108].

The largest randomized Phase III APBI trial is the NSABP B-39/RTOG 0413 protocol, which compared interstitial multi-catheter or balloon brachytherapy or 3D-CRT EB-APBI modalities with WBRT [109]. Treatment evaluation metrics included non-inferiority comparison in terms of ipsilateral breast tumour recurrence, OAR toxicities, and cosmesis. A summary of select key randomized controlled APBI trials and their results are provided in Table 1.2. In addition to these trials, a small study has shown the feasibility of using VMAT as an EB-APBI modality for elderly and frail patients [110].

Table 1.3 A summary of select randomized controlled APBI trials (administered as adjuvant radiotherapy after BCS). Trials utilizing external beam radiotherapy techniques are highlighted in bold text. The control arms for all these trials were WBRT techniques. Abbreviations: APBI= accelerated partial breast irradiation, BCS= breast conserving surgery, EB= external beam, CRT= conformal radiotherapy, IMRT= intensity modulated radiotherapy, WBRT= whole breast radiotherapy, IORT= intraoperative radiotherapy, MIB= Mammosite interstitial brachytherapy, HDR= high dose rate brachytherapy, PDR= pulsed dose rate brachytherapy, IBTR= ipsilateral breast tumour recurrence, QOL= quality of life.

Trial	Trial Design	Start Year	Status	Number of patients accrued	Median follow-up	APBI Dose Fractionation and Technique	Arm Comparison (result)
TARGIT-A [111]	Non-inferiority	2000	Accrual closed 2012	n = 2298	2.4 years	IORT: 20 Gy/ 1 fraction, low energy X-rays (50 kV)	No difference in IBTR
ELIOT (Milan) [112]	Non-inferiority	2000	Accrual closed 2007	n = 1305	5.8 years	IORT: 21 Gy/ 1 fraction, electrons with energies up to 9 MeV	Higher rate of IBTR compared with WBRT, no difference in overall survival
GEC-ESTRO [113,114]	Non-inferiority, non-relevant, 3% difference	2004	Accrual closed 2009	n = 1184	6.6 years	MIB: 32 Gy/ 8 fraction HDR: 30.1 Gy/ 7 fractions PDR: 50 Gy/ 0.60-0.80 Gy per pulse	No difference in IBTR, no difference in QOL

Table 1.2 continued....

<i>Trial</i>	<i>Trial Design</i>	<i>Start Year</i>	<i>Status</i>	<i>Number of patients accrued</i>	<i>Median follow-up</i>	<i>APBI Dose Fractionation and Technique</i>	<i>Arm Comparison (result)</i>
NSABP B-39/ RTOG 0413 [115]	Non-inferiority	2005	Accrual closed 2013	n = 4216	10.2 years	MIB: 34 Gy/ 10 fractions 3D CRT: 38.5 Gy/ 10 fractions (5-8 days)	Did not meet non-inferiority criteria, however <1% absolute difference in 10-year cumulative IBTR incidence
Florence [116]	Non-inferiority	2005	Accrual closed 2013	n = 520	10.7 years	IMRT: 30 Gy/ 5 fractions	No increase in IBTR, improved acute/ late toxicity and cosmesis
RAPID [117]	Non-inferiority	2006	Accrual closed 2011	n = 2135	3 years	3D CRT: 38.5 Gy/ 10 fractions BID in 5-8 days with a daily fraction interval of 6-8 hours	Did not meet non-inferiority criteria. Inferior cosmesis.

Table 1.2 continued....

<i>Trial</i>	<i>Trial Design</i>	<i>Start Year</i>	<i>Status</i>	<i>Number of patients accrued</i>	<i>Median follow-up</i>	<i>APBI Dose Fractionation and Technique</i>	<i>Arm Comparison (result)</i>
IMPORT-LOW [118]	Non-inferiority	2007	Accrual closed 2010	n = 2018	6 years	Arm I: IMRT: 40 Gy/ 15 fractions to tumour bed with 36 Gy/ 15 fractions to low-risk region Arm II: IMRT: 40 Gy/ 15 fractions to primary tumour bed	No difference in IBTR, and equivalent or fewer late normal-tissue toxicity
IRMA (abstract) [119]	Non-inferiority	2007	Unspecified	n = 983	5 years	3D CRT: 38.5 Gy/ 10 fractions, BID with a daily fraction interval of at least 6 hours	No difference in toxicity

Table 1.2 specifies trials for adjuvant APBI to the breast tumour bed with 10 to 20 mm margins. However, it is possible to further reduce the treatment volume for breast radiotherapy by treating the tumour pre-operatively with hypofractionated regimens. Neoadjuvant APBI is a technique that delivers an ablative dose of 21 Gy in 1 fraction to the tumour site alone in a pre-operative setting with EB-APBI, and has demonstrated promising results so far [120]. This technique is further developed in an ongoing neoadjuvant EB-APBI phase I/II SIGNAL [85,121,122], which employs the merits of excellent soft tissue differentiation in MR (see Section 1.3.2), added functional information provided by PET, and reduced setup uncertainty of a prone treatment to evaluate improvements in radiation response and clinical outcome.

1.4 The use of phantoms in medical physics applications

Regardless of treatment modality or approach, the radiotherapy treatment process entails acquiring 3D anatomical information of a patient to plan and customize an effective dose distribution that sufficiently covers the treatment target volume while sparing as much healthy tissue as possible. Medical physicists play an active role in ensuring that anatomical information is accurately and adequately captured by ensuring that the medical imaging devices used are safe and reliable through routine quality assurance (QA) testing. Furthermore, through rigorous QA measurements, they also ensure that the prescribed dose distribution is delivered accurately and precisely. Due to the nature of these experiments, measurements are not routinely performed with the patient, but rather, with objects called

“phantoms”. These objects can serve different purposes within various medical physics domains, such as in radiological/ diagnostic imaging and radiotherapy applications.

In radiological imaging applications, phantoms vary in design, material, and use according to the modality of interest—whether X-ray (including mammography), CT, MRI, or ultrasound. Generally, they are used during QA to verify medical image quality, image fidelity, X-ray radiation imaging dose, and to generally evaluate, analyze and optimize the performance of different imaging modalities [123].

Medical physics phantoms that are specifically used for X-ray, CT, and MRI image fidelity verification will be further discussed in Chapters 2 and 3, while various breast phantoms used for quantitative and qualitative image testing on CT, MRI, and ultrasound will be reviewed in Chapter 4.

In radiotherapy medical physics applications, phantoms can be used for radiation dose calibration [124–126], or to act as a surrogate to patient anatomy by facilitating direct measurement of radiation dose distribution. Since human tissue is primarily composed of water, has uniform density, and is widely available, water is a common choice as a phantom material. For the purpose of radiation dose measurements, early work by Kroenig [127] and Quimby [128] investigated the use of water and beef muscle. White [129] provides a historical overview of different phantom materials used, and several key medical physics publications cite the use of many phantoms and types used in radiotherapy applications [37,130].

As an alternative to water, other, practical materials are commonly used to construct radiotherapy phantoms. These materials offer practical setups and ease of use, but must be first validated to be “water equivalent”. Examples of commercially available products include Solid Water™ (Gammex-RMI, WI, USA), Blue Water™ (Standard Imaging Inc., WI, USA), and Plastic Water® (CIRS Inc., VA, USA).

Most non-water radiotherapy phantoms are available as uniform solid “plastic-like” slabs or cylinders; however, it may be desirable to use a phantom that can resemble a human shape and anatomy. As an alternate solution, the Alderson Radiation Therapy (ART™) Anthropomorphic Phantom (Alderson Research Laboratories Inc., CT, USA), which is the new version of the Rando™ Anthropomorphic Phantom (Alderson Research Laboratories Inc., CT, USA), is also made of tissue equivalent solid material, but is offered with different shapes and sizes that mimic geometric aspects of female and male human anatomy. Nevertheless, these materials are also rigid, and so are not suitable to test deformable image registration algorithms [77], or to capture the deformation of various deformable organs, such as the breast. As such, finding alternate materials to construct deformable, water equivalent phantoms would be necessary to construct a realistic breast phantom.

According to DeWerd *et al.* [123], phantoms used in radiotherapy dose measurements must satisfy several design goals. These are categorized depending on materials first and geometry second, and are quoted as follows:

Material-specific radiotherapy phantom design goals:

- 1- Similarity to tissue to allow radiation dose measurements in the material to be related to tissue.
- 2- Composition can be well characterized.
- 3- Readily available.
- 4- Robust to radiation damage.
- 5- Exhibits reproducible and well-understood response with respect to radiation type and energy.
- 6- Allows for traceability to reference standards.

Geometry-specific radiotherapy phantom design goals:

- 1- Must accommodate planned radiation beam sizes and shapes.
- 2- Allows 3D dose distribution localization.
- 3- Simple to set up, align, and reproduce positions accurately and efficiently.

Medical physics phantoms that are specifically designed for breast imaging and breast radiotherapy applications will be further reviewed in Chapters 4, 5, and 6.

Overall, as outlined in Figure 1.3, radiotherapy treatments are a multi-step process that include radiotherapy image simulation, treatment planning, treatment setup, and treatment delivery. These individual components are routinely tested on an individual basis, using different types of QA phantoms. For high-precision, high-accuracy radiotherapy techniques, it is advantageous to evaluate the entire radiotherapy treatment

process using “end-to-end” (E2E) testing. This can be performed with an E2E phantom, such as Accuray’s E2E anthropomorphic head phantom, which will be described in Section 2.2.1.

1.5 Thesis motivation

Over the last few decades, there have been many technological advancements developed with the aim of improving treatment planning and delivery accuracy and precision for adjuvant external beam breast radiotherapy. In this chapter, several key contributions were reviewed, such as modern surgical approaches (which improved patient treatment cosmesis and QOL), including more recent developments in OBS techniques, respiratory motion management and IGRT, MRI simulation for breast radiotherapy, and improved dose delivery accuracy and beam shaping with modern radiotherapy technologies. With increasing interest in APBI protocols, having reduced treatment volumes and smaller treatment planning margins, it is essential to improve treatment planning and delivery accuracy and precision.

The purpose of this thesis is to develop medical physics approaches to advance treatment accuracy of APBI. This is achieved through several contributions. First, practical, efficient medical physics phantoms and analysis methods were developed to investigate radiological image geometric distortion for various imaging modalities (including CT, CBCT, and MRI). Second, a novel, deformable breast phantom prototype was constructed and validated for surgical simulation, radiological imaging, and dosimetric applications.

Then, a set of these breast phantoms were used to investigate the reliability of surgical clips for tumour bed delineation in adjuvant radiotherapy treatment planning following OBS.

1.6 Thesis overview

This thesis is comprised of seven chapters. **Chapter 1** provided a background and literature review on breast cancer, breast cancer treatment, including conventional BCS and new OBS techniques, as well as, external beam adjuvant breast radiotherapy, the breast radiotherapy process, recent key advancements in external beam adjuvant breast radiotherapy, and finally, the use of phantoms in radiological imaging and radiotherapy applications.

Chapter 2 introduces a 3D printed phantom used to measure geometric distortion on various radiological image modalities (CT, CBCT, and MRI) that are clinically used at The Ottawa Hospital Cancer Centre in robotic stereotactic radiosurgery for intracranial treatments. An analysis technique is also introduced to facilitate quantitative assessment of geometric distortion. In addition to this phantom, two other phantom designs (one commercial, one built in-house) and another analysis technique (based on commercial software) are utilized to cross-compare data obtained from the same radiological images.

These concepts are further developed for **Chapter 3**, in which, a custom-built large volume 3D printed phantom and analysis technique are utilized to measure geometric distortion on MRI images specifically used for breast radiotherapy planning.

In **Chapter 4**, a novel realistic, deformable breast phantom, made of moldable silicone, is presented. The process for constructing a phantom is described, and the phantom is then validated for the purposes of surgical simulation, radiological imaging, and dosimetric application. The validation processes included optimization based on the stated applications, and quantitative assessment of the phantom materials' mechanical properties, assessment and OBS simulation by expert breast surgeons, and characterization of various radiological properties on multiple imaging modalities used in adjuvant breast radiotherapy (CT, ultrasound, and MRI).

With the eventual goal of developing an E2E deformable breast phantom, **Chapter 5** then presents detailed dosimetric assessment of two types of moldable silicones, which was achieved by determining associated key physical and dosimetric quantities, and by experimental quantification of differences in relative radiation doses, treatment planning system calculations to calculate these differences, and Monte Carlo simulations to verify experimental and calculated results.

In **Chapter 6**, a collaborative study with breast surgeons, radiation oncologists, and medical physicists is described, where a set of the constructed breast phantoms were employed to simulate the surgery-to-radiotherapy treatment target delineation chain for adjuvant breast radiotherapy treatment planning. This process provided detailed new insight on tumour bed displacement and deformation with different OBS techniques and facilitated investigating the reliability of surgical clips for accurate tumour bed delineation post-OBS. The study results relayed potential clinical consequences for APBI treatments.

Finally, **Chapter 7** provides a summary of results presented in this thesis and the impact on improved treatment accuracy for APBI. This chapter concludes with perspectives on future directions.

Chapter 2: Geometric Distortions and Image Co-Registration Errors of Radiological Images Used in Robotic Stereotactic Radiosurgery

2.1 Introduction

In radiotherapy, computed tomography (CT) images are used to simulate a patient's treatment position and to define the radiotherapy treatment target(s) and organs at risk (OARs). Section 1.2.1 provided a summary of how CT simulation is used in breast radiotherapy, specifically. In general, a similar process is adopted during radiotherapy simulation when treating other anatomical sites, with appropriate setups and immobilization devices in place. Along with CT images, complimentary radiological imaging modalities are often used for target delineation during high-precision, high-accuracy treatments, such as for hypofractionated treatment regimens that deliver high levels of radiation doses to small (< 50 mm in width) radiotherapy intracranial malignant and non-malignant diseases. These types of treatment techniques can be offered with stereotactic radiosurgery (SRS).

Due to the high precision of SRS treatments, radiological image fidelity is an important consideration. Thus, it is necessary to minimize or account for any inaccuracies related to image geometric distortions and image co-registration. Image geometric distortions are spatial distortions that cause an inaccurate representation of a 3D object on a 2D or 3D radiographic image. Geometric distortions related to magnetic resonance imaging (MRI) were described in Section 1.3.2, with detailed discussions to follow in

Chapter 3. Image co-registration is the process of determining a geometric transformation to relate identical, anatomical points in two image sets (such as with a CT and an MRI of an individual patient's brain) [77].

In this chapter, we investigate three different medical physics phantoms and two analysis approaches that can be used to quantify inaccuracies related to radiological image distortion and image co-registration. The discussion in this chapter is limited to intracranial SRS delivered on the CyberKnife® Robotic Radiosurgery System (Accuracy Inc., Sunnyvale, CA, U.S.A). In Chapter 3, this approach is further developed and applied to quantify geometric distortions for MRI radiotherapy simulation images used in accelerated partial breast irradiation (APBI).

Overall, secondary imaging modalities play a critical role in intracranial SRS workflows. Helical X-ray CT is typically used as the reference image set for dose calculation and treatment planning, but secondary image sets are required to accurately delineate the treatment target(s) and many OARs. Most intracranial SRS cases require, at a minimum, gadolinium contrast enhanced T1-weighted (T1w) magnetic resonance imaging (MRI) in addition to the reference planning image set [131]; both acquired with a thin image slice thickness (≤ 1 mm). In addition to the reference CT and secondary MRI image sets, the accuracy of target delineation for arterio-venous malformation (AVM) radiosurgery is improved with the use of dynamic CT angiography (dCTA) [132] and 3D DynaCT angiography (DynaCTA) [133]. This has been demonstrated for two radiosurgery

systems; the frameless CyberKnife® Robotic System (Accuracy Inc., Sunnyvale, CA, U.S.A) [132,134] and the Gamma Knife® (Elekta, Stockholm, Sweden) [135].

Depending on the imaging modality, image fidelity can be affected by several factors. The DynaCTA system utilizes cone beam CT (CBCT). Factors impacting image fidelity on these systems include inherent physical limitations of the system (*e.g.*, poor low contrast resolution of a flat panel detector [136]); presence of anatomy or reconstruction-based artifacts; scan parameters [77], or geometric distortions [137]. In MRI, geometric distortions are a well-known issue and are often one of the primary concerns with radiotherapy applications, especially for SRS [138]. A brief discussion on challenges associated with MRI, including geometric distortion, was provided in Section 1.3.2.

The steep dose gradients and high dose per fraction used in SRS necessitate submillimeter overall precision and accuracy. The use of multiple imaging modalities requires carefully executed image co-registration for SRS planning [139,140]— a task which can be integrated in a modern commercial treatment planning system (TPS). Nearly all modern TPS's come with built in tools to facilitate manual and/or automated image co-registration. Manual image co-registration results in a larger inter-observer uncertainty compared with automated image co-registration [77]. There are different types of automated image co-registration algorithms that have been demonstrated to be useful for brain imaging (*e.g.*, maximum gradient technique, matching moments, and chamfer matching) [141–143]. It has been reported that the overall co-registration errors based on

these algorithms is ≤ 2.0 mm [65]. For SRS applications, these uncertainties may be considered large [144].

There are additional uncertainties beyond those inherent in the algorithm used for image co-registration. These include inter-scan anatomical changes, such as post-operative brain edema, or the presence of geometric distortion inherent to different imaging modalities as discussed above. Historically, frames were rigidly fixed to a patient's skull to reduce setup uncertainty for intracranial SRS treatments. Until recently, radiotherapy planning with Gamma Knife relied on these frames for image co-registration. For example, the invasive Leksell frame was used to transform stereotactic frame coordinates to 2D angiography image coordinates. The new Leksell Gamma Knife® Icon™ (Elekta, Stockholm, Sweden) [145] offers image guided frameless SRS. The Gamma Knife's TPS utilizes the normalized mutual information (NMI) image co-registration algorithm [146]. For this new model, image co-registration accuracy with the NMI algorithm was assessed and found to be < 1.01 mm for CBCT on-board imaging and MRI. The CyberKnife is also a frameless image guided radiosurgery system, which also uses the NMI algorithm for image co-registration [147]. To our knowledge, prior to this study, the image co-registration uncertainty has not been reported for the CyberKnife implementation of NMI.

The uncertainties in co-registration of a secondary image set could lead to errors in delineation of the target structure and OARs. Such errors, which are introduced prior to the planning process, propagate throughout all treatment sessions of a patient.

With the incorporation of multiple imaging modalities in SRS planning, there is a need to ensure image fidelity and accurate image co-registration. This can be determined with commercial phantoms [148] and software solutions or with in-house built phantom prototypes. Unfortunately, commercial phantoms can be expensive, and in-house phantoms can require additional resources including machining support and time.

Since existing options may not be readily available to all radiotherapy departments, an alternate option for evaluating image geometric distortion is presented in this chapter, where a method for measuring image geometric distortion is demonstrated by building on existing tools available to all CyberKnife users. In addition, the work presented aims to:

- (1) Validate three different phantom designs compatible for the CyberKnife platform as quality assurance (QA) tools for measuring geometric distortion on X-ray and MRI based imaging modalities used in SRS planning, and (2) Quantify the combined errors due to geometric inaccuracy as well as image co-registration using the CyberKnife System's clinical workflow for treatment planning of AVM disease using SRS.

2.2 Materials and methods

Errors arising from any inherent geometric distortion of different imaging modalities as well as imperfect image co-registration were quantified using the MultiPlan® TPS (version 5.2.1, Accuracy Inc., Sunnyvale, CA, U.S.A, version 5.2.1). Three different phantom configurations were employed to facilitate measurements of these errors on X-ray and MRI based imaging modalities. All configurations are compatible with

CyberKnife's existing tools. The following sub-section describes these phantoms in detail. The imaging modalities investigated, as well as the imaging protocols, are described in Section 2.2.2. Image preprocessing and analysis methods are then discussed in Section 2.2.3.

2.2.1 Phantoms and definitions of points of interests (POI's)

Accuray's E2E anthropomorphic head phantom (see Figure 2.1) was used for X-ray based imaging systems. This phantom is manufactured and provided by Accuray as part of the CyberKnife® System for its recommended routine quality control program [149,150]. In conjunction with this phantom, three phantom inserts were used:

Phantom Cube A (Ball-Cube II Film Cassette): This cube is also provided by Accuray with the head phantom. It contains a hidden target and fits two custom cut orthogonal films. It is intended for end-to-end testing of the fiducial and skull tracking modalities used by the CyberKnife® System. It is a 63.0 mm × 63.0 mm × 63.0 mm cubic insert, which houses six gold fiducials placed in different orientations. Additionally, eight plastic posts with embedded copper markers fix the two films to the hidden target via four precise laser cut holes in each film. The centres of both types of high-density objects (gold fiducials and copper markers) are identified as 3D points of interest (POIs). The POIs' 3D positions on a given image set were determined by two methods: (1) using the MultiPlan® TPS, and (2) using an in-house written MATLAB script (MathWorks, Inc., Natick, MA, U.S.A,

v. R2015b). These image analysis approaches are described in detail in Section 2.2.3, below.

Because the materials used in this phantom insert are not suitable for MRI imaging, two additional phantom insert designs (Cubes B and C) were used for quantifying uncertainties from these images.

Phantom Cube B: A polymethyl methacrylate (PMMA) cube was constructed in-house, with 30 parallel air-filled and sealed phenolic plastic rods embedded in an MRI contrast solution (H_2O $NiSO_4$), see Figure 2.1 and Figure 2.2. The rods were placed along different orientations (superior-inferior and right-left). On each image slice, each rod's centre appeared as a disc. The centroid of each disc was used as a POI ($n= 310$) and identified on co-registered image slices. Therefore, only 2D slice-by-slice analysis in MATLAB was possible for this phantom. An in-house written MATLAB script was used to measure each POI's 2D position, as described below.

Phantom Cube C: An in-house 3D printed cubic lattice with a specially constructed PMMA housing was used (see Figure 2.1 and Figure 2.3). The housing allowed the lattice structure to be imaged surrounded by air, which provided the best image contrast for X-ray protocols, or immersed in MRI contrast solution (H_2O $NiSO_4$) providing a suitable signal for MRI imaging protocols. The lattice inner intersection points were identified as POI's ($n= 64$). Autodesk Inventor 2013 (Autodesk, San Rafael, CA, U.S.A) was used to design and generate a standard triangle language (STL) file. 3D printing was performed using

acrylonitrile butadiene styrene (ABS) and a uPrint® SE Plus 3D printer (Stratasys Ltd., MN, U.S.A) using the following settings: 0.330 mm layer resolution, 1.194 mm wall thickness, solid interior fill and the “SMART” setting for support material use during printing. An in-house written MATLAB script was used to measure the POI’s 3D position, as described below.

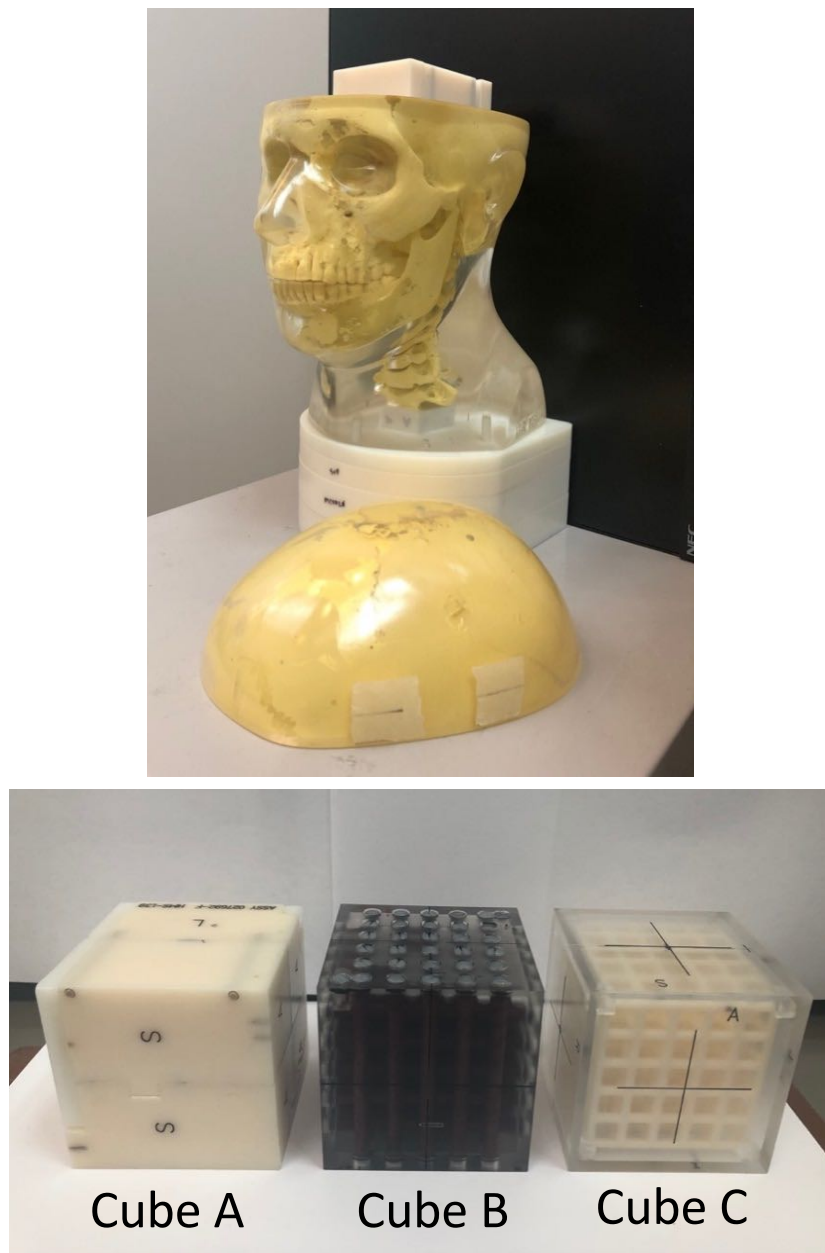


Figure 2.1 Top: Accuray's E2E anthropomorphic head phantom, with the commercial phantom insert (Cube A) in place. Bottom: The three investigated phantom insert cubes assessed in this study. All inserts have identical external dimensions, but with different designs. On the left is the commercial phantom containing gold fiducials and copper markers, the middle is the rod phantom (Cube B), and on the right is the 3D printed lattice phantom in the acrylic housing (Cube C).

Cube B

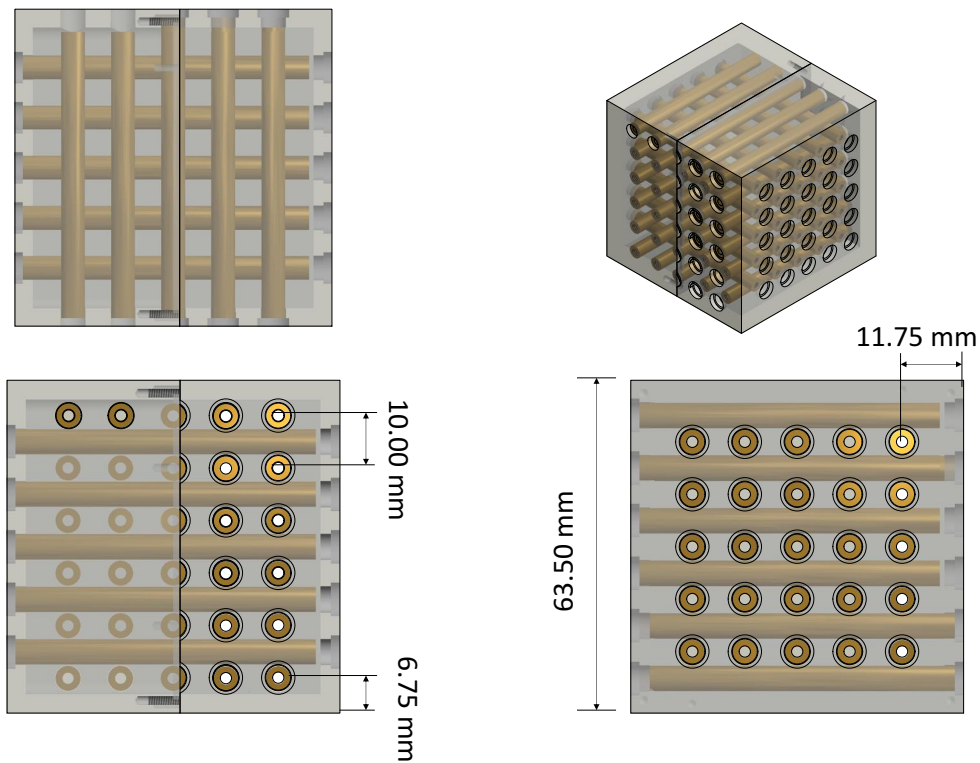


Figure 2.2 Multiple views of the rod phantom's (Cube B) 3D computer-aided design (CAD) drawing. The acrylic rods (filled with air) were placed orthogonally and on different levels in the cube. The inter-rod space was filled with MR contrast.

Cube C

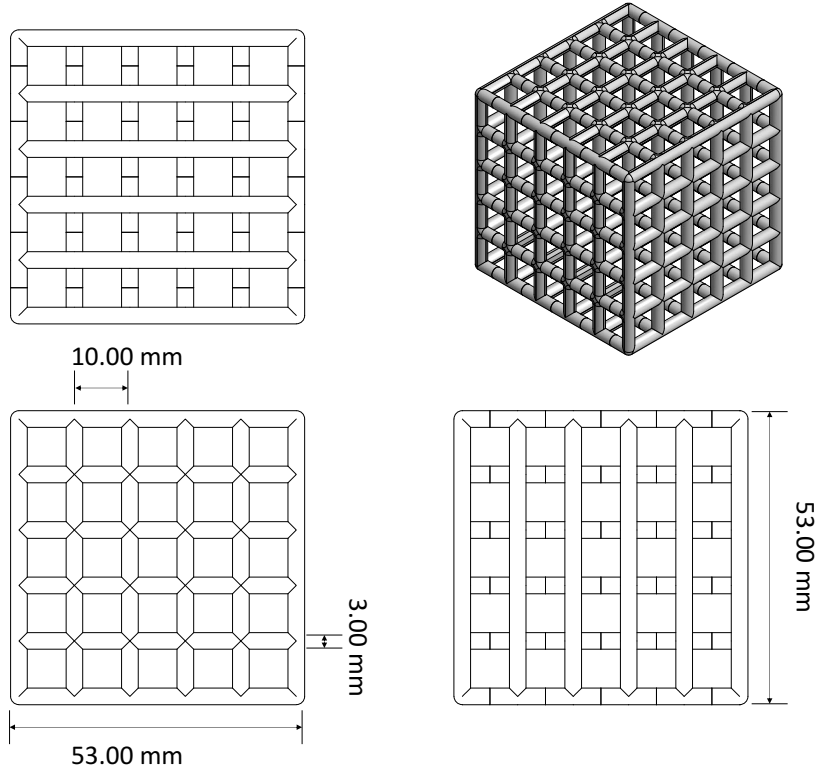


Figure 2.3 Multiple views of the 3D printed phantom's (Cube C) CAD drawing. The lattice is shown without the external acrylic housing, which was filled with contrast solution for MR imaging and provided an additional thickness of 10.00 mm on each cube side.

2.2.2 Imaging setup, modalities, and characteristics

The three phantom configurations were imaged using a helical CT radiotherapy simulator (*i.e.*, with the treatment planning CT, or TPCT) as well as the helical CT and DynaCT imaging systems used for angiography (dCTA and DynaCTA, respectively). Phantom Cubes B and C were also imaged using a 3 Tesla MRI scanner. Images were acquired using The Ottawa Hospital Cancer Centre Radiation Oncology Department's

imaging protocols for SRS treatment planning of AVM disease. For CT imaging, the cubes were placed inside the head phantom then imaged. Whereas for MRI imaging, the cubes were scanned without the head phantom since, in this case, the head phantom was not used during the image co-registration process. Table 2.1 lists the imaging modalities and parameters used.

Table 2.1 Imaging modalities, scan parameters and phantoms included in this study. Scan parameters were chosen based on the department's standard imaging protocols for stereotactic radiosurgery planning using CyberKnife®. For DynaCT: $\Delta\theta$ is the angular range of the data acquisition arc for the DynaCT cone beam system, and t is the rotation time. Abbreviations: TPCT= treatment planning CT, dCTA= helical CT imaging system used for angiography, DynaCTA= DynaCT imaging system used for angiography, TR= repetition time, TE= echo time, FA= flip angle, T1w= T1 weighting, T2w= T2 weighting.

	<i>TPCT</i> <i>(reference)</i>	<i>CT</i> <i>(for dCTA)</i>	<i>DynaCT</i> <i>(for DynaCTA)</i>	<i>MRI</i>
<i>Vendor</i>	Brilliance Big	Aquilion ONE	Artis Q with DynaCT	3T Discovery
	Bore 16 Slice	320 slice		
<i>Make</i>	Philips	Toshiba Medical Systems	Siemens Medical Solutions	GE Medical Systems
<i>Scan Parameters</i>	120 kVp 450 mAs	80 kV, 300 mA t=0.5 s	70 kVp, 400 mA $\Delta\theta= 240^\circ$, $t= 20$ s 496 frames	- 3D Fast-SPGR (T1w): TR/ TE=12.8 ms/ 2.90 ms, FA=12° - 2D FIESTA (T2w): TR/ TE= 1.50 ms/ 0.52 ms, FA= 0°
<i>In-plane resolution (mm²)</i>	0.4 x 0.4	0.5 x 0.5	0.4 x 0.4	1.0 x 1.0
<i>Slice thickness (mm)</i>	1.0	1.0	1.0	1.0
<i>Phantom Cube</i>	A, B, and C	A and C	A and C	B and C
<i>Total number of image sets studied</i>	22	3	3	3

In the CT simulator suite, the head phantom was placed in a supine position, head first on the CT table and aligned such that the cube (either Cube A, B or C) was aligned with the axes of the scanner’s imaging coordinate system. Using phantom Cubes A and C, five repeatability scans were acquired using The Ottawa Hospital Cancer Centre Radiation Oncology Department’s standard CT imaging protocol for CyberKnife® brain (refer to the TPCT column in Table 2.1). Variations in post processing techniques, scan parameters and phantom setup were then introduced to test the dependence of POI detection on scan acquisition parameters. Five additional “historical” image sets (acquired between 2012 and 2017) of the head phantom with the commercial Cube A were also analyzed. The influence of phantom “misalignment” was also tested to establish if not aligning the phantom lattice lines with the scanner’s imaging axes would affect the analysis method and results. This was done by deliberately positioning the phantom so that a large rotation of approximately 10-15° about each axis was introduced. Table 2.1 lists the scanning parameters tested and the associated scan dates for Cube A. Cube B was scanned in a similar setting to get the reference image set (TPCT). A reference image set was also acquired using Cube C (lattice in air), and additional image sets were obtained using the same variations in imaging protocol and setup listed above for Cube A. A final image set of Cube C, this time in H₂O NiSO₄ solution, was acquired to verify that no physical changes occurred to the lattice structure when it was submerged in MR contrast solution (H₂O with 0.125% NiSO₄ + 0.5% NaCl). This scan is also used to test the robustness of our algorithm for finding the lattice intersection points under low contrast conditions, since the Hounsfield Units (HU) of the lattice material and water differ by only approximately 20% using our standard imaging protocol for treatment planning CT’s.

The CT and DynaCT scanners used for dCTA and 3D dCTA, respectively, was also used to acquire images of phantom Cubes A and C, using a similar setup as that done for the TPCT scans; supine, head first, with the cube carefully aligned with the scanner axes.

Table 2.2 Scan parameter changes for image sets acquired with CT using the head phantom with the Ball-Cube II (Cube A). Scan No. 1 is taken as the reference image for this phantom only. A reference image set of the rod phantom (Cube B) was also acquired, and image sets of the 3D printed phantom lattice (Cube C) were also required under all the setup conditions listed below.

<i>Scan No.</i>	<i>Varied Parameter</i>	<i>Scan Date</i>	<i>Scan No.</i>	<i>Varied Parameter</i>	<i>Scan Date</i>
1	Reference image	17-March-2017	11	Repeatability	25-Jan-2018
2	Slice spacing= 0.4 mm	17-March-2017	12	Repeatability	25-Jan-2018
3	Historical	03-Aug-2012	13	Reconstruction FOV= 512 mm	25-Jan-2018
4	Historical	07-Aug-2012	14	Filter= Standard Brain	25-Jan-2018
5	Historical	21-Nov-2014	15	Filter= Smooth Brain	25-Jan-2018
6	Historical	30-Dec-2014	16	mAs= 100	25-Jan-2018
7	Historical	05-Jan-2016	17	kVp= 90	25-Jan-2018
8	Repeatability	25-Jan-2018	18	Collimation= 160 mm x 175 mm	25-Jan-2018
9	Repeatability	25-Jan-2018	19	Small scan FOV= 200 mm x 200 mm	25-Jan-2018
10	Repeatability	25-Jan-2018	20	Phantom misaligned	25-Jan-2018

2.2.3 Image analysis and measurement of POI positions

For each phantom, image sets were first imported into the MultiPlan TPS and co-registered to a reference image set acquired using the standard TPCT imaging protocol. Image co-registration was performed using the TPS's rigid registration algorithm, where, following our typical clinical workflow, an initial manual alignment is performed, and the final auto-registration was completed by the software. For CT images, the registration volume of interest regions was kept at approximately 200 mm × 200 mm × 200 mm surrounding the skull above the mandible. For MRI images, the registration volume of interest was limited to a phantom cube only. Figure 2.4 shows an example of the registration box used on a CT image. After co-registration, the co-registered, resampled secondary image sets were exported out and re-imported back into MultiPlan. The POI positions (of the gold fiducials and copper markers) were determined on the resampled images using MultiPlan's automatic fiducial localization, as described below. After co-registration, all image sets were also exported from MultiPlan in DICOM format, to be analyzed using MATLAB as described in the subsequent section.

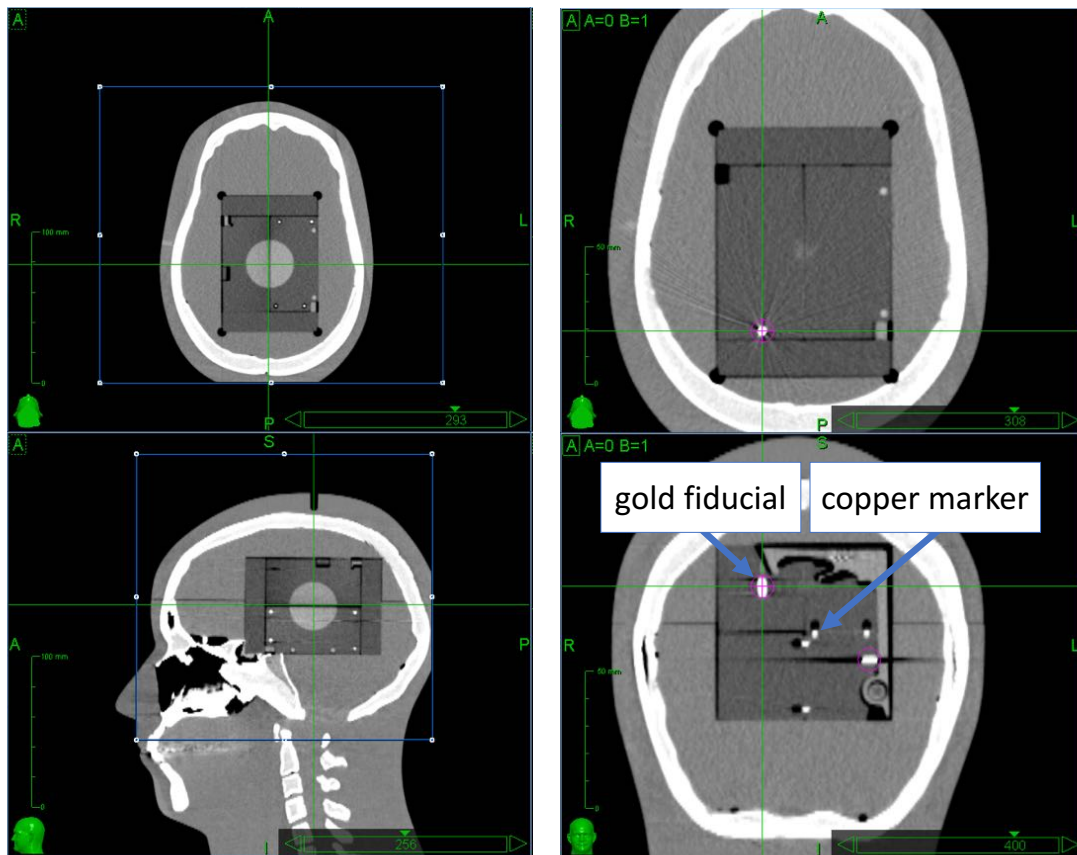


Figure 2.4 The registration box (shown on a CT image) used to define the volume of interest for image co-registration is shown on the left. The magenta circles show the gold fiducials as found by MultiPlan's Auto Centre algorithm. The smaller high density objects are the copper markers.

Measuring POI positions using MultiPlan

Image sets of Cube A were analyzed using MultiPlan's built-in Auto Center algorithm. This feature is used for fiducial tracking on the CyberKnife System. The user's manual describes the Auto Center algorithm as a tool for locating the center of the fiducial at the center of a grayscale intensity in a small volume around a user-identified fiducial location [151]. Each image set was displayed with a bone window and level of W=1200,

$L=1350$, respectively. A small spherical search region (small volume) was centred on each gold fiducial or copper marker to find the x, y, and z centroid coordinates. The repeatability of this process was estimated by determining the x, y, and z centroid coordinates for a minimum of three attempts per fiducial or marker ($\sigma < 0.20$ mm).

Measuring POI positions using MATLAB

The centroids of each gold fiducial or copper marker were also determined using an in-house written MATLAB script which finds the image intensity weighted centroid of all voxels above a given threshold within a spherical search region. A search of radius of 8 mm for the gold fiducials and 3 mm for the copper markers were used with a HU threshold of $> 95\%$ of the maximum value in the search region for both, fiducials and markers.

As described in Section 2.2.1, for Cube B, the air-filled rods appear as discs on each image slice. The centroid of these discs form 2D POIs. The grayscale of the images was inverted prior to determining the X-Y centroid positions. On a few image slices, air-filled rods running orthogonally to each other caused susceptibility artifacts (see Figure 2.5). Those POIs were excluded from the centroid positions' dataset, and only the slices where the discs were clearly distinguishable were analyzed. For the CT images, a search diameter of 5 mm was used. In the MR images, compared to contrast medium, the air and surrounding plastic rods were both hypo-intense, therefore, a larger search radius of 8 mm was used.

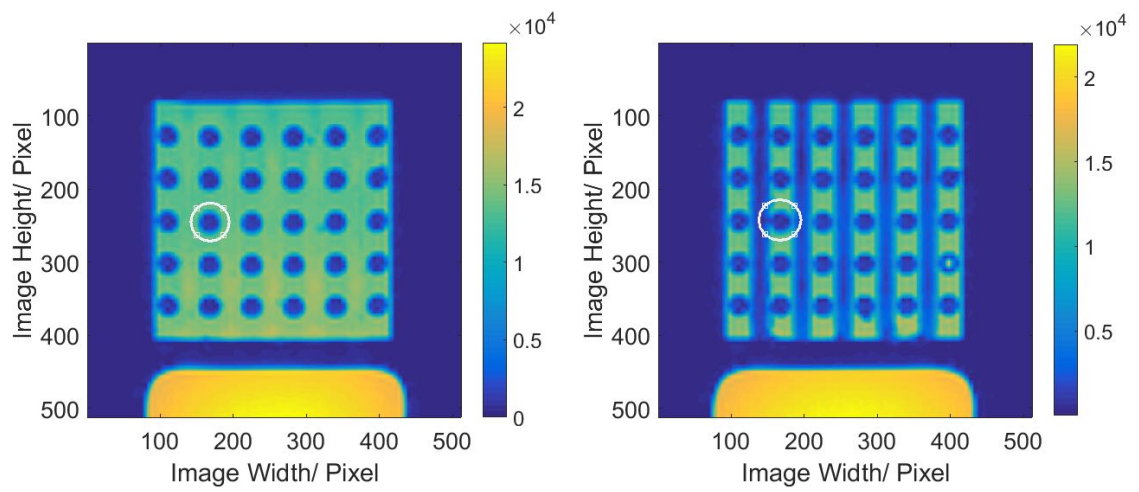


Figure 2.5 Two axial MR image slices from different positions along the longitudinal direction of phantom Cube B (the rod phantom). The white circles highlight the same rod shown on an axial slice showing a region of interest where clear distinction of the rod is found (left side image), and on another axial slice showing a region of interest where MRI artifacts cause two adjacent orthogonal rods to appear connected, thus biasing the calculated centre of mass for that rod on that axial slice (right side image).

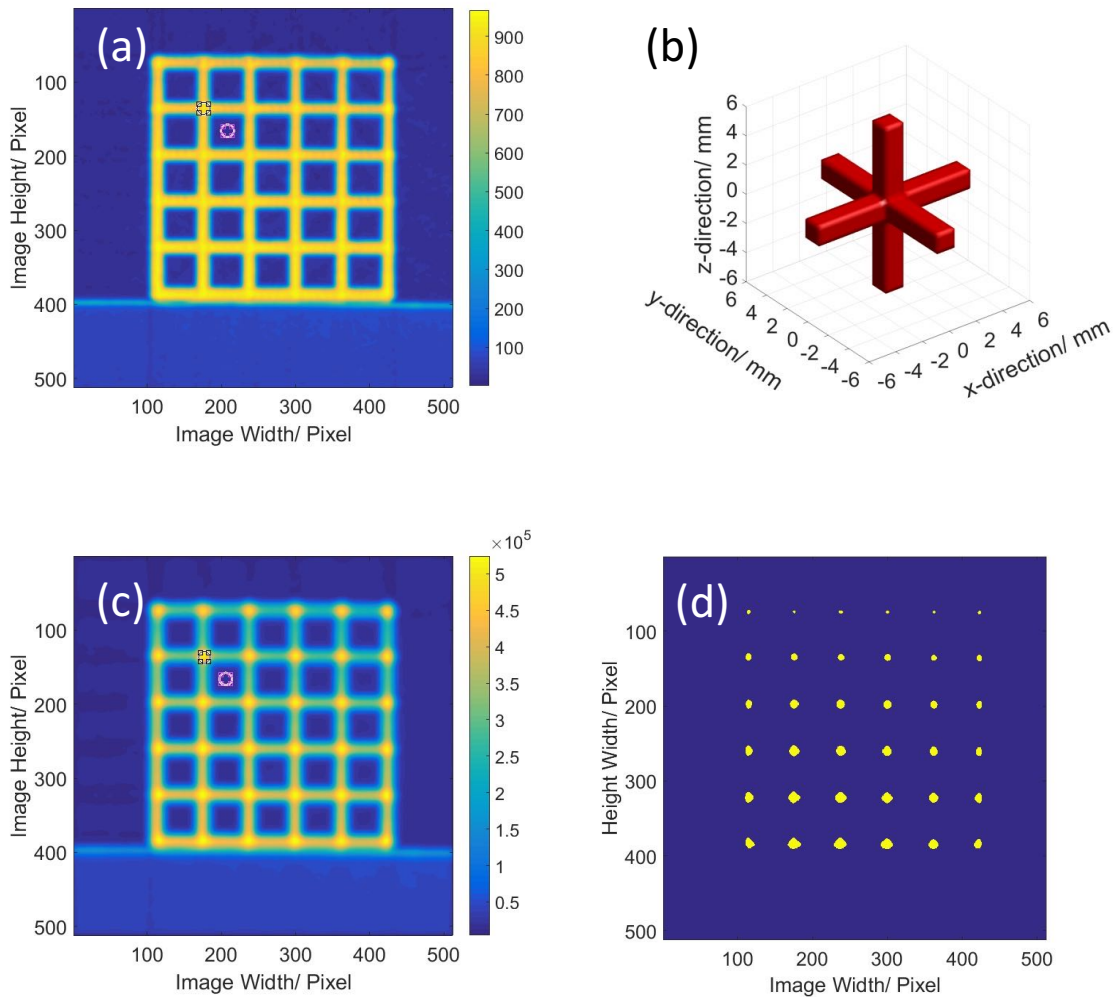


Figure 2.6 An illustration of the effect of convolution on a reference CT image slice. (a) An axial image from the raw data shown in pixel representation (physical dimensions= $53.00 \times 53.00 \times 53.00 \text{ mm}^3$), (b) the 3D cross-like convolution filter, shown with voxels set to one as red. (c) The resulting convolved image. (d) The convolved image after a threshold is applied, where the threshold is based upon the maximum value in spherical regions of interest (ROIs) around the expected lattice intersection points. The centroid inside the thresholded data inside each spherical ROI is determined using data after the step shown in (d). The ROIs used for the CNR analysis are also shown in (a) and (c), where the black circles show the signal region, and the magenta circles show the background regions.

Image sets of phantom Cube C (the 3D printed lattice phantom) were also analyzed using a MATLAB script which included the following steps (also illustrated graphically in Figure 2.6):

- (1) Image slices from the DICOM file were converted into a $512 \times 512 \times 168$ matrix. The data were first normalized to the maximum image intensity.
- (2) MR images were then inverted so that the lattice structure appears as the high intensity region compared to the surrounding medium.
- (3) To enhance the intensity of the POI's, a spatially symmetric 3D cross-like filter was used. The filter's dimensions were selected to have each arm's length equal to half the distance between inter-lattice intersections (5.0 mm), and arm's width equal to 1.5 mm.
- (4) The original 3D matrix was convolved with the 3D filter.
- (5) An initial approximation of the 3D location of each POI is obtained by using *a priori* knowledge of the inter-lattice intersection distance. These initial 3D positions are used to centre the search region used in the final step.
- (6) The lattice intersection points are then accurately determined within a spherical search region, and by using the image intensity weighted centroid of the convolved image for all voxels $> 85\%$ of the global maximum signal.

To quantify the effect of the 3D filter on convolved image intensities, the contrast-to-noise ratio (CNR) was measured on co-registered image sets acquired with different modalities and normalized to the CNR values obtained on the same image slice number of

the CT scan of Cube C (in the air-filled cube). The CNR used in this calculation is defined as:

$$\text{CNR} = \frac{(s_\mu - b_\mu)}{\sigma} \quad (2.1)$$

Where s_μ is the mean signal, b_μ is the mean background signal and σ is image noise. The region of interest (ROI) was manually selected for the signal and background on each image slice and varied between 90-105 pixels because of intraobserver ROI selection repeatability within that small area. An example of the ROIs used for the CNR analysis are shown in Figure 2.6(a) and (c).

A useful metric for quantifying image registration accuracy is the “Target Registration Error”, or TRE. In The American Association of Physicists in Medicine’s (AAPM) Task Group 132 Report [77], the TRE is defined as “the average residual error between the identified points on a secondary image set and the points identified on the reference image set, mapped onto the reference image set through image registration”. This definition can be expressed as;

$$\text{TRE} = \sqrt{(x - x_{\text{ref}})^2 + (y - y_{\text{ref}})^2 + (z - z_{\text{ref}})^2} \quad (2.2)$$

Where x, y, z are the 3D position coordinates of a POI on a secondary image set, and $x_{\text{ref}}, y_{\text{ref}}, z_{\text{ref}}$ are the position coordinates of the same POI on the reference image set.

For Cubes A, B and C the difference between a POI's position on a given image set was compared to its position on the corresponding TPCT image set (*i.e.*, reference image set), and a TRE for that point was computed. A mean TRE of an n number of POI's on a co-registered image set was then reported, where:

$$\text{mean TRE} = \frac{\sum_{i=1}^n \sqrt{(x_i - x_{\text{ref},i})^2 + (y_i - y_{\text{ref},i})^2 + (z_i - z_{\text{ref},i})^2}}{n} \quad (2.3)$$

2.3 Results

2.3.1 CNR comparison

As mentioned previously, prior to determining the POI locations, images of Cubes A and B were analyzed without additional processing steps, whereas images of Cube C were first convolved with the 3D cross-like filter. This resulted in an enhancement of the lattice intersection POIs' intensities. To illustrate the influence of this processing step on the images, Table 2.3 lists the relative CNR values for the convolved radiological images. The gain in signal intensity allowed the POI's locations to be determined more accurately. Figure 2.7 shows example axial image slices from X-ray based imaging systems using Cubes A and C placed inside the head phantom, Figure 2.8 shows example image slices from the CT (both in air and in H₂O NiSO₄ solution) and T1w and T2w MRI scans of Cube C without the head phantom.

Table 2.3 Relative CNR values of original and filtered (post image inversion) CT and MR image sets of phantom Cube C (i.e., the 3D lattice phantom). Calculated CNR values are normalized to the original readings obtained from the non-filtered CT. Negative values indicate that the signal intensity in the ROI within the lattice structure was low compared to the contrast medium. Example image slices corresponding to these image sets are shown in Figure 2.8.

<i>Image Set</i>	<i>Relative CNR for</i>	<i>Relative CNR for</i>
	<i>Original Images</i>	<i>Filtered Images</i>
(a) CT (air-filled cube)	1.00	13.42
(b) CT (MR contrast filled cube)	-0.09	0.19
(c) MRI T1w	-0.72	1.71
(d) MRI T2w	-252.67	6.05

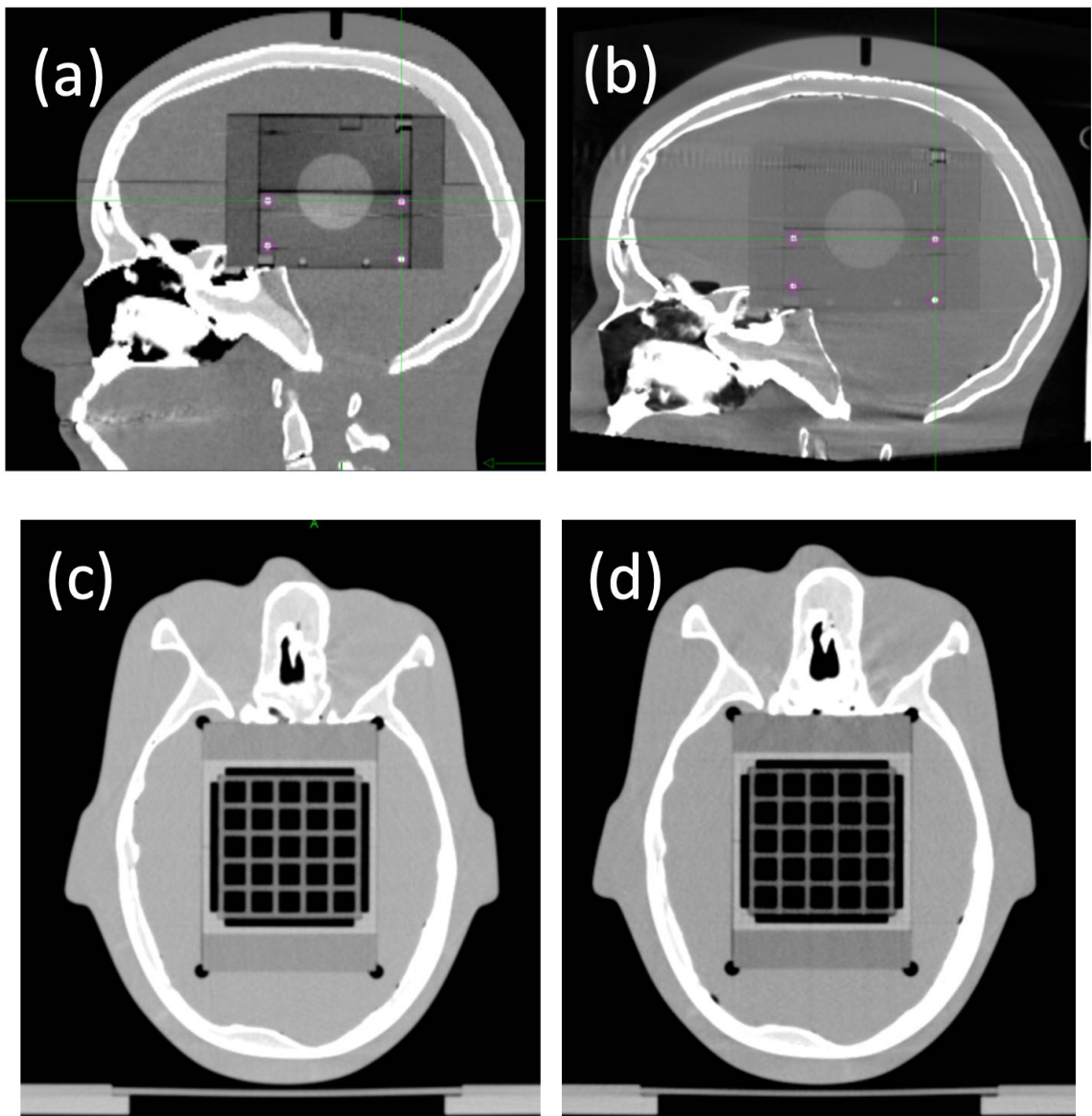


Figure 2.7 Representative images of the CyberKnife head phantom with different Cube inserts: (a) a reference TPCT of Cube A, (b) DynaCT of Cube A, (c) reference TPCT of Cube C, and (d) DynaCT of Cube C. Image slices from the CT system used for angiography are not shown due to their similarity to the reference TPCT.

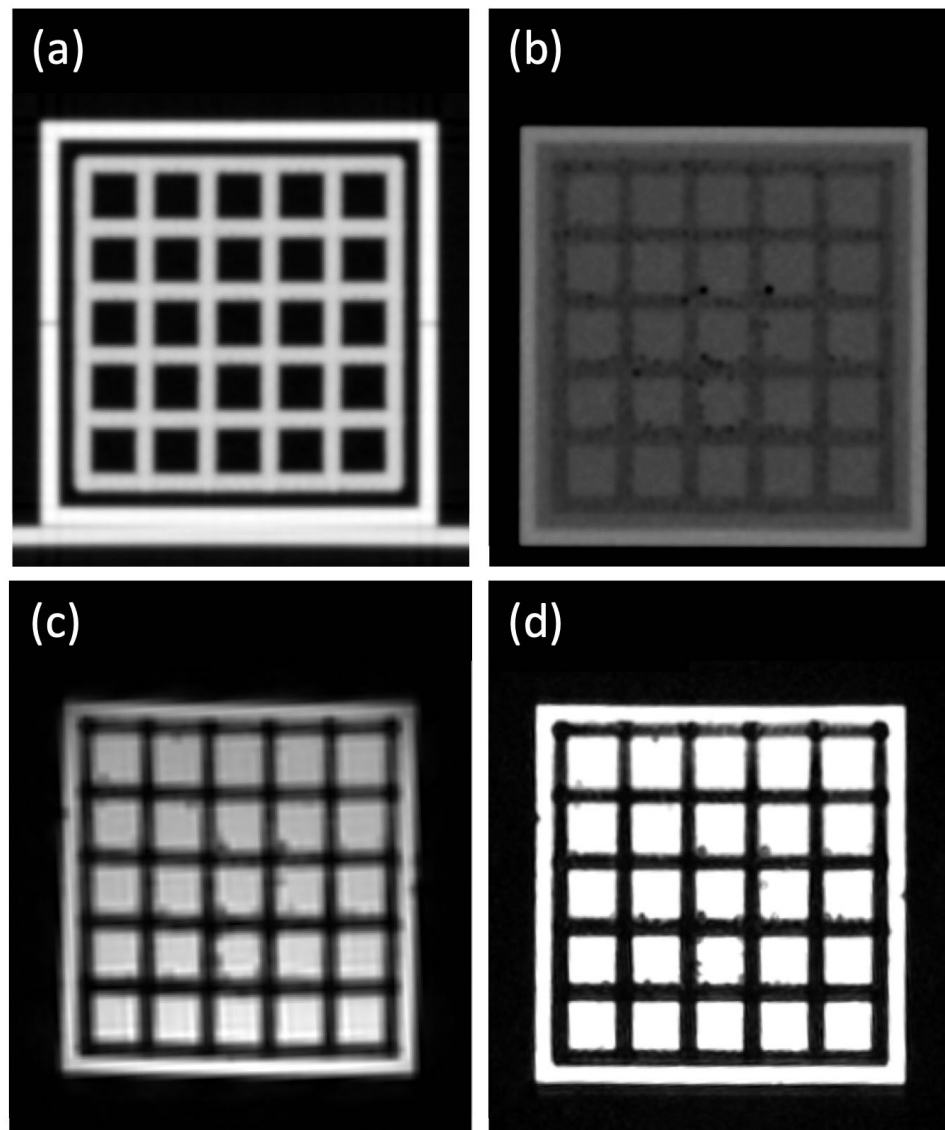


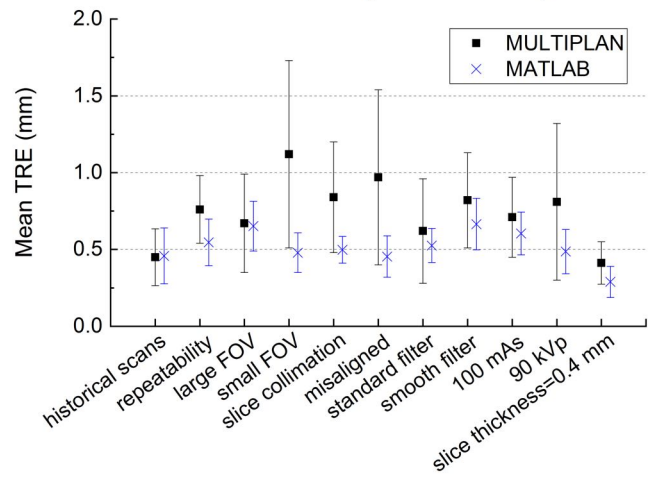
Figure 2.8 Example axial image slices of phantom Cube C from co-registered image sets; (a) a reference TPCT (in air), (b) a low contrast TPCT (in MRI contrast solution), (c) a T1w MRI, and (d) a T2w MRI. Images shown are from the same z slice on co-registered image sets. The measured relative CNR for these image slices are provided in Table 2.3.

2.3.2 Target registration errors for treatment planning CT's with varying imaging protocols

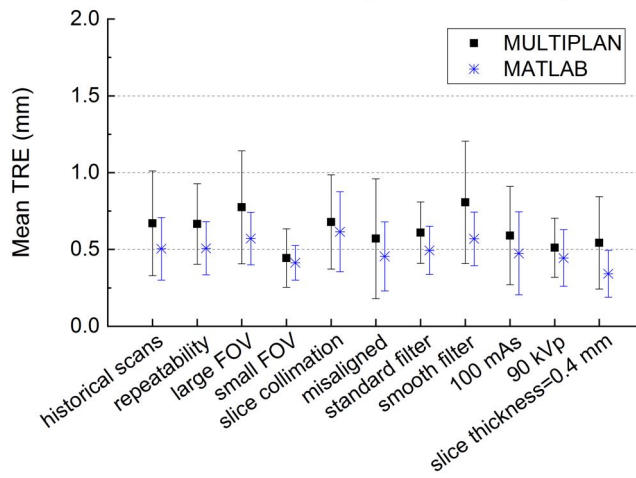
For Cube A (Accuray's Ball-Cube II), when MultiPlan's software was used to identify the POIs, the mean TRE for intra-scan repeatability demonstrated good agreement and was 0.12 ± 0.07 mm for both the gold fiducials and copper markers. The mean TRE using this method to determine POIs for historical CT image sets was 0.93 ± 0.64 mm and 0.67 ± 0.34 mm, for gold fiducials and copper markers, respectively. Using MATLAB, the mean TRE for intra-scan repeatability decreased to 0.02 ± 0.03 mm, and the mean TRE values for historical CT image data also decreased to 0.46 ± 0.18 mm and 0.50 ± 0.20 mm, for gold fiducials and copper markers, respectively. The relatively higher results for historical CT scans indicate that potential setup differences may have existed within this period.

Figure 2.9 compares the mean and standard deviation values of TRE's determined using MultiPlan and MATLAB, Cube A and Cube C (3D printed lattice cube). For nearly all image sets, smaller mean TRE's were found using MATLAB compared to MultiPlan. By comparing Figure 2.9(a) and Figure 2.9(b), it can also be observed that mean TRE values were higher for the gold fiducials than for the copper markers in nearly all image sets studied. Finally, Figure 2.9(c) demonstrates an overall decrease in mean TRE's for all variations in CT image protocols and for Cube C in comparison to Cube A.

Cube A: Commercial Phantom (Gold Fiducials)



Cube A: Commercial Phantom (Copper Markers)



Cube C: 3D Printed Lattice

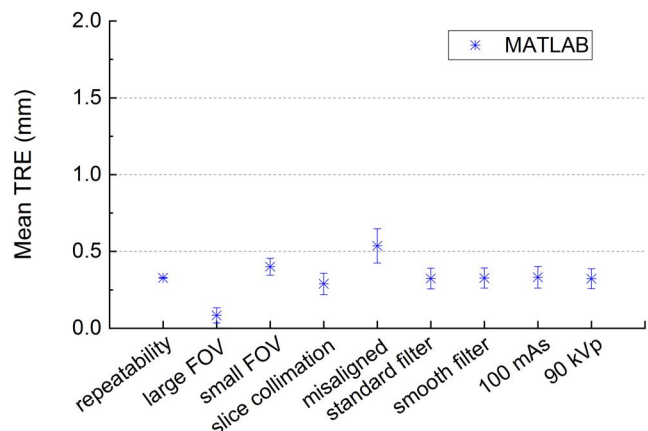


Figure 2.9 Measured mean target registration errors (TRE's) for Cubes A and C with the treatment planning CTs (Philips Big Bore scanner) acquired using variable imaging parameters. Results for Cube A (Accuray's commercial phantom) are shown using MultiPlan and MATLAB, for two cases: when the gold fiducials are taken as the points of interest (top figure), and when the copper markers are taken as the points of interest (middle figure). In comparison, the mean TRE's using the 3D printed lattice phantom are shown in the lower figure. The error bars represent one standard deviation of the mean TRE value determined for that respective image set.

2.3.3 Target registration errors (TRE's) for different imaging modalities

A comparison of the mean TRE for different imaging modalities for each of the three phantom cubes considered is shown in Figure 2.10. Since all MRI scans were acquired using phantoms placed in MR contrast, the CT scan of Cube C under that condition was included with the intermodality results. The CT data in MR contrast also demonstrates the robustness of this method to low contrast of the lattice since the relative CNR was lowest for this image set (see Table 2.3).

For each phantom cube, DynaCT image sets had the highest mean TRE. Using Cube A and MultiPlan, the mean TRE was 0.99 ± 0.52 mm for gold POIs, and 0.81 ± 0.24 mm for copper POIs. On the other hand, the highest mean TRE was 0.44 ± 0.18 mm with MATLAB processing for both Cubes A and C. MRI T1w image sets provided a mean TRE < 0.40 mm for Cube B with 2D based analysis and < 0.30 mm for Cube C, with 3D based analysis. MRI T2w image sets using Cube C showed slightly higher mean and standard deviations for the mean TRE compared to T1w images.

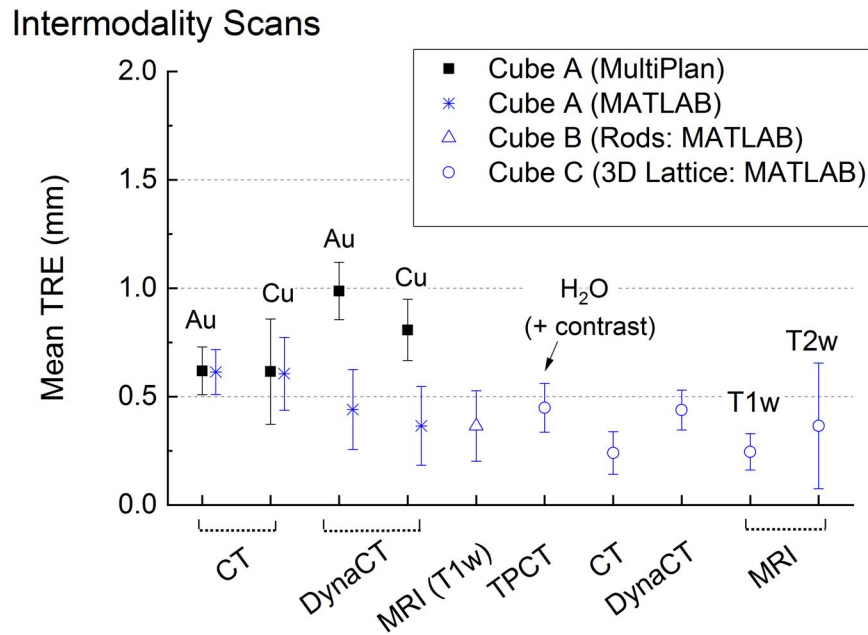


Figure 2.10 Measured mean target registration errors (TRE's) for different imaging modalities as given by Cube A (with both gold (Au) fiducials and copper (Cu) markers), Cube B (rod phantom) and Cube C (3D printed lattice). TPCT refers to the CT simulator (Philips Big Bore) used as the reference scanner. The CT (Toshiba Aquilon) and DynaCT (Siemens Artis Q) scanners are those used for dCTA and DynaCTA, respectively. Results from MultiPlan are shown in black, and those from MATLAB are in blue. The error bars represent one standard deviation of the mean TRE value determined for that respective image set.

2.4 Discussion

The AAPM Task Group 132 Report [77] recommends the use of the TRE metric to quantify image co-registration accuracy. In the presented study, inaccuracies related to 3D POI positions resulting from combined geometric inaccuracies and image co-registration errors were quantified through a combined TRE. Image voxel integrity is a voxel's representation of the true image signal of a scanned object at that particular point in image space [77]. In CT imaging, voxel integrity of the registered image set can be compromised by the contributions of sampling/ resampling effects and voxel size, the presence of image artifacts, and the overall fidelity of the imaging modality [77]. These factors can be altered by changing the scan parameters. For example, the presence of high-density objects along the x-ray beam's path can lead to photon starvation, which causes a noisy projection when insufficient photons reach the detector [152]. The noise is magnified during the reconstruction process and causes streaks to appear in the image. This can be mitigated by increasing the tube current (mAs). Yet, an increase in mAs is directly associated with an increase in patient imaging dose. With this in mind, manufacturers have developed techniques for overcoming this type of artifact, as summarized by Barrett *et al.* [152].

Using MultiPlan to localize the gold fiducials, the mean TRE from intra-scan repeatability scans for Cube A were all found to be less than the maximum voxel size dimension of the reference image set (*i.e.*, < 1 mm). The exception observed was with the small FOV scan (mean TRE= 1.2 ± 0.6 mm). We tested if a significant reduction in mAs (from 450 mAs to 100 mAs) will affect MultiPlan's ability to repeatedly find the markers/

fiducials’ positions on a “noisier” image. As shown in Figure 2.9, even after varying the mAs, kVp, slice collimation, reconstruction FOV (large FOV), and applying post processing filters, measured mean TRE’s remained < 1 mm (less than the maximum voxel dimension). The TRE values were lowest when copper markers were used (also refer to Figure 2.9). In comparison, when fiducial locations were determined using the image intensity weighted centroids in MATLAB, all image sets of Cube A (for gold fiducials and copper markers) yielded POI’s with mean TRE < 1 mm. Using the copper markers in lieu of the gold fiducials to identify POI’s offered more consistent results (smaller standard deviations over the measured sample). Although, it is worth noting that the copper markers are arranged in only two planes within Cube A, whereas the gold fiducials are arranged in different orientations and distributed more uniformly throughout the entire phantom.

Each image set of Cube C was analyzed in MATLAB by using an initial convolution step with a 3D filter. The 3D filter’s size was chosen to be smaller than the phantom’s 3D lattice’s width and height dimensions, which in turn caused the image voxel value intensities to increase in a manner that depended on the imaging modality. From the relative CNR values in Table 2.3, the filter’s effect was found to be highest for in the “lattice in-air” Cube C phantom configuration, showing its efficacy in enhancing the lattice intersection POI. Indeed, the shape of this convolution filter has previously been demonstrated [153], albeit as a 2D cross-like template in the x-y plane. In this investigation, a symmetric 3D cross filter was adopted, which we found to be more reliable and appropriate because it corresponded with the design of the lattice phantom.

Although the reference image set for Cube C also had a largest voxel dimension of 1 mm, a mean TRE < 0.5 mm were observed in nearly all image sets. The only exception found was in the case of the misaligned phantom, which also showed higher mean TRE's and slightly higher standard deviations, similar to that exhibited with Cube A (see Figure 2.9). In this case, we hypothesize that this is due to a compromise in voxel integrity, where the small high-density objects are not represented accurately on the reconstructed and resampled fused secondary image set. This causes a slight blurring effect in the resampled post-registered and post-convolved image set, that may offset the 3D position of POI's found by image thresholding. Using a higher imaging resolution and a thinner lattice structure can further reduce this affect. Nevertheless, we found that a radius of 1.5 mm offers 3D printing fidelity, low cost (which would increase if a higher resolution printer were used) and is appropriate for the chosen imaging slice thickness and desired overall setup uncertainty.

The flat panel detector of DynaCT systems has been shown to cause degraded image quality for areas outside the central plane, increasing as a function of distance from the central plane [154]. For 3D image acquisition on DynaCTA, high image quality requires projection data to be acquired over 180° plus a fan angle [155]. Furthermore, image quality is related to the system's mechanical stability, and visible artifacts can result even if minute misalignments are present. A spatial inaccuracy of up to 1.4 mm has been reported to arise from the mechanical wobble of the C-Arm gantry during gantry rotation alone [137]. In addition, as with any X-ray based imaging system, DynaCT systems also suffer from beam hardening artifacts. There is also higher scatter due to a lack of

collimation in the z-direction relative to helical CT [156]. Appendix A provides an example of how an inadequate imaging protocol can result in significant geometric distortions on a DynaCT scanner. In this study, it was found that if MultiPlan and Cube A (with gold or copper POI's) were solely used to assess geometric accuracy and co-registration errors, this may cause an overestimation of the TRE in the DynaCT images (> 1.0 mm with MultiPlan vs. < 0.50 mm with MATLAB). The mean TRE were all smaller (< 0.5 mm) with smaller standard deviations using the 3D printed phantom (Cube C) than those for the gold or copper marker-based phantom (Cube A)—for both the CT and DynaCT systems (see Figure 2.10). As expected, results from the CT scanner used for dCTA were comparable to those obtained with our CT simulator.

MRI geometric distortion is known to increase with increasing off-axis distance from the scanner's isocentre (as discussed in Section 1.3.2). It has been reported that the expected geometric distortion for a 1.5 T MRI scanner is < 0.8 mm along a 20 cm phantom, after geometric corrections are applied using vendor recommended techniques [157]. In comparison, our cube phantoms' dimensions were 63.0 mm to a side, offering a volume that was sufficient to cover typical stereotactic cranial radiosurgery planning volumes (in which both the target volume and nearby organs at risk are placed at the imaging isocentre). Although noticeable geometric distortions can be perceived on the MR images (see Figure 2.8), mean TRE values for MRI T1w image sets using phantom Cubes B and C were less than half of the voxel's dimensions (< 0.50 mm). Using Cube C, the T2w image set showed a slightly higher mean TRE and a larger standard deviation compared to the T1w image set.

Geometric distortion in MRI has previously been evaluated using 2D analysis approaches with phantoms containing rods [158–161] and grids [162,163]. Furthermore, it has been reported that 3D analysis was made possible through the use of phantoms containing 3D regions of interest (ROI's), such as 11 mm diameter spheres [164], or 3D grids [153,165]. In this study, in addition to the commercial Cube II (Cube A), two in-house phantom designs were evaluated; namely, phantom Cube B (rods: 2D analysis), and Cube C (lattice/grid: 3D analysis). Both in-house built phantoms were compatible with the CyberKnife head phantom, and showed adequate SNR on MR images. Nevertheless, a few limitations were observed for Cube B. The high precision required to guarantee reliable measurements made Cube B resource intensive (~40 hours of machining using conventional milling units). Moreover, due to the machining-limited arrangement of the rods (see design shown in Figure 2.2), Cube B can only be evaluated on an image slice-by-slice basis using 2D methods (x: right-left and y: anterior-posterior), any inaccuracies which simultaneously exist along the third dimension (z: superior-inferior) remain undetected. Finally, due to the small separations between the air-filled rods positioned along different planes, intensity thresholding was compromised on several image slices where susceptibility artifacts were observed. To minimize uncertainties, these regions were not included in our TRE measurements.

The commercial phantom Cube A and MultiPlan software approach has the advantage that any user of the CyberKnife system will have the tools necessary to implement testing of image co-registration errors and/ or geometric inaccuracy without the

need for additional phantoms or specialized programming tools. As mentioned before, however, this approach is limited to testing X-ray based systems only.

Overall, compared to the other two phantoms, Cube C has several advantages. 3D printing offered a fast and practical method to construct the main phantom body. The design and materials used were found to be simple and effective, but over a prolonged period of time, the PMMA housing will absorb water [166] causing air bubbles to appear in the phantom. This can be seen in Figure 2.8, on TPCT in water solution and MR images. Additionally, although the highest in-fill density 3D printing option was used, Fused Deposition Modeling (FDM) 3D printing caused sub-millimeter diameter air bubbles to be trapped in the printed lattice. If this is not accounted for, these bubbles can bias the analysis of MRI images since they create a lack of signal (or void) in the MR image that appears similar to the plastic lattice structure on MR images. By optimizing the relative intensity and search radius used in our MATLAB script, we were easily able to overcome this challenge. There are different types of 3D printing technologies that can offer higher resolution and higher in-fill density print options than FDM 3D printing [167] (see Appendix B for a summary of 3D printing technologies used in medicine). Recently, selective laser sintering (SLS) has been used to generate a 3D printed phantom for MRI geometric distortion assessment [168]. For the purpose of this study, dual extrusion FDM 3D printing was found to be efficient and more cost effective than SLS, which was the alternate type of 3D printer at The Ottawa Hospital's Medical 3D Printing Laboratory. The MR contrast solution used offered excellent image contrast on both T1w and T2w images. The acrylic water-absorption issue can be prevented by draining the phantom housing after

every use, or by filling the phantom housing with alternate MR compatible liquids such as mineral oil (with the drawback of this material being not as bright as H₂O NiSO₄ on T2w images). Additionally, with the use of a vibration plate, Jafar *et al.* [168] described an effective method of minimizing air bubbles, which can further improve the accuracy of identifying the lattice intersection points for Cube C.

2.5 Conclusions

In this chapter, different phantoms and analysis methods for measuring and verifying image quality and fidelity for radiological images used in radiotherapy target delineation were presented. The importance of this process was discussed for high-precision high-accuracy radiotherapy treatments, particularly for SRS. During SRS planning, images such as angiography scans and MRI might be acquired in a radiology department—which may be outside the radiation oncology department’s QA program’s oversight. Regardless, these tests should ideally be performed on a routine basis. To facilitate this practice, efficient and reliable testing phantoms and methods are required.

Building on Accuray’s anthropomorphic head phantom, three different phantom insert designs were presented. They were utilized to measure combined errors resulting from image co-registration and geometric inaccuracy on radiological image sets acquired with a CT scanner, both CT and DynaCT angiography systems, and a 3T MRI scanner. The mean TRE for each image set and with each phantom was used to quantify the errors. Thus, the lower bounds of uncertainties achievable purely due to errors arising from image

co-registration and multiple imaging modalities' geometric inaccuracies were determined on a the MultiPlan TPS.

It was found that while it is convenient for a CyberKnife user to use the commercial phantom (Cube A) in conjunction with the MultiPlan fiducial Auto Centre tool, the user may overestimate the combined errors on X-ray based systems by relying on the TPS software and the phantom's high-density points of interest. In this case, the maximum measured mean TRE was 1.12 ± 0.61 mm using gold fiducials as POI's and a small FOV CT; compared to 0.48 ± 0.13 mm using the same phantom and MATLAB, and 0.40 ± 0.05 mm using our 3D printed phantom (Cube C). Cube A is a versatile tool for end-to-end testing. However, if being used to measure geometric inaccuracy on X-ray based systems, the copper markers offered a more reliable POI compared to the gold fiducials, which cause more metal streaking artifacts.

When phantom Cubes A (fiducials), B (rods), and C (3D printed lattice) were compared, it was found that Cube C provided the lowest mean TRE values on all intermodality image sets (< 0.5 mm). The 3D printed phantom is superior in its insensitivity to variations in x-ray based imaging parameters, making it a more precise tool for geometric distortion measurements. It is a suitable QA tool for both X-ray and MR based imaging and offers a straightforward and cost effective approach to measuring geometric accuracy in 3D for all imaging modalities used in SRS planning.

In Chapter 3, a new large volume 3D printed lattice cube phantom will be presented for measurement of geometric distortion on radiological images that can be used to improve treatment accuracy of accelerated breast radiotherapy (APBI). Chapter 3 will describe how the phantom has been redesigned to mitigate several challenges encountered with the current prototype (Cube C), including those associated with the potential presence of air-bubbles. This new phantom better facilitates geometric distortion measurement on both X-ray and MRI based radiological imaging modalities with breast imaging protocols and realistic breast radiotherapy simulation setups.

Chapter 3: Measurement of MRI Geometric Distortion for Breast Radiotherapy Treatment Planning

3.1 Introduction

In the previous chapter, different types of imaging modalities used for intracranial stereotactic radiosurgery (SRS) simulation and treatment planning were presented, including computed tomography (CT), helical CT for angiography, cone beam CT for angiography, and magnetic resonance imaging (MRI). Standard-of-care breast radiotherapy planning is also performed using CT simulation images. Unfortunately, as mentioned in Chapter 1, Section 1.3.2, CT scans have limited soft-tissue contrast, making the task difficult for accurate and reproducible target delineation [60,61,169,170]. This can impact treatment quality and efficacy for accelerated partial breast irradiation (APBI) [68,171]. In contrast, MRI provides excellent soft tissue visualization and improved target delineation accuracy. This provides a more reliable imaging modality for visualizing the treatment target and presents new opportunities for evaluating APBI techniques [68,73,80]. MRI can be particularly advantageous for neoadjuvant APBI, in which *in situ* tumours can be clearly visualized. Furthermore, as discussed in Section 1.2.3, the use of MRI in image-guided radiotherapy (IGRT) for APBI treatments can significantly reduce treatment setup error margins.

MR imaging protocols can be very flexible and are often chosen depending on the anatomical information sought. They combine several MR sequences that are optimized to

maximize anatomical information presented to clinicians during the radiotherapy target delineation and treatment planning process. For example, in the post-operative setting, T1-weighted (T1w) MR sequences with fat suppression provide differentiation between glandular breast tissue and seroma [79,80,172]. T1w sequences without fat suppression are useful for visualizing surgical clips [80]. T2w sequences, with or without fat suppression, can be used to visualize the lumpectomy cavity and seroma, and to differentiate between glandular breast tissue and seroma [72,73,81,173]. In the pre-operative (neoadjuvant) setting, T1w contrast enhanced sequences are applied with fat suppression to visualize the tumour and tumour boundaries, and T2w sequences [85,174,175], with or without fat suppression, can offer differentiation between tumour tissue and post-biopsy benign tissue changes [120]. This greater imaging flexibility is enabled by the relatively more complex imaging system, components, and imaging acquisition methods employed, which can also be associated with increased geometric distortion.

In Section 1.3.2 several challenges associated with MR imaging were briefly highlighted. Of note was the known issue of geometric distortion. Geometric distortion is inherent to MR imaging, and is primarily due to two sources, system-dependent sources [165,176,177]; and patient-dependent sources (also referred to as object-dependent sources) [178–180]. In the case of system-dependent sources, geometric distortions arise from the primary static magnetic field (B_o) inhomogeneity and gradient field non-linearity. During the MR scanner acceptance and commissioning process, MR scanners undergo passive magnetic field shimming to optimize B_o homogeneity [165]. Vendor-based image post-processing corrections are typically available to mitigate gradient field non-linearity

distortions [165,181]; however, these corrections are not perfect and residual geometric distortions may still present in MR images [165,177]. In fact, distortions arising from B_0 inhomogeneity and gradient field non-linearity typically increase with radial distance from the centre of the scanner, and can be expected to be up to 4 to 4.5 mm at a radial distance of 250 mm from the centre of the scanner, near where the breast would be positioned for breast radiotherapy MR simulation [138].

Geometric distortions related to patient-dependent factors are due to magnetic susceptibility differences at tissue interfaces (*e.g.*, the nasal cavity in cranial sites, or when using patient immobilization devices for radiotherapy simulation) [182,183] and chemical shifts (*e.g.*, fat or silicone implants) [184]. These distortions are independent of radial distance from the scanner isocentre. Here, global geometric distortion corrections are not possible since the source, and therefore the characterization of geometric distortions, is patient or object dependent. Pappas *et al.* [185] provides an overview of various techniques that can be utilized to characterize and reduce patient-dependent geometric distortions, including how chemical shift artifact can be reduced by increasing receiver bandwidth. For low field MRI scanners (<1 T), it is often assumed that these distortions are negligible [186,187]. Nonetheless, this is not the case for breast radiotherapy MR simulation, where typical MR simulators have magnetic field strengths of 1.5 T to 3.0 T.

Furthermore, for the purpose of image geometric distortion correction, it is common to divide MR geometric distortions into MR sequence-independent or sequence-dependent geometric distortions [178]. In this categorization, gradient nonlinearities lead to sequence-

independent distortions, and B_o inhomogeneity, magnetic susceptibility and chemical shift leads to sequence-dependent spatial distortions.

In this chapter and building on the experimental process demonstrated in Chapter 2, the use of a large, 3D printed geometric distortion phantom is demonstrated for the purpose of characterizing and differentiating between sequence-independent and sequence-dependent geometric distortions. The method is used to extract quantitative and spatial characterizations of image geometric distortions with multiple sequences used for breast MRI imaging, and to gain insight on potential margin sizes required to account for target delineation accuracy in APBI treatment planning after MRI simulation.

3.2 Materials and methods

The materials and methods presented in Chapter 2 were further developed and used to measure errors arising from geometric distortions of MRI images acquired with common MRI breast imaging sequences. The following sub-section describes the new geometric distortion phantom prototype. Imaging protocols are then defined, following which, image handling and analysis techniques are discussed.

3.2.1 Phantom design

A new, large, in-house designed geometric distortion phantom was optimized to measure MRI geometric distortion arising from system-dependent or object-dependent

geometric distortion specifically introduced by a prone setup breast immobilization board (refer to Figure 1.5 for photographs of a similar board). The phantom was designed as a modular phantom, allowing it to be placed at different locations in the MR scanner’s bore. The phantom’s dimensions were selected to fit inside the breast board opening, where the breast would hang. The cubic lattice phantom was designed in a similar configuration as the 3D printed phantom described in Chapter 2, however, its larger size (150.0 mm × 150.0 mm × 150.0 mm) offered significantly more points of interest for point-to-point location comparisons ($n= 2744$ vs. 64). Two techniques were used to mitigate the air-bubble formation issue observed with the previous 3D printed phantom. First, a different 3D printer with improved printing accuracy was employed. Here, stereolithography (SLA) ProJet 7000 3D printer (3D Systems, Santa Clarita, California, United States), with Accura 25 resin, 100% solid interior fill, and Accura 25 supports offered 0.1016 mm layer resolution (compared with the 0.330 mm layer resolution provided by the FDM printer employed in the smaller geometric distortion phantom presented in Chapter 2). Second, to prevent water absorbance by the PMMA housing, the phantom’s housing was redesigned and built to allow easy filling and draining of the MRI contrast mixture ($\text{H}_2\text{O NiSO}_4$) such that the MR contrast solution would not be absorbed over time. The phantom design and images are shown in Figure 3.1(a), (b), and (c). In addition to these design improvements, a custom built 3-point flat leveling platform was employed to ensure that the phantom’s lattice lines were aligned parallel to the imaging setup lasers before any type of imaging was performed. With this new design, and depending on whether CT or MRI imaging applications were used, the 3D printed lattice cube can be setup with higher accuracy and be imaged suspended in air or submerged in

MRI contrast inside the housing (see Figure 3.1(b) and (d) for example setups in CT and MRI).

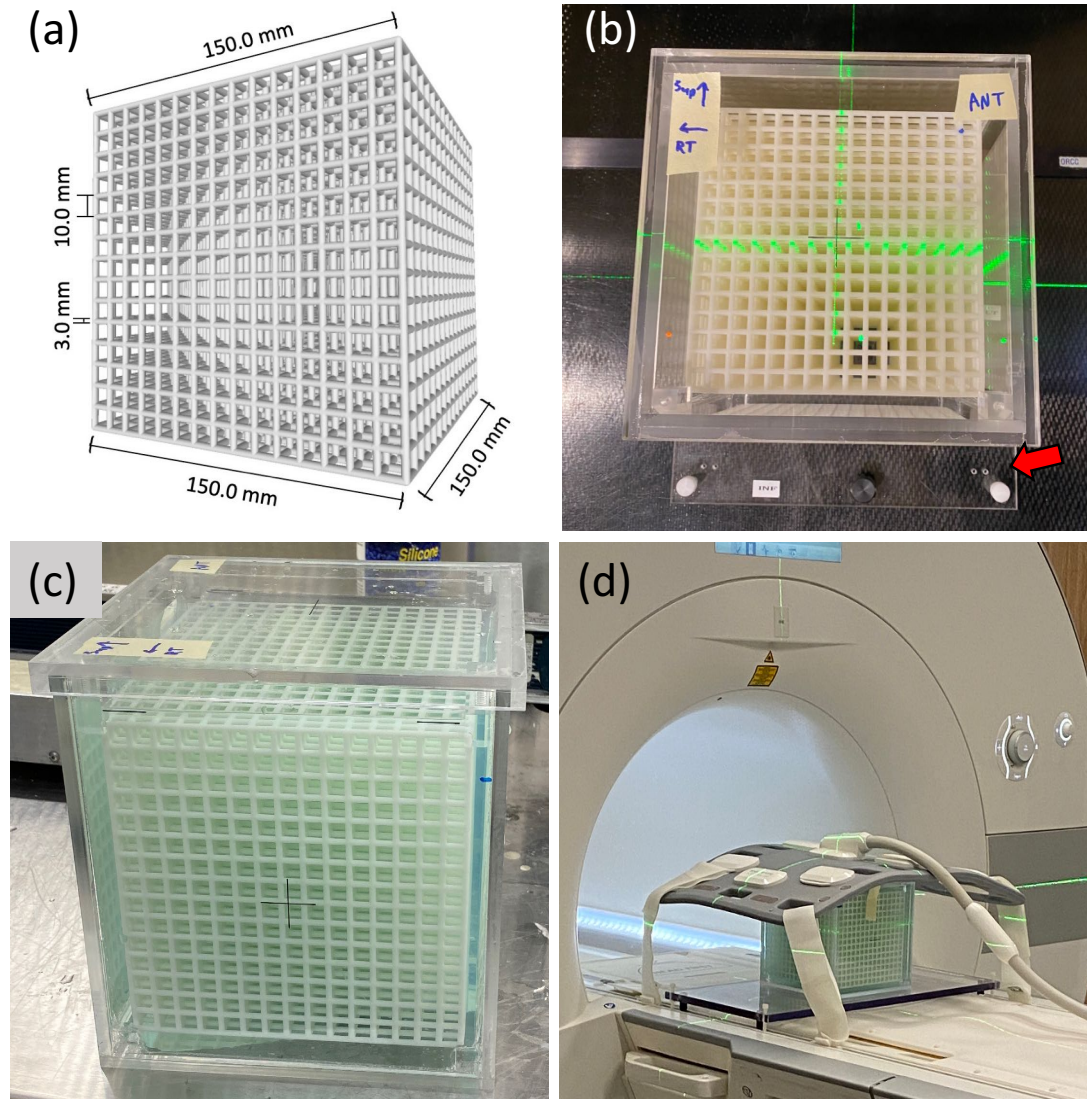


Figure 3.1 (a) Design of the large 3D printed lattice cube phantom with measurements showing the cube's dimensions, the inter-lattice line distance (10.0 mm), and the lattice line thickness (3.0 mm). (b) A top view of the 3D printed phantom inside the custom built PMMA housing with the lid on. In this photo, the phantom was setup for CT imaging with the lattice in air. The leveling platform is indicated by the red arrow. (c) A front view of the phantom, with the lattice submerged in MR contrast. (d) An image of the phantom's centre setup in alignment with the MR scanner's isocentre.

3.2.2 Imaging setup and protocols

At the time of experiments, the prone breast immobilization board was undergoing parts replacements to modify it into an MRI compatible breast board. Therefore, only system-related geometric distortion errors were measured, and the data reported here does not include data pertaining to phantom images acquired in conjunction with prone breast board.

The geometric distortion phantom was set on its leveling platform, directly on the imaging couch, and at the imaging isocentre of a helical CT radiotherapy simulator (Brilliance Big Bore 16 Slice, Philips, Amsterdam, Netherlands). The phantom was imaged in air using three different imaging protocols including the CT reference image (as listed in Table 3.1). The phantom's housing was then filled with MRI contrast, repositioned at the CT imaging isocentre, and additional CT images were acquired. Immediately afterwards, the phantom was setup on its leveling platform and on the imaging couch of a radiotherapy MRI simulator (MAGNETOM Aera, 1.5 Tesla, Siemens Healthineers, Erlangen, Germany (see setup shown in Figure 3.1(d)). MRI images were similarly acquired using different imaging protocols commonly used for breast imaging. The phantom was positioned at three locations in the MRI scanner bore: centred in the bore (at the isocentre), shifted 150 mm to the scanner's left-side, and shifted 150 mm towards the scanner's right side.

Table 3.1 and Table 3.2 provide details of imaging parameters used for CT and MRI, respectively.

Table 3.1 Details of the phantom setups and imaging parameters and phantom setups used for the reference CT image (image series number 1), as well as scans used to test the robustness of the phantom design, 3D printing quality, and image analysis method applied in this study.

<i>image series number</i>	<i>phantom setup</i>	<i>mAs</i>	<i>kVp</i>	<i>scan orientation</i>	<i>in-plane resolution (mm²)</i>	<i>slice thickness (mm)</i>
1	lattice cube in air (reference image)	350	120	axial	0.4 × 0.4	0.5
2	lattice cube in air	590	120	axial	0.4 × 0.4	0.5
3	lattice cube in MR contrast	350	120	axial	0.4 × 0.4	1.0

Table 3.2 Details of the phantom setups and MR imaging pulse sequences used to measure system and sequence-dependent geometric distortions.

N.B.: MRI pulse sequences were adopted from standard-of-care MRI pulse sequences used for breast imaging [188,189], with the omission of fat suppression in T1 MRI pulse sequences since fat suppression is used to differentiate between tumour and normal human tissue, which is not applicable in this phantom study.

<i>image series number</i>	<i>phantom setup</i>	<i>MRI pulse sequence / acquisition type</i>	<i>scan orientation</i>	<i>phase encoding (PE) direction</i>	<i>TE/ TR/ FA (ms/ ms/ °)</i>	<i>receiver bandwidth (Hz/ pixel)</i>	<i>in-plane resolution (mm²)</i>	<i>slice thickness (mm)</i>
4	no shift	T1w VIBE / 3D	axial	A>>P	7.16/ 10.9/ 10	220	0.7 × 0.7	1.5
5		T1w VIBE / 3D	axial	P>>A	7.16/ 10.9/ 10	220	0.7 × 0.7	1.5
6		T2w TSE / 2D	axial	A>>P	93/ 7160/ 150	250	0.6 × 0.6	2.0
7		T2w TSE / 2D	axial	P>>A	93/ 7160/ 150	250	0.6 × 0.6	2.0
8		T2w SPACE / 3D	coronal	R>>L	116/ 1100/ 120	590	0.9 × 0.9	0.6
9		T2w SPACE / 3D	coronal	L>>R	116/ 1100/ 120	590	0.9 × 0.9	0.6
10	shifted 150 mm to scanner right	T1w VIBE / 3D	axial	A>>P	7.16/ 10.9/ 10	220	0.7 × 0.7	1.5
11		T1w VIBE / 3D	axial	P>>A	7.16/ 10.9/ 10	220	0.7 × 0.7	1.5
12		T2w TSE / 2D	axial	A>>P	93/ 7160/ 150	250	0.6 × 0.6	2.0
13		T2w TSE / 2D	axial	P>>A	93/ 7160/ 150	250	0.6 × 0.6	2.0
14		T2w SPACE / 3D	coronal	R>>L	116/ 1100/ 120	590	0.9 × 0.9	0.6
15		T2w SPACE / 3D	coronal	L>>R	116/ 1100/ 120	590	0.9 × 0.9	0.6
16	shifted 150 mm to scanner left	T1w VIBE / 3D	axial	A>>P	7.16/ 10.9/ 10	220	0.7 × 0.7	1.5
17		T1w VIBE / 3D	axial	P>>A	7.16/ 10.9/ 10	220	0.7 × 0.7	1.5
18		T2w TSE / 2D	axial	A>>P	93/ 7160/ 150	250	0.6 × 0.6	2.0
19		T2w TSE / 2D	axial	P>>A	93/ 7160/ 150	250	0.6 × 0.6	2.0
20		T2w SPACE / 3D	coronal	R>>L	116/ 1100/ 120	590	0.9 × 0.9	0.6
21		T2w SPACE / 3D	coronal	L>>R	116/ 1100/ 120	590	0.9 × 0.9	0.6

3.2.3 Image analysis techniques

Comparison of point-of-interests' 3D positions

The experimental method and analysis approach adopted was similar to that described in Chapter 2 for the small 3D printed cube (*i.e.*, Cube C presented in Section 2.2.1). With the primary difference being that MRI images were not co-registered to the reference CT image prior to image analysis. The new 3D printed lattice cube had a total of $n=2744$ inner lattice intersection points. This excludes the intersections at the faces of the cube, which do not fully resemble the 3D cross shape of the convolution filter used (see analysis steps below). Each inner lattice intersection point was considered a point-of-interest (POI), and its 3D location on a raw secondary image was compared with that on the reference CT image.

To find the 3D location of each POI, image sets of the large cube phantom were directly analyzed in MATLAB (MathWorks, Inc., Natick, MA, U.S.A, v. R2015b) using a script similar to that described in Chapter 2. This included the following steps with added modifications listed in Steps 6-7:

- (1) Image slices from the DICOM file were first converted into a 3D matrix, and the intensity values were normalized to the maximum image intensity.
- (2) To enhance the intensity of the POIs, a spatially symmetric 3D cross-like filter was used. The filter's dimensions were selected to have each arm's length equal to half

the distance between inter-lattice intersections (5.0 mm), and arm's width equal to 1.5 mm.

- (3) The original 3D image matrix was convolved with the 3D filter.
- (4) MR images were inverted so that the lattice structure appeared as the high intensity region compared to the surrounding medium.
- (5) An initial approximation of the 3D position of each POI was obtained by using *a priori* knowledge of the inter-lattice intersection distance, assuming the lattice structure was perfectly aligned with the image axes. These initial 3D positions defined the centres of search regions used in the next step.
- (6) The POIs' 3D positions, corresponding to the lattice intersection points, were determined using the image intensity weighted centroids of the convolved image. The centroid was determined within a spherical search region (4 mm search radius) for voxels greater than a threshold of the global maximum signal around each of the initial 3D positions from Step 5. For the CT in air and MR images, the threshold value used was >80%. For the CT with the lattice in MRI contrast, the threshold value used was >80%. For the CT images with the lattice in MRI contrast solution, the threshold used was >95%.
- (7) The POIs' 3D positions found in Step 6 were then further refined in a second search iteration using the same search radius and threshold values.

A set of POI 3D positions were then available for each image set; however, to directly compare the 3D POI positions from secondary image sets to those from the reference CT image set (and subsequently measure geometric distortion) an additional step

was required. For each set of 3D POI positions, a 3D transform matrix was calculated and applied to transform POI positions within the secondary image set's coordinate system to the reference CT's coordinate system. The transform matrix for each image set (and corresponding 3D POIs) was calculated using a subset of eight POIs, located at the centre of the cube where minimal geometric distortion was expected, and by using an iterative closest point 3D rigid registration algorithm in MATLAB (MathWorks, Inc., Natick, MA, U.S.A, v. R2021a). For each image set, the 3D matrix of x , y , z coordinate locations for all POIs (A) was related to the reference coordinate system by applying a translation and rotation, such as:

$$A' = \begin{bmatrix} \cos(\theta) & \sin(\theta) & 0 \\ -\sin(\theta) & \cos(\theta) & 0 \\ 0 & 0 & 1 \end{bmatrix} * A + \begin{bmatrix} x' \\ y' \\ z' \end{bmatrix} \quad (3.1)$$

Where A' is the 3D matrix of x , y , and z coordinate locations for all POIs after rotation followed by the translation, θ is the rotation angle about the z-axis in this example, and x' , y' , and z' are the translation shifts. The sine and cosine signs varied depending on the direction of rotation required for each image set.

Once each image set's 3D POI positions were related to the reference CT's coordinate system, it was possible to calculate the magnitude of the radial geometric distortion error (r) for each POI as follows:

$$r = \sqrt{(x_t - x_{\text{ref}})^2 + (y_t - y_{\text{ref}})^2 + (z_t - z_{\text{ref}})^2} \quad (3.2)$$

Where x_t, y_t, z_t are the 3D position coordinates of a POI on secondary image set after transformation to the reference CT's coordinate system, and $x_{\text{ref}}, y_{\text{ref}}, z_{\text{ref}}$ are the position coordinates of the same POI on the reference CT image set, in its (reference) coordinate system.

Equation 3.2 is expressed similar to Equation 2.2; however, both are defined differently. In Equation 2.2, the mathematical expression was referred to as the “target registration error” and was used to quantify combined errors resulting from image geometric distortion as well as image co-registration. On the other hand, Equation 3.3 is used to quantify image geometric distortions only.

CT images were used to assess the robustness of the 3D printed phantom and analysis method. No geometric distortion was expected for this modality, and the mean radial geometric distortion error was plotted for each POI separately.

To visualize geometric distortions on MR images obtained with different setups and different imaging protocols, the mean radial geometric distortion error was plotted against the radial distance from centre of the scanner bore (isocentre).

Additionally, a mean radial geometric distortion error (r_{avg}) of n POIs for each secondary image set was also reported, as:

$$r_{\text{avg}} = \frac{\sum_{i=1}^n \sqrt{(x_{t,i}-x_{\text{ref},i})^2 + (y_{t,i}-y_{\text{ref},i})^2 + (z_{t,i}-z_{\text{ref},i})^2}}{n} \quad (3.3)$$

For MR image sets, the total number of POIs n ranged from 2739 to 2744 points, when excluding POIs that suffered from image susceptibility artifacts or those at the edge of the usable field of view from analysis. Such POIs were unreliable because their thresholded volumes do not provide a true image representation of the lattice intersection.

3.3 Results

3.3.1 CT imaging

Figure 3.2 shows image slices of the 3D printed phantom scanned on CT with different imaging protocols, in air, and when the phantom housing was filled with MR contrast.

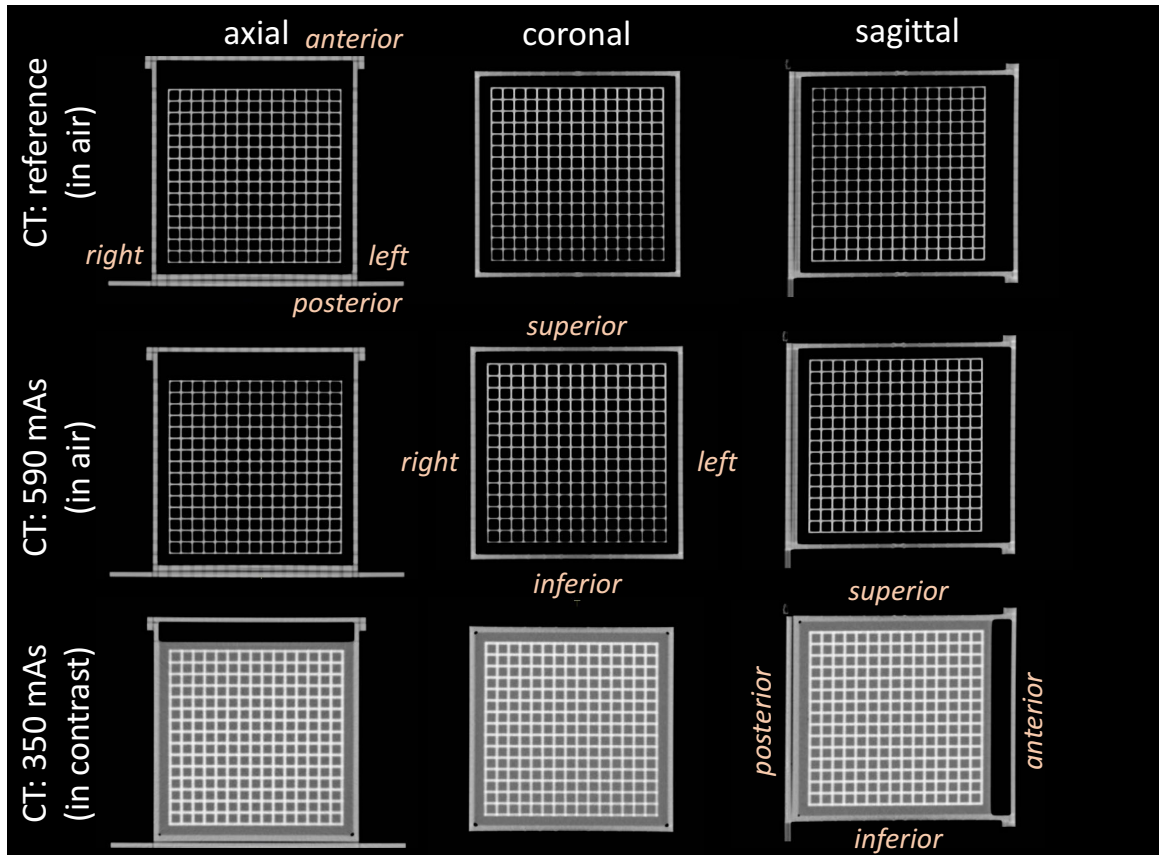


Figure 3.2 4 Image slices from CT scans of the 3D printed phantom in the phantom housing. Images are shown along orthogonal slice directions (axial, coronal, and sagittal) and the physical directions with respect to the phantom are shown for orientation purposes. CT scans were taken with different parameters and setups, details of which are listed in Table 3.1. Displayed CT image slices were acquired at the same axial slice with image window= 600 and image level= 40.

The magnitudes of radial geometric distortion errors (r) for all POIs measured on CT images with different imaging protocols and setups are shown in Table 3.3. For CT scans with the phantom in air and with varying mAs and slice thicknesses, errors increased with increasing slice thickness, but were small relative to the voxel (see Figure 3.3(a) and (b)). In air, the maximum errors for CT were 0.09 mm and 0.24 mm, for slice thickness of 0.5 mm and 1.0 mm, respectively. When the phantom was submerged in water, the

maximum error for all POIs increased to 0.52 mm. Figure 3.3(c) shows the error for all POIs in the latter setup condition.

Table 3.3 A summary of the maximum and mean geometric radial distortion errors (r) for different phantom setups and different CT imaging protocols.

	<i>description of image set</i>				r (mm)	
<i>phantom setup</i>	<i>mAs</i>	<i>kVp</i>	<i>slice thickness (mm)</i>	<i>number of POIs</i>	<i>maximum</i>	<i>mean</i>
lattice cube in air	590	120	0.5	2744	0.09	0.01 ± 0.01
lattice cube in air	350	120	0.5	2744	0.24	0.10 ± 0.04
lattice cube in MR contrast	350	120	1.0	2744	0.52	0.21 ± 0.09

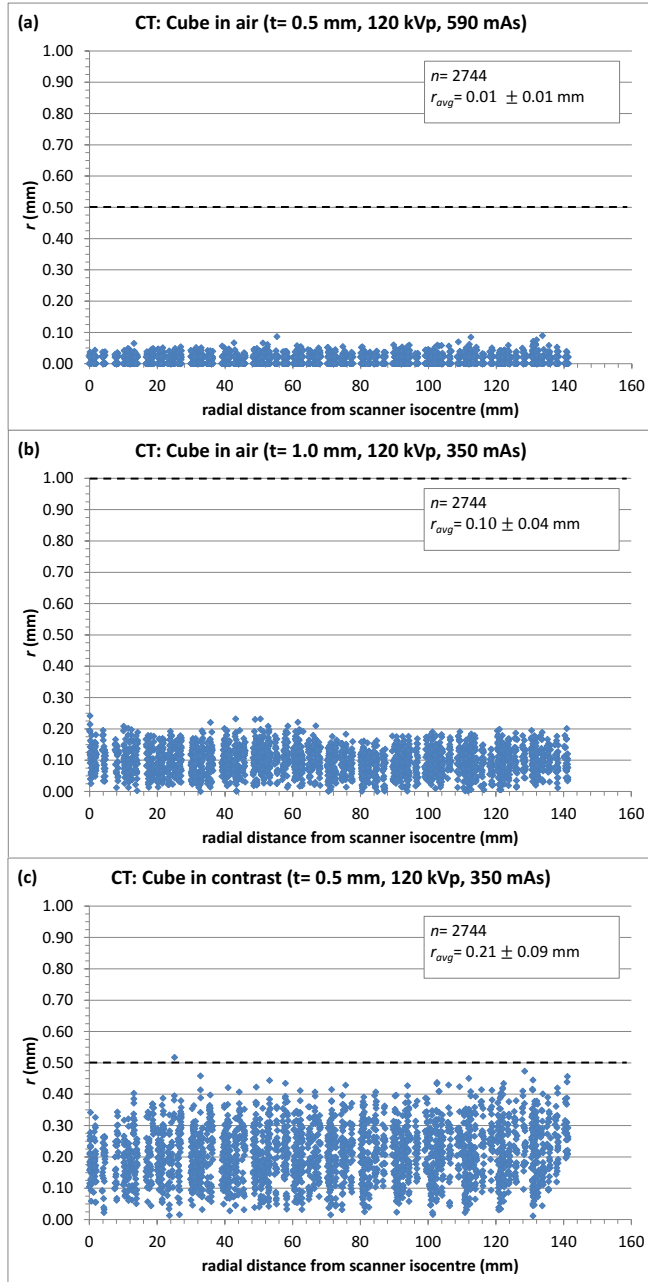


Figure 3.3 The magnitude of radial geometric distortion errors (r) for images of the 3D printed phantom acquired with the CT scanner shown as a function of radial distance from the scanner isocentre. The radial geometric distortion error represents the difference between the radial position of a particular POI compared with its radial position on the reference CT scan, which was acquired in air, with slice thickness (t) of 0.5 mm, 120 kVp, and 350 mAs. The dashed black lines show the magnitude of the slice thickness in mm for each scan used and are provided for visual comparison purposes only.

3.3.2 MR imaging

Figure 3.4, Figure 3.5, and Figure 3.6 show image slices of the phantom scanned with different MR imaging sequences at the central axis, shifted to the right side of the scanner isocentre, and shifted to the left side of the scanner isocentre, respectively. At the scanner isocentre, and through qualitative assessment, the phantom's geometrical integrity qualitatively appears preserved along all slice directions and with all MR sequences used (see Figure 3.4). Although, the effects of geometric distortion become visible when the phantom was shifted by 150 mm from the scanner isocentre to the right (see Figure 3.5) and to left side (see Figure 3.6) of the scanner isocentre. Here, the degree of distortions varied depending on MR sequence used, direction, and the right vs. left position of the phantom. In these last two figures, geometric distortion is clearly visible as geometric warping at the field-of-view edges, and through the lack of discontinuity of the 3D printed phantom's lattice lines. Furthermore, some intersection points were cut off from the usable field-of-view which caused undetectable POIs, as mentioned in Section 3.2.3.

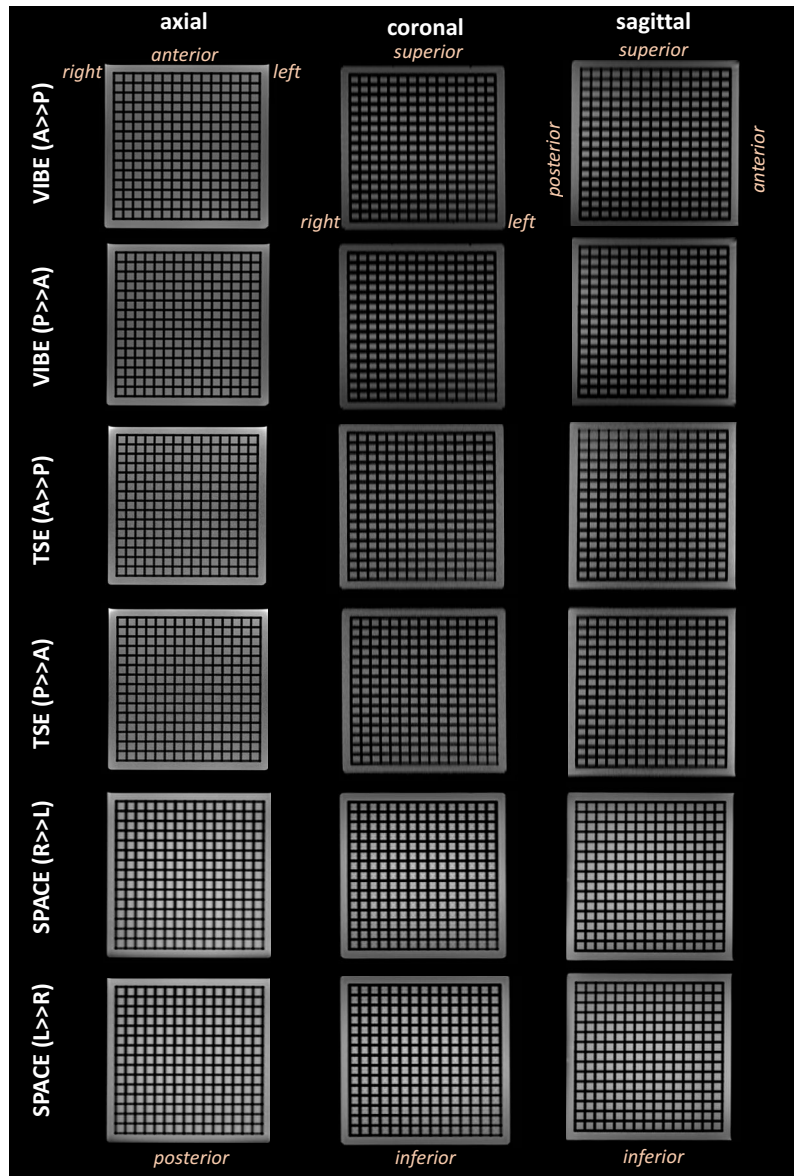


Figure 3.4 MR images of the 3D printed phantom in the phantom housing filled with MR contrast when the phantom was positioned at the scanner isocentre. The image series are presented in reformatted orthogonal views (axial, coronal, and sagittal) through the centre of the phantom for comparison. The physical directions with respect to the phantom are shown for orientation. MR sequence details are listed in Table 3.2, and phase encoding direction is indicated in parenthesis. Displayed MR image slices were captured at the same imaging position, and with image window= 663 and image level= 370 for T1w VIBE and T1w TSE sequences, and image window= 350 and image level= 200 for T2w SPACE sequences.

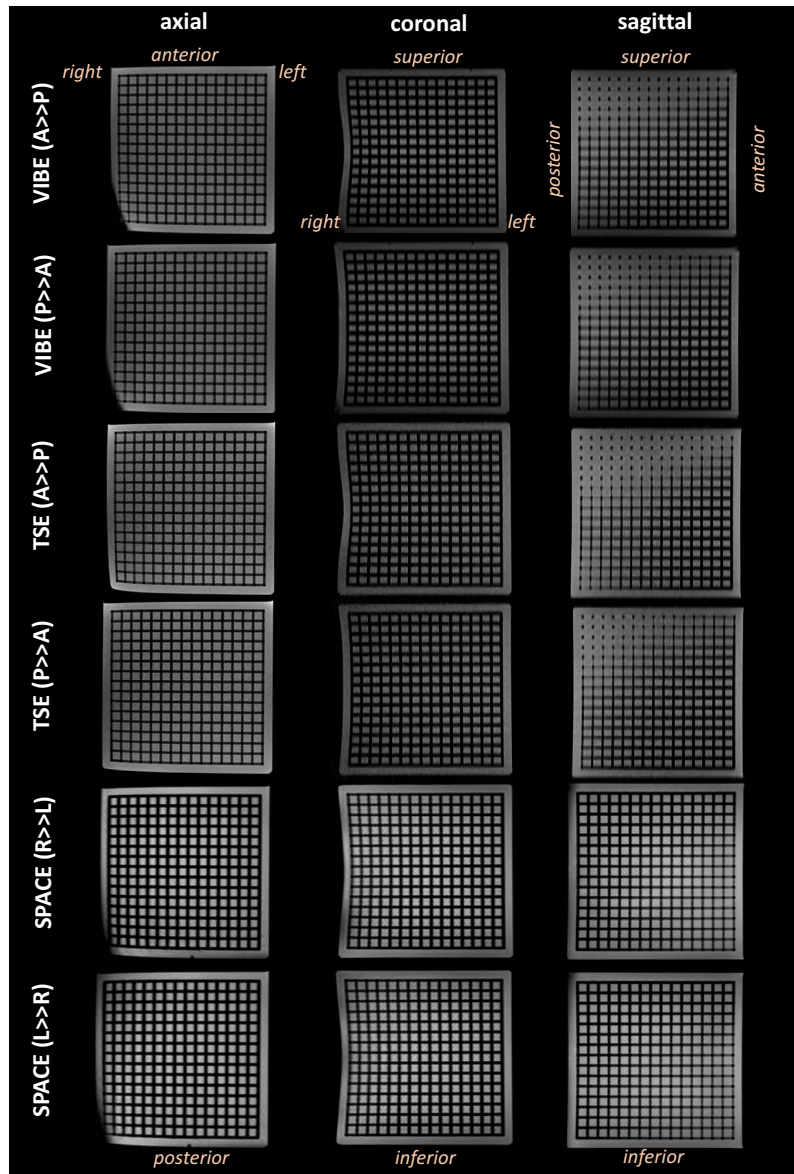


Figure 3.5 MR images of the 3D printed phantom in the phantom housing filled with MR contrast when the phantom was shifted by 150 mm towards patient's right with respect to the centre of the scanner isocentre. The image series are presented in reformatted orthogonal views (axial, coronal, and sagittal) through the centre of the phantom for comparison. The physical directions with respect to the phantom are shown for orientation. MR sequence details are listed in Table 3.2, and phase encoding direction is indicated in parenthesis. Displayed MR image slices were captured at the same imaging position, and with image window= 663 and image level= 370 for T1w VIBE and T1w TSE sequences, and image window= 350 and image level= 200 for T2w SPACE sequences.

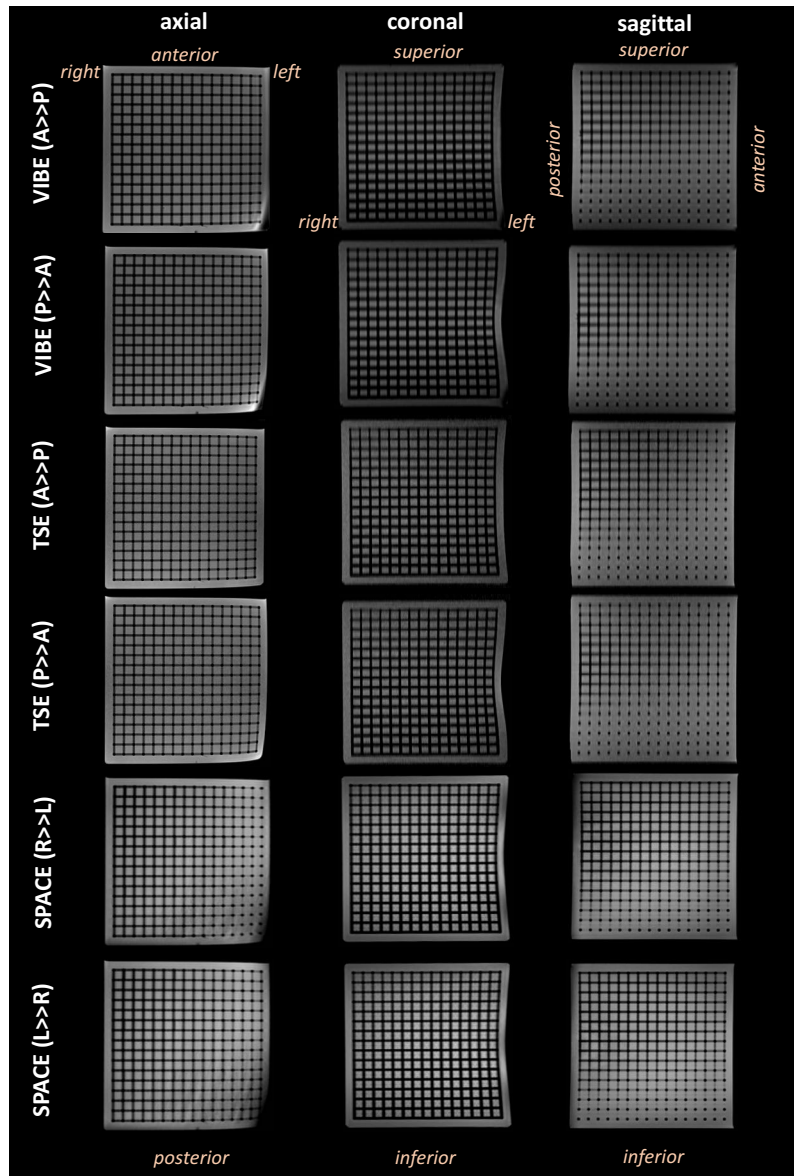


Figure 3.6 MR images of the 3D printed phantom in the phantom housing filled with MR contrast when the phantom was shifted by 150 mm towards patient's left with respect to the centre of the scanner isocentre. The image series are presented in reformatted orthogonal views (axial, coronal, and sagittal) through the centre of the phantom for comparison. The physical directions with respect to the phantom are shown for orientation. MR sequence details are listed in Table 3.2 and phase encoding direction is indicated in parenthesis. Displayed MR image slices were captured at the same imaging position, and with image window= 663 and image level= 370 for T1w VIBE and T1w TSE sequences, and image window= 350 and image level= 200 for T2w SPACE sequences.

The magnitudes of radial geometric distortion errors (r) for all POIs measured on MR images with different imaging protocols and phantom setups are summarized in Table 3.4. In this table, geometric distortions were reported through the maximum and mean r values for all POIs in each image set. As expected, differences in r were observed depending on the phantom's setup location and increased at the lateral edges of the MRI scanner's field of view. The maximum errors observed were for T1 VIBE sequences and were 3.96 mm (when the centre of the cube was shifted 150 mm to the left side of the scanner isocentre) and 3.88 mm (when the centre of the cube was shifted 150 mm to the right side of the scanner isocentre). The mean r for these two image sets were similar and were 0.70 ± 0.42 mm and 0.76 ± 0.40 mm, for the left and right sided setups, respectively. Differences in r were also observed for all sequences when the phase encoding directions were flipped, with the maximum differences being for 2.49 mm for T1w VIBE, followed by 1.50 mm for T2w TSE. These reported r values are also shown in scatter plots for all POIs in each image set obtained at different positions with respect to the radial distance from the MR scanner isocentre in Figure 3.7 (with no offset), Figure 3.8 (with the cube's central axis shifted 150 mm to the right side of the scanner isocentre), and Figure 3.9 (with the cube's central axis shifted 150 mm to the left side of the scanner isocentre).

Table 3.4 A summary of the maximum and mean geometric radial distortion errors (r) for different phantom setups and different MR pulse sequences. The pairwise maximum and mean differences in r for each image sequence, and under the same setup, but with opposing phase encoding readout directions are also compared.

phantom setup	description of image set				r (mm)		difference in r with PE direction (mm)	
	MRI pulse sequence	phase encoding (PE) direction	scan orientation	number of POIs	maximum	mean	maximum	mean
no shift	T1w VIBE	A>>P	axial	2743	1.21	0.47 \pm 0.23	0.31	0.05 \pm 0.05
	T1w VIBE	P>>A	axial	2743	1.21	0.46 \pm 0.23		
	T2w TSE	A>>P	axial	2744	1.18	0.50 \pm 0.22	0.90	0.13 \pm 0.11
	T2w TSE	P>>A	axial	2743	1.21	0.46 \pm 0.23		
	T2w SPACE	R>>L	coronal	2744	1.52	0.64 \pm 0.32	0.23	0.04 \pm 0.04
	T2w SPACE	L>>R	coronal	2744	1.60	0.65 \pm 0.33		
shift 150 mm to scanner right	T1w VIBE	A>>P	axial	2741	2.52	0.60 \pm 0.35	1.47	0.20 \pm 0.18
	T1w VIBE	P>>A	axial	2744	3.88	0.76 \pm 0.40		
	T2w TSE	A>>P	axial	2744	2.01	0.62 \pm 0.31	1.43	0.16 \pm 0.16
	T2w TSE	P>>A	axial	2744	3.40	0.71 \pm 0.41		
	T2w SPACE	R>>L	coronal	2740	2.96	0.77 \pm 0.46	1.37	0.08 \pm 0.09
	T2w SPACE	L>>R	coronal	2740	2.55	0.81 \pm 0.47		
shift 150 mm to scanner left	T1w VIBE	A>>P	axial	2743	3.96	0.70 \pm 0.42	2.49	0.21 \pm 0.21
	T1w VIBE	P>>A	axial	2739	2.69	0.63 \pm 0.35		
	T2w TSE	A>>P	axial	2744	3.54	0.70 \pm 0.41	1.50	0.16 \pm 0.17
	T2w TSE	P>>A	axial	2744	2.12	0.64 \pm 0.30		
	T2w SPACE	R>>L	coronal	2741	3.29	0.75 \pm 0.44	1.24	0.06 \pm 0.08
	T2w SPACE	L>>R	coronal	2741	3.29	0.74 \pm 0.42		

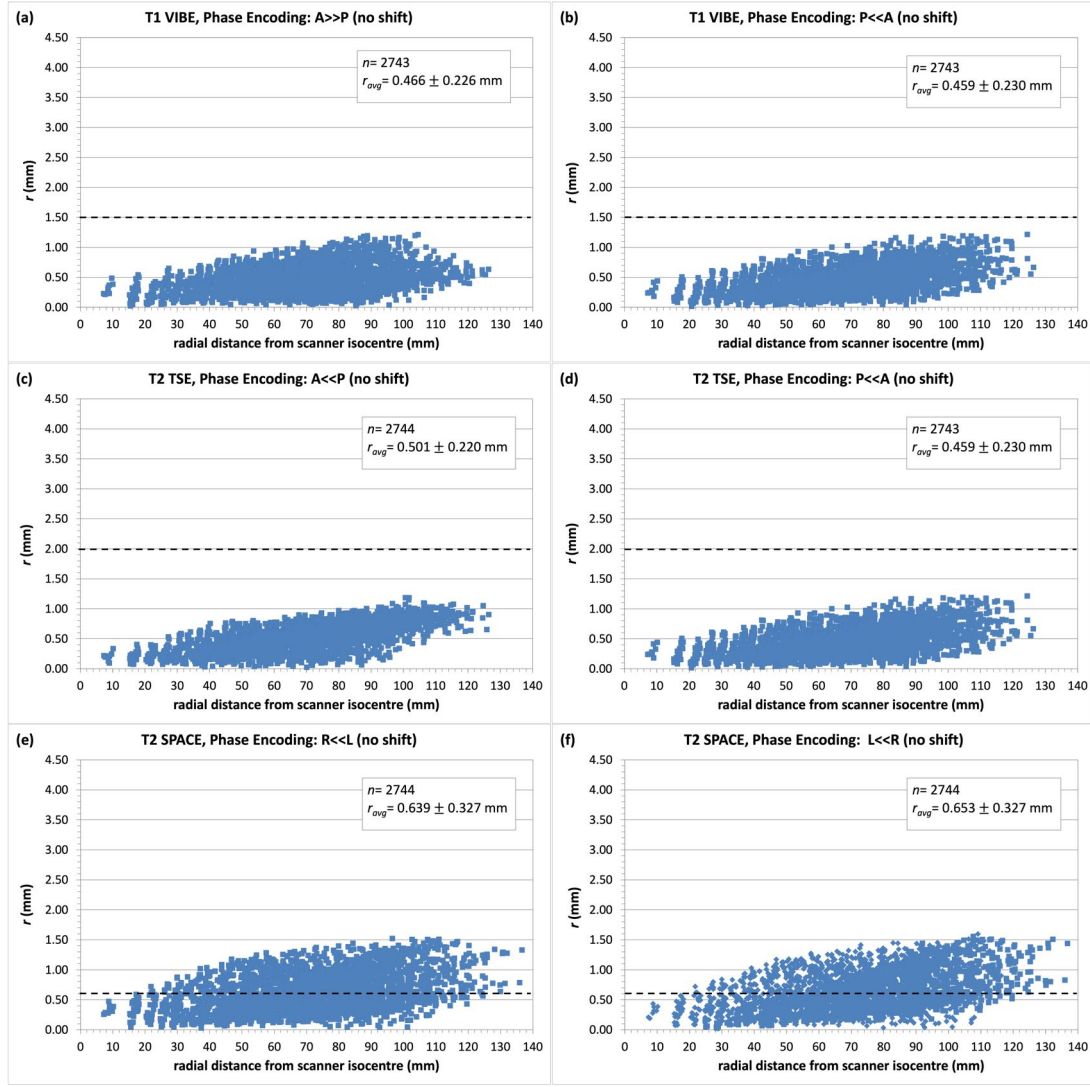


Figure 3.7 The magnitudes of the radial distortion errors (r) shown as a function of the radial distance from the isocentre when the phantom cube was centered in the scanner bore. The radial distance includes the x, y, and z coordinates of each POI. Each subfigure shows the effect of a particular MR imaging sequence, as well as the phase encoding readout direction. The mean radial geometric error (r_{avg}) and the total number of POIs (n) included in the analysis are provided for each image set. The dashed black lines show the magnitude of the slice thickness in mm for each MR sequence used and are provided for visual comparison purposes only.

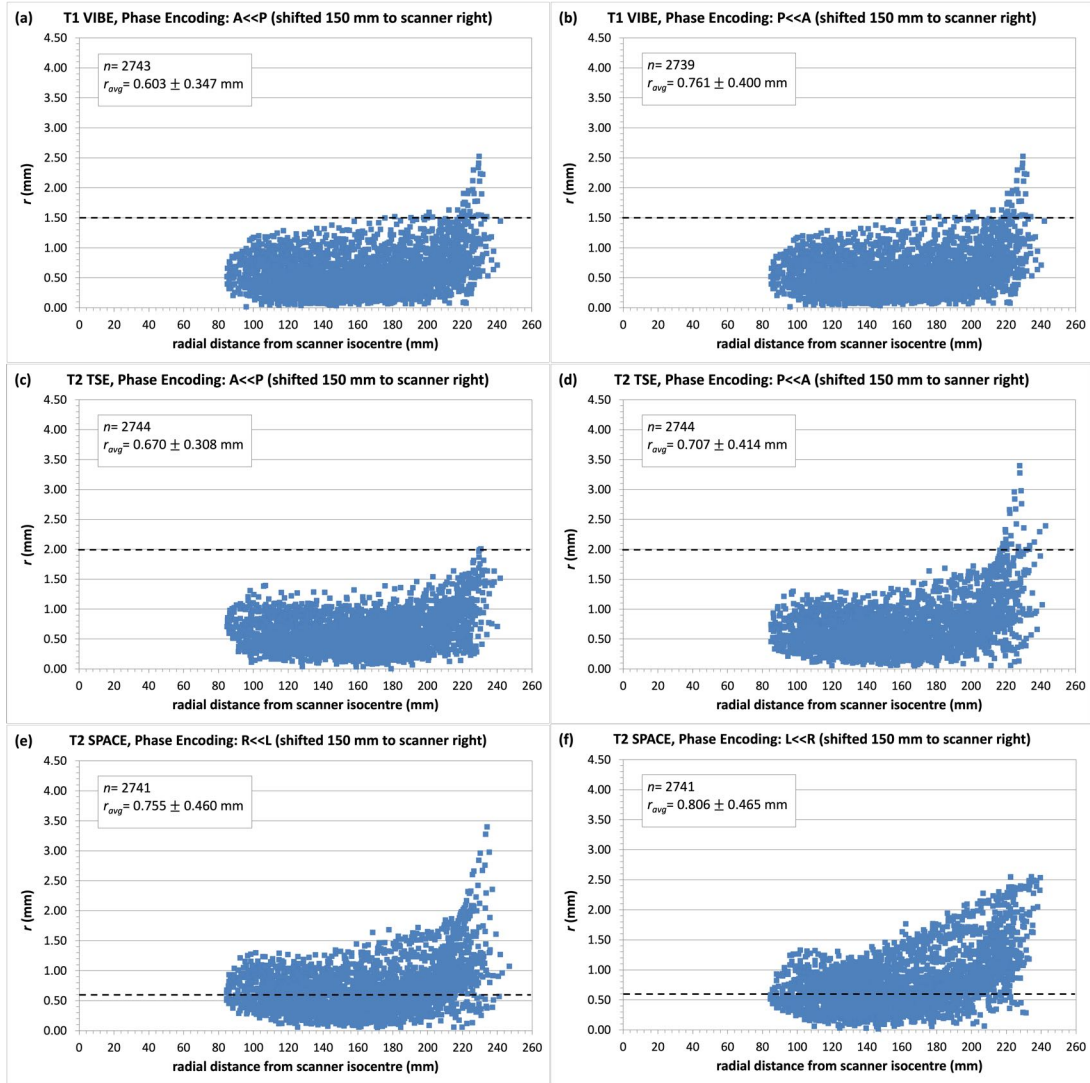


Figure 3.8 The magnitudes of the radial distortion errors (r) shown as a function of the radial distance from the scanner isocentre when the phantom cube was shifted 150 mm to the right from the scanner isocentre (as viewed from the foot of the couch). The radial distance includes the x, y, and z coordinates of each POI. Each subfigure shows the effect of a particular MR imaging sequence, as well as the phase encoding readout direction. The mean radial geometric error (r_{avg}) and the total number of POIs (n) included in the analysis are provided for each image set. The dashed black lines show the magnitude of the slice thickness in mm for each MR sequence used and are provided for visual comparison purposes only.

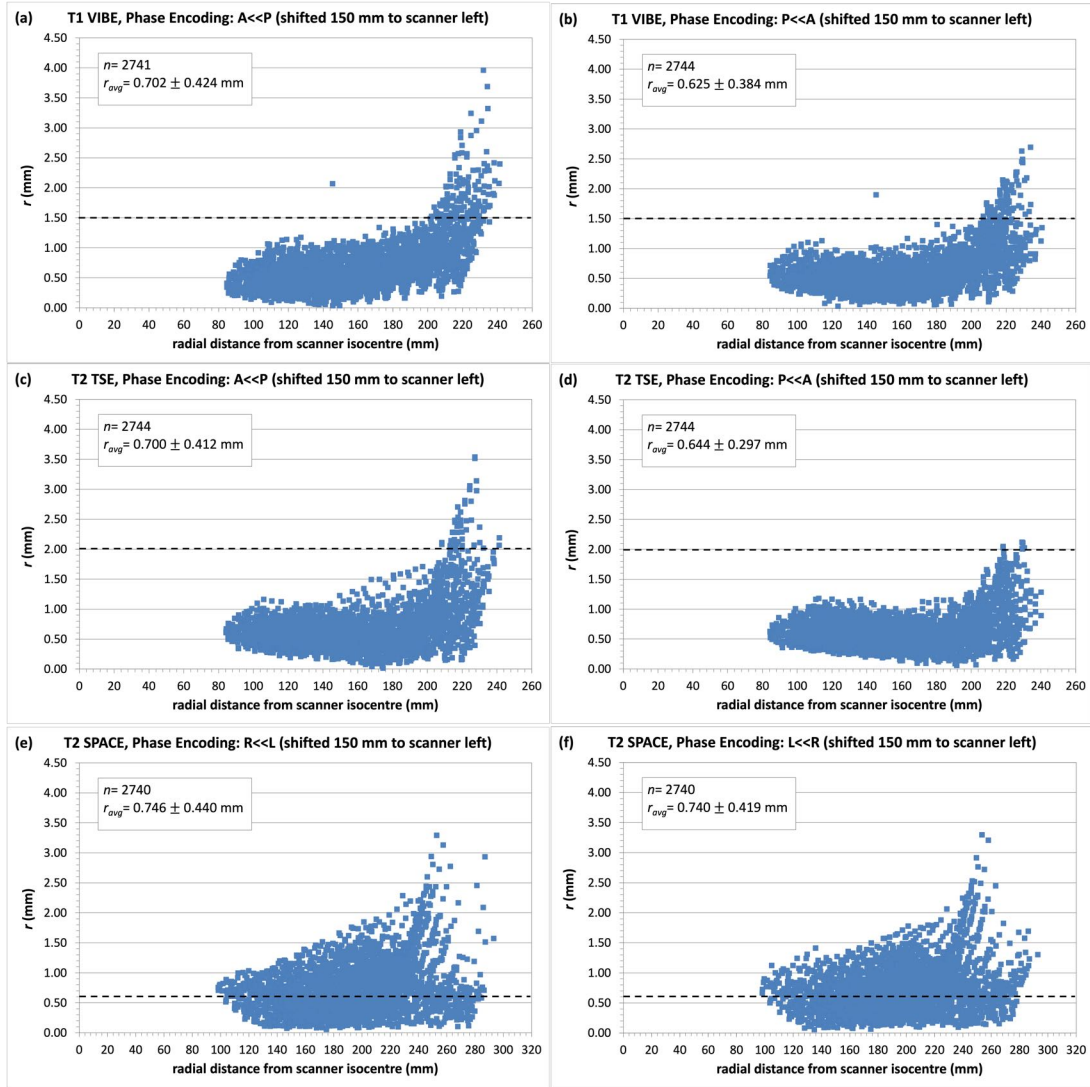


Figure 3.9 The magnitudes of the radial distortion errors (r) shown as a function of the radial distance from the scanner isocentre when the phantom cube was shifted 150 mm to the left from the scanner isocentre (as viewed from the foot of the couch). The radial distance includes the x, y, and z coordinates of each ROI. Each subfigure shows the effect of a particular MR imaging sequence, as well as the phase encoding readout direction. The mean radial geometric error (r_{avg}) and the total number of ROIs (n) included in the analysis are provided for each image set. The dashed black lines show the magnitude of the slice thickness in mm for each MR sequence used and are provided for visual comparison purposes only.

3.4 Discussion

The large number of POIs and the phantom's modular design facilitated accurate quantification of geometric distortion errors at various positions in the MRI scanner's bore. Having a modular design that can be placed at different positions in the scanner's bore allowed greater flexibility in positioning, and the option to use the phantom in conjunction with a breast immobilization board. Furthermore, compared with a phantom that encompasses the entire scanner's imaging FOV, this design is practical to build, is easier to carry and position (compared with large, heavy commercial phantoms), and significantly reduces 3D printing costs. The efficacy of image analysis methods has previously been demonstrated in Chapter 2, but it was important to characterize any differences related to the utilization of a different 3D printing technology (SLA vs. FDM), printing material (Accura 25 resin vs. ABS), and printing specifications as well. The results presented in Table 3.3 showed that when no geometric distortion was expected (on CT), differences in POI positions were minimal and were mainly attributed to the size of the slice thickness chosen.

Once the commissioning process is complete, most cancer centres adopt MRI simulation for cranial sites first [190,191] which is relatively easier to implement due to the skull's rigid nature allowing reproducible setups at the scanner's central axis and reliable MR-to-CT image co-registration. Other common sites are head and neck [192] and the pelvic region [193–196]. Optimized MRI protocols and clinical experience are available and well established for these anatomical sites [66]. Interest in using MRI

simulation for breast radiotherapy is increasing as alternatives to whole breast radiotherapy (WBRT), such as PBI or APBI, have become more common; however, there is less clinical experience with MR simulation for breast radiotherapy and recommendations for MR sequences for simulation for this site are not available. Therefore, in this study, the standard-of-care sequences used for MRI diagnostic breast imaging [197] were selected. For these precise radiotherapy techniques, it was also important to use 3D sequences where vendor-based geometric distortion corrections would apply along all three imaging planes.

When the phantom was centered in the scanner bore, the radial distortion errors were of similar magnitude, ranging between 0.46 ± 0.23 mm and 0.65 ± 0.33 mm depending on the imaging sequence used (refer to the “no shift” section in Table 3.4, Figure 3.4, and Figure 3.7). This means that geometric distortions inside of a volume of $150\text{ mm} \times 150\text{ mm} \times 150\text{ mm}$ around the center of the imaging bore are relatively small compared to other resolution limiting factors, such as the image slice thickness. This was not the case when the phantom was shifted towards the MR scanner FOV edges, however. The increase in geometric distortions with increasing radial distance from the scanner bore are visible on MR images shown in Figure 3.5 and Figure 3.6 for different sequences and phantom positions. Figure 3.8 and Figure 3.9 show that the magnitudes of radial distortions for the same MR sequences can be relatively large considering other sources of uncertainty in high-precision radiotherapy planning and delivery, with maximum radial distortions nearly 4 mm at the shifted phantom positions. Although not explicitly measured, this value coincides with Walker *et al.*’s [138] predicted distortions of 4 to 4.5 mm where the breast is normally situated in the MRI bore.

Overall, the mean radial distortion errors were similar for all sequences and for both phase encoding directions (see Table 3.4). The maximum difference in radial distortion errors, obtained from a pairwise comparison of the radial distortion error for each POI with reversed phase encoding directions, varied depending on the sequence used and on phantom positions within the scanner bore. The largest errors observed were for VIBE sequence (A>>P phase encoding direction), with the maximum error being 3.96 mm at the scanner's left. The maximum error for the T1 VIBE sequence on the scanner's right was 3.88 mm, albeit with a P>>A phase encoding direction. If we compare Figure 3.8 and Figure 3.9, differences in the radial distortion errors can be observed with the phantom offset in opposite directions in the bore. While further investigation is needed, these preliminary results may indicate that B_0 inhomogeneities and gradient non-linearity exist along the scanner's FOV edges. The combined effect manifests as warping artifacts and image cut off that can reduce the usable imaging FOV size to be smaller than the scanner's actual FOV. This would entail patients undergoing MRI simulation for breast radiotherapy can only be positioned within a limited volume inside the scanner bore.

Compared with T1 VIBE, which is a gradient echo-based sequence, T2 sequences (TSE and SPACE) are spin echo-based pulse sequences. Spin echo sequences intrinsically correct for signal loss owing to B_0 inhomogeneities by applying an additional 180° refocusing pulse during signal acquisition [70]. Therefore, spin echo pulse sequences can be advantageous for regions of high magnetic susceptibility gradients [198]. On the other hand, T1 VIBE sequences are 3D isotropic and have faster acquisition times (due to the shorter echo times) and are also desirable for MRI simulation. A typical MRI simulation

protocol would contain several spin echo and gradient echo sequences, which must be well understood and characterized for geometric distortion prior to clinical adoption. Based on preliminary findings, we can expect that the radial geometric distortion errors for sequence-dependent distortions at the FOV edges tested will be in the order of 3 to 4 mm. Generally, during MR simulation (particularly for high precision stereotactic techniques) it is possible to avoid areas of high geometric distortion by positioning the patient close to MR scanner's isocentre. However, this can be challenging for lateral radiotherapy targets, such as the breast, particularly in cases where patients may have a large body habitus. This is also challenging for a prone setup where breast immobilization board positions the patient anterior to the scanner's isocentre, and considerations such as avoiding breast contact with the imaging couch are required. In these cases, if MR simulation will be utilized then target delineation errors must be accounted for by considering the maximum geometric distortions characterized for the MR sequence used at the expected target setup location in the scanner's bore. The errors would subsequently be included in the planning-target-volume margin calculation recipe [199].

An additional component of geometric distortion, which has yet to be addressed, is the optimization of receiver readout bandwidth. In this work, the severity of distortions related to chemical shift artifacts were not investigated. As mentioned before, these types of distortions are patient-dependent, and would ideally be characterized with materials that resemble the distribution of tissue in human or animal subjects [200]. For example, instead of the 3D printed phantom used, these distortions can be isolated by using a tissue-equivalent MRI compatible phantom. For this experiment and materials, chemical shift

artifacts were minimized by increasing the receiver bandwidth in each MR sequence so that any fat/ water chemical shifts were within one pixel. For a clinical setting, the receiver bandwidth can be optimized for each scenario. It is important to note, however, that while receiver bandwidth can be increased to minimize chemical shift distortions, this also comes at the expense of reducing the signal-to-noise (SNR) ratio in MR images [198].

One limitation of this work is that the reported radial distortion errors obtained with the phantom's central axis positioned at the isocentre appear to correspond with the slice thickness dimensions for T1 VIBE and T2 TSE. With the slice thickness settings used (based on clinical MR sequences) it is challenging to observe if the errors are actually less than the slice thickness values. Although smaller slice thicknesses would result in lower SNR, longer scan times for patient and subsequently would likely not be adopted, it is still possible to systematically test how the slice thickness value influences the reported radiation distortion errors. This can be achieved by incrementally repeating this study's experiments with smaller slice thicknesses for each scan until an adequate measurement resolution is achieved.

3.5 Conclusions

In this chapter, the use of a large 3D printed, modular geometric distortion phantom with an accurate analysis technique were demonstrated to quantify distortions relevant for breast MRI radiotherapy treatment simulation and planning. This work was built on the methods validated in Chapter 2, where a small 3D printed geometric distortion phantom

was adopted to quantify similar errors for cranial stereotactic radiosurgery radiotherapy treatment simulation and planning. In this chapter specifically, and by using the large geometric distortion phantom, radial geometric distortion errors for different breast MRI sequences were measured. Sequence-dependent and sequence-independent distortions were studied by isolating the potential influence of reversing phase encoding readout directions. It was observed that when the phantom's centre was placed at the scanner's isocentre, geometric distortions between different the MR sequences evaluated were comparable to each other. On the other hand, when the phantom was placed at different sides of the scanner bore, geometric distortions varied depending on the sequence used and phase encoding direction. Preliminary results demonstrate that B_0 inhomogeneities and residual gradient non-linearities may exist at the scanner bore's edges. The magnitude of reported radial geometric distortion errors can be used to inform clinical margin sizes applicable for APBI treatment techniques involving MRI simulation.

With this, we conclude the discussion on geometric distortion in the context of breast MRI radiotherapy simulation and treatment planning. In the upcoming chapters of this thesis (Chapters 4, 5, and 6), the discussion will shift towards the development, characterization, validation, and applications of a novel, deformable breast phantom with several demonstrated medical physics applications in breast radiotherapy.

Chapter 4: Development and Characterization of a Deformable, Realistic Breast Phantom for Surgical, Radiotherapy Planning, and Dosimetric Applications

4.1 Introduction

This chapter describes the development and characterization of a deformable, realistic breast phantom that can be used for several applications, including surgical simulation, radiotherapy treatment planning, and dosimetric measurements. This chapter begins by highlighting the motivation of this work and describes how the phantom was developed and characterized. Details on how the dosimetric properties of the phantom materials were determined are then described in Chapter 5. Finally, Chapter 6 demonstrates how a set of these breast phantoms were used to determine the accuracy of breast tumour bed delineation after oncoplastic breast surgery (OBS).

It is important to define the post-operative tumour bed accurately on breast radiotherapy planning simulation images during adjuvant radiotherapy treatment planning for both, conventional boosts and accelerated partial breast irradiation (APBI). As mentioned in Section 1.2.2, surgical clips are often used as a radiographic surrogate of tumour bed locations for patients who have undergone traditional breast conserving surgery (BCS). Recently, there has been a wider adoption of OBS techniques worldwide (see discussions in Section 1.1.2 and in Chapter 6). There has also been more recognition that the relationship between surgical clips and tumour bed location is not always

clear [201]. Therefore, it is important to establish how OBS differs from BCS, and how surgical clip placement during OBS may influence the radiotherapy planning process. To answer these questions, we developed a novel, realistic breast phantom that allowed us to simulate OBS and understand how it differs from traditional BCS. As will be described in this chapter, this breast phantom was developed with the intent to facilitate OBS simulation by surgeons, and to allow the radiotherapy team to gain insight on the surgical details relevant to the adjuvant breast radiotherapy planning process.

There are several types of commercial breast phantoms available for different purposes. For example, the Mastotrainer Breast Surgical Trainer (ProDelphus, Pernambuco, Brazil) is a realistic breast model used for surgical training. However, such commercial products are costly, non-customizable, and details of their mechanical properties are not usually disclosed by manufacturers or in literature. For instance, Zucca-Matthes *et al.* [202] conveyed the use of the Mastotrainer breast phantom for OBS training, but did not provide details on the material's tactile properties or the suturing material that can be used. Aside from commercial phantoms, cadavers are often used for surgical training, but these are not readily available and are costly as well. Kilic *et al.* [203] highlighted the importance of having realistic breast phantoms to facilitate OBS training for surgeons, developed and reported on the use of a breast phantom for this purpose. Although, they did not provide a quantitative comparison of the phantom's physical properties and how it compares with human breast tissue. For the purpose of our work, validating the mechanical properties of a breast phantom is a key aspect, as this information confirms if OBS can be simulated realistically on the phantom, and if traditional suture

materials can be used. Furthermore, optimizing the mechanical properties would allow the formation of an accurate depiction of breast parenchyma deformation under OBS, as well as the associated influence on a tumour bed. It would also enable the development of accurate models of the breast for further studies, including augmented reality applications, thus allowing various steps of OBS to be visualized and studied by the radiotherapy team.

In addition to surgical training applications, other commercial breast phantoms are often used for various radiological imaging applications. Examples include ultrasound (US) phantoms or US guided minimally invasive biopsies, such as the commercial Blue Phantom Ultrasound Phantom (CAE Healthcare, FL, USA), and a custom made phantom reported on by Ustbas *et al.* [204]. Another custom made breast phantom used for minimally invasive procedures is one developed by Ruschin *et al.* [205], who showed that their breast phantom is suitable for use with US, computed tomography (CT), as well as magnetic resonance imaging (MRI). Although it had the same shape as a patient's breast, their phantom did not form a realistic model of the breast since multiple anatomical features (*e.g.*, epidermis layer, parenchyma, and nipple) were not modeled. None of the phantoms described would be suitable for surgical simulation.

It is also possible to create a breast phantom for MRI imaging. In fact, many types of materials have been used to mimic tissue on MRI. The most commonly used phantoms employ the use of water, agarose and agar [206]. Other gels such as those based on polyvinyl alcohol [207], polysaccharides [208,209], gelatin [210], and materials such as Carbomer-980 and Carbopol-974p [211] have also been investigated. While these gels

provide MR relaxation times similar to those of human tissue, they have a limited shelf life and do not have the structural integrity nor stability to allow them to be used as phantoms for OBS training.

In this chapter, we discuss the process of developing a realistic breast phantom that facilitates OBS simulation, multi-modality imaging, and dosimetric applications. This chapter begins by discussing how the ideal material composition of this phantom was chosen, and continues to describe how the phantom's surgical, mechanical, and radiological properties were validated and measured. The phantom's surgical, mechanical, and radiological characteristics are then reported. The dosimetric properties of the phantom material will be covered in detail later in Chapter 5.

4.2 Materials and Methods

In this section, the breast phantom construction process is described by reviewing material selection criteria and design of the final breast phantom prototype. After which, the validation methods for each of the phantom's surgical, mechanical, and radiological properties are discussed.

4.2.1 Breast phantom fabrication

The process of constructing a realistic, deformable breast phantom relied on choosing materials that would facilitate the objectives stated above, which included

utilizing the phantom as a tool for surgical simulation, multi-modality imaging, and for dosimetry measurements to facilitate end-to-end testing. After the material was chosen and validated, a simple technique for molding and finishing breast phantoms was developed. Both processes are described in the subsections below.

Determining the Ideal Material Composition

In our search for suitable materials, moldable silicone composites were found to be a promising candidate. These materials are generally non-toxic, easy to use, cost-effective, customizable, biocompatible, chemically stable, thermally stable, and durable. Due to their favourable properties, silicone composites have found widespread applications in medicine, with silicone breast implants being the most widely recognized use [212,213].

In this work, we demonstrated the use of a specific commercial product line of moldable silicones called Ecoflex™ (Smooth-On Inc., PA, USA). We focused our tests on four different products Ecoflex™ 00-10 (E10), Ecoflex 00-20™ (E20), Ecoflex 00-30™ (E30), and Ecoflex 00-50™ (E50). Due to their manufacturer reported mechanical properties (see Table 4.1) these materials are commonly used for making prosthetics in orthotics and in special effects applications to mimic human tissue. These specific materials are also moldable, and non-toxic, which make them practical for radiotherapy applications.

Table 4.1 The manufacturer reported [214] mechanical properties of Ecoflex™ silicone products (Smooth-On Inc., PA, USA) used for initial testing while constructing a realistic breast phantom.

	<i>Ecoflex™</i> 00-10 (E10)	<i>Ecoflex™</i> 00-20 (E20)	<i>Ecoflex™</i> 00-30 (E30)	<i>Ecoflex™</i> 00-50 (E50)
mass density (g/cm ³)	1.04	1.07	1.07	1.07
tensile strength (psi)	120	160	200	315
100% modulus (psi)	8	8	10	12
useful temperature (°C)	-54 to 232	-54 to 232	-54 to 232	-54 to 232

In order to fully simulate breast surgeries on a phantom, it is important for the breast phantom to possess a minimum number of anatomical features; namely, an epidermis layer (skin), breast parenchyma, and a chest wall. Each component has different tactile and mechanical properties, and so were created individually to account for these differences.

Ecoflex™ silicone can be molded to visibly resemble skin or other organs, however, due to its relatively higher rigidity, silicone alone do not always feel like human tissue. To make the breast parenchyma more “flesh-like”, two additive materials were tested in the silicone mixture, a silicone tactile mutator (Slacker®, Smooth-On Inc., PA, USA), and 350 centistoke (cSt) agricultural grade silicone oil (Ruichem USA, Ruijiang Group, Zhejiang, China). To make the epidermis layer less susceptible to ripping during surgical suturing, a 90% polyester and 10% Spandex “power mesh net” fabric (purchased from FabricAndSewing, Amazon.ca) was added to reinforce the epidermis layer. Using a small round plastic container as a mold, various breast phantom prototypes were first created by testing combinations of different mixtures and materials. Table 4.2 lists the different

material mixtures and additives tested for each component of these breast phantom prototypes (epidermis layer, breast parenchyma, and chest wall), as well as their amounts as a percentage ratio of the total volumes. The prototypes were qualitatively examined by a surgeon to assess how realistic they felt during surgical simulation and were then validated by quantifying their elasticities as explained in Section 4.2.3.

The final breast phantom material (prototype number 8 in Table 4.2) was chosen to mimic breast tissue in terms of palpation and accommodation of surgical maneuvers (*e.g.*, incision, skin undermining, tumour resection, suturing *etc.*). The breast phantom was also required to be chemically and physically stable over prolonged periods of time, simple to produce and cost efficient. The following section describes the material composition and molding process related to the phantom prototype that eventually fulfilled all requirements.

Table 4.2 Different types of Ecoflex® silicone materials tested for fabricating various breast phantom prototypes and their components (the epidermis, parenchyma, and the chest wall). Additive materials were also used to reinforce the epidermis (using mesh fabric), or to increase the elasticity and softness of the breast parenchyma (such as the Slacker® silicone mutator or silicone oil). The final breast phantom prototype is based on prototype number 8.

<i>prototype number</i>	<i>silicone type (epidermis, parenchyma, chest wall)</i>	<i>additives (material (%vol))</i>
1	E30, E50, N/A	mesh fabric (N/A)
2	E10, E10, E30	mesh fabric (N/A)
3	E20, E10, N/A	mesh fabric (N/A)
4	E10, E10, E10	Slacker® (33%)
5	E10, E10, E10	Slacker® (66%)
6	E10, E10, E10	mesh fabric (N/A)
7	E10, E10, N/A	silicone oil (30%)
8	E10, E10, E10	mesh fabric (N/A), silicone oil (30%)
9	E10, E10, E10	silicone oil (50%)

Final Breast Phantom Prototype Molding Process

The final breast phantom prototype was fabricated using an inverse mold. First, the mold was formed using a 1 cm thick thermoplastic sheet (Orfitrans Stiff®, Orfit Industries, Antwerp, Belgium), which was heated in an oven at 200°C for approximately two minutes, fit over a breast attachment of The Anthropomorphic Alderson Female Radiation Therapy

Phantom (Radiology Support Devices Inc., Alderson Phantoms, CA, USA), and then allowed to cool for approximately five minutes at room temperature (see Figure 4.1). The mold was then adjusted to become more tear-shaped by using a heating gun (Master-Mite®, 10008, Master Appliances Corp., WI, USA) and by gently pushing the inside of the mold outwards using a 10 cm diameter metal ball. The mold shape was adjusted in an iterative process based on surgeons' feedback to provide a more ptotic breast shape. The final mold was made to accommodate a full breast phantom volume of 900 cm³.

A 2.0 cm diameter glass sphere was used as a palpable "tumour". The marble was suspended inside the breast mold while the silicone comprising the breast parenchyma cured. A marble was chosen so that it would be rigid enough to be palpable during pre-operative planning.

To make the breast parenchyma, 600 g in total of E10 silicone was mixed with silicone oil. The ratio of E10 silicone-to-silicone oil was optimized based on surgeons' feedback on the phantom's tactility compared to real breast tissue. The mixture was poured into the mold and left to cure for three hours. To make the chest wall layer, a total of 140 g of E10 silicone (without silicone oil) tinted with Silc Pig™ maroon pigment (PMS 7421C, Smooth-On Inc., PA, USA) was then poured on top of the parenchyma layer and left to cure for an additional two hours. Following which, the phantom parenchyma with chest wall was removed from the mold and wrapped with the mesh fabric to act as the base of the epidermis layer. To complete the epidermis layer, 80 g of the E10 silicone (without silicone oil) was tinted with Silc Pig™ pink flesh pigment (PMS 488C, Smooth-On Inc.,

PA, USA) and applied on top of the mesh fabric using a paint brush. The thickness of the epidermis was adjusted by applying a few layers, allowing the silicone to cure for one hour, and reapplying more layers as needed with a similar wait time between each layer. Three iterations were found to form a realistic epidermis layer of 0.5 to 0.7 mm [215], which was suitable for our applications. A breast phantom nipple with areola was made using the epidermis mixture and a silicone baby bottle nipple (Avent™ Natural Baby Bottle, Philips, Amsterdam, Netherlands) as the mold. The nipple with areola was placed on the uncured epidermis material prior to curing the epidermis layer for an additional two hours. Using caulk as an adhesive material (Silicone II Sealant, General Electric, Massachusetts, USA), the phantom was then adhered onto an acrylic plate to facilitate handling and to allow positioning on an inclined angle during surgical simulation.

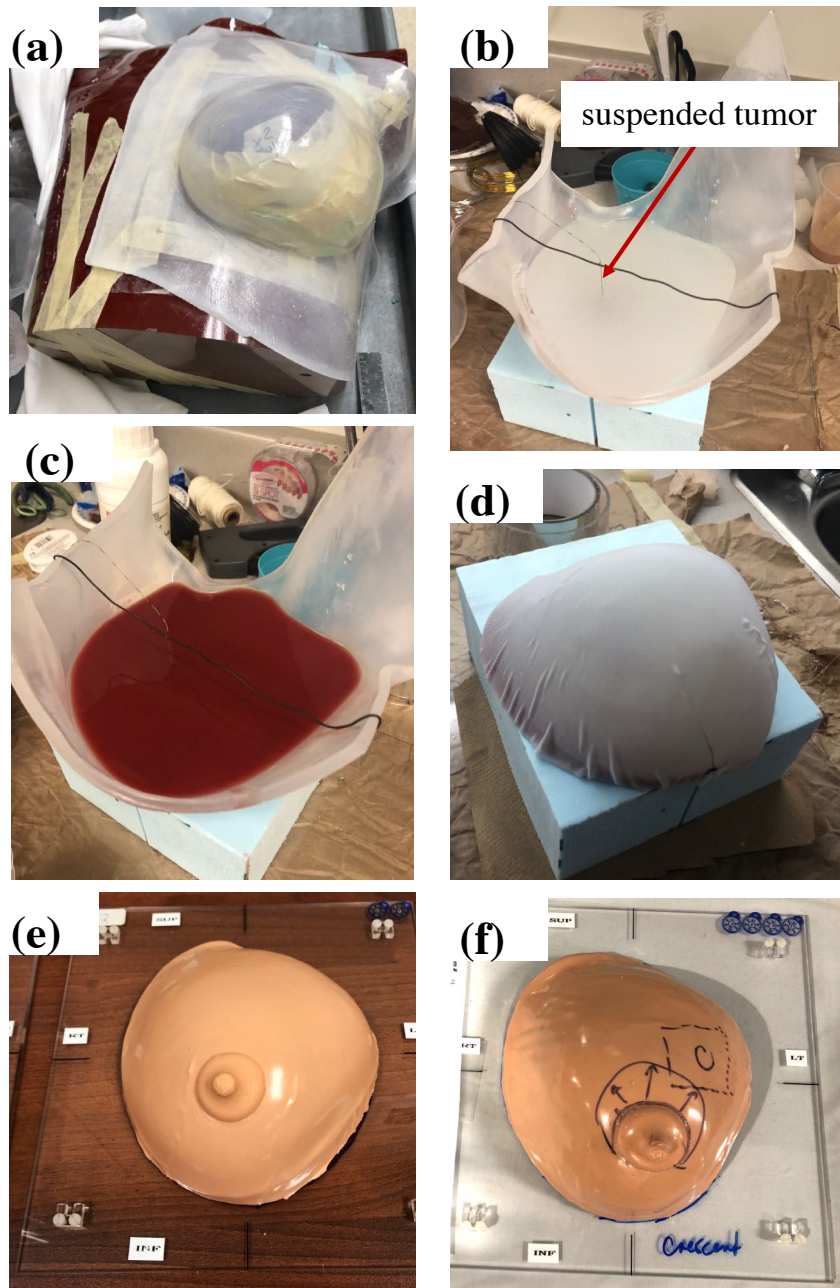


Figure 4.1 A step-by-step illustration of the breast phantom fabrication process. (a) The breast inverse mold being shaped from the breast attachment of an anthropomorphic body phantom, (b) The mold and phantom parenchyma with the marble tumour suspended in the desired position by a string. (c) The setup for adding the chest wall layer. (d) The phantom after adding the mesh fabric. (e) The final phantom after adding the epidermis, areola, and nipple components. (f) A phantom marked for pre-op incision planning using an oncoplastic breast surgery crescent incision approach.

4.2.2 Validation through surgical simulation

Seven replicas of the phantom were made to test the phantom's suitability for simulation of various OBS techniques (namely; racquet, round block, crescent and pedicle mammoplasty [12]). Each phantom contained one or two tumours placed at variable depths ranging from 0.5 cm to 7.0 cm. Tumours were also placed within different quadrants of the breast (upper outer, upper inner, lower outer, lower inner and subareolar), with four phantoms containing a tumour in the upper outer quadrant to reflect where the highest proportion of breast tumours have been reported to arise [216].

The phantom was tested by two experienced breast surgeons. Prior to surgical simulation, the tumour was located through palpation and CT scout images by the surgeons. After the surgeons agreed on the appropriate surgical approach for each case, a felt marker was used to draw the planned incision pattern on each breast phantom (see Figure 4.1(f)). Incisions and skin undermining were performed. The tumour(s) was (were) resected with 1 cm margins. To mark the tumour cavity, 8 titanium surgical clips (Medium size, Weck Horizon, Teleflex Medical, Ireland) were placed, four along each cavity wall at the position of the tumour, and four at the level of the chest wall, and closure followed. Various materials were tested for suturing and closing the phantom parenchyma and epidermis: surgical skin staples, 3/0 and 4/0 thick vicryl, prolene and nylon surgical sutures, polyester sewing thread, and 0.3 mm thick cotton knitting yarn.

4.2.3 Characterization of mechanical properties

As mentioned previously, one of the main considerations considered while designing this phantom was its tactility and endurance to surgical maneuvers, including incisions and suturing. These properties were optimized by feedback from surgeons based on their experience during the developmental stage (see breast phantom fabrication process in Section 4.2.1). To provide a more quantitative assessment, the final prototype's mechanical properties were also measured by determining the value of the shear strength and elasticity of the breast phantom's parenchyma and epidermis layer, as described below.

Measurement of sheer strength

The ultimate tensile strength (UTS) and strain on rupture for the phantom parenchyma and epidermis layer were measured using a BioTester Biaxial Test System (CellScale Biomaterials Testing, Ontario, Canada). Using the same setup, the UTS is defined as the force required to rupture the sample divided by the cross-sectional area of the sample. The strain on rupture was also simultaneously determined, where the strain on

rupture = $\frac{\Delta x}{x}$; Δx being the displacement along the x direction and x is the average width.

Phantom material measurements were experimentally compared to pig fat and pig epidermis. The animal was euthanized four hours prior, and the samples were transported in an insulated cooler. The samples were prepared and kept hydrated in saline water until they were measured. Measurements were conducted within three hours of obtaining the sample. Samples were cut to a size of 5.0 mm × 5.0 mm × 3.0 mm using a custom made

cutter. Sample measurements (thickness, width and length) were performed three times with a caliper (within 0.01% measurement accuracy), and the average was taken to calculate the cross-sectional area. Uniaxial testing was performed at room temperature ($T \approx 23$ °C), with the force applied along the x (width) direction until the sample ruptured. The UTS and strain on rupture were determined from the recorded stress (N/m²) vs. strain (%) curves. Figure 4.2 shows the experimental setup, as well as sequential images of the phantom parenchyma undergoing testing. UTS values were compared to published data for human tissue, where available.

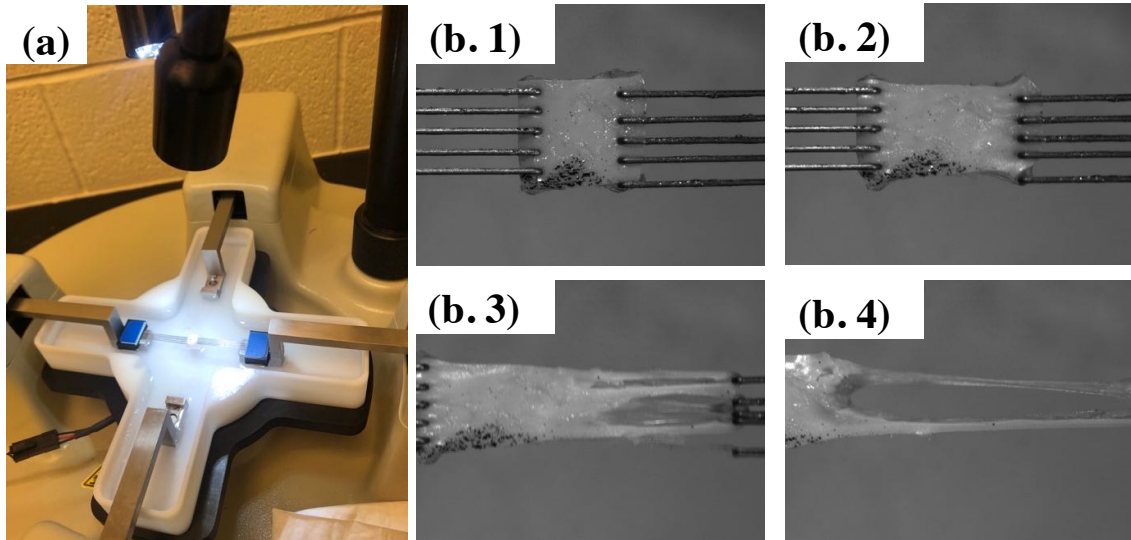


Figure 4.2 The setup for ultimate tensile strength measurements. (a) A photo of the BioTester's measurement plane with the sample suspended in place by the two biaxial claw attachments. (b) Sequential images of the phantom skin being tested at four different time points ($t=0$ s, 0.8, 2.4 and 4.8 s, corresponding to $F= 0$, 561, 1923, and 309 mN, respectively). The sample's cross-sectional area along the testing plane was approximately 5×5 mm².

Measurement of elasticity

The Young's modulus of each of the breast phantom's epidermis layer and parenchyma were measured using two methods: mechanical testing and shear wave elastography.

First, the Young's modulus was measured for breast phantom parenchyma, epidermis layer, and pig fat by calculating the slope of the linear portion of the stress (N/m^2) vs. strain (%) curves obtained from the experiment shown in Figure 4.2.

The Young's modulus for each breast phantom prototype described in Table 4.2 was measured using Shear WaveTM Elastography (Aixplorer®, Supersonic Imagine SA, Cedex, France), with an SL15-4 linear array transducer, 10 MHz central frequency, and 70% gain. More extensive measurements were also performed for the final phantom prototype. First, measurements were conducted at room temperature ($T = 23.5^\circ\text{C}$), after allowing the phantom to equilibrate for 45 minutes. Because Shear Wave Elastography may offer variable results depending on the user's scanning technique [217], interobserver reproducibility tests were also conducted. To examine the effect of temperature on the phantom's elasticity, the phantom was then submerged for 30 minutes in a bucket of ice water to achieve a thermal equilibrium temperature of 13.2°C and then scanned. The phantom was then submerged in heated water (for 30 min) to achieve a thermal equilibrium temperature of 34.2°C . An average of four readings per setup (intra- and interobserver, cold and hot temperatures) were acquired. For all readings, the phantom parenchyma's

Young's modulus was measured using a 3 mm ROI diameter at 1 cm depth in the phantom, at the same location on the ultrasound image. The final breast phantom prototype's Young's modulus at room temperature was compared to published patient data from breast elastography studies.

4.2.4 Characterization of radiological properties

Radiological properties of the phantom were characterized on multiple imaging modalities, as described below. Since a real breast is composed of various anatomical features (*e.g.*, breast parenchyma, nipple, and chest wall), for our application, visualizing and discerning between these features on multiple imaging modalities was necessary. As will be highlighted in Chapter 6, because the eventual goal of this study was to be able to relate OBS practice to radiotherapy target delineation (which relies on surgical clips), it was also important that the implanted surgical clips were clearly distinguishable from the phantom parenchyma.

Computed Tomography (CT)

CT images of the breast phantom were acquired using the Radiation Oncology Department's CT scanner (Brilliance Big Bore, Philips Medical Systems, Cleveland, USA), with an image resolution of 0.4 mm × 0.4 mm × 1.0 mm, 120 kVp, and 450 mAs. The image set was imported into the Monaco Treatment Planning System (TPS), (v. 5.11.02 Elekta, Sweden). The mean and standard deviation of the Hounsfield Units

(HU) was measured for the breast phantom parenchyma using a volume of interest (VOI) diameter of 1.5 cm. The HU measurements were limited to the parenchyma alone, since the other phantom components (epidermis, nipple, areola, and chest wall) were also made of the same type of silicone, and adding silicone oil was found to cause insignificant changes to the HU values (\pm 5 HU).

Magnetic Resonance Imaging (MRI)

MR images of the breast phantom were acquired on a 1.5 T MRI scanner (MAGNETOM Aera, Siemens Healthcare GmbH, Germany), with the scanner's 4-channel small flex coil. T1 weighted (T1w) images were acquired with the following parameters: repetition time (TR)/ echo time (TE)= 10.9 ms/ 7.16 ms, flip angle (FA) of 10°, pixel size of 0.7 mm \times 0.7 mm \times 1.5 mm, and a reconstruction matrix of 320 \times 320 \times 144. T2 weighted images were acquired with the following parameters: TR/ TE= 716 ms/ 93 ms, FA of 150°, pixel size of 0.6 mm \times 0.6 mm \times 0.4 mm, reconstruction matrix of 384 \times 384 \times 52. Standard-of-care breast MRI protocols can apply several sequences, including T1w imaging without fat suppression T2w imaging with fat suppression [197]. Due to the high level of oil in the phantom's contents, both T1w and T2w scans were obtained without fat suppression.

For the phantom material, T₁ and T₂ relaxation times were measured using inversion recovery and spin echo sequences, respectively. Both of these methods were

demonstrated to be reliable methods for quantitative relaxation parameter mapping by Tofts [218].

To measure the T_1 relaxation time, seven scans were obtained using TR/ TE= 2500 ms/ 7.7 ms, FA of 180°, pixel size of 0.6 mm x 0.6 mm x 3.0 mm, and a reconstruction matrix of $128 \times 128 \times 10$. The inversion time (TI) was varied to be 50, 100, 200, 400, 800, 1400, and 2000 ms, for image sets one to seven, respectively. Using ImageJ, and for each image set, the mean signal and standard deviation was measured on the central image slice with an ROI diameter of 1.5 cm. The mean signal was then plotted as a function of TI, and the T_1 relaxation time was obtained using a commercial data fitting software (Origin 2019, OriginLab Corporation, MA, USA) with a Levenberg-Marquardt algorithm [219,220] to fit the data with following equation;

$$S(TI) \propto (1 - 2e^{\frac{-TI}{T_1}} - e^{\frac{-TR}{T_1}}), \quad (4.3)$$

where S is signal from the inversion recovery sequence.

To measure the T_2 relaxation time, five scans were obtained using a TR of 2500 ms, FA of 90°, pixel size of 0.6 mm × 0.6 mm × 3.0 mm, reconstruction matrix of $128 \times 128 \times 10$, and a variable TE (20, 60, 100, 200, and 400 ms, for image sets one to five, respectively). Once again, the mean signal and standard deviation was measured on the central slice with an ROI diameter of 1.5 cm. The mean signal was then plotted as a

function of TE, and the T₂ relaxation time was obtained by using a Levenberg-Marquardt algorithm to fit the data with the following equation:

$$S(\text{TE}) \propto e^{\frac{-\text{TE}}{\text{T}_2}}, \quad (4.4)$$

where S is the signal from the spin echo sequence.

T₁ and T₂ relaxation times were compared with published data for breast tissue, as well as for silicone breast implants.

Ultrasound (US)

US images of the phantom were acquired with a diagnostic US imaging system (EPIQ 7G Ultrasound System, Philips Medical Systems, Cleveland, USA) and a L12-5 50 mm linear array transducer, using B-Mode imaging, 72% gain, 10 MHz scan frequency, a focal length of 3.5 cm, and a lateral image resolution of 0.5 mm × 0.6 mm. Images were qualitatively evaluated by an experienced radiologist to assess for similarity to breast fat, and to evaluate the contrast of surgical clips vs. parenchyma (see below). The speed of sound in phantom material was not measured, since we were primarily interested in visualizing surgical clips and breast phantom parenchyma on US images rather than US wave penetration depth or axial resolution.

Contrast-to-noise and signal-to-noise ratios

Parenchyma and surgical clip visibility were quantitatively assessed by measuring the contrast-to-noise ratio (CNR) of surgical clips vs. parenchyma, and the signal-to-noise ratio (SNR) of the parenchyma and surgical clips. The CNR and SNR values were determined on CT, MRI and US, for both materials of interest, with the exception of MRI; where only phantom SNR was measurable due to the clips' lack of MRI signal.

On each imaging modality (CT, MRI and US), four repeatability scans of one phantom prototype were acquired using the imaging protocols described in the previous sections. These scans were acquired over a period of nine months and were used to determine the intraphantom variability for the CNR and SNR, as well as to monitor the stability of the phantom on radiological images. Additionally, the CNR and SNR interphantom variability were also evaluated on CT and MRI, by comparing the CNR and SNR values obtained from scans of four different phantom prototypes.

For each image set, the CNR and SNR were determined using an open source image analysis software (ImageJ, v. 1523, NIH, USA) [221], based on the following definitions:

$$\text{CNR} = \frac{S_A - S_B}{\text{image noise}}, \quad (4.1)$$

$$\text{SNR} = \frac{S}{\text{image noise}}, \quad (4.2)$$

where S_A and S_B are the mean signal intensities for the surgical clips and the breast parenchyma, respectively. S is the mean signal intensity for the material of interest. Image noise is taken as the standard deviation between the measured mean signal intensity. In the case of CNR, image noise was obtained from the standard deviation of the parenchyma mean reading. Whereas, in the SNR measurements, image noise was obtained from the standard deviation of the material of interest's mean reading (which was either parenchyma or surgical clips). The surgical clip readings were obtained by sampling four different regions showing surgical clips on the image slices. On a single image slice, the parenchyma readings were obtained by sampling four different regions at the 3, 6, 9 and 12 O' Clock positions surrounding a surgical clip. Each region was approximately 1.5 cm from the centre of the surgical clip. The mean of each set of four readings was used to calculate both the CNR and SNR. A region of interest (ROI) of 0.2 cm diameter was used for CT images, and 0.5 cm for MRI images (due to the acquired imaging voxel size). For each image set, mean and standard deviations of signal intensities are computed across all regions of interest considered, reported CNR and SNR values and their standard deviations are computed across all repeatability scans.

4.3 Results

4.3.1 Validation through surgical simulation

According to the surgeons, the breast phantom was found to be a realistic model of the breast for surgical simulation purposes. The phantom's multiple components

accommodated realistic OBS approaches. Surgeons qualitatively confirmed that the phantom's palpated density and stretching characteristics resembled a fibroglandular breast, which is usually attributed to a younger patient who is often eligible for OBS. The phantom was amendable to rotations, re-approximations, and allowed surgical simulation of a wide range of OBS techniques including reduction mammoplasty (levels 1 to 3 [12]). Although the epidermis was easily closed with vicryl, prolene, or nylon sutures, it was not amendable to subcuticular closure because the parenchyma material, which had silicone oil, was not amendable to traditional suture material. However, the phantom parenchyma was easily sutured with cotton yarn, and surgical simulation was possible. Furthermore, since the phantom was limited to the breast, some larger closures (*e.g.* mammoplasty with wise pattern skin incision) caused too much tension for proper skin closure.

4.3.2 Characterization of mechanical properties

Figure 4.3 shows how the elasticity (Young's modulus) changes when different materials and additives are used for each of the breast phantom prototype tested. These results are limited to US elastography measurements.

The effect of sample temperature on the final phantom prototype's parenchyma's Young's modulus is presented in Figure 4.4. The Young's modulus of the phantom epidermis, and pig fat are also presented. In this figure, both results obtained by means of mechanical testing as well as shear wave US elastography are given. As a comparison, the published range of the Young's modulus [222] for normal breast tissue of patients is

highlighted between the dashed lines. All measurements conducted with elastography were found to be within the published range, however, those obtained with mechanical testing were outside this range. This is expected since, although considered more accurate, mechanical testing is a different modality that is not appropriate for testing human organs *in vivo* since it requires *ex vivo* sample preparation. For shear wave US elastography, interobserver repeatability scans were found to lie within one standard deviation of the Young's Modulus at room temperature.

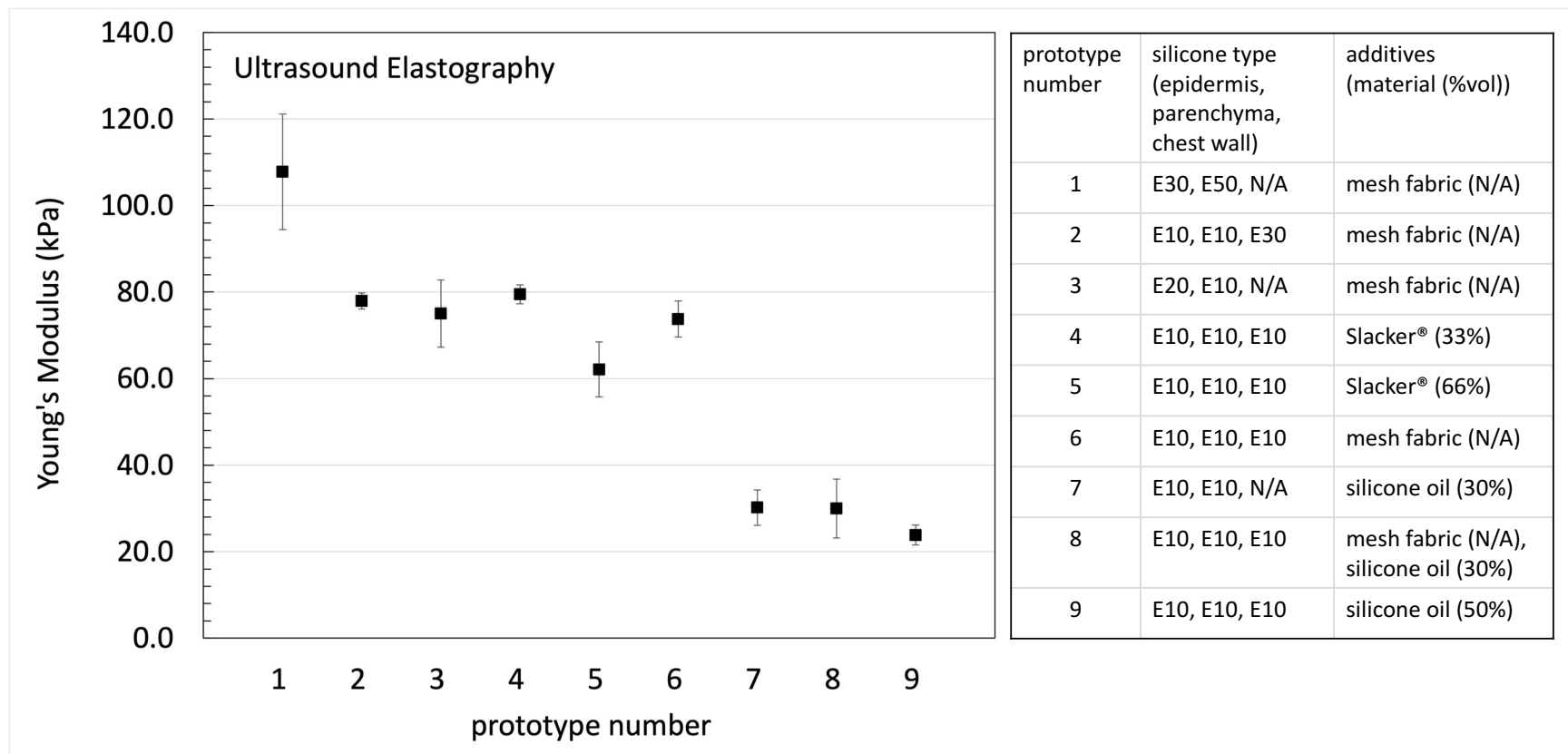


Figure 4.3 Elasticity measurements for the different breast phantom prototypes tested. For reference, the material composition of each breast phantom components from Table 4.2 are repeated in this figure. Measurements were conducted using shear wave US elastography only.

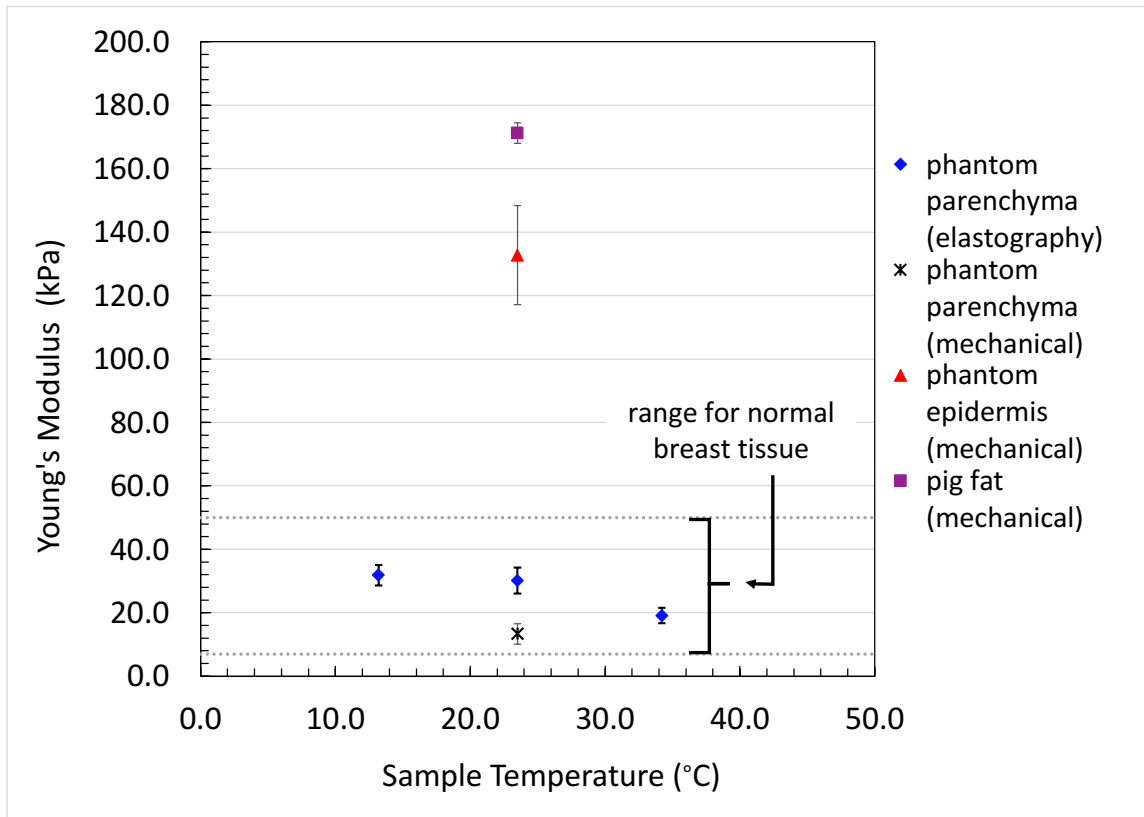


Figure 4.4 Elasticity measurements for the final breast phantom prototype's components (parenchyma and epidermis) and pig fat, at various sample temperatures. Measurements were conducted using shear wave US elastography as well as mechanical testing. The reported range of patient data for breast fat and parenchyma acquired using shear wave US elastography [222] is shown between the dashed lines to contrast with the elastography measurements obtained.

The UTS and strain on rupture for phantom epidermis, phantom parenchyma, pig skin, and pig fat are shown in Table 4.3. The pig skin required more force than the load cell capacity available with the CellScale Biotester (which is 5 N). Consequently, we were not able to obtain the UTS and strain on rupture for that sample. To provide a comparison, the reported values in Table 4.3 are for obtained from published UTS values for human skin.

Table 4.3 The ultimate tensile strength and strain on rupture as measured for the phantom parenchyma and skin, measured pig fat, and human skin (as reported in literature [223]).

<i>material</i>	<i>UTS (MPa)</i>	<i>strain on rupture ($\mu\text{m}/\mu\text{m}$)</i>
phantom parenchyma	0.05 ± 0.01	5.63 ± 1.20
phantom skin	0.23 ± 0.12	1.93 ± 0.69
pig fat	0.09 ± 0.02	0.66 ± 0.20
human skin	2.9 to 150 [223]	--

4.3.3 Characterization of radiological properties

The breast phantom's components (chest wall, parenchyma, epidermis, and areola/ nipple) were visible on all imaging modalities. Figure 4.5 displays image slices from CT, MRI T1w, MRI T2w, and US scans after the tumour was extracted, surgical clips were placed, and OBS was conducted.

For CT images, the measured mean HU is 130 ± 10 .

The measured SNR and CNR for both the phantom parenchyma and surgical clips on CT, MRI (only parenchyma), and US images are listed in Table 4.4.

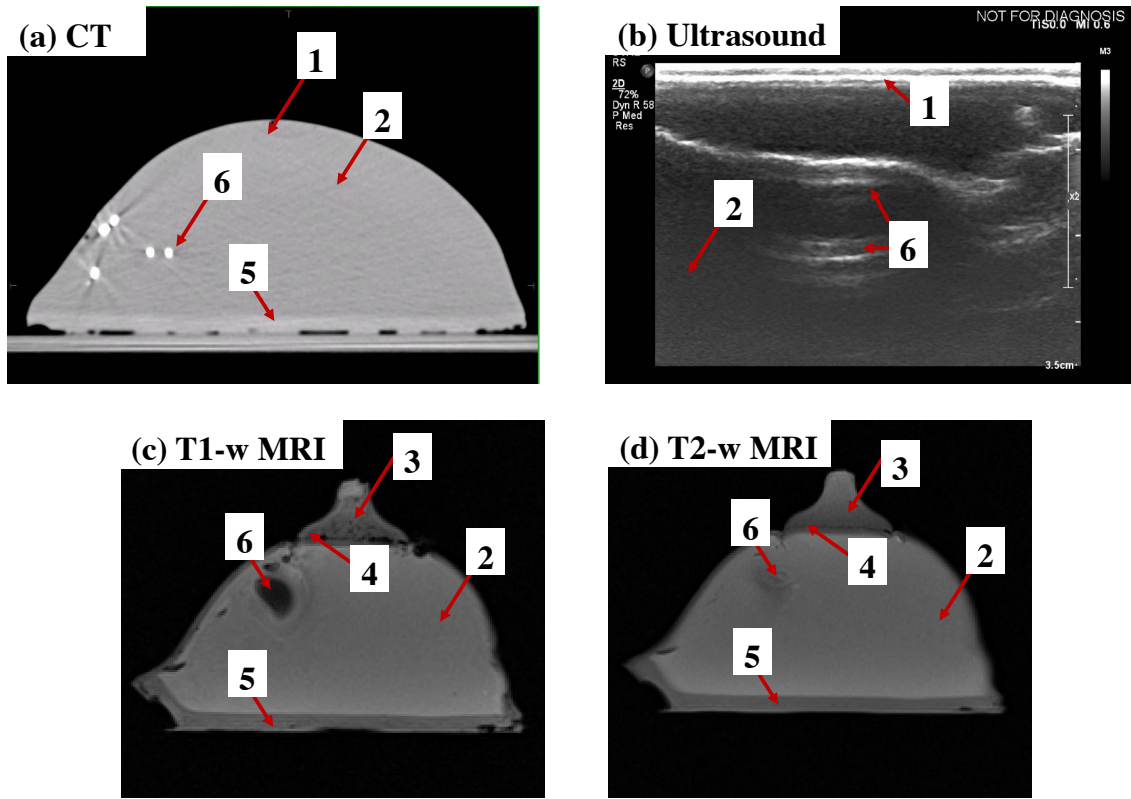


Figure 4.5 The breast phantom as appearing on a) a CT axial view (window= 600, level=400), b) an ultrasound planar view (window=250, level=130), c) MRI T1w (window= 650, level= 300) and d) T2w (window= 800, level= 300) sagittal views. Breast components are identified as 1- epidermis layer, 2- parenchyma, 3-nipple, 4- areola, 5- chest wall, 6- surgical clips. Note that MRI and CT views are not taken along the same axial slice to show different components. Images were acquired after the tumour was resected and surgical clips were placed. Surgical clips appear as a signal loss on MRI.

Table 4.4 Measured SNR and CNR for the phantom parenchyma and surgical clips on various imaging modalities (CT, MRI, and US). Imaging protocols can be found in Section 4.2.4.C.1. CNR is calculated between surgical clips and phantom parenchyma. Note that SNR and CNR involving surgical clips were not calculated on MRI images due to their lack of signal.

<i>imaging modality</i>	<i>SNR</i>		<i>CNR</i>	
	<i>phantom parenchyma</i>	<i>surgical clips</i>		
CT	13		205	193
MRI	T1w	46	--	--
	T2w	44	--	--
Ultrasound	27		49	36

The breast phantom's MRI T₁ and T₂ relaxation curves are shown in Figure 4.6, and the measured T₁ and T₂ relaxation times are listed in Table 4.5. As a comparison, values found in literature for patient data and silicone breast implants are also listed in this table.

Table 4.5 A comparison of the measured T₁ and T₂ relaxation times for the breast phantom parenchyma to those of published values for silicone breast implants and patient breast fat.

	<i>relaxation time (ms)</i>		
	<i>breast phantom parenchyma</i>	<i>silicone breast implant</i>	<i>breast fat (patient data)</i>
		<i>Ref. [224]</i>	<i>Ref. [225]</i>
T ₁	764 ± 11	899 ± 32	372 ± 9
T ₂	140 ± 10	160 ± 5	53 ± 2

4.4 Discussion

One of the objectives for developing this breast phantom was to have a realistic model to mimic breast tissue for surgical simulation. The phantom had to be simple, practical to produce, and cost efficient. This phantom fabrication process relies on first making inverse molds, which can be customized to any shape or size. The inverse molds can be made of different materials. We found that thermoplastic molds are fast, taking less than 15 minutes to set, easy to make, and accessible. A silicone baby bottle was used to mold the nipple/ areola, which offered a stable and practical mold for our purposes. Contrary to our findings, while constructing a spongy silicone surgical breast model for oncoplasty training, Kilic *et. al.* [203] did not find that silicone based molds provided stable molds, and relied on specially machined aluminum molds.

The overall cost per phantom was approximately 60 USD. Minimal materials were needed to make the phantom (the mold, a small scale, paint brushes, and a mixing bowl, and spatula) in a standard laboratory environment without the need of biosafety equipment. Each phantom required approximately 20 hours to complete, with the majority of time spent curing each component for >3-4 hours. Several phantoms can be made simultaneously if multiple molds are made. The phantom is made of non-toxic material and was constructed out of a two-part composite silicone and silicone pigment, which are commonly used for special effects in the film industry as demonstrated by Smooth-On Inc., USA, URL: <https://www.smooth-on.com/applications/special-effects-props/> (accessed on May 18, 2021). Due to its tactile similarities to breast tissue, silicone was found to be a suitable material to test. It is familiar in the medical field in its use as implantable materials [226], and implantable breast prostheses [227]. Using silicone breast prostheses

themselves would not have been appropriate for surgical simulation because they are not a solid material, but rather a sac-like object filled with silicone gel which leaks if the sac is punctured. In comparison, while the breast phantom had a similar “feel” to silicone breast prostheses, the final composition provided a stable (solid) material, with multiple layers to simulate various anatomical features (*i.e.*, chest wall, parenchyma, epidermis, areola, and nipple). This provided a good model for surgeons to practice incision, skin undermining (which facilitates wide excision patterns and allows reshaping), tumour dissection, and suturing.

According to the surgeons, the phantom’s feel and response to gravity resembled that of fibroglandular tissue. Moreover, the phantom material was also amendable to rotations and re-approximation, which is important for surgical maneuvers used in OBS. Without the silicone oil, the phantom parenchyma was too rigid for surgical simulation (Young’s modulus > 50 kPa). A material was needed to soften the silicone. The silicone manufacturer recommends a silicone tactile mutator (Slacker®, Smooth-On Inc., PA, USA), which works with their Ecoflex products to make the silicone rubber more “flesh-like”. Through our experiments, we found that even the maximum recommended amount of the Slacker material in a silicone rubber mixture did not provide the desired elasticity (as shown in Figure 4.3), and that mixing in more of the Slacker material in an attempt to improve the tactility compromised the integrity of the phantom—which became inconsistent, lumpy, and brittle, creating non-viable prototypes for surgical simulation. On the other hand, silicone oil was an effective additive and provided the desired result (see Figure 4.3 and Figure 4.4 for elasticity measurements). The main disadvantage of adding silicone oil to the phantom’s parenchyma was that the cured parenchyma could not withstand the use of traditional suture materials within the parenchyma tissue. Nevertheless, suturing was easily achievable using

cotton yarn, which facilitated full surgical simulation. This can be explained by the measured UTS for phantom parenchyma which was nearly half that compared to measured pig fat; 0.05 ± 0.01 MPa vs. 0.09 ± 0.02 MPa, respectively. The epidermis layer is considered by the surgeons to be more important for OBS closure, and in the case of the phantom's epidermis, it was suitable for suturing with 3/0 suture. This was also confirmed with the measured UTS (for phantom epidermis, UTS= 0.23 ± 0.12 MPa). Human skin's UTS varies largely depending on where the skin sample was obtained from, as well as the subject's natural biological variation [228]. The lowest UTS value reported for human skin is 2.9 MPa [223], meaning that the phantom's epidermis layer was roughly ten times weaker. The phantom's skin layer could be additionally strengthened if more layers of the power mesh fabric were applied during that step, and a thicker coating of material was used to add a dermis layer as well. Initially, we also found that the phantom did not initially allow for large mammoplasty and wise pattern skin incision patterns. This challenge was overcome by adding more tissue surrounding the breast, to capture more of the anatomical features surrounding a breast that allowed the phantom to accommodate submammary fold closures. Another potential drawback is that with the addition of silicone oil, the phantom parenchyma's viscosity increased. This effect was more noticeable when the phantom was warm. While it did not hinder the surgeons from completing their surgical simulation, subjectively they agreed that it was an undesirable effect. This can be mitigated if the phantom were to be stored at a temperature of 20-22°C prior to use.

Radiological characterization showed that the phantom is compatible for CT, MRI, and ultrasound imaging. The breast phantom's anatomical features (chest wall, parenchyma, epidermis, areola, and nipple) were discernable on all imaging modalities. Sufficient CNR and

SNR were reported for parenchyma, and surgical clips (except on MRI, where those clips resulted in signal voids). Preliminary studies show that the phantom can be used as a quality assurance (QA) tool for deformable image registration, and image guided radiotherapy; *e.g.*, as in the case of fiducial tracking for liver stereotactic body radiotherapy, or potentially APBI.

If prepared appropriately, agarose and agar MR gel phantoms can have similar T₁ and T₂ relaxation times as human tissue [211]. Due to the fact that they are made of organic materials, agarose and agar MR phantoms suffer from having a short shelf life. Mazzara *et al.* [208] reported the use of polysaccharide gel to make an MR breast phantom that was found to be stable over a six-month period. However, as in the case of silicone breast prostheses, gel phantoms lack mechanical integrity. This work reports on a breast phantom with measured MR relaxation times closer to those found with silicone breast implants. Subsequently, while it cannot be used as a surrogate for breast tissue in quantitative MR imaging, its potential also lies as a QA phantom for deformable image registration (as in CT vs. MRI), as well as a QA tool for MR based radiotherapy applications (*e.g.*, to assess needle placement for MRI guided brachytherapy).

As mentioned earlier, sufficient SNR and CNR were reported for the surgical clips and phantom parenchyma. This suggests that the phantom can also be used as a QA or training tool to assess needle placement in US guided biopsies (such as in radiological breast biopsy) or brachytherapy (as in the case of prostate brachytherapy). One potential disadvantage of the phantom as a quantitative US phantom is that the expert radiologist regarded the breast parenchyma as hypoechoic compared to breast tissue. Indeed, as reported in literature [229], the phantom's silicone based parenchyma provides low acoustic attenuation compared to breast tissue.

Nevertheless, this can be mitigated by adding scattering material such as Metamucil, as demonstrated by Bude *et.al.* [204]. Additional investigations are being conducted to address this issue.

The phantom's potential use as a biopsy or needle placement medium is supported by its measured UTS (refer to Table 4.3) and Young's modulus, mechanically measured as 13.4 ± 4.2 kPa and with shear wave US elastography as 30.2 ± 4.1 kPa, see Figure 4.4. Which also confirms that the breast phantom's elasticity is similar to that of a fibroglandular tissue [222]. Ruschin *et al.* [205] reported on a breast phantom, which they also described as fibroglandular, given its Young's modulus of 15.8 kPa ± 0.7 kPa (as measured by shear wave US elastography). Their gelatine gel-based phantom for brachytherapy needle insertion, however, the authors highlighted that it must be refrigerated and wrapped in cellophane to prevent drying, has a short shelf life, and is not reusable. As shown in Figure 4.4, our phantom's elasticity was observed to be influenced by large variations in temperature. This is expected since the phantom contains 30% silicone oil.

It has been shown that for breast tissue, different methods of measuring the Young's modulus (*e.g.*, mechanical or shear wave US elastography) may yield variable results [217]. This is due to many factors, including the conditions that the sample was measured under. For example, different preload compressions, testing techniques and inter-observer variability, as well as whether the sample was tested *in vivo* or *ex vivo*. Our results confirm that a variability in Young's modulus measurements can exist depending on the testing technique (Figure 4.4). Based on the underlying physics, the mechanical results are more reliable [217]. Most often, it is difficult to

validate various techniques used to measure the mechanical properties of a single human tissue sample. Thus, the breast phantom can be used a quality assurance tool for testing the reliability and reproducibility of shear wave US elastography measurements.

Given its properties, other potential applications for the phantom are; for low-cost, hands-on training for fellows or residents to simulate highly invasive techniques (such as OBS) or less invasive techniques (such as biopsies); mass production for workshops; or for teaching in low-resource areas without access to cadavers or commercial surgical models. The phantom can also be used to educate patients on breast cancer self-examination or as a model for OBS demonstration. It can be adapted for multidisciplinary pre-operative planning with general surgeons and plastic surgeons and can be used to facilitate communication of post-operative surgical clip placement with radiation oncologists.

4.5 Conclusions

In this chapter, we described a realistic breast phantom which improves on and combines the virtues of several existing phantoms used for various applications. The deformable breast phantom contained several anatomical features; breast parenchyma, chest wall, epidermis, areola, and nipple. The phantom is suitable for surgical simulation, and specifically for simulation of different OBS techniques. It has similar tactile properties as breast tissue. It is also compatible for multi-modality imaging on CT, MRI, and US. The phantom's different anatomical features were visible on all imaging modalities. The phantom can be used by surgeons, radiation oncologists and

medical physicists in radiotherapy (*e.g.*, for surgical simulation/ brachytherapy needle placement, as a QA tool for fiducial tracking, deformable image registration, and multi-image modality validation. It is also non-perishable, reusable, and made from non-toxic materials that can be safely prepared in any radiation oncology workshop or mold room.

We conclude that the phantom's ease of manufacturing, cost effectiveness, customizability, and radiological and mechanical properties make it a useful tool for multidisciplinary applications allied to radiotherapy. In addition to these properties, in order to be useful as a true radiotherapy end-to-end phantom, the phantom's medium must also have suitable dosimetric characteristics. The next chapter (Chapter 5) addresses the dosimetric aspects of moldable silicone in detail, and the potential use of silicone as a material for constructing radiotherapy phantoms and bolus. After which, in Chapter 6, we show how a set of the same realistic breast phantoms introduced in this chapter are adopted to investigate the reliability of surgical clips placed during OBS as radiographic surrogates of breast tumour beds during breast radiotherapy treatment planning, and specifically, for APBI.

Chapter 5: Dosimetric Considerations of Moldable Silicones for Radiotherapy Bolus and Phantom Applications

5.1 Introduction

In the previous chapter, a novel deformable breast phantom was presented and demonstrated for surgical simulation and multi-modality imaging applications. A breast phantom which can be adapted for these applications can potentially be a useful tool for radiotherapy applications. Nevertheless, a phantom that is truly compatible as an end-to-end (E2E) radiotherapy tool (which includes radiation dose measurements, as defined in Section 1.4) must be made of material that is suitable for dosimetric applications. For this reason, the focus of this chapter is to investigate if the breast phantom material (*i.e.*, moldable silicone) fulfills the required criteria for dosimetric applications as well. Moldable silicones have the potential to meet the growing demand for solid materials that are deformable and water-equivalent in radiotherapy, which are particularly useful for constructing patient-customized bolus and deformable phantoms.

In radiotherapy, treatments are often prescribed for anatomical sites with irregular surfaces—such as the nose, ear, or breast. In these circumstances, the use of tissue equivalent material (bolus) compensates for or replaces missing tissue. This provides sufficient dose build up and ensures that the prescribed dose is delivered to the treatment site [30,38,230]. There are several characteristics that bolus materials require. Aside from being tissue equivalent, a bolus must be safe, cost-effective, and conform to an irregular skin surface. The latter is important to minimize air gaps and subsequently reduce undesirable dosimetric effects. To satisfy these requirements,

several materials have been historically used *e.g.*, uncooked rice, dough, and water bags [129]. Practicality and ease of use are important factors in clinical application as well, and so wet cotton gauze, wet towels, or sheets of synthetic gel, such as Superflab (Radiation Products Design, Inc., Albertville, MN, USA), have become more popular over time. Other practical, tissue-equivalent moldable alternatives have also been investigated, such as dental BeesWax (Dentsply, York, PA, USA) [231] or even Play-Doh (Hasbrow, Pawtucket, RI, USA) [232]. Vyas *et al.* [231] presented a comprehensive overview on different types of bolus materials used in radiotherapy applications, and included information on their tissue-equivalence as well as other clinical considerations of commonly used materials such as Superflab, paraffin, uncooked rice, and thermoplastic pellets. They also provide information on early attempts in making bolus from silicone composites.

As mentioned in the previous chapter, moldable silicones are generally non-toxic, easy to use, cost-effective, customizable, biocompatible, chemically stable, thermally stable, and durable (all of which are characteristics of an ideal bolus). From a chemical point of view, these silicones are generally categorized as synthetic polymers, which are made by repeating silicon to oxygen bonds, forming the primary inorganic polymeric chain, which also bonds to organic groups (usually methyl groups). The primary repeating unit of silicone is known as polydimethylsiloxane, or PDMS. Depending on the application and use, silicone is usually transformed into a stable composition by repeating the basic polymeric chain through cross-linking reactions, allowing the formation of chemical bonds between adjacent polymeric chains. The details of these chemical reactions can be found elsewhere [233], but in summary: there are three main mechanisms for curing or “cross-linking reactions”—cross-linking by condensation, cross-linking with radicals, and cross-linking by addition. Cross-linking by condensation requires no mixing and begins when

the prepared silicone product is released from its container and meets moisture in the air. Cross-linking with radicals occurs when vinyl groups are present on the polymer chains and requires additional measures to ensure a stable product. Cross-linking by addition relies on reacting two chemical products, vinyl end blocked polymers and Si-H groups, and is catalyzed by Platinum or Rhodium compounds. The preferred mechanism varies by application. The preferred systems for silicone materials used in medical applications are condensation cross-linking or cross-linking by addition (*i.e.*, Platinum cure) [233]. In addition to the silicone polymer chain, silicones (also referred to as silicone composites, silicone rubbers or silicone polymers) contain “filler” materials, which act to modify properties such as mechanical durability, hardness, and stickiness. To meet various application requirements, commercial silicones are available with different formulations and instructions for curing.

Due to their many favourable properties, silicones have found widespread applications in medicine. These include their use in orthopedics, catheters, heart-bypass machines and valves, dental molds, restorative implants, and aesthetic implants (with silicone breast implants being the most widely recognized use) [212,213]. Recently, the use of silicone-based materials has been reported as advantageous for constructing customized bolus for high-energy photon and electron radiotherapy [234,235]. These materials have a similar mass density to water, which from a dosimetry point of view, is nearly equivalent to human tissue and is often used in dosimetric measurements. Silicone materials can also be manufactured to have similar tactile properties as human tissue. Nevertheless, the dosimetric properties of these materials must be accurately characterized before they can be safely used for radiotherapy applications.

Few experimental studies have investigated dose attenuation properties and tissue interface effects of silicone boluses. Perhaps the first group to report on this were Dubois and Bice *et al.* [236]. They looked at two different forms of silicone, an addition silicone impression material called Reprosil® (Caulk, Dentsply Lakeview & Clark Abe., Milford, DE, USA) which has a mass density of 1.470 g/cm³, and a condensation silicone impression material called Neo-Sil® (Pforzheim, Germany) which has a mass density of 1.079 g/cm³ and evaluated their use in 9 MeV electron beams. Compared with Solid Water™ (a practical commercial product used in lieu of water in medical physics experiments), they found that the dose reduction at a depth of 2.86 cm was 51.7% and 12.3%, for Reprosil and Neo-Sil, respectively, and eliminated their use as potential bolus materials in subsequent investigations using other beam energies. More recently, Canters *et al.* [234] created custom virtual bolus with a treatment planning system (TPS) using treatment planning CTs of 15 patients. In which, a digital shell was created, 3D printed, then used as a mold for forming an actual bolus made of silicone rubber (the exact type is not mentioned). Their proposed workflow for bolus construction was assessed based on comparing the geometric overlap of each constructed bolus to the originally contoured bolus. They also observed small differences in dose distributions of generated plans and measured setups. Chiu *et al.* [235] also proposed a similar workflow for generating a patient-specific bolus for head and neck radiotherapy with 6 and 9 MeV electron beams and 6 MV photon beams. In their method, a shell is first created using 3D printing and then filled with platinum cure silicone. They reported that for the seven patients treated, in-vivo measurements with bolus were within 5% of the prescribed dose.

In addition to the use of silicone composites as bolus, there has been increasing recent interest in employing these materials in anthropomorphic phantoms for radiotherapy applications.

For example, the durability and flexibility of these materials makes them useful for constructing deformable phantoms for adaptive radiotherapy and magnetic resonance guided radiotherapy. Applications include deformable phantoms for various anatomical sites, such as the thorax [237], prostate [238,239], liver [240], and breast [241] (also discussed in Chapters 4 and 6). In these studies, dose measurements were conducted using radiochromic film [238,240], optically simulated luminescent dosimeters [238], ionization chambers [241], or scintillators [240]. As mentioned before, however, a thorough investigation of the dosimetric properties of silicone has yet to be reported.

In this chapter, we investigate the dosimetric properties of two types of moldable silicones used to construct the breast phantom prototype discussed in the previous chapter (Chapter 4). Here, dosimetric properties are characterized in high energy photon and electron beams, and the materials' suitability as water substitutes for constructing bolus materials and radiotherapy phantoms is determined.

This chapter begins with an overview of the materials (type of silicones) and investigation methodology adopted, which included empirically determining various dosimetric properties, experimental measurements, TPS calculations, and finally, Monte Carlo simulations. The results of each data set are discussed and contrasted., Following which, recommendations are provided for using silicones for dosimetric applications in radiotherapy for bolus and phantom construction.

5.2 Materials and Methods

Two types of two-part composite platinum catalyzed moldable silicones were investigated using experimental measurements, TPS calculations, and Monte Carlo simulations. These are the same types of moldable silicones investigated in Chapter 4 (*i.e.*, Ecoflex™ 00-10 (E10) and Ecoflex 00-50™ (E50) (Smooth-On Inc., PA, USA) moldable silicones (MS)), and represent the extreme ends of this product line's range, which are commonly used for making prosthetics in orthotics and in special effects applications to mimic the appearance of human tissue. Since Solid Water is generally regarded as dosimetrically equivalent to water, but is more practical to use than water in medical physics experiments, the dosimetric properties of moldable silicones were compared with Solid Water's. In this study, we specifically sought to answer two questions: The first is, are there relative differences in high energy photon and electron radiation beam absorptions in moldable silicone (MS) compared with Solid Water (SW)? And the second is, how do these relative differences change when an interface of MS and SW is introduced at different depths? These questions are relevant to consider for bolus and deformable phantom construction. For bolus, the dose at the interface between the silicone material and skin (a water-like media) is of concern to clinical dose prescription with different thicknesses of bolus. For deformable phantom construction, it may be desirable to fix a dosimeter rigidly in Solid Water located at different depths within a surrounding deformable media to reduce measurement uncertainty.

For any material of interest, it is possible to use stoichiometric data to determine key theoretical physical quantities that are relevant for evaluating radiation absorption of materials, such as the mass density (ρ), relative electron density (RED), effective atomic number (Z_{eff}), mean

excitation energy, relative mean mass energy-absorption coefficient ratio for a medium ($(\frac{\bar{\mu}}{\rho})_{water}^{med}$),

and the relative mean mass restricted stopping power ratio for a medium ($(\frac{\bar{L}}{\rho})_{water}^{med}$). Because it

was not feasible to obtain the exact formulation of E10 and E50 (due to proprietary information),

the formula for generic silicone [233] was used to determine silicone's quantities (*i.e.*, C₂H₆OSi),

and filler material (which is usually added in small amounts as parts per million) was not

quantified. Table 5.1 lists stoichiometric data for this generic form of silicone, Solid Water, and

water that were used to determine the aforementioned quantities. In this work, Z_{eff} values were

calculated using the classic Mayneord formulae [242]. The mean excitation energy was obtained

from NIST's ESTAR database [243]. The RED, $(\frac{\bar{\mu}}{\rho})_{water}^{med}$ for Co-60 and 6 MV spectra, as well as

$(\frac{\bar{L}}{\rho})_{water}^{MS}$ with a cut-off energy of Δ = 10 keV for Co-60 and 6 MV spectra were determined using

the same method reported by Ho and Paliwal [244] and Cunningham and Schulz [245], and by

using data from the NIST ESTAR [243] and XCOM [246] databases.

Table 5.1 Stoichiometric data and fractional weight of each element found in different media of interest used in this study. Each element is listed with its atomic number (Z), provided in brackets.

Medium	<i>fractional weight</i>						
	H (1)	C (6)	N (7)	O (8)	Si (14)	Cl (17)	Ca (20)
Silicone	0.081	0.324	--	0.216	0.379	--	--
Solid Water (RMI457)	0.081	0.672	0.024	0.198	--	0.001	0.023
Water	0.112	--	--	0.888	--	--	--

5.2.1 Description of phantoms

A custom-built, acrylic cuboid (15 x 15 cm² inner base area, 6 mm wall thickness, 10 cm height) was used as a mold for constructing silicone slabs with variable thicknesses (heights). This allowed measurements to be performed in a simple, reproducible geometry. Six silicone slabs were constructed: Three using E10, and three using E50— each three corresponding to each silicone type having different features. The first slab types were 1.5 cm thick (with a 15 x 15 cm² base area). The second were 5.0 cm thick (with a 15 x 15 cm² base area). The third was also 5.0 cm thick (with a 15 x 15 cm² base area) with an enclosed embedded slot for securely positioning an Advanced Markus® plane-parallel ionization chamber (IC) (S/N: 00815, Model TN34045, PTW Freiburg, Germany) flush against one of the slab's surfaces. The slot was created by placing a plastic IC dummy (which had the same dimensions as this parallel-plate IC) at the central axis on the base of the mold, such that when the silicone cured the dummy would be removed and replaced by the Markus IC. Figure 5.1 shows the custom-built mold, Markus IC dummy, and molded silicone slabs. Both types of silicone were left to cure for a minimum of four hours, as

recommended by the manufacturer. Since silicone is a deformable material (particularly the E10 type), the total uncertainties related to producing and setting up silicone slabs with the stated thicknesses were determined by measuring the dimensions of cured silicone slabs with a caliper (within 0.1% measurement precision).

In addition to the six silicone phantom slabs, four Solid WaterTM slabs (Gammex-RMI, WI, USA) were used in our experimental measurements. One of these slabs was 1.5 cm thick, two were 5.0 cm thick, and the fourth was also 5.0 cm thick with an embedded slot to fit a Markus IC flush against one of its surfaces.

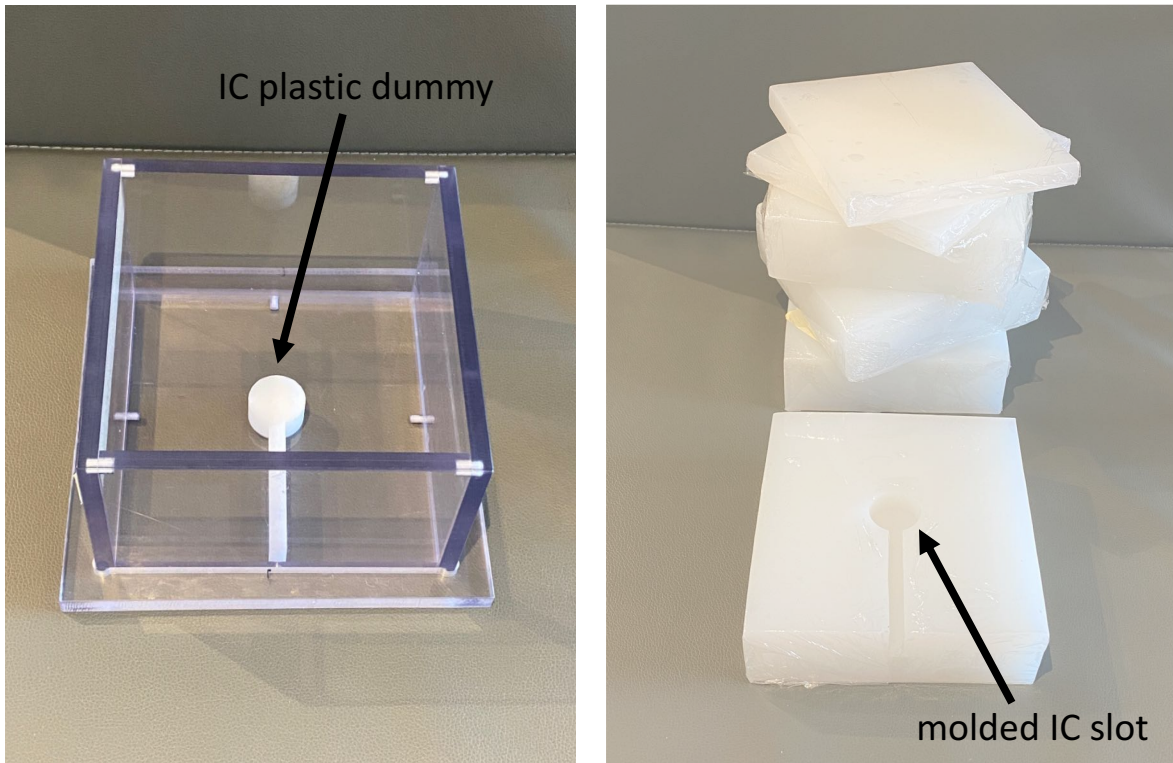


Figure 5.1 The molding process for the silicone slabs included using a custom-built acrylic open faced cuboid container, which had an optional Markus IC dummy insert that can be added at the base to form a slot for IC placement. The molded E10 and E50 silicone slabs are shown on the right-hand image. Slabs were wrapped in a thin cellophane plastic to prevent accumulation of dust.

5.2.2 Experimental setup

As stated above, this study focused on two main aspects of using silicone; when it is used as a full medium for radiation absorption measurements (dose measurements), or when a certain thickness of silicone is placed on top of another type of medium, creating an interface at the point of dose measurement. Figure 5.2(a) provides a pictorial representation of the six slab configurations used experimentally, in CT imaging and TPS calculations, and in Monte Carlo simulations. Details of each process are provided separately below. As described below,

experimental measurements were performed in Co-60 and 6 MV photon beams and 6 MeV and 15 MeV electron beams, using both radiochromic film and a parallel-plate IC.

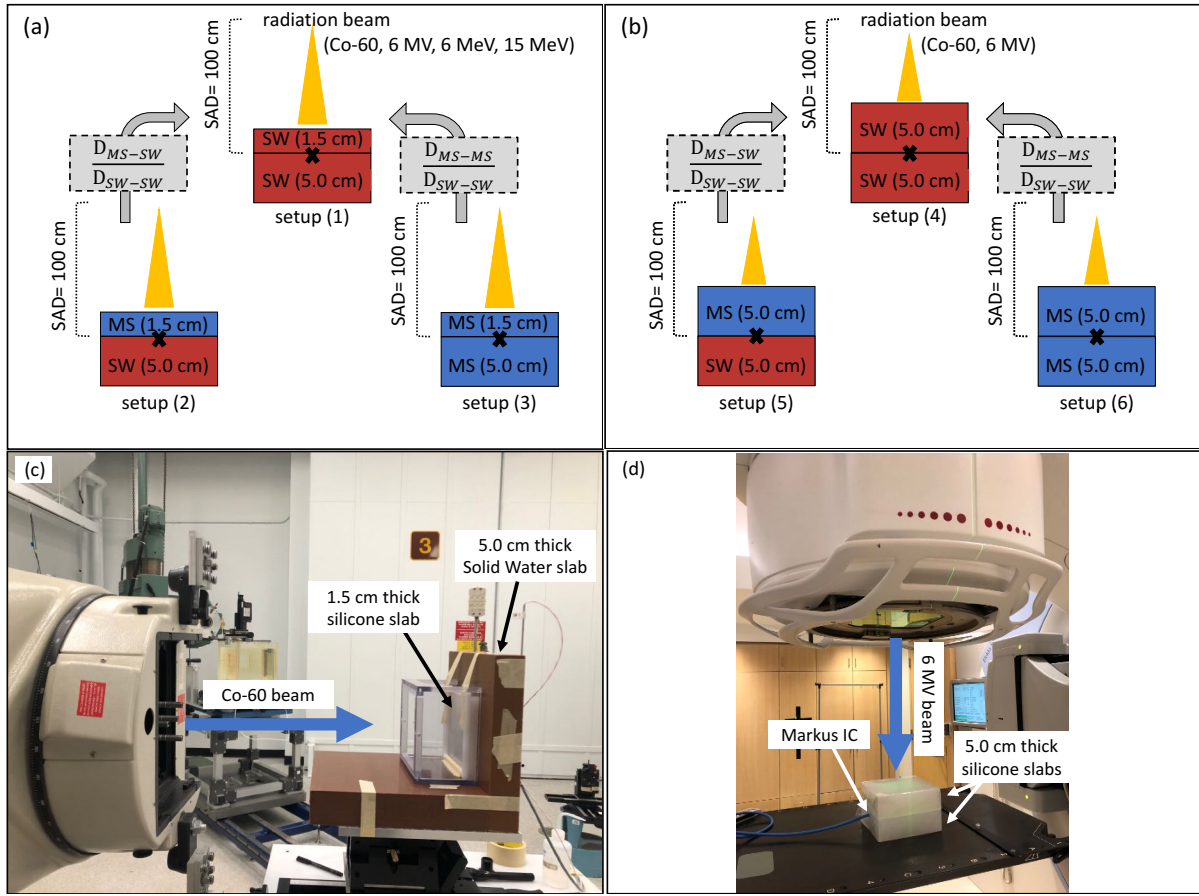


Figure 5.2 Pictoral representations of the experimental setups used for each beam type. Photon beams were measured at depths of 1.5 cm and 5.0 cm: setups (1), (2), (3), (4), (5), and (6) as shown in (a) and (b). Electron beams were measured using 1.5 cm depth slabs: setups (1), (2), and (3) as shown in (a). IC measurements were conducted in the lower MS slabs that were made to fit the IC flush against its surface. The measurement points (at the interfaces) are identified with the “x” marker in the illustrations shown in (a) and (b) and evaluated dose ratios are shown in grey boxes. Measurements are compared to Monaco TPS calculations for 6 MV and to EGSnrc Monte Carlo simulations for Co-60 and 6 MV at the same depths. An example of one of the setups used for measurements in the Co-60 beam is provided in (c), in which the acrylic mold was used as a frame (the base was removed) to maintain the silicone slabs in an upright position for a lateral beam orientation. An example of one of the setups used for measurements in the 6 MV beam, using the Markus IC, is provided in (d). Measurements for 6 MeV and 15 MeV electron beams were conducted with a $10 \times 10 \text{ cm}^2$ electron applicator in a similar setup to that shown in (d).

Radiochromic Film:

Radiochromic film is known to have negligible effects on radiation fluence, and so film measurements were performed to validate IC measurements which were acquired at phantom slab interfaces. EBT3 Gafchromic films (Ashland Inc., Wayne, NJ, USA) were pre-cut and divided into two pieces. For each irradiation, a larger piece was used for film dose measurement, and a smaller piece was used as dedicated control piece to account for darkening due to heat and light exposure and to estimate unirradiated film baseline homogeneity and scan repeatability. Because two separate batches of films were used for Co-60 measurements and for linac measurements, two separate calibrations were performed. For Co-60 measurements, film calibration was performed using the primary standard Co-60 gamma teletherapy irradiator (GammaBeam X200™, Best Theratronics Ltd., Ottawa, Ontario, Canada) at the Ionizing Radiation Standards Laboratory at the National Research Council in Canada. At the time of measurements, it had a nominal dose rate of 48.8 cGy/min at a reference depth of 5 cm in water, for a $10 \times 10 \text{ cm}^2$ field size, 100 cm SSD. For linac measurements, film calibration was performed using a 6 MV photon beam from a clinical linear accelerator (Elekta Synergy, Elekta Instrument AB, Stockholm, Sweden). Film calibration was performed following a procedure similar to what was described by Devic *et al.* [247]. Film orientation was maintained by marking the upper left edge of the film, and by using a custom-made template which exactly fits both the measurement film as well as its control piece. The films were always placed in the same location on the scanner bed for pre-irradiation and post-irradiation scans. Each film was scanned three times and averaged, and three warm-up scans were taken prior to scanning. All films were scanned and irradiated using the same configuration: in transmission mode, 48-bit color, 150 DPI, with an Epson 10000XL scanner (Seiko Epson Corporation, Suwa,

Nagano, Japan), and by using the red channel for Co-60 measurements, and the green channel for linac measurements. Film readout was performed using MATLAB (MathWorks, Inc., Natick, MA, U.S.A, v. R2020b) by using a 0.5 cm diameter region-of-interest sampled to the centre of each film. An average of the mean net optical density in each region of interest was used to calculate the average dose for each setup.

Measurements in photon and electron beams:

For each of the configurations shown in Figure 5.2(a) and (b), dose measurements at the central-axis position were performed using film and the Markus IC (with the protection cap on). IC measurements were conducted using a Keithley electrometer (S/N: 8-8278, Model 35040, Advanced Therapy Dosimeter, Fluke Biomedical, Everett, WA, USA) set on -300 V bias. Photon beam measurements were performed using the Co-60 irradiator described above (setup shown in Figure 5.2 (a) and (b)) as well as 6 MV photon beam from a clinical linear accelerator (Elekta Synergy, Elekta Instrument AB, Stockholm, Sweden, setup shown in Figure 5.2(d)). Measurements were performed at depths of 1.5 cm and 5.0 cm, $10 \times 10 \text{ cm}^2$ field size, 100 cm source-to-axis distance (SAD), as shown in Figure 5.2(c) and using an irradiation time of 2.05 minutes to deliver 100.0 cGy at the measurement point. 6 MV photon beam measurements were also performed (setup shown in Figure 5.2(d)) using a clinical linear accelerator (Elekta Synergy, Elekta Instrument AB, Stockholm, Sweden), at depths of 1.5 cm and depths of 5.0 cm, $10 \times 10 \text{ cm}^2$ field size, 100 cm SAD, and 1000 Monitor Units (MU). Electron beam measurements were performed using 6 MeV and 15 MeV beams with a clinical linear accelerator (Elekta Infinity, Elekta Instrument AB, Stockholm, Sweden), at depths of 1.5 cm, $10 \times 10 \text{ cm}^2$ electron applicator

size, 100 cm SAD, and 1000 MU. Measurements conducted at the NRC employed a fixed Co-60 head to irradiate with a highly precise and reproducible lateral beam setup. Because the silicone slabs could sag when positioned on their short side, the acrylic mold was used as a frame to maintain the silicone slabs in a flat upright position for a lateral beam orientation (as shown in Figure 5.2(c)), keeping the beam direction orthogonal to the slab surface. The base of the mold was removed so it would not interfere with the dose readings. In order to reduce the overall uncertainty on film readings [248], four pieces of film were stacked on top of each other and irradiated simultaneously for 6 MV and 6 MeV linac measurements. Due to the low dose rate of the Co-60 beam, the need of a long irradiation time to achieve a sufficient dose level, and other logistical reasons (such as the lateral irradiation geometry and limited access) this set of measurements permitted only one piece of film to be used per setup during Co-60 irradiations. Similarly, due to limited access during the COVID-19 pandemic Ontario lockdown restrictions, and since no significant differences were expected between dose ratios from 6 MeV and 15 MeV electron beam energies, 15 MeV dose measurements were performed using one piece of film as well. Measurements conducted using the linac were performed using a vertical beam orientation (in Figure 5.2(d)). In order to reduce the overall uncertainty on film readings [248] for these experiments, slabs were used which allowed for four pieces of film stacked on top of each other to irradiated simultaneously.

Three readings were obtained for each beam type, beam energy, and setup configuration, and dose ratios were determined as illustrated in in Figure 5.2(a). The dose/ reading measured with an upper slab of silicone and a lower slab of Solid Water (MS-SW), relative to the dose/ reading measured with an upper slab of Solid Water and a lower slab of Solid Water (SW-SW): *i.e.*,

D_{SW-SW}^{MS-SW} (at 1.5 cm depth for photon and electron beams) and D_{SW-SW}^{MS-SW} (at 5.0 cm depth for photon beams). Similarly, an average of the three readings were used to determine the dose/ reading measured with an upper slab of silicone and a lower slab of silicone (MS-MS), relative to the dose/ reading measured with an upper slab of Solid Water and a lower slab of Solid Water (SW-SW): *i.e.*, D_{SW-SW}^{MS-MS} (at 1.5 cm depth for photon and electron beams) and D_{SW-SW}^{MS-MS} (at 5.0 cm depth for photon beams). Alongside these ratios, the total uncertainties for film and IC measurements were also estimated by considering the film calibration process, the precision of the silicone molding process, dose calibration factors, beam setup, silicone slab thickness during measurements, as well as setup uncertainty and dose/ reading reproducibility, where applicable. These were determined for the different radiation beams separately and listed in an uncertainty budget below.

D_{SW-SW}^{MS-SW} and D_{SW-SW}^{MS-MS} values and associated uncertainties were then compared to values determined from TPS calculations and MC simulations, as described below.

5.2.3 CT imaging and TPS calculations

Using the slab orientation for vertical beam irradiation (Figure 5.2(c)), CT images of the six configurations (shown in Figure 5.2(a) and (b)) were acquired with a radiotherapy CT simulator (Brilliance Big Bore, Philips Medical Systems, Cleveland, USA), and with an image resolution of 0.4 mm × 0.4 mm × 0.4 mm, 120 kVp, 350 mAs. The image sets were imported into the Monaco® TPS (v. 5.11.02, Elekta Instrument AB, Stockholm, Sweden), and the external contours of each slab were contoured.

The Monaco® TPS [249] uses a specified CT-to-Electron Density (ED) table to convert a CT image pixel's Hounsfield Unit (HU) value to an ED value [250]. The HU values for each image pixel in the contoured structure are mapped to RED values using a user specified CT-to-ED file. This file is based on measurement data obtained with a phantom which houses inserts made of tissue mimicking materials with standard compositions [251] such as lung, adipose, water, muscle, cartilage, bone, aluminum, and iron. Once the ED is determined, this value is subsequently used by the dose calculation algorithm to determine material characteristics required for dose calculation: such as, mass density (ρ), photon mass attenuation coefficient ($\frac{\mu}{\rho}$), electronic (collisional) mass collisional stopping power ($\frac{S_{\text{col}}}{\rho}$), electron scattering power, *etc.* Consequently, for accurate dose calculation using the TPS, it is important to use the correct RED value for a particular material.

When plastic or silicone materials are used, the CT-to-ED file may not be appropriate to apply directly since the composition of these materials can differ from tissue's. To ensure that TPS dose calculations were free of systematic errors resulting from a potential material misrepresentation, the correct RED value was applied by overriding the silicone slab contours' voxels during calculations. The RED value automatically reported by the TPS was measured at the centre of each silicone slab and noted for comparison purposes only.

A treatment plan was generated for each of the setup configurations shown in Figure 5.2(a) and (b), and in accordance with measurement conditions. The plan isocentre (100 cm SAD) was set as the interface of the two slabs. For 6 MV photon beams, both 1.5 cm thick and 5.0 cm thick

upper slabs were used (a total of six plans). For 6 MeV and 15 MeV electron beams, only 1.5 cm thick upper slabs were used (a total of three plans).

Two dose calculation algorithms were employed for 6 MV photon beam calculations. Collapsed Cone Convolution (CC) and XVMC [252] Monte Carlo implementation (MC). The dose-to-medium was calculated using 0.1 cm grid spacing, and for MC with 0.1% uncertainty. The central-axis (CAX) dose was measured at 100 cm SAD, using a 0.25 cm area-of-interest radius (or corresponding to 81 points). The beam model used for all calculations was for an Agility MLC linear accelerator (Elekta, Instrument AB, Stockholm, Sweden). For 6 MeV and 15 MeV, the VMC [253] MC implementation dose calculation algorithm was used to calculate dose-to-medium with 0.1 cm grid spacing, and 10^6 histories, with a 0.1 cm area-of-interest radius was used (corresponding to seven points of interest and a standard deviation of 1%). Similar to experiments, for 6 MV, 6 MeV, and 15 MeV, the values reported from TPS calculations are D_{SW-SW}^{MS-SW} and D_{SW-SW}^{MS-MS} for depths of 1.5 cm (for photon and electron plans) and 5.0 cm (for photon plans).

5.2.4 Monte Carlo simulations

In order to validate experimental data and TPS calculations with photon beams, Monte Carlo simulations were carried out using EGSnrc/DOSXYZnrc [254]. Voxelized dose calculation geometry files were created to emulate the experimental setups and phantom material geometries described above. Simulations were performed using HEN_HOUSE input spectra data files c060.spectrum and mohan6.spectrum, for Co-60 and 6 MV beams, respectively. The number of particle histories were set at 7×10^9 to maintain a statistical uncertainty of $\leq 0.3\%$ ($k=1$) over the

scoring depth. The cross-section data was generated using the PEGSLESS option, using the stoichiometric data for silicone and Solid Water, as provided in Table 5.1 and Table 5.2. Photon and electron cut off energies were set as 0.010 MeV, and 0.521 MeV, respectively. The EXACT boundary crossing algorithm, PRESTA-II electron-step algorithm, spin effects were on (to accurately model backscattering effects), Bremsstrahlung angular sampling was set as Simple, and the Bethe-Heitler bremsstrahlung cross sections were used. No other variance reduction techniques were employed. For each energy, and all the configurations shown in Figure 5.2, the dose was scored for a 1.0 x 1.0 cm² region-of-interest area and sampled along the central-axis of the beams in phantom material at 100.0 cm SAD \pm 0.5 cm in 0.1 cm increments. For each energy and depth, the dose was then normalized to the dose obtained at 100 cm SAD for a SW-SW setup (*i.e.*, D_{SW-SW}^{MS-SW} and D_{SW-SW}^{MS-MS}).

5.3 Results

5.3.1 Dosimetric quantities of silicone

Table 5.2 lists the dosimetric quantities determined for generic silicone. Within the energy range investigated, $\left(\frac{\bar{\mu}}{\rho}\right)_{water}^{med}$ is predominantly due to incoherent scattering (Compton interactions).

Table 5.2 Physical quantities related to radiation attenuation and absorption, as reported for generic silicone, and compared to common materials used in radiotherapy dosimetry (namely, Solid Water and Water).

	<i>Material</i>		
	<i>Silicone</i>	<i>Solid Water (RMI457)</i>	<i>Water</i>
ρ (g/cm ³)	1.01	1.03	1.00
Z_{eff}	10.65	7.40	7.42
RED	0.983	1.01	1.00
Mean Excitation Energy (eV)	93.80	70.00	75.00
$\left(\frac{\bar{\mu}}{\rho}\right)_{\text{water}}^{\text{med}}$ for Co-60	0.975	0.944	1.00
$\left(\frac{\bar{\mu}}{\rho}\right)_{\text{water}}^{\text{med}}$ for 6 MV	0.975	0.973	1.00
$\left(\frac{\bar{\mu}}{\rho}\right)_{\text{water}}^{\text{med}}$ for Co-60, with $\Delta = 10$ keV	0.930	1.067	1.00
$\left(\frac{\bar{\mu}}{\rho}\right)_{\text{water}}^{\text{med}}$ for 6 MV, with $\Delta = 10$ keV	0.929	1.080	1.00

5.3.2 Experimental and TPS calculations

Table 5.3 and Table 5.4 list the sources of uncertainties for the Markus IC and EBT3 film measurements, respectively, and for both photon and electron measurement conditions. The combined uncertainty ($k=1$) for measurements conducted in all beam types and energies were 0.92% for IC with all beam types and energies. The combined uncertainties ($k=1$) for film measurements were higher for Co-60 and 15 MeV beams (2.06%) compared with 6 MV and

6 MeV beams (1.11%), also confirming that using four pieces of film and film-specific control piece greatly can greatly reduce the combined uncertainty on dose reading measurements.

Table 5.3 Uncertainty budget of dose value readings of the Markus IC measurements in both photon (Co-60 and 6 MV) and electron (6 MeV and 15 MeV) beams.

<i>Category of uncertainty</i>	<i>Source of uncertainty</i>	<i>Uncertainty (%)</i>	<i>Remark</i>
Measurement Setup	Front-pointer setting	0.03	Measured
	Field size setting	0.02	Measured
	Depth setting (drilling accuracy)	0.17	Measured
	Temperature and pressure variation	0.01	Measured
	Humidity change	0.05	Measured
	Silicone slab thickness variation (sag)	0.26	Measured
	Shutter error (for Co-60 beams)	0.00	Measured shutter error is 3 milliseconds
Ionization chamber-related	$N_{D,W}^{Co-60}$	0.50	Obtained directly at the NRC
	Ionization chamber stability	0.00	Measured
	Leakage current	0.05	Measured
	Solid Water phantom material variability	0.70	Source: AAPM TG-51 Addendum [125]
<i>Combined uncertainty (k=1)</i>		0.92	
<i>Combined uncertainty (k=2)</i>		1.84	

Table 5.4 Uncertainty budget of net optical density readings obtained with EBT3 film for photon and electron beams.

Note that Co-60 photon beams and 15 MeV electron beams were performed using one piece of film only, whereas 6 MV photon beams and 6 MeV electron beams were performed using four pieces of film which resulted in a reduced overall uncertainty.

Category of uncertainty	Source of uncertainty	Uncertainty (%)		Remark
		Co-60 and 15 MeV beams	6 MV and 6 MeV beams	
Measurement Setup	Front-pointer setting	0.03	0.03	Measured
	Field size setting	0.02	0.02	Measured
	Depth setting (drilling accuracy)	0.17	0.17	Measured
	Temperature and pressure variation	0.01	0.00	Measured
	Humidity change	0.05	0.00	Measured
	Silicone slab thickness variation (sag)	0.26	0.26	Measured
	Shutter error (for Co-60 beams)	0.00	0.00	Measured shutter error is 3 milliseconds
	$N_{D,W}^{Co-60}$	0.50	0.00	Obtained directly at the NRC
Ionization chamber-related	Ionization chamber stability	0.00	0.00	Measured
	Leakage current	0.05	0.05	Measured
	Solid Water phantom material variability	0.70	0.70	Source: AAPM TG-51 Addendum [125]
	Scanner uniformity	0.28	0.28	Source: Van Battum et al [248]
	Lateral correction	1.00	0.00	Measured
EBT3 Film-related	Calibration curve fitting	0.50	0.30	Measured
	Intrabach variations	0.28	0.28	Measured
	Background	0.50	0.00	Measured
	Energy dependence	0.50	0.00	Source: Van Battum et al [248]
	Angular dependence	0.50	0.00	Source: Van Battum et al [248]
	Intrinsic film homogeneity	1.10	0.60	Source: Van Battum et al [248]
	<i>Combined uncertainty (k=1)</i>	2.06	1.11	
	<i>Combined uncertainty (k=2)</i>	4.12	2.21	

A comparison of D_{SW-SW}^{MS-SW} and D_{SW-SW}^{MS-MS} values in phantom material at the measurement plane (for 1.5 cm and 5.0 cm depths, 100 cm SAD, 10 x 10 cm² field size) from experimental measurements and MC simulations in the Co-60 photon beam are listed in Table 5.5. In addition to experimental measurements and MC simulation ratios, the ratios obtained from TPS calculations are also listed for the 6 MV photon beam and electron beams (6 MeV and 15 MeV) in Table 5.5, Table 5.6, and Table 5.7, respectively. For electron beams, only ratios at 1.5 cm depths are provided. In Table 5.5, Table 5.6, and Table 5.7, experimental data for the two silicone types (E10 and E50) are provided separately, whereas data from TPS calculations and MC simulations are provided for the generic form of silicone.

Table 5.5 D_{SW-SW}^{MS-SW} and D_{SW-SW}^{MS-MS} values at 100 SAD and variable depths, in a Co-60 photon beam from experimental measurements and MC simulations (DOSXYZnrc). Note that MC simulations were performed for a generic form of silicone, therefore the same simulation output data is provided for both types of silicone (E10 and E50).

		D_{SW-SW}^{MS-SW}		D_{SW-SW}^{MS-MS}	
<i>Depth (cm)</i>	<i>Method</i>	<i>E10 Silicone</i>	<i>E50 Silicone</i>	<i>E10 Silicone</i>	<i>E50 Silicone</i>
1.5	<i>Markus IC</i>	0.943 ± 0.013	0.945 ± 0.013	0.951 ± 0.013	0.945 ± 0.013
	<i>Film</i>	0.950 ± 0.028	0.959 ± 0.028	1.009 ± 0.029	1.025 ± 0.030
	<i>MC (DOSXYZnrc)</i>	0.983 ± 0.004		0.990 ± 0.004	
5.0	<i>Markus IC</i>	0.937 ± 0.013	0.935 ± 0.013	0.925 ± 0.013	0.932 ± 0.013
	<i>Film</i>	0.968 ± 0.028	0.983 ± 0.029	1.037 ± 0.030	1.018 ± 0.030
	<i>MC (DOSXYZnrc)</i>	0.991 ± 0.004		1.001 ± 0.004	

Table 5.6 D_{SW-SW}^{MS-SW} and D_{SW-SW}^{MS-MS} values at 100 cm SAD and two depths, in a 6 MV photon beam from experimental measurements, TPS-CC calculations (using Collapsed Cone Convolution Algorithm), TPS-MC (using Monaco's MC Calculation Algorithm) and MC simulations (DOSXYZnrc). Note that MC simulations and TPS calculations were performed for a generic form of silicone, therefore the same resulting output data is provided for both types of silicone (E10 and E50).

		D_{SW-SW}^{MS-SW}	D_{SW-SW}^{MS-MS}	
<i>Depth (cm)</i>	<i>Method</i>	<i>E10 Silicone</i>	<i>E10 Silicone</i>	<i>E50 Silicone</i>
1.5	<i>Markus IC</i>	0.960 ± 0.012	0.961 ± 0.012	0.957 ± 0.012
	<i>Film</i>	0.970 ± 0.012	0.959 ± 0.012	0.998 ± 0.012
	<i>TPS-CC</i>	1.001 ± 0.011		0.998 ± 0.011
	<i>TPS-MC</i>	1.001 ± 0.008		0.999 ± 0.013
	<i>MC (DOSXYZnrc)</i>	0.979 ± 0.003		1.009 ± 0.003
	<i>Markus IC</i>	0.932 ± 0.012	0.947 ± 0.012	0.944 ± 0.012
5.0	<i>Film</i>	0.948 ± 0.011	0.960 ± 0.012	0.995 ± 0.012
	<i>TPS-CC</i>	0.992 ± 0.018		0.996 ± 0.017
	<i>TPS-MC</i>	0.998 ± 0.018		0.996 ± 0.017
	<i>MC (DOSXYZnrc)</i>	0.978 ± 0.003		1.009 ± 0.003

Table 5.7 D_{SW-SW}^{MS-SW} and D_{SW-SW}^{MS-MS} values at 100 cm SAD and 1.5 cm depth, in a 6 MeV and 15 MeV electron beams from experimental measurements and TPS-MC (using Monaco's MC Calculation Algorithm). Note that TPS calculations were performed for a generic form of silicone, therefore the same calculation data is provided for both types of silicone (E10 and E50).

Energy (MeV)	Method	D_{SW-SW}^{MS-SW}		D_{SW-SW}^{MS-MS}	
		E10 Silicone	E50 Silicone	E10 Silicone	E50 Silicone
6	<i>Markus IC</i>	1.022 \pm 0.013	1.001 \pm 0.013	1.027 \pm 0.013	1.000 \pm 0.013
	<i>Film</i>	1.003 \pm 0.012	0.983 \pm 0.012	1.041 \pm 0.012	1.019 \pm 0.012
	<i>TPS-MC</i>	1.005 \pm 0.005		0.988 \pm 0.005	
15	<i>Markus IC</i>	1.011 \pm 0.013	1.013 \pm 0.013	1.014 \pm 0.013	1.010 \pm 0.013
	<i>Film</i>	1.022 \pm 0.030	1.008 \pm 0.029	1.011 \pm 0.029	1.020 \pm 0.030
	<i>TPS-MC</i>	1.012 \pm 0.006		1.001 \pm 0.006	

5.3.3 Monte Carlo simulations

The relative doses obtained through MC (DOSXYZnrc) for the simulated photon beams are shown in Table 5.3 as follows: (a) Co-60 at 1.5 cm depth; (b) Co-60 at 5 cm depth; (c) 6 MV at 1.5 cm depth; and (d) 6 MV at 5 cm depth. Data plotted is presented along the beam's direction in phantom material. The values at 100 cm SAD are the relative doses (D_{SW-SW}^{MS-SW} and D_{SW-SW}^{MS-MS}) presented in Table 5.6. For all beam energies and depths in phantom material, a visible perturbation is present just beyond 100 cm SAD are shown when an interface of silicone and Solid Water (MS-SW) is present.

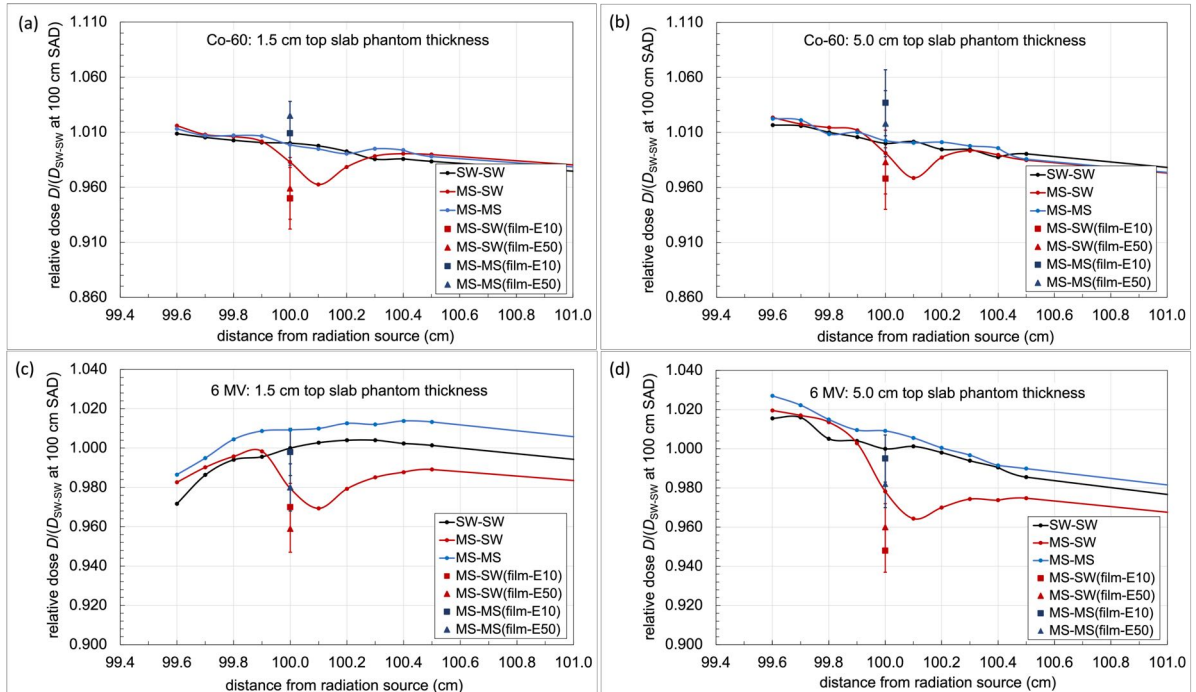


Figure 5.3 MC (DOSXYZnrc) simulation results showing relative dose values around the interface of two phantom slabs when different configurations of material placements were used: top and bottom phantoms slabs are Solid Water (SW-SW), the top slab is molded silicone and the bottom slab is solid water (MS-SW), or the top and bottom slabs are molded silicone (MS-MS). Results are shown using a Co-60 photon beam with a 1.5 cm top phantom slab thickness (a) and a 5.0 cm top phantom slab thickness (b), as well as for a 6 MV photon beam with a top phantom slab thickness of 1.5 cm (c), and a top phantom slab thickness of 5.0 cm (d). In all cases, the dose is presented relative to the dose at 100 cm SAD for the SW-SW setup at each respective depth and beam energy. The field size and SAD for all simulations were $10 \times 10 \text{ cm}^2$, and 100 cm, respectively, and all simulations yielded values with uncertainties below 0.3%. Dose ratios from film measurements made with silicone E10 and E50 types are also shown for comparison.

5.4 Discussion

E10 and E50 silicone composites provide ease of use for accurate construction of molded phantoms. The molding process demonstrated was simple and provided a reproducible setup for conducting IC and film dose measurements at the interface of two slab phantom planes.

Due to their mass density and electron density being similar to water's, E10 and E50 were expected to be suitable for applications in MV photon radiotherapy and dosimetry—where Compton scattering interactions dominate. If we consider measurements conducted with Co-60 and 6 MV photon beams using film (which is more reliable than the Markus IC measurements since film has negligible radiation fluence perturbation effects), the relative dose ratios resulting from MS-MS or MS-SW setups were up to 5% different than with a SW-SW setup see (Table 5.5 and Table 5.6). In these cases, the difference in dose ratios were more prominent when the phantom setup configuration comprised an interface of two media (MS-SW), as opposed to being fully constructed of silicone (MS-MS). Indeed, when silicone was used alone (MS-MS), the dose ratios were up to 4% higher, and 2% lower, in Co-60 and 6 MV photon beams, respectively. That is to say that using a phantom made purely of silicone would have more dosimetric tissue equivalence in the higher energy photon beam at both measurement depths (1.5 cm or 5.0 cm). Furthermore, based on its relative dose attenuation in 6 MV photon beams, E10 (which is more deformable than E50 and is mechanically similar to human tissue [241]) seems to be better suited for phantom and bolus applications.

The difference between measured dose values obtained in E10 and E50 materials may be related to differences in their chemical composition. As mentioned previously, in addition to the repeating silicone polymers in silicone composites, these materials are manufactured to incorporate small amounts of “filler” material. Filler material types range from carbon, to silica, titanium, or barium sulfate. Due to proprietary information, it was not possible to obtain the exact formulation of E10 and E50 from the manufacturer, so the measured dose differences between the two materials could not be identified with certainty because of the presence of differences in filler materials. Only a detailed chemical analysis could offer quantifiable data. It is important to note that different silicone composite product lines or different manufacturers can rely on different types and quantities of filler materials to generate variable degrees of hardness or softness, radiopacity, or viscosities for example. Nevertheless, due to the predominance of the photoelectrical effect at low photon energies, it was expected that the potential presence of more high atomic number elements in E50 (which is inferred from its higher shore-hardness compared to E10) would reflect increased dose attenuation when measurements were conducted in the lower photon energy. Indeed, we found that compared with measurements in Solid Water, using E10 and E50 in 6 MV photon beams caused less dose differences than in Co-60 photon beams. Dose discrepancies would likely be even more noticeable for kV photon energy ranges, particularly due to the presence of a high amount of silicon ($Z= 14$) in silicone composites (see Table 5.1).

For all photon beam measurements, dose ratios obtained with the IC were consistently lower than those obtained with film (see Table 5.5 and Table 5.6). MC

simulations were employed to investigate these differences. Simulations results showed that for a generic form of silicone (with no distinction between E10 and E50) at both depths in Co-60 (see Table 5.5) and 6 MV photon beams (see Table 5.6), D_{SW-SW}^{MS-SW} and D_{SW-SW}^{MS-MS} dose ratio values had the same trend as those obtained with film.

In accordance with film measurements, D_{SW-SW}^{MS-SW} and D_{SW-SW}^{MS-MS} values differed at both depths in 6 MV photon beams MC simulations (see Figure 5.3). This again alludes to the fact that conducting dose measurements entirely within silicone material will yield results within 2% of those conducted in Solid Water, but larger differences can be expected if silicone is placed on top of Solid Water to create an interface of the two materials. While further investigation is needed, this may be due to local changes in electron fluence within the two materials, as discussed below. These results can also be clearly visualized from MC simulation data shown in Figure 5.3, where, at both 1.5 cm and 5.0 cm depths, a reduction in the scored dose is observed at (~2%) and 0.1 cm beyond (~4%) the interface of MS-SW phantom configurations. This finding is relevant to consider in applications where silicone composites may be used to mold a bolus for a patient's radiotherapy treatment [235,255], or when they are used to construct phantoms for radiotherapy applications using multiple materials [237,238,240,256].

TPS calculations were also performed using a generic form of silicone. In this case, a corrected RED value of 0.983 was used instead of the TPS determined value of 1.055 ± 0.003 . Two dose calculation algorithms (TPS-CC and TPS-MC) were applied to establish any potential errors caused by using an algorithm that did not fully account for

lateral scatter (CC) [257]. In the simple geometry used, no observable differences were found when comparing the point dose ratios obtained with the two dose calculation algorithms (refer to Table 5.6) where D_{SW-SW}^{MS-SW} and D_{SW-SW}^{MS-MS} were all below 1.0%. CC algorithms are generally regarded as accurate for simple geometries [258], such as the configurations tested. For accurate TPS dose calculation, and in the case that more complicated calculation geometries and material configuration are to be used, the TPS-MC dose calculation algorithm would offer more reliable results. When an interface of MS-SW was used, results from MC simulations were approximately 2% lower than those from TPS

calculations. This is related to the differences in $(\frac{\mu}{\rho})_{water}^{silicone}$ and $(\frac{L}{\rho})_{water}^{silicone}$ (see Table 5.2),

because the TPS will not accurately model silicone's true dose absorption compared to water. During MV photon dose calculation, the Monaco TPS uses the RED value to determine the associated mass density, which, according to Monaco's TPS Dose Calculation Manual [249], equates to a mass density of 0.983 g/cm³ for silicone's RED of 0.983. Moreover, in the Monaco TPS, the relative mass collisional stopping power for a medium, $(\frac{s_{col}}{\rho})_{water}^{med}$, is calculated as a function of mass density using equations applicable over variable ranges of mass densities, where $(\frac{s_{col}}{\rho})_{water}^{med} = 1.000$ between the range of $0.98 < \rho < 1.02$ [249]. This is not entirely accurate since, as determined [241], $(\frac{s_{col}}{\rho})_{water}^{silicone}$ is 0.948 for 6 MV photon beams. Silicone has a mean excitation energy that is ~25% higher than water's (see data provided in Table 5.2) which in turn lowers the mass stopping power for silicone relative to water. This signifies that the TPS does not account for changes in electron fluence when using a medium that is dissimilar to water, and that for accurate TPS-dose calculation to measurement comparisons, it is necessary to apply a correction to

the TPS-determined dose value. The primary correction to the TPS dose calculation would account for changes in the charge particle fluence which would be reflected by the difference between the TPS applied ($\frac{S_{\text{col}}}{\rho}$)_{water}^{silicone} and its actual value. These corrections alone can be in the order of an increase in calculated dose by 1 to 2%.

Contrary to photon beam measurements, IC and film readings agreed well in electron measurements (refer to Table 5.7). Here, film results showed the overall differences in dose ratios were within -2% to +4%, depending on the silicone type and setup. TPS calculations showed large discrepancies (>7%) for D_{SW-SW}^{MS-MS} with 6 MeV electron beams. Overall, using silicone composites for dose measurements in high energy electron beams can be advantageous if the differences between D_{SW-SW}^{MS-SW} and D_{SW-SW}^{MS-MS} are taken into consideration. It is also worth noting that the reported dose ratios in electron beams are high (as opposed to in MV photon beams, where the reported ratios were generally low), meaning that dose measurements in silicone result in a higher dose value than in Solid Water. This can also be attributed to the fact that the collisional mass stopping power for silicone is lower than that of water, and so the magnitude of electron fluence attenuated by silicone would be less than that in water of equal physical thickness. Once again, this finding is relevant to consider in applications where silicone composites may be used to mold a bolus to increase skin dose for a patient's radiotherapy treatment.

The choice of using the Markus IC was based on practicality and offered a conceptualized benefit for establishing the dose readings at the interface of silicone and Solid Water. It would have been challenging to use a Farmer type IC in this type of phantom

slab geometry due to the molding process and the larger volume of Farmer IC's which would lead to volume averaging effects. Although, it was found that the Markus IC generally yielded lower readings than with film, and, if these measurements were not corroborated by other tools, would have indicated that D_{SW-SW}^{MS-SW} and D_{SW-SW}^{MS-MS} yielded similar results. The IC readings were found to differ from data obtained by film measurements, TPS calculations, and MC simulations. These inconsistencies are related to how parallel plate ICs are constructed. The Advanced Markus IC is manufactured for absolute dosimetry in high-energy electron beams and is made of poly-methyl methacrylate (PMMA) with a 0.03 mm thick polyethylene CH₂ entrance foil (2.76 mg/cm²). Its protection cap is also made of PMMA (0.87 mm thickness and 1.19 g/cm³) and has a small sensitive volume with a radius of 2.5 mm (for a depth of 1.0 mm) [259]. Based on these specifications, it is designed to minimize dose perturbation effects and minimize volume averaging in the depth direction, which was necessary for the measurements conducted in this study. This has been previously validated both experimentally and through MC simulations in Co-60 photon beams, and have shown that the associated correction for attenuation and scatter in the chamber wall (P_{wall}) is close to unity [259,260]. However, an under-response in measured dose was still observed in our experimental results for photon beams, in which no measurable difference in relative dose was found between interfaces made by SW-SW and MS-SW. This is due to the fact that the backplate of the parallel-plate IC is sufficiently thick to be the primary source of backscatter fluence measured by its body [261–263]. As such, for pre-clinical dose verification, radiochromic film offers a more reliable alternative for measuring dose in silicone material, as well as different material interfaces, in setups similar to those applied in our study.

A limitation of this work is that only open field photon and electron beams were used to evaluate beam attenuation in silicone, whereas more modulated radiation beams are often encountered in clinical settings. With intensity modulated beams, the use of multi-leaf collimators can result in low-energy scatter, which, due to silicone's higher Z_{eff} , results in a dramatic increase in photoelectric interactions. For these situations, it may be interesting in the future to also evaluate how dose distributions measured in silicone composite materials differ from those measured in with Solid Water.

5.5 Conclusions

In this chapter, we investigated the dosimetric properties of two types of commercial moldable silicones (Smooth-On Inc.'s EcoflexTM 00-10 and Ecoflex 00-50TM, *i.e.*, E10 and E50, respectively). These materials were tested and/or used to build the breast phantom prototype described in Chapter 4. We conclude that these types of moldable silicones offer practical advantages for constructing customized patient bolus and radiotherapy phantoms for use in high-energy photon and electron beams. We also confirmed that silicone compositions differ from Solid Water's, and that it is important to consider associated differences in beam attenuation properties. Experimental, TPS calculations and MC simulation data showed that compared with the dose measured in Solid Water, differences in measured dose are relatively high when silicone is used in conjunction with Solid Water to form an interface of two materials. Alternatively, using silicone alone can offer a more tissue-equivalent medium for constructing phantoms for use in absorbed dose measurement under high-energy photon and electron beams. Due to

the variability of these effects on the type of silicone used, it is important to characterize the dosimetric properties of silicone for a given radiation type and energy prior to clinical use or phantom applications.

Based on our findings, we found that E10 can be used to construct a deformable breast phantom that allows dose measurements. This will facilitate future work, including the design and implementation of a moving end-to-end breast phantom prototype to investigate implanted marker tracking accuracy and dose delivery accuracy with robotic stereotactic radiosurgery for APBI treatments.

The next chapter presents the use of the deformable, realistic breast phantom prototype (which was introduced in Chapter 5) to investigate the reliability of surgical clips as radiographic surrogates of tumour beds following oncoplastic breast surgery.

Chapter 6: The Reliability of Surgical Clips as Radiographic Surrogates of Tumour Beds Following Oncoplastic Breast Surgery

6.1 Introduction

In Chapter 4, a novel realistic, deformable breast phantom was presented. One of the motivations for developing this phantom was to have a realistic model to simulate and study oncoplastic breast surgery (OBS) in detail and establish if this modern surgical approach presents new considerations related to adjuvant radiotherapy in general, and accelerated partial breast irradiation (APBI) specifically.

For many decades, breast conserving surgery (BCS) has been the main surgical treatment for breast cancer. Section 1.1.2 outlined how like conventional BCS, OBS is also followed by adjuvant radiotherapy to decrease the risk of local reoccurrence. On the other hand, this section also reviewed how OBS differs from conventional BCS, and established that while OBS can provide wide tumour excision and preserve oncological principles, it also offers improved cosmesis. To achieve the desired cosmetic outcome, OBS utilizes complex deformation and relocation of breast parenchyma (refer to Figure 1.2 and Table 1.1), and often manipulates the original tumour bed. The resulting tumour bed is irregularly shaped and sometimes distributed into adjacent parts of the breast parenchyma. In addition, and contrary to BCS (where incisions are usually made anterior to the tumour) in OBS, a tumour may be accessed by making incisions along different anatomical planes. Consequently, a post-OBS tumour bed may not have a spatial correlation with oncoplastic

incisions [264]. Furthermore, during OBS, surgeons focus on eliminating possible seroma formation by filling the tumour cavity defect. For this reason, a seroma may not be present or may not be in the tumour bed region, but rather in a clinically uninvolved region of the breast [265].

Tumour bed delineation is an important step during radiotherapy planning for patients requiring a breast boost, and for those undergoing any type of partial breast irradiation (PBI), including APBI. In the past, when radiotherapy planning was based on 2D simulation, target definition of the tumour bed for breast boost relied on the surgical scar alone [266]. This approach did not always provide insight on the actual surgical bed or anatomical features related to the resected tumour's location. Over time, the use of CT images in radiotherapy planning has demonstrated improved delineation accuracy of the tumour bed for breast boost [267,268]. Nevertheless, clinical studies using various tools and target volume definitions showed overall small benefits of additional breast boost compared to whole-breast radiotherapy (WBRT) [31,269], and so, in this scenario, a high level of delineation accuracy of the tumour bed may not be critical. On the other hand, the accuracy of tumour bed target definition can be more imperative for adjuvant radiotherapy techniques that deliver radiation dose that is focused to the tumour bed, such as in PBI and APBI.

As discussed in Section 1.3.4, hypofractionated PBI techniques (including APBI) have been shown to be an effective alternative to WBRT in early stage breast cancer [109,270–272]. These approaches deliver focused radiation doses to the tumour bed plus a

margin. The tumour bed volume is expanded to include a safety margin for residual disease that is not visible on radiographic data, and another safety margin to account for a patient's setup uncertainty [273]. Overall, the typical margins applied can be in the order of 5 to 20 mm. Although relatively large margins are employed, it has been cautioned not to use some OBS techniques when PBI is indicated because accurate tumour bed delineation following OBS (with or without mammoplasty) could be challenging [274–276].

Traditionally, radiation oncologists use information provided by the surgical incision, postoperative seroma, and surgical clips to define the tumour. As discussed above, however, in the context of OBS, these methods are not necessarily reliable. It has been reported that for OBS techniques (and in particular for those with a mammoplasty), tumour beds delineated based on surgical clips could extend beyond the original breast quadrant in up to 73% of cases [264,265]. Moreover, significant intra- and interobserver variabilities in tumour bed delineation using surgical clips post-OBS have also been reported in literature [277]. Riina *et al.* [278] recently evaluated the use of surgical clips post-OBS in reducing interobserver tumour bed contouring variability. While they demonstrated that using four surgical clips was sufficient to minimize interobserver variabilities, they also disclosed that it was still unclear how the delineated tumour beds compared with the ground truth tumour bed.

Thus, to better understand the spatial relationship between surgical clips and the post-OBS tumour bed, there is a need to directly compare radiation oncologists' contoured tumour beds with the clinically true tumour bed. In theory, these data could be obtained if

the entire tumour bed is intraoperatively demarcated with radiopaque material and/or multiple CTs are acquired during a patient's OBS procedure, but no such clinical studies have been published. The paucity of data on this topic could be justified by ethical considerations and the logistical challenges encountered to obtain this information in clinical settings.

This chapter focuses on addressing this very matter. To overcome the caveats associated with a patient study, the realistic breast phantoms introduced in Chapter 4 were used to evaluate the reliability of surgical clips for accurate tumour bed delineation post-OBS. This chapter begins by discussing the methods employed to conduct this study. The quantitative data obtained are then presented. Following which, the clinical implications of these new findings are discussed.

6.2 Materials and Methods

This section begins with a brief description of the breast phantoms used for simulating OBS. A comprehensive description of the phantom prototype has been provided in Chapter 4, therefore, the description provided here is on how the phantoms were adopted to study surgical clip displacement and tumour bed delineation accuracy.

The following sections describe the OBS techniques investigated, how surgical simulations were conducted on the breast phantoms, and how each case was carried through a simulated "clinical care path"; which included surgery, CT simulation, and

treatment planning delineation by radiation oncologists. The methods for extracting ground truth tumour beds are then provided. Finally, the analysis metrics adopted to compare these ground truth tumour beds with radiation oncologists' tumour beds are described.

6.2.1 Breast phantom preparation

Six realistic breast phantoms were used in this study. These are the same breast phantoms described in Chapter 4, which had several anatomical features relevant for facilitating OBS practice (namely, breast parenchyma, epidermis, areola, nipple, chest wall, and at least one “tumour”). Breast phantom volumes, tumour positions, and tumour sizes were customized to represent realistic and commonly encountered surgical scenarios. This was determined by reviewing post-operative surgical reports of a randomly selected cohort of 30 patients treated with post-OBS adjuvant radiotherapy at our institution. Of this sample, which had a mean age of 59 ± 9.5 years, 63% of patients were found to have tumours located in the upper outer left breast quadrant, with a maximum tumour width of 2.1 ± 1.4 cm. The patients' breast volumes were obtained from their dose-volume-histogram reports and were found to be 887 ± 457 cc.

Once the phantom was made (see Section 4.2 for a step-by-step summary), each phantom was adhered to an acrylic plate having a surface area of $30\text{ cm} \times 30\text{ cm}$, as shown in Figure 6.1. Each plate had CT setup laser alignment lines, and a unique number (from one to six) portrayed using radio-opaque ball bearing (BB) markers. The BBs were used to ensure that each phantom was distinguishable on CT images. Prior to CT imaging, each

phantom's plate was fit with a custom-built reference frame (as shown in Figure 6.1(b)). The frame had three other BB markers, two lateral and one superior, with respect to the CT system's coordinate system, that were used to align the phantom with the CT setup lasers, and to provide an external CT image reference system that can be used for image co-registration.

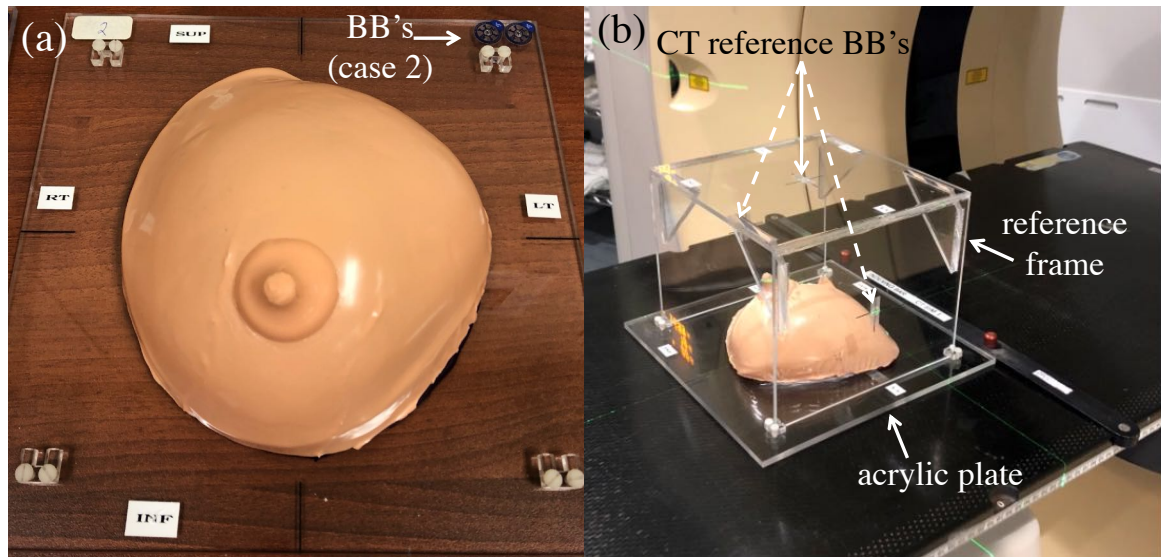


Figure 6.1 An example breast phantom (case 2) adhered to an acrylic plate (shown on the right). The BBs that were used to identify each phantom on the CT image are shown in the upper right corner of the plate (in this example, two were used). Prior to imaging each phantom, a reference frame was attached to the acrylic plate, as shown on the right. The reference frame had three additional BBs (one anterior and two lateral) that were used for setup laser alignment and to co-register multiple CTs of the same phantom.

Table 6.1 Details of each phantom case and the corresponding OBS technique used. The distance from the nipple and depth of the tumours were measured on projection radiographs generated from CT images. The breast, tumour, and specimen volumes (extracted tissue) were derived from CT images. The number of surgical clips and surgical staples used were counted prior to surgical closure and verified on CT images.

Case	OBS Technique	Breast Volume (cc) ^a	No. of Tumours	Volume of Tumour(s) (cc)	O'Clock Position of Tumour(s)	Distance from Nipple (cm)	Depth (cm)	Specimen Volume (cc)	No. of Preliminary Cavity Wall Interfaces	No. of Surgical Clips ^b	No. of Surgical Staples
1	Roundblock	1017	1	10	3	2	6.7	184	4	10	24
2	Inferior pedicle reduction mammoplasty	1043	2	3 & 3	1 & 12	5 & 8.5	0.5 & 1.2	228	9	8	50
3	Racquet	980	1	10	10	4	1.5	57	4	9	26
4	Crescent	1125	1	10	1	4	0.1	149	4	9	25
5	Superior medial pedicle reduction mammoplasty	1018	1	10	11	3	2	106	7	8	43
6	Superior medial pedicle vertical reduction mammoplasty	494	2	10 & 3	10 & 6	4 & 4	0.5 & 1.0	56	5	9	42

^aThe breast volumes listed are the initial intact breast volumes, prior to surgery and tumour excision.

^bThe number of surgical clips provided to radiation oncologists for tumour bed delineation were eight for each case only.

6.2.2 Preoperative planning, surgical simulation, and CT imaging

Two experienced surgeons, who regularly perform OBS, were asked to simulate OBS on the breast phantoms. As part of the pre-operative planning process, a CT image of each phantom was acquired using a CT Simulator (Brilliance Big Bore, Philips Medical Systems, Cleveland, USA), with an image resolution of 0.4 mm × 0.4 mm × 1.0 mm, 120 kVp, and 450 mAs. This pre-operative CT scan will herein be referred to as CT1. Two planar views (anterior-posterior and lateral) were generated from CT1. Based on these views, the depth of the tumour(s) and the location(s) with respect to the nipple (i.e., the o'clock position) were recorded (see Table 6.1).

For each case, and depending on the tumour position, breast volume, and palpated tumour, the surgeons decided on a suitable OBS technique, also listed see Table 6.1. Once a consensus was reached between the surgeons, each phantom was then marked with the incision pattern (as shown in Figure 6.2).

Tumours were resected with 1 cm isotropic margins using standard surgical tools and techniques. For each case, a minimum of eight titanium surgical clips (Medium Size, Weck Horizon, Teleflex Medical, Ireland) were then placed by the surgeons in each cavity wall, with four at the level of the tumour and four at the level of the chest wall. Unlike for a real patient, up to 50 additional radiopaque markers (Surgical Sterile Disposable Stapler with Disposable Staples, Instruments GB®) were also used to precisely mark true extensions of each tumour bed (along anterior-posterior, right-left, and superior-inferior

directions). A second CT (CT2) was then acquired for each phantom prior to surgical closure. Table 6.1 provides more details for each case.

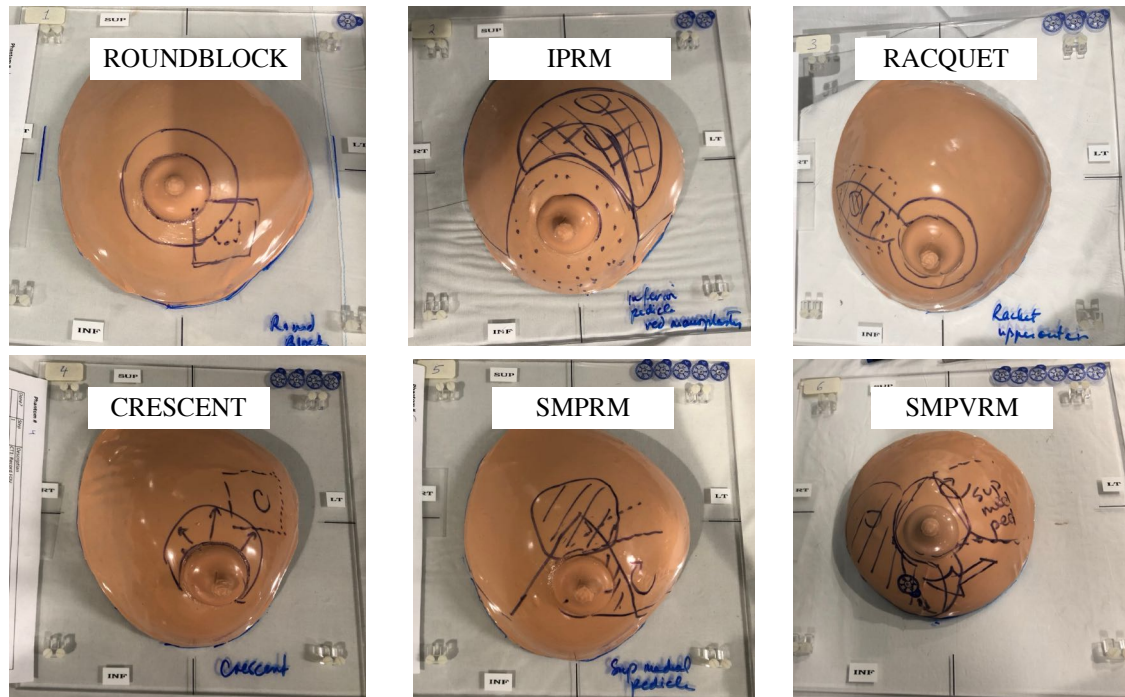


Figure 6.2 The six breast phantoms used to simulate oncoplastic breast surgery with intended surgical incision lines indicated by the pen markings. This planning process is similar to what occurs during preparation of patients for a surgery, however, this type of photo/ diagram is usually not provided in a patient's post-operative note following oncoplastic breast surgery. Abbreviations: IPRM= inferior pedicle reduction mammoplasty, SMRM= superior medial reduction mammoplasty, and SMPVRM= superior medial pedicle vertical reduction mammoplasty.

Following tumour resection and CT2 imaging, surgeons continued each OBS technique (covering levels I-III as described in Table 1.1); by performing tissue undermining, volume displacement and replacement, tissue redistribution and rotation into the lumpectomy cavity, deep tissue suturing, and subcuticular and/or simple interrupted

suturing. After surgical closure, a CT wire was placed on the epidermal incision/suture lines, and a final CT (CT3) was acquired. An example of one of the phantoms undergoing the all the steps involved, including the final step as described below, is shown in Figure 6.3.

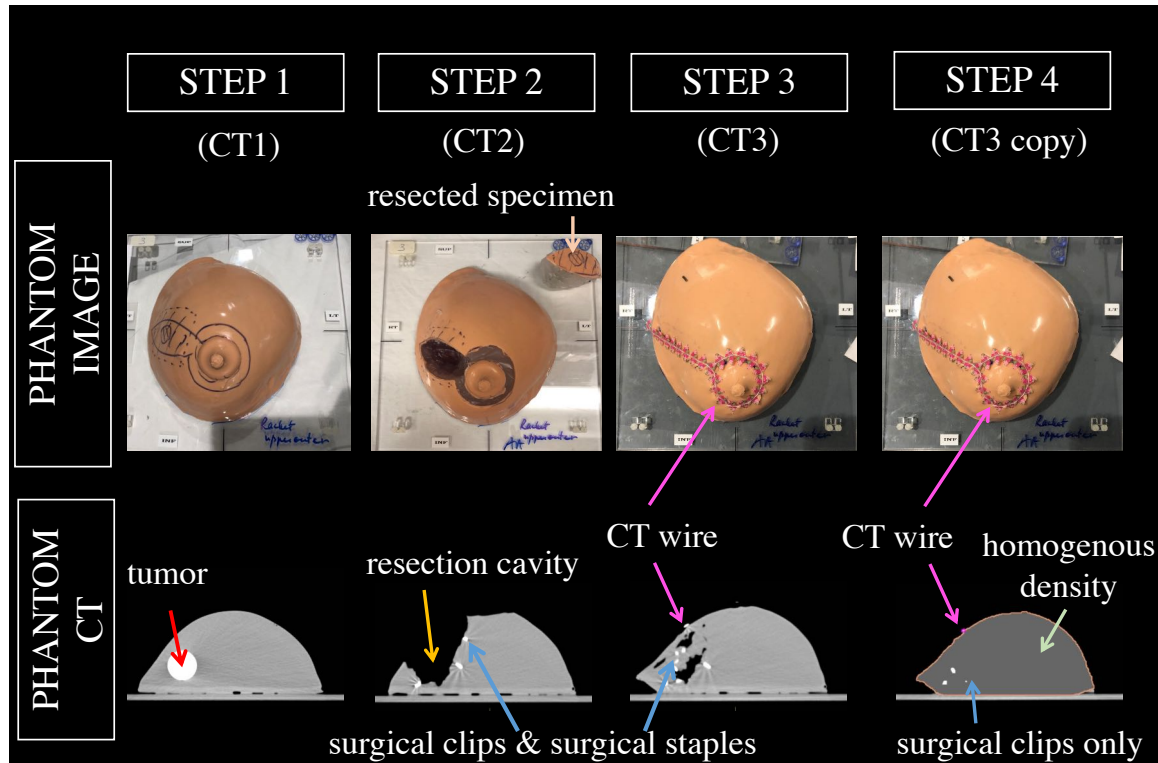


Figure 6.3 An example case (case 3, with a racquet OBS technique) shown during different phases and with the corresponding CTs. Step 1: CT1 is acquired prior to beginning surgery. Step 2: CT2 is acquired after the tumour was resected. Step 3: CT3 is acquired after OBS was performed and surgical closure was complete. Step 4: A copy of CT3 is generated, and a homogenous override of the relative electron density is applied to mask all features except the surgical clips. All steps show the breast phantom along the same CT slice.

All surgeries were also video recorded to document surgical maneuvers used and their influence on each tumour bed, as well as the location of surgical clips with respect to the tumour bed.

6.2.3 Image handling and contouring

CT images were imported into the Monaco Treatment Planning System (TPS), (v.5.11.02, Elekta, Sweden). For each phantom, CT2, and CT3 were first co-registered to CT1. Contours were delineated on co-registered CT2 and CT3 image sets, as described below.

Tumour bed delineation using *a priori* knowledge

For each case, surgical clips were identified according to anatomical location and labeled on CT2 and CT3. Then, the x, y, and z CT positions of each surgical clip were recorded to determine its 3D displacement. Based on geometric appearance of the fully marked TB on CT3, verification of cavity wall motion on recorded videos, comparison of CT2 and CT3, and knowledge of the OBS technique employed, a true tumour bed (TB_{True}) was determined for each case on CT3.

Tumour bed delineation by radiation oncologists

For all cases, an additional step was performed. This is referred to as Step 4 in Figure 6.3. In this step, a copy of CT3 was generated and the additional markers (*i.e.*, surgical staples) were masked by overriding the entire breast parenchyma contour to a relative electron density of 0.991 using MATLAB (MathWorks, Inc., Natick, MA, USA, R2018b). The copy of CT3 was then re-imported into the TPS, and only a standard of eight

surgical clips and CT wires were visible for treatment planning target delineation. Two experienced breast radiation oncologists were provided with typical surgical information found in postoperative reports: tumour location, tumour dimension, excision type and margins. For each case, this modified CT3 was used by the radiation oncologists (RO) to delineate a tumour bed (TB_{RO1} and TB_{RO2} contours). In practice, this is initially defined as the surgical clips with a 5 mm margin [268], followed by manual editing of the tumour bed structure to eliminate CT slice-to-slice contour discontinuities. Additionally, RO_1 was asked to score the difficulty of each case (1 being easy to 10 being very difficult). To evaluate intraobserver reproducibility, RO_1 was asked to delineate the tumour bed again for all cases after a six-month period, using the same information and conditions (with the same computer workstation, image window-level settings, and ambient light setting).

TB_{RO1} contours were also expanded isotropically by applying 5 mm, 10 mm, and 15 mm expansion margins that were selected based on typical tumour bed to clinical-target-volume (CTV) margins adopted by existing PBI protocols [272,279]. All expansion volumes were generated by first clipping the tumour bed from skin by 5 mm, then the resulting volume was also clipped from skin by 5 mm. The clinical implications of clipping from skin were not considered in this study.

6.2.4 Comparison metrics

For each case, the average and standard deviation of surgical clip displacements were measured by comparing the individual 3D position of each surgical clip on CT3 compared to its initial position on CT2.

To investigate the impact of relying on surgical clips and tumour bed contouring accuracy, radiation oncologists' contours were compared with TB_{True} using these following metrics:

Dice similarity coefficient (DSC): The degree of overlap of two delineated contours is expressed as twice the value of contours' overlapping area normalized to their union—numerically varying from 0 (no overlap) to 1 (complete overlap) [280]. CT3 image sets containing structures of interest were exported from Monaco, and the DSC values were measured using SlicerRT [281] (v. 4.10.2).

Hausdorff Distance (HD): The distance between surfaces of two comparison volumes [282], usually reported as the maximum HD. The maximum (HD_{max}), 95th percentile (HD_{95%}) and average HD (HD_{avg}) were reported. The HD values were also measured using SlicerRT.

Over- and under-contoured volumes: Compared with the actual tumour bed, the radiation oncologists' over-contoured volumes (i.e., the potentially over-irradiated healthy tissue)

and under-contoured volumes (i.e., potentially missed/diseased tissue) were calculated with Monaco TPS's Boolean operations.

For all cases, three sets of tumour bed contours were compared:

- 1- TB_{True} : The “reference” tumour bed generated from *a priori* knowledge of the relocated tumour bed.
- 2- TB_{RO1} : The tumour bed contoured by the first radiation oncologist (RO₁).
- 3- TB_{RO2} : The tumour bed contoured by the second radiation oncologist (RO₂).

Additionally, TB_{RO1} and TB_{RO2} contours were compared against each other as a measure of interobserver reproducibility. Intraobserver reproducibility was assessed using the two sets of contours provided by RO₁. Expanded contours were compared with the reference TB_{True} .

6.3 Results

The breast phantom was found to be an effective tool for surgical simulation of all aspects of various OBS techniques. The methods proposed and studied demonstrated that it is possible to monitor surgical clip displacements, identify tumour bed cavity walls, and compare contoured versus true tumour beds (*i.e.*, the ground truth).

Figure 6.4 shows the surgical clip displacements for the six OBS techniques investigated. Individual surgical clip displacements were within ± 35.0 mm. The largest

3D surgical clip average displacements were 16.3 ± 11.7 mm, and 14.3 ± 15.0 mm, for cases 5 and 2, respectively. Both of these cases employed mammoplasties.

A detailed example of one of the cases (case 3), with the identified tumour bed cavity walls on CT2 and CT3 (as well as corresponding tumour beds for TB_{True} and TB_{ROI}) is shown in Figure 6.5. From this 3D rendering, it is visually clear that the tumour bed undergoes significant deformation and relocation after OBS. It is also qualitatively evident that TB_{ROI} does not match TB_{True} , neither in shape nor position. The difference in contoured structures is also demonstrated through another example (case 2, inferior pedicle reduction mammoplasty), which is shown in Figure 6.5((b), (c), (d), and (e)), where TB_{ROI} is visually compared with TB_{RO2} , as well as with TB_{True} . This figure also shows the type of CT images that were used by the ROs for contouring. In these images, the breast parenchyma was overridden to hide any features on the CT with the exception of surgical clips. Particularly interesting to note is the shape of TB_{True} , which appears more irregular, and concave compared to both TB_{ROI} and TB_{RO2} . Furthermore, as can be seen in the sagittal view of Figure 6.5, due to the absence of surgical clips on the anterior cavity wall, both ROs did not identify that part of the breast anatomy as a tumour bed.

The average contour structure volumes for TB_{True} , TB_{RO2} , and TB_{ROI} (as well as those with expanded margins) are provided in Table 6.2. Compared with TB_{ROI} , TB_{RO2} contours were all larger, resulting in lower under-contoured volumes and higher over-contoured volumes for RO₂. Overall, the largest TB volumes were for the inferior pedicle reduction mammoplasty case. This was observed for TB_{True} , TB_{ROI} , and TB_{RO2} , with

absolute volumes of 93.4 cc, 104.4 cc, and 118.4 cc, respectively. After applying expansions to TB_{ROI} , and compared with TB_{True} , it was found that under-contoured volumes decreased, while over-contoured volumes increased.

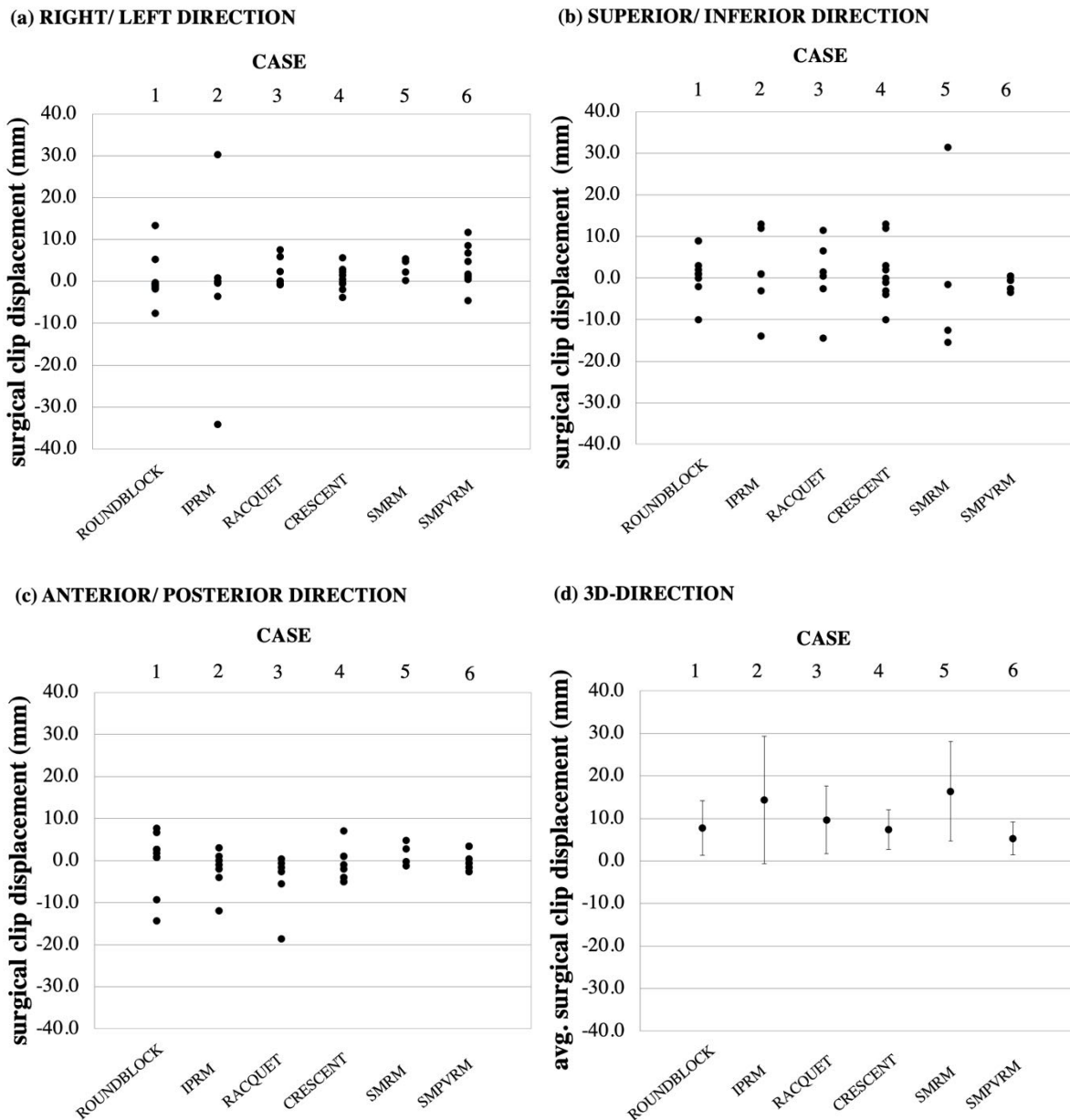


Figure 6.4 Surgical clip displacements measured on CT for each breast phantom case. Each clip displacement is shown separately along the three CT axis directions (a, b, and c), and the average and standard deviations of 3D displacement for all clips in each case (d). The displacements were calculated by comparing the final position of each surgical clip after oncoplastic breast surgery closure, with that to the initial clip position as found just after tumour excision. Abbreviations: IPRM= inferior pedicle reduction mammoplasty, SMRM= superior medial reduction mammoplasty, and SMPVRM= superior medial pedicle vertical reduction mammoplasty.

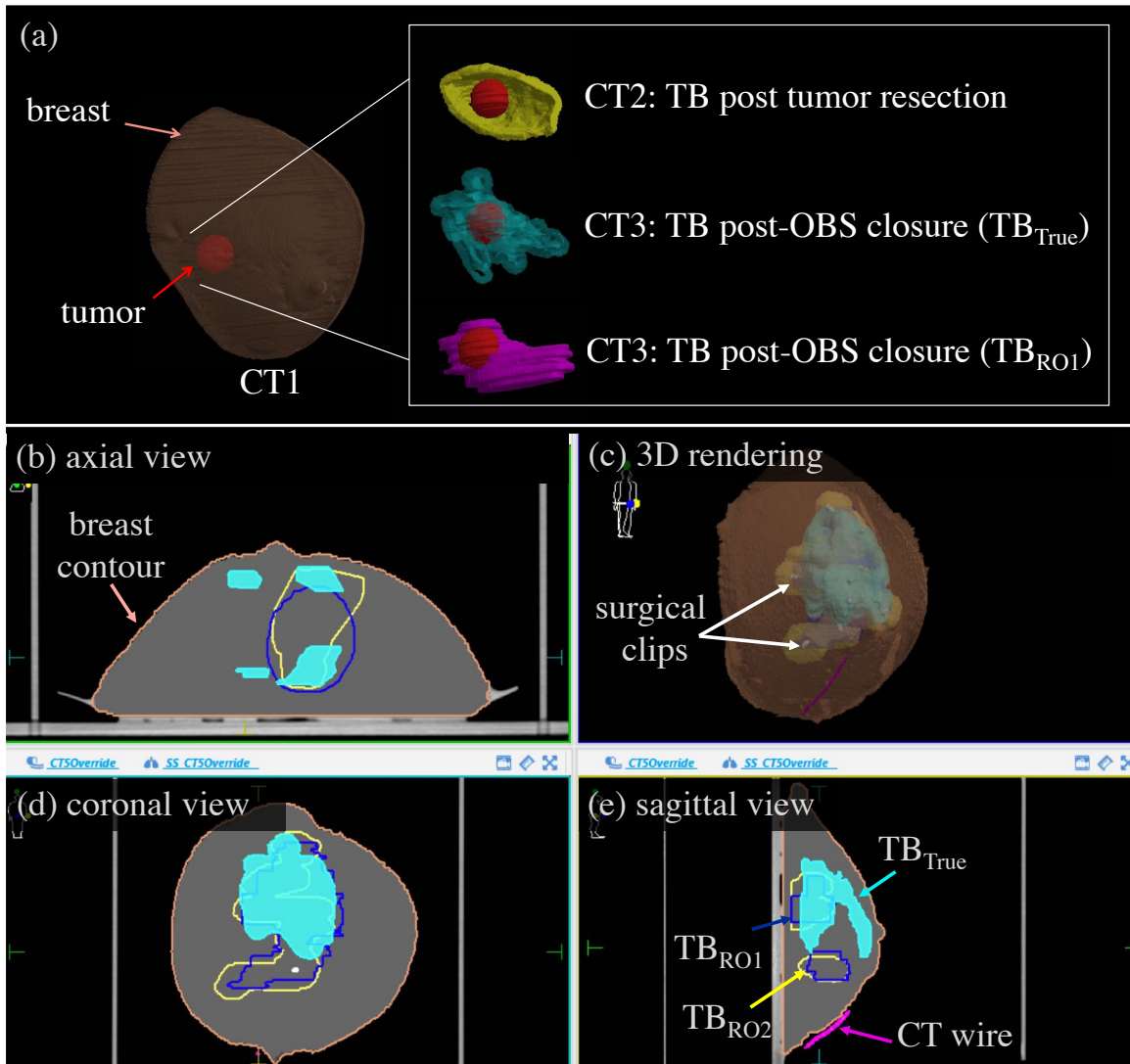


Figure 6.5 (a) A visual comparison of 3D rendered TBs for the same phantom case (case 3, racquet technique), before (CT2) and after OBS closure (CT3). CT image slices of a breast phantom with homogenous parenchyma density after OBS (case 2, inferior pedicle reduction mammoplasty) are shown on (b), (d) and (e).

Table 6.2 The ranges of tumour bed (TB) contour structure volumes, before and after applying expansion margins, as well as the ranges of under-contoured volumes (*i.e.*, TB_{True} volumes that were not included in radiation oncologists TB_{ROI} and TB_{RO2} contours) and over-contoured volumes (*i.e.*, “healthy” breast volumes that were included in radiation oncologists TB_{ROI} and TB_{RO2} contours). Note: all radiation oncologists’ contours are taken in comparison with TB_{True} .

Contour	Contour Structure Volume		Under-contoured Volume		Over-contoured Volume	
	cc	% of breast	cc	% of TB_{True}	cc	% of breast
TB_{True}	[43.4 - 93.3]	[4.5 - 12.3]	0	0	0	0
TB_{ROI}	[34.1 – 104.4]	[4.2 – 12.6]	[12.4 - 57.3]	[28.4 - 58.3]	[5.9 – 50.9]	[0.6 – 6.1]
TB_{RO2}	[43.9 – 130.7]	[7.4 – 14.3]	[7.6 – 44.9]	[17.4 – 71.6]	[16.0 – 69.8]	[2.2 – 8.4]
$TB_{ROI} + 5\text{ mm}$	[56.5 – 196.4]	[7.9 – 23.7]	[1.2 – 32.2]	[2.6 – 84.9]	[20.5 – 118.0]	[2.2 – 14.2]
$TB_{ROI} + 10\text{ mm}$	[76.3 – 276.8]	[11.4 – 33.4]	[0.0 – 14.5]	[0.0 – 95.2]	[33.3 – 191.3]	[4.8 – 23.1]
$TB_{ROI} + 15\text{ mm}$	[98.3 – 347.6]	[15.0 – 42.0]	[0.0 – 4.3]	[0.0 – 98.3]	[49.6 – 261.4]	[7.9 – 31.6]

Table 6.3 presents the DSC for all contoured structures. Both intra-RO and inter-RO contour congruences were acceptable for all cases ($DSC > 0.7$). However, the radiation oncologists' contours did not overlap well with TB_{True} . The lowest congruence was found for case 6 (superior medial pedicle vertical reduction mammoplasty), which had the highest difficulty, where the DSC was <0.5 for both radiation oncologists. Using expansion margins on RO_1 's contours did not improve contour congruence.

Table 6.3 Comparison of the Dice Similarity Coefficient (DSC) of contour structure volumes for each OBS technique. The radiation oncologists' contours are relative to TB_{True} . The Difficulty Score for each case was provided by RO_1 . Abbreviations: IPRM= inferior pedicle reduction mammoplasty, SMRM= superior medial reduction mammoplasty, and SMPVRM= superior medial pedicle vertical reduction mammoplasty.

Case	OBS Technique	Difficulty Score	DSC						
			Intra- RO	Inter- RO	TB_{RO2}	TB_{ROI}	TB_{ROI}	TB_{ROI}	TB_{ROI}
							+5 mm	+10 mm	+15 mm
1	<i>Roundblock</i>	3-4	0.86	0.71	0.69	0.60	0.72	0.69	0.60
2	<i>IPRM</i>	7-8	0.77	0.71	0.46	0.53	0.52	0.45	0.39
3	<i>Racquet</i>	2-3	0.72	0.81	0.50	0.53	0.49	0.41	0.34
4	<i>Crescent</i>	3-4	0.73	0.80	0.59	0.57	0.55	0.49	0.42
5	<i>SMRM</i>	4-5	0.84	0.80	0.53	0.59	0.59	0.53	0.44
6	<i>SMPVRM</i>	8-9	0.78	0.78	0.47	0.38	0.52	0.56	0.55

Finally, the HD data are plotted in Figure 6.6. Intra-RO and Inter-RO contour groups coincided well within each other (all below 20.0 mm). However, significantly larger spatial differences were observed when comparing the radiation oncologists' contours with the TB_{True} contours. Here, the largest HD_{max} values were for cases 2 and 6, which were 38.0 mm and 34.7 mm, respectively.

By using expansion margins on TB_{RO1} , HD_{max} , $HD_{95\%}$, and HD_{avg} values systematically increased—the largest HD_{max} value being 41.5 mm for $TB_{RO1}+15mm$ for case 2. The exception is for case 6, where HD_{max} decreased when 15 mm margins were applied. Overall, HD_{max} was large for cases 2 and 6, and both cases were considered difficult.

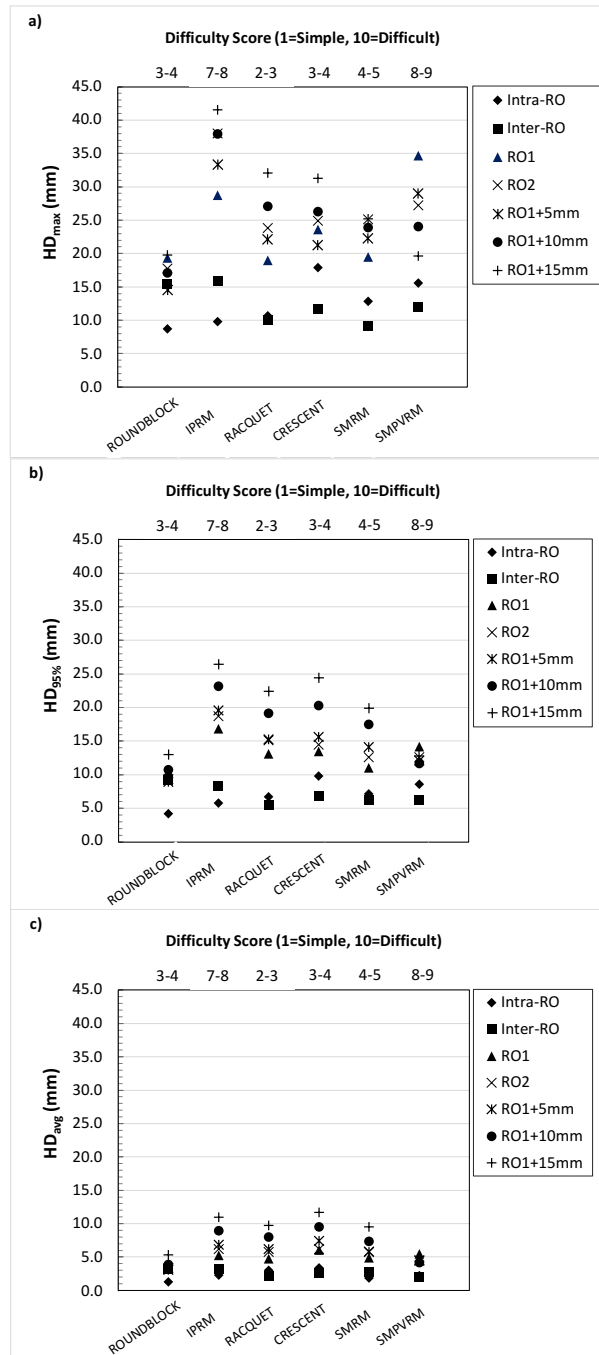


Figure 6.6 Comparison of the 3D distances between RO contours against each other (Intra-RO and Inter-RO). As well as differences between TB_{True} and RO contours (without and with expansion margins). The HD_{max} , $HD_{95\%}$, and HD_{avg} values are provided for each OBS technique as shown on the abscissa.

Abbreviations: IPRM= inferior pedicle reduction mammoplasty, SMRM= superior medial reduction mammoplasty, and SMPVRM= superior medial pedicle vertical reduction mammoplasty.

6.4 Discussion

Significant surgical clip displacements were observed for OBS cases, particularly with a mammoplasty (see Figure 6.4). Post-OBS surgical clips were frequently displaced into a different breast quadrant. Surgical clip displacements were more prominent along the right-left axis, as also observed by Kirova *et al.* [267]. Equally significant displacements also occurred along the superior-inferior direction for mammoplasty cases. This could be explained by the fact that these OBS techniques utilize breast lifts to achieve the desired cosmetic outcome.

Post-OBS inter-RO contouring variability results were similar to what was observed after breast tumour bed post-lumpectomy in prior studies [60,61,169,170,283–286]. Generally, all contoured structures (including TB_{True}) were within 200 cc, and/or 30% of the breast phantom volume. This is an important consideration during RT planning when patient eligibility for PBI is established [273,287]. Yet, when larger expansion margins were applied to TB_{ROI} , these criteria were often not met. Furthermore, compared with the original contour (TB_{ROI}), with increasing margins, the over-contoured volumes relatively increased by 5.5 times. This is an important consideration as irradiation of a large portion of the uninvolved ipsilateral breast increases the risks developing subsequent toxicities [288] as well as poor cosmesis.

Based on the DSC results, both contours provided by two radiation oncologists during the same time interval, and those provided by one radiation oncologist after a period

of time has elapsed, did not perfectly overlap but were considered satisfactory (with a DSC >0.70 recognized as good overlap [280]). Nonetheless, when compared to TB_{True} , the average DSC values for both RO contours were low (<0.55). Meaning that the overlapping volumes between the tumour bed contours defined based on surgical clips and the TB_{True} contours were far from the optimal value of 1.00. Applying conventional isotropic expansions did not eliminate under-contoured volumes nor improve contour congruence. This lack of overlap is attributed to the fact that TB_{True} contours were irregularly shaped and radiation oncologists' contours were ellipsoidal.

The HD data confirmed both inter- and intra-RO contour agreements (refer to Figure 6.6). These values are within expected ranges [289] and are similar to margin sizes used for breast boost and PBI target delineation [118,270,272,290,291], meaning that they are typically accounted for during the radiotherapy contouring process. Despite this process, differences in HD_{max} and $HD_{95\%}$ (for RO contours relative to TB_{True}) are significant and, again, cannot be mitigated by applying isotropic expansion margins. In the post-OBS setting, these findings question the efficacy of these margins in including the entire true tumour bed in the treatment target volume defined. This is especially important to consider given the variability and complexities of OBS approaches by surgeons [12,292,293], how and where surgical clips are placed, as well as the variability in surgeon preferences and training [294]. Thus, a “one size fits all” approach of applying conventional isotropic expansions is not necessarily appropriate for post-OBS patients.

Larger TB_{ROI} and TB_{RO2} vs. TB_{True} contour discrepancies were found with mammoplasty cases. The largest component of under-contoured volumes was found along the anterior extent of the breast (see Figure 6.5). Substantial breast tissue is excised in a mammoplasty, resulting in more significant tissue displacement to fill the tumour bed defect and achieve improved cosmesis, which shifts the anterior portion of the tumour bed [292]. After tumour excision, the anterior extents of the tumour bed cavity walls are not often marked by surgical clips and radiation oncologists may miss important information. For these cases, the use of additional surgical clips along the anterior clinical extent of each cavity wall may, to some degree, help in improving tumour bed delineation accuracy.

The number of eight surgical clips provided to radiation oncologists for tumour bed delineation was chosen based on recent recommendations on surgical clips placement post-OBS for adjuvant radiotherapy [171], which stated the following: At least four surgical clips are necessary in OBS and should be placed along the four side walls of the cavity, with possible addition of one to four more along the chest wall where the tumour was localized to demarcate the posterior margin of the tumour bed. Hence, using eight surgical clips for all cases provided a realistic representation of the “best-case scenario” of the number of surgical clips available. Nevertheless, this study confirmed that even eight surgical clips cannot fully capture the 3D deformations and relocations of post-OBS tumour beds.

There are some limitations in using a breast phantom for the purpose presented: one arises from the nature of the phantom material that does not allow complete fusion of tumour bed cavity walls post-OBS (this would be analogous to healing in human tissue). This led to the presence of air pockets in the breast parenchyma in regions where incisions were made, which were also visible in the post-OBS closure CT (CT3). In a patient's case, a similar affect may form a seroma over time. Nonetheless, in an ideal OBS case, a seroma is usually absent due to intentional tissue redistribution inside the tumour cavity, forming a "closed cavity" [11,295]. Accordingly, the air pockets were masked to look like breast parenchyma on the digitally processed CTs provided to the radiation oncologists for tumour bed delineation (*i.e.*, CT3 copy, as shown in Figure 6.3). The second limitation is related to the above and the masking of a large number of radio-opaque markers (surgical staples) that were initially used to track cavity wall motion. As a result, the phantom breast parenchyma was seen by radiation oncologists as having uniform density with only surgical clips visible. GEC-ESTRO's Breast Cancer Working Group's Recommendations describe a rigorous process for target delineation for PBI or APBI; which includes careful consideration of preoperative radiographic information, surgical information, closed or open cavity scoring, seroma formation, breast tissue changes, as well as surgical clip placement. Therefore, one can argue that the CT image features presented are not representative of reality, and we would be in agreement with this argument. We can also state, however, that in practice and when contouring real breast patients post-OBS, even if the density of the breast parenchyma is heterogenous, it is common to only see surgical clips, with no visible TB cavity and no other visible post-operative changes on a

radiotherapy planning CT. In these cases, the delineation procedure adopted for these patients would be similar to the one used on these realistic breast phantoms.

APBI and PBI require accurate tumour bed delineation, which, as demonstrated by this study, can be difficult to achieve in certain OBS cases. Newer hypofractionated WBRT regimens have gained rapid adoption during radiotherapy clinical response [296] to the COVID-19 pandemic (such as START B [297], FAST-Forward [298]), and have shown equivalently fast and convenient treatments as PBI. Compared with APBI/ PBI, in post-OBS situations, based on our findings and in the absence of clinical trials, these types of techniques would also account for potential target-miss. Nevertheless, if APBI/ PBI is still the favored approach, then expansion margins must be large enough to account for any target delineation uncertainty. Yet, this would mean that a large volume of healthy breast tissue would also be irradiated.

Overall, more tools and efforts are necessary to improve tumour bed contouring accuracy, especially for PBI or APBI. Contouring accuracy can be improved by providing radiation oncologists with additional training and awareness on different OBS techniques [171], as demonstrated by this study. An alternative approach could be to provide detailed records of a patient's OBS technique. This could be by uploading a diagram in the patient's chart, or by appending a 3D simulated video model to the patient's chart to communicate how breast tissue deformed and relocated during a particular OBS technique.

6.5 Conclusions

In this chapter, the use of realistic breast phantoms as a surgical simulation tool was demonstrated to investigate the reliability of surgical clips as radiographic surrogates of tumour beds post-OBS. It was shown that post-OBS surgical clips can be significantly displaced, and that relying on post-OBS surgical clips for tumour bed delineation can lead to inaccurate tumour bed contours. It was also determined that using typical expansion margins to account for contouring uncertainties did not improve contour overlap, and merely led to an unnecessary increase of normal tissue contoured. For all OBS cases investigated, it was found that surgical clips are not reliable radiographic surrogates of tumour beds, which makes post-OBS tumour bed delineation a challenging task for radiation oncologists. This study concludes that for complex OBS cases, new hypofractionated WBRT regimens may be warranted in lieu of any type of PBI or APBI regimen.

Chapter 7: Conclusions and Future Work

7.1 Summary and conclusions

Breast cancer was one of the first diseases to be treated by radiotherapy. It is also one of the most common forms of cancer, and one of the most frequently treated diseases in radiation oncology departments worldwide. Since its initial implementation, breast radiotherapy has undergone significant advancements to improve treatment quality and a patient's quality of life. A recent advancement in external beam radiotherapy is the adoption of accelerated partial breast irradiation (APBI) techniques. Contrary to standard-of-care whole breast radiotherapy (WBRT), APBI treatments focus radiation to the tumour bed with a surrounding 5 to 20 mm overall treatment margin [92]. Consequently, to ensure successful treatment outcomes, these precise treatment techniques require a higher level of treatment accuracy than WBRT. The purpose of this thesis was to contribute to the advancement of treatment accuracy for APBI. This was achieved as follows:

In the first component of the thesis (Chapters 2 and 3), 3D printing was utilized to construct phantoms for assessing image fidelity and for quantifying geometric distortions on multiple radiological imaging modalities that are used for radiotherapy target delineation. In Chapter 2, the proof of concept was demonstrated using a small version of the phantom and on co-registered helical computed tomography (CT), cone beam computed tomography (CBCT), and magnetic resonance imaging (MRI) image sets. These imaging modalities are routinely employed during stereotactic radiosurgery planning for

cranial disease where targets are delineated and treated with sub-mm precision and accuracy. In addition to the 3D printed phantom, a commercial phantom and two different analysis approaches were used (the first being a commercial software and the second an in-house implementation) to quantify geometric distortion. In this study, the combined errors of image co-registration and image geometric distortion were reported as a mean target registration error (TRE), and the mean TRE was reported for each image set acquired. Compared to the commercial phantom and commercial software, the 3D printed phantom and accompanying in-house analysis technique offered a reliable technique to measure and quantify geometric distortion. Study results showed that the largest reported mean TRE was for the CBCT (which is used for angiography) followed by T2-weighted (T2w) MR images (albeit all < 1 mm). It was also concluded that because these types of diagnostic images are acquired outside of the radiation oncology department, routine quality assurance (QA) of multi-modality scanners should include image geometric distortion testing, and the tools and methods presented can meet this clinical need.

The second part of this work, which continued in Chapter 3, was motivated by the fact that MRI offers excellent soft tissue visualization. In breast radiotherapy, the current standard of practice is to perform target delineation on CT images, which has poor soft tissue contrast. Therefore, MRI can be particularly advantageous for breast radiotherapy techniques requiring high delineation accuracy, such as APBI. However, unlike the cranial site, where the target is typically close to the central axis of the MR scanner bore, breast imaging is performed with the breast offset laterally from the centre of the bore, where geometric distortion is drastically increased. In Chapter 3, a method for measuring image

geometric distortions in a large field-of-view (FOV) that would encompass the breast site was presented. There, techniques and methods demonstrated in Chapter 2 for the cranial site were further developed to construct a modular, large volume 3D printed phantom. Geometric distortion was measured on image sets acquired with MRI sequences that are often utilized for clinical breast imaging. These sequences included T1w volumetric interpolated breath-hold examination (VIBE) and T2w turbo spin echo (TSE) and sampling perfection with application optimized contrasts using different flip angle evolution (SPACE). For this study, geometric distortions were reported as radial geometric distortion errors (r) to help inform the margin sizes required for APBI treatments where target delineation employs MRI simulator images. In addition to the different sequences, the influence of different phase encoding readout directions was also investigated. This approach provided information on the potential sources of geometric distortion, which were categorized as being either sequence-dependent or sequence-independent factors. Results showed that geometric distortions varied depending on the sequence used and phase encoding readout direction, with the largest reported errors being nearly 4 mm for T1w VIBE scans at the left edge of the MR scanner's bore. Preliminary results also showed that maximum radial distortion errors can be in the order of 3 to 4 mm. These errors are important to consider when evaluating treatment margin sizes for highly precise APBI techniques, especially in the neoadjuvant setting.

The second component of this thesis was provided in Chapters 4, 5, and 6. It centered on the development, optimization, validation, and utilization of a novel, realistic and deformable breast phantom for multiple applications including multi-modality

radiological imaging (CT, MRI, and ultrasound), radiation absorption (dosimetric) measurements, and surgical simulation. Chapter 4 presented a phantom prototype made of moldable silicone that has several realistic anatomical features, including breast parenchyma, an epidermis layer, nipple, areola, chest wall, and lateral chest fat. This chapter presented how the phantom was constructed, and how various multi-modality imaging properties and mechanical properties were measured and validated. Imaging properties included measurement of signal-to-noise (SNR), and contrast-to-noise (CNR) ratios of various phantom components on CT, MRI, and ultrasound, as well as measurement of T1 and T2 MRI relaxation times. The phantom's components were visible on all imaging modalities, and T1 and T2 MRI relaxation times were similar to breast silicone implants. Mechanical properties included measurement of elasticity (*i.e.*, Young's Modulus), ultimate tensile strength (UTS), and strain on rupture of the phantom's epidermis layer and parenchyma. The phantom's epidermis layer and breast parenchyma mechanical properties were also quantitatively compared with the mechanical properties of human breast tissue for the epidermis and breast fat, respectively.

In addition to imaging and mechanical properties, the phantom's suitability as a realistic surgical simulation tool was evaluated by experienced surgeons who simulated various oncoplastic breast surgery (OBS) techniques with varying levels of complexity. The surgeons' confirmed that the breast phantom was realistic for surgical simulation. This suggests that it could be used as an OBS simulation and training tool. The phantom was also deemed suitable as a training tool for ultrasound or MRI guided breast biopsy,

ultrasound or MRI guided brachytherapy needle insertion, and for patient education. These results were presented in detail in Chapter 4.

Chapter 5 focused on evaluating the suitability of the material used to construct the breast phantom for radiation absorption (dosimetric) measurement applications. This was achieved by investigating moldable silicone's radiation dose properties in radiation beams used for breast radiotherapy treatments, and by comparing those properties to that of water and radiologically water-equivalent plastic. The study provided a comprehensive assessment of the dosimetric properties, including performing empirical calculations to determine key physical quantities that are relevant for radiation dose absorption, carrying out experimental measurements with ionization chambers and radiochromic film, conducting treatment planning system calculations, and validating both experimental and calculated results with Monte Carlo simulation results. Results showed that compared with water-equivalent materials, radiation absorption of moldable silicone was within $\pm 2\%$. These findings confirmed that if these dose differences are taken into consideration, then moldable silicone can potentially be used for dosimetric applications as well.

As an application of the breast phantoms presented in Chapter 4, Chapter 6 demonstrated the use of these realistic breast phantoms in investigating how OBS differs from conventional breast conserving surgery (BCS). These findings highlighted how OBS can potentially impact breast radiotherapy planning and treatment for APBI. In this investigation, the phantoms were carried through a “simulated patient care path”, which included OBS and surgical clip placement by surgeons, radiotherapy simulation by medical

physicists, and radiotherapy contouring by radiation oncologists (ROs). In clinical practice, surgical clips are often used for radiotherapy target (tumour bed) contouring during adjuvant breast radiotherapy planning. Therefore, their reliability as radiographic surrogates of tumour bed locations post-OBS was of primary interest in the presented study. Here, ROs relied on post-OBS surgical clips to delineate tumour beds as per standard clinical practice. To evaluate if tumour bed contouring inaccuracy can be accounted for, RO contoured tumour beds were also expanded by typical APBI margins (5, 10, and 15 mm). The study showed that RO contoured tumour beds significantly differed from the ground truth tumour beds, both in anatomical locations and in volume sizes, and that the use of expansion margins did not mitigate these discrepancies. These results provided new insight into what occurs during OBS, including how breast tissue is manipulated and deformed, and how this influences the locations of surgical clips. This demonstrated that accurate tumour bed delineation is challenging following OBS. This also showed how for adjuvant radiotherapy following OBS, patient selection criteria for APBI can be impacted owing to the reduced tumour bed delineation accuracy.

7.2 Future work

The main purpose of this thesis was to inform and advance treatment accuracy of APBI; however, treatment accuracy cannot be achieved without target delineation accuracy. Below is a discussion on research areas that can further develop the tools and methods presented in this thesis.

7.2.1 Optimization of MRI protocols for APBI

As discussed in Chapters 1 and 3, due to its superior soft tissue contrast, MRI has the potential of improving target delineation for adjuvant and neoadjuvant APBI. When it comes to the adoption of MRI in high-precision, high-accuracy radiotherapy treatment planning techniques, geometric distortion present in MRI imaging poses a challenge. To this end, the 3D printed phantoms and methods presented in Chapters 2 and 3 were demonstrated to be effective in quantifying MRI geometric distortion in radiotherapy simulation for breast cancer and for other sites of disease.

Future work includes utilizing the modular design of the phantom to measure geometric distortion along the entire extent of the imaging FOV, and to use the phantom to evaluate the influence of an MRI compatible prone immobilization breast board on MRI geometric distortion by setting up the phantom in conjunction with the board. As our institution prepares for clinical implementation of MRI breast radiotherapy simulation for APBI, the demonstrated tools and techniques can also be used for ongoing quantitative QA testing of geometric distortion for clinically adopted MR sequences.

Ideally, however, clinically adopted MR sequences should have demonstrated benefits based on human data. This includes the ability to reproducibly position patients for radiotherapy treatments, increased target visualization, preservation of image fidelity, and accurate tumour bed delineation. This data can only be acquired through clinical experience and patient trials. While geometric distortion associated with MRI imaging is

an important consideration, the deformable nature of breast tissue poses another problem for high precision treatments. The impact of these combined factors is not assessed in the present work. Patient trials with MRI simulation as part of APBI treatment planning could help decide which MRI protocols should be adopted for APBI techniques, and evaluate the utility of MRI for APBI treatment planning.

7.2.2 Further applications of the realistic breast phantom

The presented breast phantom prototype was characterized and validated for multi-modality radiographic imaging, surgical simulation, and dosimetric applications. The findings suggest that such a phantom can be used as a deformable end-to-end breast phantom. This would allow applications that simulate the entire treatment chain of an adjuvant radiotherapy breast cancer case including surgery, radiotherapy simulation, radiotherapy treatment planning, and radiotherapy dose delivery and measurement. We are currently developing a breast phantom that can be used to evaluate the feasibility of tumour bed target tracking accuracy using surgical clips on CyberKnife's Synchrony System. For this study, the deformable breast phantom is placed on a moving platform that simulates normal human breathing motion, and continuous target tracking accuracy is assessed. The phantom is designed to allow imaging and dosimetric applications as well, where radiochromic film can be used to measure delivered radiation dose and compare it with the planned radiation dose. In the future, the breast phantom construction process will also be adapted to create deformable phantoms for other anatomical sites (such as the liver or

prostate). The breast, liver, and prostate deformable phantoms would also be of potential interest to MRgRT applications, particularly with the utilization of MRI linacs.

In Chapter 6, the study involving realistic breast phantoms showed how for adjuvant radiotherapy, post-OBS surgical clips are not reliable radiographic surrogates of tumour bed locations. The study demonstrated that for post-OBS cases, current clinical methods of contouring tumour beds using surgical clips are limited, and that even generous expansion margins may not account for potential target-miss. Furthermore, using large margins may include excessive healthy tissue, reducing APBI treatment eligibility. Nevertheless, there may be alternative solutions. Recently, a new radiographic, 3D surgical filament marker was introduced to improve tumour bed marking for radiotherapy planning [299]. A similar study as that demonstrated in this thesis (one conducted by a multi-disciplinary team involving breast phantoms) can be conducted with different surgical markers to assess their reliability in improving tumour bed delineation accuracy. This would provide a practical preliminary validation technique to demonstrate the marker's efficacy, and to justify if further clinical investigations involving patient trials are necessary.

7.3 Outlook

Women with low-risk breast cancer now have multiple adjuvant radiotherapy treatment options, including APBI and hypofractionated WBRT [297,300]. APBI offers a practical and advantageous radiotherapy treatment technique for patients with low-risk

breast cancer. Compared with adjuvant APBI, neoadjuvant APBI has the potential to further decrease irradiated healthy tissue and organ-at-risk volumes [301]. While hypofractionated WBRT cannot be offered to patients with certain breast cancers, such as with ductal carcinoma *in situ*, nor for patients with large breasts [302], it has still gained wide adoption for eligible patient populations during the COVID-19 pandemic [296,297,300]. As clinical evidence for these hypofractionated treatment regimens continues to accrue, collaborative multi-disciplinary efforts present medical physicists with an important opportunity to establish these techniques. For example, radiation dose delivery accuracy can be advanced and controlled through medical physics technical expertise and understanding of radiotherapy equipment used in high precision treatments. Medical physicists can also contribute to comparative APBI planning studies, such as with the use of different dose delivery techniques (conformal radiotherapy, fixed beam-angle intensity modulated radiotherapy, or volumetric modulated arc therapy), or the use of MRI treatment simulation for the purpose of improving target delineation accuracy. These efforts would reduce variability in target delineation, treatment planning, and radiation delivery, consequently providing higher treatment accuracy and more homogenous clinical outcome data. The work provided in this thesis offers some of the necessary tools to support such studies.

Appendices

Appendix A . Example of an Inadequate Imaging Protocol on DynaCT for Stereotactic Radiosurgery Treatment Planning

As discussed in Chapter 2, one of the reasons why 3D image acquisition on DynaCT systems can suffer from poor image quality is due to the implementation of an inadequate imaging protocol. Figure A.1 demonstrates an example in which a diagnostic imaging protocol (see Table A.1) was assessed using the small lattice cube phantom (Cube C) which was presented in Chapter 2. The diagnostic imaging protocol is routinely used for digital subtraction angiography (DSA). The treatment planning CT (TPCT) and the correct imaging protocol (also provided in Table A.1) that is clinically used for stereotactic radiosurgery (SRS) treatment planning at The Ottawa Hospital are shown alongside for comparison. The only difference between these two protocols is the reduction in rotation time, yet this resulted in a significant decrease in image quality. The 3D printed phantom used (Cube C) provided a practical method of qualitatively visualizing the image fidelity differences, and the MATLAB script implemented provided a quantitative assessment of the observed geometric distortion. Here, the diagnostic DynaCT protocol yielded a mean target registration error (TRE) of 0.56 ± 0.40 mm. Whereas the SRS DynaCT protocol's mean TRE was 0.44 ± 0.18 mm (see Chapter 2 for the definition of TRE and more information on analysis methods). This example demonstrates the importance of ensuring that imaging protocols adopted for SRS planning are appropriate, effective communication with the diagnostic team is present, and that any radiological images used in SRS are routinely assessed through quality assurance testing.

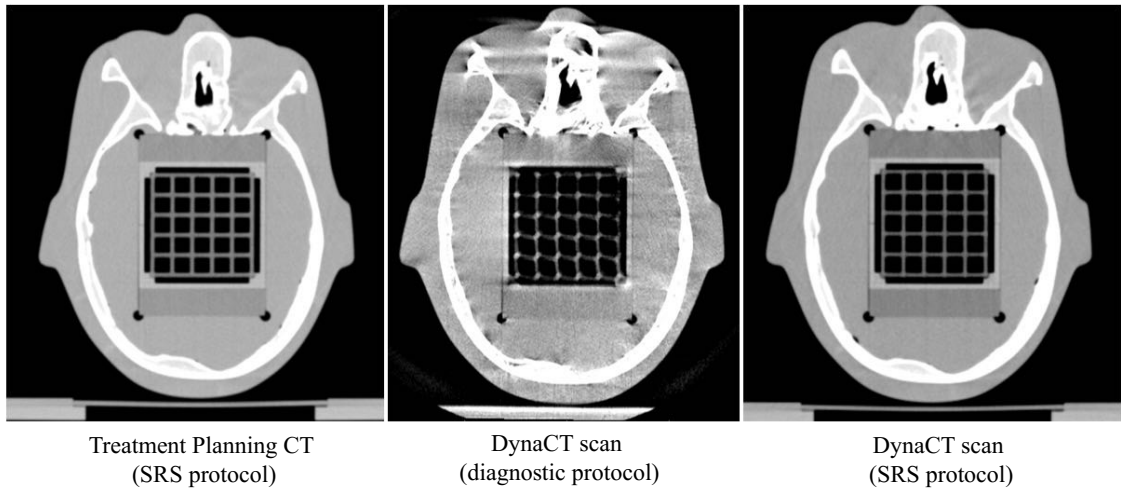


Figure A.1. Image slices from data sets of phantom Cube A (commercial phantom); shown on the reference TPCT, DynaCT, using the diagnostic protocol specified in Table A.1, and DynaCT, using the SRS specified in Table A.1.

Table A.1. Comparison of the imaging protocols used to acquire images shown in Figure A.1.

	<i>TPCT</i> <i>(SRS</i> <i>protocol)</i>	<i>DynaCT</i> <i>(diagnostic protocol)</i>	<i>DynaCT</i> <i>(SRS protocol)</i>
<i>Vendor</i>	Brilliance	Artis Q with DynaCT	Artis Q with DynaCT
	Big Bore		
<i>Make</i>	16 Slice	Siemens Medical Solutions	Siemens Medical Solutions
	Philips	Solutions	
<i>Scan Parameters</i>	120 kVp	70 kVp, 400 mA	70 kVp, 400 mA
	450 mAs	$\Delta\theta = 240^\circ, t = 5 \text{ s}$	$\Delta\theta = 240^\circ, t = 20 \text{ s}$
		496 frames	496 frames
<i>In-plane resolution (mm²)</i>	0.4 x 0.4	0.4 x 0.4	0.4 x 0.4
<i>Slice thickness (mm)</i>	1.0	1.0	1.0

Appendix B . Summary of 3D Printing Technologies Used in Medical Applications

In Chapter 2, a lattice cube phantom was 3D printed for the purpose of measuring geometric distortion on radiological images. This prototype was printed using Fused Deposition Modeling (FDM) 3D printing technology. In Chapter 3, a large lattice cube phantom was 3D printed for the same purpose but using Multi Jet Modeling (MJM) 3D printing technology. These are two different technologies commonly used in medical applications. Table B.1 presents a summary of other options in 3D printing technologies commonly used in medical applications, as well as a list of their advantages and disadvantages.

Table B.1. This table has been reproduced from Table 1 in the manuscript by George E, Liacouras P, Rybicki F J, et al. Measuring and Establishing the Accuracy and Reproducibility of 3D Printed Medical Models. *RadioGraphics* 2017;37:1424-1450, with permission granted by the Journal Business Publications Office of the Radiological Society of North America.

<i>3D Printing Technology</i>	<i>Description</i>	<i>Typical Layer Thickness in mm (Printing Resolution)</i>	<i>Model Surface Texture</i>	<i>Advantages</i>	<i>Disadvantages</i>
<i>Fused Deposition Modeling (FDM)</i>	Thermoplastics are melted and extruded by a tip onto the build platform	z axis: 0.1 – 0.5 x-y axis: 0.1 – 0.4	Very rough	*Low cost *Strong materials *Model can be printed by using one or two materials and different colors	*Slow *Spatial resolution is lower than that with other modalities *Models can be permeated by liquids owing to layer adhesion imperfections
<i>Multi Jet Modeling (MJM)</i>	Droplets of epoxy- or acrylic-based liquid photo polymers are jetted onto a tray and polymerized and solidified by means of exposure to ultraviolet light	z axis: 0.03 x-y axis : 0.05	Slightly rough	*Short term biocompatible material is available *Models can be printed by using one or two materials and different colors	*Expensive *Slow

Continued on next page...

<i>3D Printing Technology</i>	<i>Description</i>	<i>Typical Layer Thickness in mm (Printing Resolution)</i>	<i>Model Surface Texture</i>	<i>Advantages</i>	<i>Disadvantages</i>
<i>Stereolithography (SLA)</i>	Photopolymer held in a vat is polymerized by, for example, an ultraviolet laser by means of illumination of the top or bottom surface of the liquid	z-axis: 0.02-0.20 x-y axis: 0.075-0.200	Smooth	*Ideal for hallow model prints because they do not require support materials, depending on the orientation *Biocompatible materials are available	*Labor intensive removal of support struts *Only one material can be used
<i>Selective Laser Sintering (SLS)</i>	Powder of plastic, metal, ceramic, or glass is sintered by a high-power laser	z-axis: 0.1-0.2 x-y axis: 0.075-0.200	Rough	*Options for different materials *No supports required	*Expensive *Models need substantial machining post-processing
<i>Binder Jetting</i>	A liquid adhesive is jetted onto a bed of gypsum or ceramic powder	z-axis: 0.05-0.10 x-y axis: 0.05	Rough	*Models can be printed by using different colors *No supports required *Can print complex shapes	*Fragile models *Only one material can be used

References

1. Canadian Cancer Statistics Advisory Committee. *Canadian Cancer Statistics 2020*.
2. Sung H, Ferlay J, Siegel RL, et al. Global Cancer Statistics 2020: GLOBOCAN Estimates of Incidence and Mortality Worldwide for 36 Cancers in 185 Countries. *CA Cancer J Clin.* 2021;71(3):209-249. doi:10.3322/caac.21660
3. Hansen EK, Roach M. Handbook of evidence-based radiation oncology. *Handb Evidence-Based Radiat Oncol 2nd Ed.* Published online 2010:711.
4. Freeman MD, Gopman JM, Salzberg CA. The evolution of mastectomy surgical technique: From mutilation to medicine. *Gland Surg.* 2018;7(3):308-315. doi:10.21037/gs.2017.09.07
5. Blichert-Toft M, Rose C, Andersen JA, et al. Danish randomized trial comparing breast conservation therapy with mastectomy: six years of life-table analysis. *J Natl Cancer Inst Monogr.* 1992;11(11):19-25.
6. Jacobson JA, Danforth DN, Cowan KH, et al. Ten-year results of a comparison of conservation with mastectomy in the treatment of stage I and II breast cancer. *N Engl J Med.* 1995;332(14):907-911.
7. Arriagada R, Lê MG, Rochard F, Contesso G. Conservative treatment versus mastectomy in early breast cancer: patterns of failure with 15 years of follow-up data. Institut Gustave-Roussy Breast Cancer Group. *J Clin Oncol.* 1996;14(5):1558-1564.
8. van Dongen JA, Voogd AC, Fentiman IS, et al. Long-term results of a randomized

- trial comparing breast-conserving therapy with mastectomy: European Organization for Research and Treatment of Cancer 10801 trial. *J Natl Cancer Inst.* 2000;92(14):1143-1150.
9. Chakravorty A, Shrestha AK, Sanmugalingam N, et al. How safe is oncoplastic breast conservation?: Comparative analysis with standard breast conserving surgery. *Eur J Surg Oncol.* 2012;38(5):395-398.
 10. Arnaout A, Ross D, Khayat E, et al. Position statement on defining and standardizing an oncoplastic approach to breast-conserving surgery in Canada. *Curr Oncol.* 2019;26(3):e405.
 11. Macmillan RD, McCulley SJ. Oncoplastic breast surgery: what, when and for whom? *Curr Breast Cancer Rep.* 2016;8(2):112-117.
 12. Clough KB, Kaufman GJ, Nos C, Buccimazza I, Sarfati IM. Improving breast cancer surgery: a classification and quadrant per quadrant atlas for oncoplastic surgery. *Ann Surg Oncol.* 2010;17(5):1375-1391.
 13. Audretsch WP. Onco-plastic surgery:" target" volume reduction (BCT-mastopexy), lumpectomy reconstruction (BCT-reconstruction) and flap-supported operability in breast cancer. In: *Proceedings 2nd European Congress on Senology, October 2-6, 1994; Vienna/Bologna: Moncuzzi.* ; 1994:139-157.
 14. Yiannakopoulou EC, Mathelin C. Oncoplastic breast conserving surgery and oncological outcome: Systematic review. *Eur J Surg Oncol.* 2016;42(5):625-630. doi:10.1016/j.ejso.2016.02.002
 15. Grubbé EH. Priority in the Therapeutic Use of X-rays. *Radiology.* 1933;21(2):156-162. doi:10.1148/21.2.156

16. Barrett A, Morris S, Dobbs J, Roques T. *Practical Radiotherapy Planning*. CRC Press; 2009.
17. Podgorsak EB. Review of radiation oncology physics: a handbook for teachers and students. *Vienna, Austria IAE Agency*. Published online 2003:Chapter 7.
18. Boyages J, Baker L. Evolution of radiotherapy techniques in breast conservation treatment. *Gland Surg*. 2018;7(6):576.
19. Merchant TE, McCormick B. Prone position breast irradiation. *Int J Radiat Oncol Biol Phys*. 1994;30(1):197-203.
20. Cross MA, Elson HR, Aron BS. Breast conservation radiation therapy technique for women with large breasts. *Int J Radiat Oncol Biol Phys*. 1989;17(1):199-203.
21. Gagliardi G, Lax I, Rutqvist LE. Radiation therapy of stage I breast cancer: analysis of treatment technique accuracy using three-dimensional treatment planning tools. *Radiother Oncol*. 1992;24(2):94-101.
22. Gray JR, McCormick B, Cox L, Yahalom J. Primary breast irradiation in large-breasted or heavy women: analysis of cosmetic outcome. *Int J Radiat Oncol Biol Phys*. 1991;21(2):347-354.
23. Zierhut D, Flentje M, Frank C, Oetzel D, Wannenmacher M. Conservative treatment of breast cancer: modified irradiation technique for women with large breasts. *Radiother Oncol*. 1994;31(3):256-261.
24. Kurtman C, Andrieu MN, Hiçsonmez A, Celebioglu B. Three-dimensional conformal breast irradiation in the prone position. *Brazilian J Med Biol Res*. 2003;36(10):1441-1446.
25. Griem KL, Fetherston P, Kuznetsova M, Foster GS, Shott S, Chu J. Three-

- dimensional photon dosimetry: a comparison of treatment of the intact breast in the supine and prone position. *Int J Radiat Oncol Biol Phys.* 2003;57(3):891-899.
26. Varga Z, Hideghéty K, Mező T, Nikolényi A, Thurzó L, Kahán Z. Individual positioning: a comparative study of adjuvant breast radiotherapy in the prone versus supine position. *Int J Radiat Oncol Biol Phys.* 2009;75(1):94-100.
 27. Alonso-Basanta M, Ko J, Babcock M, Dewyngaert JK, Formenti SC. Coverage of axillary lymph nodes in supine vs. prone breast radiotherapy. *Int J Radiat Oncol Biol Phys.* 2009;73(3):745-751.
 28. Shin SM, No HS, Vega RM, et al. Breast, chest wall, and nodal irradiation with prone set-up: Results of a hypofractionated trial with a median follow-up of 35 months. *Pract Radiat Oncol.* 2016;6(4):e81-e88.
 29. Haffty BG. Supine or Prone Breast Radiation: Upsides and Downsides. *Int J Radiat Oncol Biol Phys.* 2018;101(3):510-512. doi:10.1016/j.ijrobp.2018.03.023
 30. Khan FM, Gerbi BJ. *Treatment Planning in Radiation Oncology.* Third Edit. Lippincott Williams & Wilkins; 2012.
 31. Bartelink H, Maingon P, Poortmans P, et al. Whole-breast irradiation with or without a boost for patients treated with breast-conserving surgery for early breast cancer: 20-year follow-up of a randomised phase 3 trial. *Lancet Oncol.* 2015;16(1):47-56.
 32. Vrieling C, van Werkhoven E, Maingon P, et al. Prognostic factors for local control in breast cancer after long-term follow-up in the EORTC boost vs no boost trial: a randomized clinical trial. *JAMA Oncol.* 2017;3(1):42-48.
 33. Mannino M, Yarnold JR. Local relapse rates are falling after breast conserving

- surgery and systemic therapy for early breast cancer: can radiotherapy ever be safely withheld? *Radiother Oncol.* 2009;90(1):14-22.
34. Hunt KK, Ballman K V, McCall LM, et al. Factors associated with local-regional recurrence following a negative sentinel node dissection: results of the ACOSOG Z0010 trial. *Ann Surg.* 2012;256(3):428.
 35. Kindts I, Laenen A, Depuydt T, Weltens C. Tumour bed boost radiotherapy for women after breast-conserving surgery. *Cochrane Database Syst Rev.* 2017;(11).
 36. Denham JW, Sillar RW, Clarke D. Boost dosage to the excision site following conservative surgery for breast cancer: It's easy to miss! *Clin Oncol.* 1991;3(5):257-261.
 37. Khan FM, Gibbons JP. *The Physics of Radiation Therapy*. Lippincott Williams & Wilkins; 2014.
 38. Bentel GC. *Radiation Therapy Planning*. Vol 162. McGraw-Hill New York; 1996.
 39. Jaffray DA. Image-guided radiotherapy: from current concept to future perspectives. *Nat Rev Clin Oncol.* 2012;9(12):688-699.
 40. Chen GTY, Sharp GC, Mori S. A review of image-guided radiotherapy. *Radiol Phys Technol.* 2009;2(1):1-12. doi:10.1007/s12194-008-0045-y
 41. Kirova YM. Recent advances in breast cancer radiotherapy: Evolution or revolution, or how to decrease cardiac toxicity? *World J Radiol.* 2010;2(3):103. doi:10.4329/wjr.v2.i3.103
 42. Brockstein BE, Smiley C, Al-Sadir J, Williams SF. Cardiac and pulmonary toxicity in patients undergoing high-dose chemotherapy for lymphoma and breast cancer: prognostic factors. *Bone Marrow Transplant.* 2000;25(8):885-894.

43. Darby SC, McGale P, Taylor CW, Peto R. Long-term mortality from heart disease and lung cancer after radiotherapy for early breast cancer: prospective cohort study of about 300 000 women in US SEER cancer registries. *Lancet Oncol.* 2005;6(8):557-565.
44. Keall PJ, Mageras GS, Balter JM, et al. The management of respiratory motion in radiation oncology report of AAPM Task Group 76. *Med Phys.* 2006;33(10):3874-3900. doi:10.1118/1.2349696
45. Remouchamps VM, Vicini FA, Sharpe MB, Kestin LL, Martinez AA, Wong JW. Significant reductions in heart and lung doses using deep inspiration breath hold with active breathing control and intensity-modulated radiation therapy for patients treated with locoregional breast irradiation. *Int J Radiat Oncol Biol Phys.* 2003;55(2):392-406.
46. Korreman SS, Pedersen AN, Nøttrup TJ, Specht L, Nyström H. Breathing adapted radiotherapy for breast cancer: comparison of free breathing gating with the breath-hold technique. *Radiother Oncol.* 2005;76(3):311-318.
47. Pratoomchart C, Klunklin P, Wanwilairat S, Nobnop W, Kittidachanan K, Chitapanarux I. The advantages of abdominal compression with shallow breathing during left-sided postmastectomy radiotherapy by Helical TomoTherapy. *PLoS One.* 2021;16(7):e0254934.
48. Vermeulen S, Cotrutz C, Buchanan C, et al. Accelerated partial breast irradiation: using the CyberKnife as the radiation delivery platform in the treatment of early breast cancer. *Front Oncol.* 2011;1:43.
49. Lu H-M, Cash E, Chen MH, et al. Reduction of cardiac volume in left-breast

- treatment fields by respiratory maneuvers: a CT study. *Int J Radiat Oncol Biol Phys.* 2000;47(4):895-904.
50. Sixel KE, Aznar MC, Ung YC. Deep inspiration breath hold to reduce irradiated heart volume in breast cancer patients. *Int J Radiat Oncol Biol Phys.* 2001;49(1):199-204.
51. Pedersen AN, Korreman S, Nyström H, Specht L. Breathing adapted radiotherapy of breast cancer: reduction of cardiac and pulmonary doses using voluntary inspiration breath-hold. *Radiother Oncol.* 2004;72(1):53-60.
52. Stranzl H, Zurl B. Postoperative irradiation of left-sided breast cancer patients and cardiac toxicity. *Strahlentherapie und Onkol.* 2008;184(7):354-358.
53. Nemoto K, Oguchi M, Nakajima M, Kozuka T, Nose T, Yamashita T. Cardiac-sparing radiotherapy for the left breast cancer with deep breath-holding. *Jpn J Radiol.* 2009;27(7):259-263.
54. Korreman SS, Pedersen AN, Aarup LR, Nøttrup TJ, Specht L, Nyström H. Reduction of cardiac and pulmonary complication probabilities after breathing adapted radiotherapy for breast cancer. *Int J Radiat Oncol Biol Phys.* 2006;65(5):1375-1380.
55. Wang W, Li J Bin, Hu HG, et al. Correlation between target motion and the dosimetric variance of breast and organ at risk during whole breast radiotherapy using 4DCT. *Radiat Oncol.* 2013;8(1):1-6.
56. Richter A, Sweeney R, Baier K, Flentje M, Guckenberger M. Effect of breathing motion in radiotherapy of breast cancer. *Strahlentherapie und Onkol.* 2009;185(7):425-430.

57. Hamming VC, Visser C, Batin E, et al. Evaluation of a 3D surface imaging system for deep inspiration breath-hold patient positioning and intra-fraction monitoring. *Radiat Oncol.* 2019;14(1):1-8.
58. Vermeulen SS, Haas JA. CyberKnife stereotactic body radiotherapy and CyberKnife accelerated partial breast irradiation for the treatment of early breast cancer. *AME Publ Co.* Published online 2014:199.
59. van Mourik AM, Elkhuzen PHM, Minkema D, Duppen JC, van Vliet-Vroegindeweij C, Group DYBS. Multiinstitutional study on target volume delineation variation in breast radiotherapy in the presence of guidelines. *Radiother Oncol.* 2010;94(3):286-291.
60. Landis DM, Luo W, Song J, et al. Variability among breast radiation oncologists in delineation of the postsurgical lumpectomy cavity. *Int J Radiat Oncol Biol Phys.* 2007;67(5):1299-1308.
61. Struikmans H, Wárlám-Rodenhuis C, Stam T, et al. Interobserver variability of clinical target volume delineation of glandular breast tissue and of boost volume in tangential breast irradiation. *Radiother Oncol.* 2005;76(3):293-299.
62. Schmitz AC, van den Bosch MAAJ, Loo CE, et al. Precise correlation between MRI and histopathology—exploring treatment margins for MRI-guided localized breast cancer therapy. *Radiother Oncol.* 2010;97(2):225-232.
63. Den Hartogh MD, Philippens MEP, van Dam IE, et al. MRI and CT imaging for preoperative target volume delineation in breast-conserving therapy. *Radiat Oncol.* 2014;9(1):1-9. doi:10.1186/1748-717X-9-63
64. Di Leo G, Trimboli RM, Benedek A, et al. MR imaging for selection of patients

- for partial breast irradiation: a systematic review and meta-analysis. *Radiology*. 2015;277(3):716-726.
65. Devic S. MRI simulation for radiotherapy treatment planning. *Med Phys*. 2012;39(11):6701-6711.
66. Schmidt MA, Payne GS. Radiotherapy planning using MRI. *Phys Med Biol*. 2015;60(22):R323.
67. Al-Hallaq HA, Mell LK, Bradley JA, et al. Magnetic resonance imaging identifies multifocal and multicentric disease in breast cancer patients who are eligible for partial breast irradiation. *Cancer*. 2008;113(9):2408-2414.
68. Groot Koerkamp ML, Vasmel JE, Russell NS, et al. Optimizing MR-Guided Radiotherapy for Breast Cancer Patients. *Front Oncol*. 2020;10(July):1-13.
doi:10.3389/fonc.2020.01107
69. Elliott S, Berlangieri A, Wasiak J, Chao M, Foroudi F. Use of magnetic resonance imaging-guided radiotherapy for breast cancer: a scoping review protocol. *Syst Rev*. 2021;10(1):1-7. doi:10.1186/s13643-021-01594-9
70. Glide-Hurst CK, Paulson ES, McGee K, et al. Task group 284 report: magnetic resonance imaging simulation in radiotherapy: considerations for clinical implementation, optimization, and quality assurance. *Med Phys*. 2021;48(7).
doi:10.1002/mp.14695
71. Dundas K, Pogson EM, Batumalai V, et al. The impact of imaging modality (CT vs MRI) and patient position (supine vs prone) on tangential whole breast radiation therapy planning. *Pract Radiat Oncol*. 2018;8(3):e87-e97.
72. Batumalai V, Liney G, Delaney GP, et al. Assessment of MRI image quality for

- various setup positions used in breast radiotherapy planning. *Radiother Oncol.* 2016;119(1):57-60.
73. Ahn K-H, Hargreaves BA, Alley MT, et al. MRI guidance for accelerated partial breast irradiation in prone position: imaging protocol design and evaluation. *Int J Radiat Oncol Biol Phys.* 2009;75(1):285-293.
 74. Rausch DR, Hendrick RE. How to optimize clinical breast MR imaging practices and techniques on your 1.5-T system. *Radiographics.* 2006;26(5):1469-1484.
 75. Liney GP, Moerland MA. Magnetic resonance imaging acquisition techniques for radiotherapy planning. In: *Seminars in Radiation Oncology*. Vol 24. Elsevier; 2014:160-168.
 76. Runge VM, Nitz WR, Heverhagen J. *The Physics of Clinical MR Taught Through Images*. Fourth Edi. Thieme; 2018.
 77. Brock KK, Mutic S, McNutt TR, Li H, Kessler ML. Use of image registration and fusion algorithms and techniques in radiotherapy: Report of the AAPM Radiation Therapy Committee Task Group No. 132: Report. *Med Phys.* 2017;44(7):e43-e76. doi:10.1002/mp.12256
 78. Major T, Gutiérrez C, Guix B, Van Limbergen E, Strnad V, Polgár C. Recommendations from GEC ESTRO Breast Cancer Working Group (II): Target definition and target delineation for accelerated or boost partial breast irradiation using multicatheter interstitial brachytherapy after breast conserving open cavity surgery. *Radiother Oncol.* 2016;118(1):199-204.
 79. Kirby AM, Yarnold JR, Evans PM, et al. Tumor bed delineation for partial breast and breast boost radiotherapy planned in the prone position: what does MRI add to

- X-ray CT localization of titanium clips placed in the excision cavity wall? *Int J Radiat Oncol Biol Phys.* 2009;74(4):1276-1282.
80. Giezen M, Kouwenhoven E, Scholten AN, et al. MRI-versus CT-based volume delineation of lumpectomy cavity in supine position in breast-conserving therapy: an exploratory study. *Int J Radiat Oncol Biol Phys.* 2012;82(4):1332-1340.
 81. Jolicoeur M, Racine M-L, Trop I, et al. Localization of the surgical bed using supine magnetic resonance and computed tomography scan fusion for planification of breast interstitial brachytherapy. *Radiother Oncol.* 2011;100(3):480-484.
 82. Kirby AN, Jena R, Harris EJ, et al. Tumour bed delineation for partial breast/breast boost radiotherapy: What is the optimal number of implanted markers? *Radiother Oncol.* 2013;106(2):231-235. doi:10.1016/j.radonc.2013.02.003
 83. Den Hartogh MD, Philippens MEP, Van Dam IE, et al. Post-lumpectomy CT-guided tumor bed delineation for breast boost and partial breast irradiation: Can additional pre-and postoperative imaging reduce interobserver variability? *Oncol Lett.* 2015;10(5):2795-2801.
 84. Al-Hammadi N, Caparrotti P, Divakar S, et al. MRI reduces variation of contouring for boost clinical target volume in breast cancer patients without surgical clips in the tumour bed. *Radiol Oncol.* 2017;51(2):160-168.
 85. Guidolin K, Yaremko B, Lynn K, et al. Stereotactic image-guided neoadjuvant ablative single-dose radiation, then lumpectomy, for early breast cancer: the SIGNAL prospective single-arm trial of single-dose radiation therapy. *Curr Oncol.* 2019;26(3):334-340.
 86. Haussmann J, Corradini S, Nestle-Kraemling C, et al. Recent advances in

- radiotherapy of breast cancer. *Radiat Oncol.* 2020;15:1-10.
87. Caudrelier J-M, Morgan SC, Montgomery L, Lacelle M, Nyiri B, MacPherson M. Helical tomotherapy for locoregional irradiation including the internal mammary chain in left-sided breast cancer: dosimetric evaluation. *Radiother Oncol.* 2009;90(1):99-105.
88. Lozza L, Fariselli L, Sandri M, et al. Partial breast irradiation with CyberKnife after breast conserving surgery: A pilot study in early breast cancer. *Radiat Oncol.* 2018;13(1):1-11. doi:10.1186/s13014-018-0991-4
89. Mutaf YD, Zhang J, Yu CX, et al. Dosimetric and geometric evaluation of a novel stereotactic radiotherapy device for breast cancer: The GammaPodTM. *Med Phys.* 2013;40(4):41722.
90. Lazow SP, Riba L, Alapati A, James TA. Comparison of breast-conserving therapy vs mastectomy in women under age 40: National trends and potential survival implications. *Breast J.* 2019;25(4):578-584.
91. Gu J, Groot G, Boden C, Busch A, Holtslander L, Lim H. Review of factors influencing women's choice of mastectomy versus breast conserving therapy in early stage breast cancer: a systematic review. *Clin Breast Cancer.* 2018;18(4):e539-e554.
92. Njeh CF, Saunders MW, Langton CM. Accelerated partial breast irradiation (APBI): a review of available techniques. *Radiat Oncol.* 2010;5(1):1-28.
93. Lazovich D, White E, Thomas DB, Moe RE. Underutilization of breast-conserving surgery and radiation therapy among women with stage I or II breast cancer. *Jama.* 1991;266(24):3433-3438.

94. Farrow DC, Hunt WC, Samet JM. Geographic variation in the treatment of localized breast cancer. *N Engl J Med.* 1992;326(17):1097-1101.
95. Ballard-Barbash R, Potosky AL, Harlan LC, Nayfield SG, Kessler LG. Factors associated with surgical and radiation therapy for early stage breast cancer in older women. *JNCI J Natl Cancer Inst.* 1996;88(11):716-726.
96. Arthur DW, Vicini FA. Accelerated partial breast irradiation as a part of breast conservation therapy. *J Clin Oncol.* 2005;23(8):1726-1735.
97. Kuerer HM, Julian TB, Strom EA, et al. Accelerated partial breast irradiation after conservative surgery for breast cancer. *Ann Surg.* 2004;239(3):338.
98. Swanson TA, Vicini FA. Overview of accelerated partial breast irradiation. *Curr Oncol Rep.* 2008;10(1):54-60.
99. Whelan TJ, Pignol J-P, Levine MN, et al. Long-term results of hypofractionated radiation therapy for breast cancer. *N Engl J Med.* 2010;362(6):513-520.
100. Hathout L, Hijal T, Théberge V, et al. Hypofractionated radiation therapy for breast ductal carcinoma in situ. *Int J Radiat Oncol Biol Phys.* 2013;87(5):1058-1063.
101. Fisher ER, Anderson S, Tan-Chiu E, Fisher B, Eaton L, Wolmark N. Fifteen-year prognostic discriminants for invasive breast carcinoma: National Surgical Adjuvant Breast and Bowel Project Protocol-06. *Cancer Interdiscip Int J Am Cancer Soc.* 2001;91(S8):1679-1687.
102. Sanders ME, Scroggins T, Ampil FL, Li BD. Accelerated partial breast irradiation in early-stage breast cancer. *J Clin Oncol.* 2007;25(8):996-1002.
103. Schaapveld M, Visser O, Louwman MJ, et al. Risk of new primary nonbreast

- cancers after breast cancer treatment: A dutch population-based study. *J Clin Oncol.* 2008;26(8):1239-1246. doi:10.1200/JCO.2007.11.9081
104. Schaapveld M, Visser O, Louwman WJ, et al. The impact of adjuvant therapy on contralateral breast cancer risk and the prognostic significance of contralateral breast cancer: A population based study in the Netherlands. *Breast Cancer Res Treat.* 2008;110(1):189-197. doi:10.1007/s10549-007-9709-2
 105. Kirova YM, Gambotti L, De Rycke Y, Vilcoq JR, Asselain B, Fourquet A. Risk of second malignancies after adjuvant radiotherapy for breast cancer: a large-scale, single-institution review. *Int J Radiat Oncol Biol Phys.* 2007;68(2):359-363.
 106. Miranda FA, Teixeira LAB, Heinzen RN, et al. Accelerated partial breast irradiation: Current status with a focus on clinical practice. *Breast J.* 2019;25(1):124-128.
 107. Zwicker RD, Arthur DW, Kavanagh BD, Mohan R, Schmidt-Ullrich RK. Optimization of planar high-dose-rate implants. *Int J Radiat Oncol Biol Phys.* 1999;44(5):1171-1177.
 108. Bennion NR, Baine M, Granatowicz A, Wahl AO. Accelerated partial breast radiotherapy: a review of the literature and future directions. *Gland Surg.* 2018;7(6):596.
 109. Vicini FA, Cecchini RS, White JR, et al. Long-term primary results of accelerated partial breast irradiation after breast-conserving surgery for early-stage breast cancer: a randomised, phase 3, equivalence trial. *Lancet.* 2019;394(10215):2155-2164.
 110. Riou O, Fenoglietto P, Bourgier C, et al. Feasibility of accelerated partial breast

- irradiation with volumetric-modulated arc therapy in elderly and frail patients.
Radiat Oncol. 2015;10(1):1-8.
111. Vaidya JS, Bulsara M, Baum M, et al. Long term survival and local control outcomes from single dose targeted intraoperative radiotherapy during lumpectomy (TARGIT-IORT) for early breast cancer: TARGIT-A randomised clinical trial. *bmj.* 2020;370.
 112. Orecchia R, Veronesi U, Maisonneuve P, et al. Intraoperative irradiation for early breast cancer (ELIOT): long-term recurrence and survival outcomes from a single-centre, randomised, phase 3 equivalence trial. *Lancet Oncol.* 2021;22(5):597-608.
 113. Ott OJ, Strnad V, Hildebrandt G, et al. GEC-ESTRO multicenter phase 3-trial: Accelerated partial breast irradiation with interstitial multicatheter brachytherapy versus external beam whole breast irradiation: Early toxicity and patient compliance. *Radiother Oncol.* 2016;120(1):119-123.
 114. Schäfer R, Strnad V, Polgár C, et al. Quality-of-life results for accelerated partial breast irradiation with interstitial brachytherapy versus whole-breast irradiation in early breast cancer after breast-conserving surgery (GEC-ESTRO): 5-year results of a randomised, phase 3 trial. *Lancet Oncol.* 2018;19(6):834-844.
 115. Vicini FA, Cecchini RS, White JR, et al. Long-term primary results of accelerated partial breast irradiation after breast-conserving surgery for early-stage breast cancer: a randomised, phase 3, equivalence trial. *Lancet.* 2019;394(10215):2155-2164. doi:10.1016/S0140-6736(19)32514-0
 116. Meattini I, Marrazzo L, Saieva C, et al. Accelerated partial-breast irradiation compared with whole-breast irradiation for early breast cancer: Long-term results

- of the randomized phase III APBI-IMRT-Florence trial. *J Clin Oncol.* 2020;38(35):4175-4183.
117. Olivotto IA, Whelan TJ, Parpia S, et al. Interim cosmetic and toxicity results from RAPID: A randomized trial of accelerated partial breast irradiation using three-dimensional conformal external beam radiation therapy. *J Clin Oncol.* 2013;31(32):4038-4045. doi:10.1200/JCO.2013.50.5511
118. Coles CE, Griffin CL, Kirby AM, et al. Partial-breast radiotherapy after breast conservation surgery for patients with early breast cancer (UK IMPORT LOW trial): 5-year results from a multicentre, randomised, controlled, phase 3, non-inferiority trial. *Lancet.* 2017;390(10099):1048-1060.
119. Meduri B, Baldissera A, Galeandro M, et al. OC-0568: Accelerated PBI VS standard radiotherapy (IRMA trial): interim cosmetic and toxicity results. *Radiother Oncol.* 2017;123:S303.
120. Horton JK, Blitzblau RC, Yoo S, et al. Preoperative single-fraction partial breast radiation therapy: A novel phase 1, dose-escalation protocol with radiation response biomarkers. *Int J Radiat Oncol Biol Phys.* 2015;92(4):846-855.
121. Guidolin K, Lock M, Yaremko B, et al. A phase II trial to evaluate single-dose stereotactic body radiation therapy (SBRT) prior to surgery for early-stage breast carcinoma: SIGNAL (stereotactic image-guided neoadjuvant ablative radiation then lumpectomy) trial. *J Radiat Oncol.* 2015;4(4):423-430. doi:10.1007/s13566-015-0227-2
122. Yaremko B, Brackstone M, Guidolin K, et al. Results of a Prospective Cohort Trial: Stereotactic Image-Guided Neoadjuvant Ablative Radiation Then

- Lumpectomy (SIGNAL) for Early-Stage Breast Cancer. *Int J Radiat Oncol Biol Phys.* 2018;102(3):S69. doi:10.1016/j.ijrobp.2018.06.188
123. DeWerd LA, Kissick M. *The Phantoms of Medical and Health Physics*. Springer; 2014.
 124. Almond PR, Biggs PJ, Coursey BM, et al. AAPM's TG-51 protocol for clinical reference dosimetry of high-energy photon and electron beams. *Med Phys.* 1999;26(9):1847-1870.
 125. McEwen M, DeWerd L, Ibbott G, et al. Addendum to the AAPM's TG-51 protocol for clinical reference dosimetry of high-energy photon beams. *Med Phys.* 2014;41(4).
 126. Andreo P, Huq MS, Westermark M, et al. Protocols for the dosimetry of high-energy photon and electron beams: a comparison of the IAEA TRS-398 and previous international Codes of Practice. *Phys Med Biol.* 2002;47(17):3033.
 127. Kroenig B. *The Principles of Physics and Biology of Radiation Therapy*. Rebman Company; 1922.
 128. Quimby EH, Copeland MM, Woods RC. *The Distribution of Roentgen Rays within the Human Body*. American Roetgen Ray Society and the American Radium Society; 1934.
 129. White DR. Tissue substitutes in experimental radiation physics. *Med Phys.* 1978;5(6):467-479.
 130. Podgorsak EB. *Radiation Physics for Medical Physicists*. Springer; 2010. doi:10.1007/978-1-4614-2146-7\}2
 131. Lawrence, S. Chin WFR. *Principles and Practice of Stereotactic Radiosurgery*.

Springer- Verlag New York; 2016.

132. Anoop H, Jillian M, Santanu C, et al. Dynamic CT angiography for cyberknife radiosurgery planning of intracranial arteriovenous malformations; a technical/feasibility report. *Radiol Oncol.* 2015;49(2):192-199.
133. van der Bom IMJ, Gounis MJ, Ding L, et al. Target delineation for radiosurgery of a small brain arteriovenous malformation using high-resolution contrast-enhanced cone beam CT. *J Neurointerv Surg.* 2014;6(5):e34-e34.
134. Holmes O, Szanto J, Tsehmaister Abitbul V, et al. *Selective and Super-Selective C-Arm Based Cone Beam CT Angiography (CBCTA) with DynaCT for CyberKnife Radiosurgery Planning of Intracranial Arteriovenous Malformations (AVMs)*. Vol 5.; 2018.
135. Safain MG, Rahal JP, Raval A, et al. Use of cone-beam computed tomography angiography in planning for gamma knife radiosurgery for arteriovenous malformations: a case series and early report. *Neurosurgery*. 2014;74(6):682-696.
136. Smyth JM, Sutton DG, Houston JG. Evaluation of the quality of CT-like images obtained using a commercial flat panel detector system. *Biomed Imaging Interv J.* 2006;2(4).
137. Bridcut RR, Winder RJ, Workman A, Flynn P. Assessment of distortion in a three-dimensional rotational angiography system. *Br J Radiol.* 2002;75(891):266-270.
138. Walker A, Liney G, Metcalfe P, Holloway L. MRI distortion: considerations for MRI based radiotherapy treatment planning. *Australas Phys Eng Sci Med.* 2014;37(1):103-113.
139. Murphy MJ. An automatic six-degree-of-freedom image registration algorithm for

- image-guided frameless stereotaxic radiosurgery. *Med Phys.* 1997;24(6):857-866.
140. Fu D, Kuduvalli G. A fast, accurate, and automatic 2D–3D image registration for image-guided cranial radiosurgery. *Med Phys.* 2008;35(5):2180-2194.
141. Hoffman JM, Coleman RE. Accuracy of registration of PET, SPECT and MR images of a brain phantom. *J Nucl Med.* 1993;34:1587-1594.
142. Alpert NM, Bradshaw JF, Kennedy D, Correia JA. The principal axes transformation-a method for image registration. *J Nucl Med.* 1990;31(10):1717-1722.
143. van Herk M, Kooy HM. Automatic three-dimensional correlation of CT-CT, CT-MRI, and CT-SPECT using chamfer matching. *Med Phys.* 1994;21(7):1163-1178.
144. Seung SK, Larson DA, Galvin JM, et al. American College of Radiology (ACR) and American Society for Radiation Oncology (ASTRO) practice guideline for the performance of stereotactic radiosurgery (SRS). *Am J Clin Oncol.* 2013;36(3):310.
145. Zeverino M, Jaccard M, Patin D, et al. Commissioning of the Leksell Gamma Knife® Icon™. *Med Phys.* 2017;44(2):355-363.
146. Chung H-T, Kim JH, Kim JW, et al. Assessment of image co-registration accuracy for frameless gamma knife surgery. *PLoS One.* 2018;13(3):e0193809.
147. Abedin-Nasab MH. *Handbook of Robotic and Image-Guided Surgery.* Elsevier; 2019.
148. Peerlings J, Compter I, Janssen F, et al. Characterizing geometrical accuracy in clinically optimised 7T and 3T magnetic resonance images for high-precision radiation treatment of brain tumours. *Phys Imaging Radiat Oncol.* 2019;9:35-42.
149. Dieterich S, Cavedon C, Chuang CF, et al. Report of AAPM TG 135: quality

- assurance for robotic radiosurgery. *Med Phys.* 2011;38(6Part1):2914-2936.
150. Vandervoort E, Patrocinio H, Chow T, Soisson E, Nadeau DB. COMP Report: CPQR technical quality control guidelines for CyberKnife® Technology. *J Appl Clin Med Phys.* 2018;19(2):29-34.
151. *Physics Essential Guide Manual, CyberKnife Robotic Radiosurgery System, 2015-09-11, Versions 10.x/5.x/3.X.*
152. Barrett JF, Keat N. Artifacts in CT: recognition and avoidance. *Radiographics.* 2004;24(6):1679-1691.
153. Wang D, Doddrell DM, Cowin G. A novel phantom and method for comprehensive 3-dimensional measurement and correction of geometric distortion in magnetic resonance imaging. *Magn Reson Imaging.* 2004;22(4):529-542.
154. Kalender WA, Kyriakou Y. Flat-detector computed tomography (FD-CT). *Eur Radiol.* 2007;17(11):2767-2779.
155. Fahrig R, Fox AJ, Lownie S, Holdsworth DW. Use of a C-arm system to generate true three-dimensional computed rotational angiograms: preliminary in vitro and in vivo results. *Am J Neuroradiol.* 1997;18(8):1507-1514.
156. Kalender WA. Computed tomography: fundamentals, system technology, image quality, applications. *Comput Tomogr Fundam Syst Technol Image Qual Appl by Willi A Kal pp 220 ISBN 3-89578-081-2 Wiley-VCH, Novemb 2000.* Published online 2000:220.
157. Wang D, Strugnell W, Cowin G, Doddrell DM, Slaughter R. Geometric distortion in clinical MRI systems: Part I: evaluation using a 3D phantom. *Magn Reson Imaging.* 2004;22(9):1211-1221.

158. Walton L, Hampshire A, Forster DMC, Kemeny AA. A phantom study to assess the accuracy of stereotactic localization, using T1-weighted magnetic resonance imaging with the Leksell stereotactic system. *Neurosurgery*. 1996;38(1):170-178.
159. Walton L, Hampshire A, Forster DMC, Kemeny AA. Stereotactic localization with magnetic resonance imaging: a phantom study to compare the accuracy obtained using two-dimensional and three-dimensional data acquisitions. *Neurosurgery*. 1997;41(1):131-139.
160. Yu C, Apuzzo MLJ, Zee C-S, Petrovich Z. A phantom study of the geometric accuracy of computed tomographic and magnetic resonance imaging stereotactic localization with the Leksell stereotactic system. *Neurosurgery*. 2001;48(5):1092-1099.
161. Sumanaweera T, Glover G, Song S, Adler J, Napel S. Quantifying MRI geometric distortion in tissue. *Magn Reson Med*. 1994;31(1):40-47.
162. Price RR, Axel L, Morgan T, et al. Quality assurance methods and phantoms for magnetic resonance imaging: report of AAPM nuclear magnetic resonance Task Group No. 1. *Med Phys*. 1990;17(2):287-295.
163. Mizowaki T, Nagata Y, Okajima K, et al. Reproducibility of geometric distortion in magnetic resonance imaging based on phantom studies. *Radiother Oncol*. 2000;57(2):237-242.
164. Breeuwer MM, Holden M, Zylka W. Detection and correction of geometric distortion in 3D MR images. In: *Medical Imaging 2001: Image Processing*. Vol 4322. International Society for Optics and Photonics; 2001:1110-1121.
165. Baldwin LN, Wachowicz K, Thomas SD, Rivest R, Fallone BG. Characterization,

- prediction, and correction of geometric distortion in MR images. *Med Phys.* 2007;34(2):388-399.
166. Stupic KF, Ainslie M, Boss MA, et al. A standard system phantom for magnetic resonance imaging. *Magn Reson Med.* Published online 2021.
167. George E, Liacouras P, Rybicki FJ, Mitsouras D. Measuring and establishing the accuracy and reproducibility of 3D printed medical models. *Radiographics.* 2017;37(5):1424-1450.
168. Jafar M, Jafar YM, Dean C, Miquel ME. Assessment of Geometric Distortion in Six Clinical Scanners Using a 3D-Printed Grid Phantom. *J Imaging.* 2017;3(3):28.
169. Hurkmans CW, Borger JH, Pieters BR, Russell NS, Jansen EPM, Mijnheer BJ. Variability in target volume delineation on CT scans of the breast. *Int J Radiat Oncol Biol Phys.* 2001;50(5):1366-1372.
170. Wong EK, Truong PT, Kader HA, et al. Consistency in seroma contouring for partial breast radiotherapy: impact of guidelines. *Int J Radiat Oncol Biol Phys.* 2006;66(2):372-376.
171. Tse T, Knowles S, Belec J, et al. Canadian Consortium for LABC Meeting Consensus Statement on The Surgeon's Role In Intraoperative Tumor Bed Localization for Adjuvant Radiation After Oncoplastic Breast Conserving Surgery. *Curr Oncol.* 27(3):326-331.
172. den Hartogh MD, Philippens MEP, van Dam IE, et al. MRI and CT imaging for preoperative target volume delineation in breast-conserving therapy. *Radiat Oncol.* 2014;9(1):1-9.
173. Paulson ES, Erickson B, Schultz C, Allen Li X. Comprehensive MRI simulation

- methodology using a dedicated MRI scanner in radiation oncology for external beam radiation treatment planning. *Med Phys.* 2015;42(1):28-39.
174. Mouawad M, Biernaski H, Brackstone M, et al. Reducing the dose of gadolinium-based contrast agents for DCE-MRI guided SBRT: the effects on inter and intra observer variability for preoperative target volume delineation in early stage breast cancer patients. *Radiother Oncol.* 2019;131:60-65.
175. Vasmel JE, Koerkamp MLG, Kirby AM, et al. Consensus on contouring primary breast tumors on MRI in the setting of neoadjuvant partial breast irradiation in trials. *Pract Radiat Oncol.* 2020;10(6):e466-e474.
176. Doran SJ, Charles-Edwards L, Reinsberg SA, Leach MO. A complete distortion correction for MR images: I. Gradient warp correction. *Phys Med Biol.* 2005;50(7):1343.
177. Pappas EP, Seimenis I, Moutsatsos A, Georgiou E, Nomikos P, Karaiskos P. Characterization of system-related geometric distortions in MR images employed in Gamma Knife radiosurgery applications. *Phys Med Biol.* 2016;61(19):6993.
178. Baldwin LN, Wachowicz K, Fallone BG. A two-step scheme for distortion rectification of magnetic resonance images. *Med Phys.* 2009;36(9):3917-3926.
doi:10.1118/1.3180107
179. Stanescu T, Wachowicz K, Jaffray DA. Characterization of tissue magnetic susceptibility-induced distortions for MRIgRT. *Med Phys.* 2012;39(12):7185-7193.
180. Adjeiwaah M, Bylund M, Lundman JA, Karlsson CT, Jonsson JH, Nyholm T. Quantifying the effect of 3T magnetic resonance imaging residual system

- distortions and patient-induced susceptibility distortions on radiation therapy treatment planning for prostate cancer. *Int J Radiat Oncol Biol Phys.* 2018;100(2):317-324.
181. Wang D, Strugnell W, Cowin G, Doddrell DM, Slaughter R. Geometric distortion in clinical MRI systems: Part II: Correction using a 3D phantom. *Magn Reson Imaging.* 2004;22(9):1223-1232. doi:10.1016/j.mri.2004.08.014
182. Schenck JF. The role of magnetic susceptibility in magnetic resonance imaging: MRI magnetic compatibility of the first and second kinds. *Med Phys.* 1996;23(6):815-850.
183. Steenbakkers RJHM, Deurloo KEI, Nowak PJCM, Lebesque J V, van Herk M, Rasch CRN. Reduction of dose delivered to the rectum and bulb of the penis using MRI delineation for radiotherapy of the prostate. *Int J Radiat Oncol Biol Phys.* 2003;57(5):1269-1279.
184. Bernstein MA, Huston III J, Ward HA. Imaging artifacts at 3.0 T. *J Magn Reson Imaging An Off J Int Soc Magn Reson Med.* 2006;24(4):735-746.
185. Pappas EP, Seimenis I, Dellios D, Kollias G, Lampropoulos KI, Karaikos P. Assessment of sequence dependent geometric distortion in contrast-enhanced MR images employed in stereotactic radiosurgery treatment planning. *Phys Med Biol.* 2018;63(13). doi:10.1088/1361-6560/aac7bf
186. Chen L, Price Jr RA, Wang L, et al. MRI-based treatment planning for radiotherapy: dosimetric verification for prostate IMRT. *Int J Radiat Oncol Biol Phys.* 2004;60(2):636-647.
187. Mizowaki T, Araki N, Nagata Y, Negoro Y, Aoki T, Hiraoka M. The use of a

- permanent magnetic resonance imaging system for radiotherapy treatment planning of bone metastases. *Int J Radiat Oncol Biol Phys.* 2001;49(2):605-611.
188. Dogan BE, Scoggins ME, Son JB, Wei W, Candelaria R, Yang WT. MRI for High-Risk Breast Cancer Study. 2018;(January):214-221.
189. Shahid H, Wiedenhofer JF, Dornbluth C, Otto P, Kist KA. An overview of breast MRI. *Appl Radiol.* 2016;45(10):7-13.
190. Schad LR, Blümli S, Hawighorst H, Wenz F, Lorenz WJ. Radiosurgical treatment planning of brain metastases based on a fast, three-dimensional MR imaging technique. *Magn Reson Imaging.* 1994;12(5):811-819.
191. Dimopoulos JCA, Schard G, Berger D, et al. Systematic evaluation of MRI findings in different stages of treatment of cervical cancer: potential of MRI on delineation of target, pathoanatomic structures, and organs at risk. *Int J Radiat Oncol Biol Phys.* 2006;64(5):1380-1388.
192. Poon I, Fischbein N, Lee N, et al. A population-based atlas and clinical target volume for the head-and-neck lymph nodes. *Int J Radiat Oncol Biol Phys.* 2004;59(5):1301-1311.
193. Milosevic M, Voruganti S, Blend R, et al. Magnetic resonance imaging (MRI) for localization of the prostatic apex: comparison to computed tomography (CT) and urethrography. *Radiother Oncol.* 1998;47(3):277-284.
194. Jackson ASN, Reinsberg SA, Sohaib SA, et al. Distortion-corrected T 2 weighted MRI: a novel approach to prostate radiotherapy planning. *Br J Radiol.* 2007;80(959):926-933.
195. Rosewall T, Kong V, Vesprini D, et al. Prostate delineation using CT and MRI for

- radiotherapy patients with bilateral hip prostheses. *Radiother Oncol.* 2009;90(3):325-330.
196. O'Neill BDP, Salerno G, Thomas K, Tait DM, Brown G. MR vs CT imaging: low rectal cancer tumour delineation for three-dimensional conformal radiotherapy. *Br J Radiol.* 2009;82(978):509-513.
197. Dogan BE, Scoggins ME, Son JB, et al. American College of Radiology-compliant short protocol breast MRI for high-risk breast cancer screening: a prospective feasibility study. *Am J Roentgenol.* 2018;210(1):214-221.
198. Benner T, van der Kouwe AJW, Kirsch JE, Sorensen AG. Real-time RF pulse adjustment for B0 drift correction. *Magn Reson Med An Off J Int Soc Magn Reson Med.* 2006;56(1):204-209.
199. Van Herk M. Errors and margins in radiotherapy. In: *Seminars in Radiation Oncology*. Vol 14. Elsevier; 2004:52-64.
200. Liney GP, Tozer DJ, Turnbull LW. A simple and realistic tissue-equivalent breast phantom for MRI. *J Magn Reson Imaging.* 1999;10(6):968-971.
doi:10.1002/(SICI)1522-2586(199912)10:6<968::AID-JMRI9>3.0.CO;2-0
201. Struik GM, Hoekstra N, Klem TM, et al. Injection of radiopaque hydrogel at time of lumpectomy improves the target definition for adjuvant radiotherapy. *Radiother Oncol.* 2019;131:8-13.
202. Zucca-Matthes G, Lebovic G, Lyra M. Mastotrainer new version: realistic simulator for training in breast surgery. *The Breast.* 2017;31:82-84.
203. Kilic D, Ustbas B, Budak EP, et al. Silicone-based composites as surgical breast models for oncoplasty training. *Procedia Eng.* 2016;159:104-107.

204. Bude RO, Adler RS. An easily made, low-cost, tissue-like ultrasound phantom material. *J Clin ultrasound*. 1995;23(4):271-273.
205. Ruschin M, Davidson SRH, Phounsy W, et al. Multipurpose CT, ultrasound, and MRI breast phantom for use in radiotherapy and minimally invasive interventions. *Med Phys*. 2016;43(5):2508-2514.
206. Christoffersson JO, Olsson LE, Sjöberg S. Nickel-doped agarose gel phantoms in MR imaging. *Acta radiol*. 1991;32(5):426-431.
207. Mano I, Goshima H, Nambu M, Iio M. New polyvinyl alcohol gel material for MRI phantoms. *Magn Reson Med*. 1986;3(6):921-926.
208. Mazzara GP, Briggs RW, Wu Z, Steinbach BG. Use of a modified polysaccharide gel in developing a realistic breast phantom for MRI. *Magn Reson Imaging*. 1996;14(6):639-648.
209. Groch MW, Urbon JA, Erwin WD, Al-Doohan S. An MRI tissue equivalent lesion phantom using a novel polysaccharide material. *Magn Reson Imaging*. 1991;9(3):417-421.
210. Blechinger JC, Madsen EL, Frank GR. Tissue-mimicking gelatin–agar gels for use in magnetic resonance imaging phantoms. *Med Phys*. 1988;15(4):629-636.
211. Hellerbach A, Schuster V, Jansen A, Sommer J. MRI phantoms—are there alternatives to agar? *PLoS One*. 2013;8(8):e70343.
212. Pangman WJ. Compound prosthesis device. United States. Patent No. 2,842,775. Published online 1958.
213. Redinger PVA, Compton RA. Silicone Gel Filled Prosthesis. United States, Patent No. 4,455,691. Published online 1984.

214. Smooth-On. EcoflexTM Series. Accessed May 18, 2021. <https://www.smooth-on.com/product-line/ecoflex/>
215. Pope JTL, Read ME, Medsker T, Buschi AJ, Brenbridge AN. Breast skin thickness: normal range and causes of thickening shown on film-screen mammography. *J Can Assoc Radiol.* 1984;35(4):365-368.
216. Lee AHS. Why is carcinoma of the breast more frequent in the upper outer quadrant? A case series based on needle core biopsy diagnoses. *The Breast.* 2005;14(2):151-152.
217. Ramião NG, Martins PS, Rynkevic R, Fernandes AA, Barroso M, Santos DC. Biomechanical properties of breast tissue, a state-of-the-art review. *Biomech Model Mechanobiol.* 2016;15(5):1307-1323.
218. Tofts PS. Methods for quantitative relaxation parameter mapping: measuring T1 and T2. In: *Proc Int Soc Magn Reson Med.* ; 2009:1-6.
219. Levenberg K. A method for the solution of certain non-linear problems in least squares. *Q Appl Math.* 1944;2(2):164-168.
220. Marquardt DW. An algorithm for least-squares estimation of nonlinear parameters. *J Soc Ind Appl Math.* 1963;11(2):431-441.
221. Schneider CA, Rasband WS, Eliceiri KW. NIH Image to ImageJ: 25 years of image analysis. *Nat Methods.* 2012;9(7):671.
222. Athanasiou A, Tardivon A, Tanter M, et al. Breast lesions: quantitative elastography with supersonic shear imaging—preliminary results. *Radiology.* 2010;256(1):297-303.
223. Annaidh AN, Bruyère K, Destrade M, Gilchrist MD, Otténio M. Characterization

- of the anisotropic mechanical properties of excised human skin. *J Mech Behav Biomed Mater.* 2012;5(1):139-148.
224. Dorne L, Stroman P, Rolland C, et al. Magnetic resonance study of virgin and explanted silicone breast prostheses. Can proton relaxation times be used to monitor their biostability? *ASAIO J (American Soc Artif Intern Organs 1992).* 1994;40(3):M625-31.
225. Rakow-Penner R, Daniel B, Yu H, Sawyer-Glover A, Glover GH. Relaxation times of breast tissue at 1.5 T and 3T measured using IDEAL. *J Magn Reson Imaging An Off J Int Soc Magn Reson Med.* 2006;23(1):87-91.
226. Navarro M, Michiardi A, Castano O, Planell JA. Biomaterials in orthopaedics. *J R Soc interface.* 2008;5(27):1137-1158.
227. Cronin TD, Gerow FJ. Augmentation mammoplasty: a new "natural feel" prosthesis. *Trans III Intern Congr Plast Surg.* 1963;66(41).
228. Griffin M, Premakumar Y, Seifalian A, Butler PE, Szarko M. Biomechanical characterization of human soft tissues using indentation and tensile testing. *JoVE (Journal Vis Exp.* 2016;(118):e54872.
229. Zell K, Sperl JI, Vogel MW, Niessner R, Haisch C. Acoustical properties of selected tissue phantom materials for ultrasound imaging. *Phys Med Biol.* 2007;52(20):N475.
230. Jungling O. Die homogene Röntgendurchstrahlung tuberkulöser Gelenke mit Umbau und Bolusfüllung. *Strahlentherapie.* 1920;10:576.
231. Vyas V, Palmer L, Mudge R, et al. On bolus for megavoltage photon and electron radiation therapy. *Med Dosim.* 2013;38(3):268-273.

232. Aras S, Tanzer IO, Ikizceli T. Dosimetric Comparison of Superflab and Specially Prepared Bolus Materials Used in Radiotherapy Practice. *Eur J Breast Heal.* 2020;16(3):167-170. doi:10.5152/ejbh.2020.5041
233. Colas. Andre, Curtis J. *Biomaterials Science: An Introduction Tot Materials In.* Second Edi. (Raner BD, Hoffman AS, Schoen FJ, Lemons JE, eds.). Elsevier Inc.; 2004.
234. Canters RA, Lips IM, Wendling M, et al. Clinical implementation of 3D printing in the construction of patient specific bolus for electron beam radiotherapy for non-melanoma skin cancer. *Radiother Oncol.* 2016;121(1):148-153.
235. Chiu T, Tan J, Brenner M, et al. Three-dimensional printer-aided casting of soft, custom silicone boluses (SCSBs) for head and neck radiation therapy. *Pract Radiat Oncol.* 2018;8(3):e167-e174.
236. Dubois D, Bice W, Bradford B, Schneid T, Engelmeier R. Moldable tissue equivalent bolus for high-energy photon and electron therapy. *Med Phys.* 1996;23(9):1547-1549.
237. Hazelaar C, van Eijnatten M, Dahele M, et al. Using 3D printing techniques to create an anthropomorphic thorax phantom for medical imaging purposes. *Med Phys.* 2018;45(1):92-100.
238. Niebuhr NI, Johnen W, Echner G, et al. The ADAM-pelvis phantom - An anthropomorphic, deformable and multimodal phantom for MRgRT. *Phys Med Biol.* 2019;64(4). doi:10.1088/1361-6560/aafdf5f
239. Bohoudi O, Lagerwaard FJ, Bruynzeel AME, et al. End-to-end empirical validation of dose accumulation in MRI-guided adaptive radiotherapy for prostate

- cancer using an anthropomorphic deformable pelvis phantom. *Radiother Oncol.* 2019;(xxxx). doi:10.1016/j.radonc.2019.09.014
240. Ehrbar S, Jöhl A, Kühni M, et al. ELPHA: Dynamically deformable liver phantom for real-time motion-adaptive radiotherapy treatments. *Med Phys.* 2019;46(2):839-850. doi:10.1002/mp.13359
241. Aldosary G, Tse T, Arnaout A, et al. Radiological, dosimetric and mechanical properties of a deformable breast phantom for radiation therapy and surgical applications. *Biomed Phys Eng Express.* Published online 2020.
242. Mayneord W V. The significance of the roentgen. *Acta Int Union Against Cancer.* 1937;2:271.
243. Berger MJ, Coursey JS, Zucker MA, Chang J. Stopping-power and range tables for electrons, protons, and helium ions, NIST Standard Reference Database 124. Published online 2017.
244. Anthony K, Paliwal BR. Stopping power and mass energy absorption coefficient ratios for Solid Water. *Med Phys.* 1986;13(3):403-404. doi:10.1118/1.595884
245. Cunningham JR, Schulz RJ. On the selection of stopping power and mass energy absorption coefficient ratios for high energy x ray dosimetry. *Med Phys.* 1984;11(5):618-623. doi:10.1118/1.595643
246. Berger MJ, Hubbell JH, Seltzer SM, et al. Xcom: Photon cross sections database, nist standard reference database 8 (xgam). URL <http://physics.nist.gov/PhysRefData/Xcom/Text/XCOM.html>. Published online 2010.
247. Devic S, Seuntjens J, Hegyi G, et al. Dosimetric properties of improved GafChromic films for seven different digitizers. *Med Phys.* 2004;31(9):2392-2401.

248. Van Battum LJ, Hoffmans D, Piersma H, Heukelom S. Accurate dosimetry with GafChromicTM EBT film of a photon beam in water: What level is achievable? *Med Phys.* 2008;35(2):704-716.
249. 2013 IMPAC Medical Systems I. *Monaco External Beam Dose Calculation Algorithms Technical Reference.*; 2014.
250. Knöös T, Nilsson M, Ahlgren L. A method for conversion of Hounsfield number to electron density and prediction of macroscopic pair production cross-sections. *Radiother Oncol.* 1986;5(4):337-345.
251. White DR, Booz J, Griffith R V, Spokas JJ, Wilson IJ. Report 44. *J Int Comm Radiat Units Meas.* 1989;os23(1). doi:10.1093/jicru/os23.1.Report44
252. Fippel M. Fast Monte Carlo dose calculation for photon beams based on the VMC electron algorithm. *Med Phys.* 1999;26(8):1466-1475.
253. Kawrakow I, Fippel M, Friedrich K. 3D electron dose calculation using a Voxel based Monte Carlo algorithm (VMC). *Med Phys.* 1996;23(4):445-457.
254. Walters B, Kawrakow I, Rogers DWO. DOSXYZnrc Users Manual PIRS-794revB. *NRCC Rep.* Published online 2020:1-132.
255. Canters RA, Lips IM, Wendling M, et al. Clinical implementation of 3D printing in the construction of patient specific bolus for electron beam radiotherapy for non-melanoma skin cancer. *Radiother Oncol.* 2016;121(1):148-153.
doi:10.1016/j.radonc.2016.07.011
256. Du Y, Wang R, Wang M, et al. Radiological tissue equivalence of deformable silicone-based chemical radiation dosimeters (FlexyDos3D). *J Appl Clin Med Phys.* 2019;20(7):87-99. doi:10.1002/acm2.12658

257. Ahnesjö A. Collapsed cone convolution of radiant energy for photon dose calculation in heterogeneous media. *Med Phys.* 1989;16(4):577-592. doi:10.1118/1.596360
258. Aspradakis MM, Morrison RH, Richmond ND, Steele A. Experimental verification of convolution/superposition photon dose calculations for radiotherapy treatment planning. *Phys Med Biol.* 2003;48(17):2873-2893. doi:10.1088/0031-9155/48/17/309
259. Mainegra-hing E, Kawrakow I, Rogers DWO, Introduction I. Calculations for plane-parallel ion chambers in 60Co beams using the EGSnrc Monte Carlo code. *Med Phys.* 2003;30(2):179-189. doi:10.1118/1.1536291
260. Stewart KJ, Seuntjens JP. Comparing calibration methods of electron beams using plane-parallel chambers with absorbed-dose to water based protocols. *Med Phys.* 2002;29(3):284-289.
261. Kleivenhagen SC. Implication of electron backscattering for electron dosimetry. *Phys Med Biol.* 1991;36(7):1013-1018. doi:10.1088/0031-9155/36/7/009
262. McEwen M, Palmans H, Williams A. An empirical method for the determination of wall perturbation factors for parallel-plate chambers in high-energy electron beams. *Phys Med Biol.* 2006;51(20):5167-5181. doi:10.1088/0031-9155/51/20/006
263. Muir BR, McEwen MR, Rogers DWO. Beam quality conversion factors for parallel-plate ionization chambers in MV photon beams. *Med Phys.* 2012;39(3):1618-1631. doi:10.1118/1.3687864
264. Pezner RD, Tan MC, Clancy SL, Chen Y-J, Joseph T, Vora NL. Radiation therapy for breast cancer patients who undergo oncoplastic surgery: localization of the

- tumor bed for the local boost. *Am J Clin Oncol.* 2013;36(6):535-539.
265. Eaton BR, Losken A, Okwan-Duodu D, et al. Local recurrence patterns in breast cancer patients treated with oncoplastic reduction mammoplasty and radiotherapy. *Ann Surg Oncol.* 2014;21(1):93-99.
266. Hepel JT, Evans SB, Hiatt JR, et al. Planning the Breast Boost: Comparison of Three Techniques and Evolution of Tumor Bed During Treatment. *Int J Radiat Oncol Biol Phys.* 2009;74(2):458-463. doi:10.1016/j.ijrobp.2008.08.051
267. Kirova YM, Fournier-Bidoz N, Servois V, et al. How to Boost the Breast Tumor Bed? A Multidisciplinary Approach in Eight Steps. *Int J Radiat Oncol Biol Phys.* 2008;72(2):494-500. doi:10.1016/j.ijrobp.2007.12.059
268. Kirova YM, Pena PC, Hijal T, et al. Improving the definition of tumor bed boost with the use of surgical clips and image registration in breast cancer patients. *Int J Radiat Oncol Biol Phys.* 2010;78(5):1352-1355.
269. Jones HA, Antonini N, Hart AA, et al. Impact of pathological characteristics on local relapse after breast-conserving therapy: a subgroup analysis of the EORTC boost versus no boost trial. *J Clin Oncol.* 2009;27(30):4939-4947.
270. Livi L, Meattini I, Marrazzo L, et al. Accelerated partial breast irradiation using intensity-modulated radiotherapy versus whole breast irradiation: 5-year survival analysis of a phase 3 randomised controlled trial. *Eur J Cancer.* 2015;51(4):451-463.
271. Vicini F, Shah C, Arthur D, Khan A, Wazer D, Keisch M. Partial breast irradiation and the GEC-ESTRO trial. *Lancet.* 2016;387(10029):1717-1718.
272. Whelan TJ, Julian JA, Berrang TS, et al. External beam accelerated partial breast

- irradiation versus whole breast irradiation after breast conserving surgery in women with ductal carcinoma in situ and node-negative breast cancer (RAPID): a randomised controlled trial. *Lancet.* 2019;394(10215):2165-2172.
273. Strnad V, Hannoun-Levi J-M, Guinot J-L, et al. Recommendations from GEC ESTRO Breast Cancer Working Group (I): Target definition and target delineation for accelerated or boost Partial Breast Irradiation using multicatheter interstitial brachytherapy after breast conserving closed cavity surgery. *Radiother Oncol.* 2015;115(3):342-348.
274. Song HM, Styblo TM, Carlson GW, Losken A. The use of oncoplastic reduction techniques to reconstruct partial mastectomy defects in women with ductal carcinoma in situ. *Breast J.* 2010;16(2):141-146.
275. Iwuchukwu OC, Harvey JR, Dordea M, Critchley AC, Drew PJ. The role of oncoplastic therapeutic mammoplasty in breast cancer surgery-A review. *Surg Oncol.* 2012;21(2):133-141.
276. Schaverien MV, Stallard S, Dodwell D, Doughty JC. Use of boost radiotherapy in oncoplastic breast-conserving surgery—a systematic review. *Eur J Surg Oncol.* 2013;39(11):1179-1185.
277. Corrao G, Rojas DP, Ciardo D, et al. Intra-and inter-observer variability in breast tumour bed contouring and the controversial role of surgical clips. *Med Oncol.* 2019;36(6):51.
278. Riina MD, Rashad R, Cohen S, et al. The Effectiveness of Intraoperative Clip Placement in Improving Radiation Therapy Boost Targeting After Oncoplastic Surgery. *Pract Radiat Oncol.* Published online 2020:1-9.

doi:10.1016/j.prro.2019.12.005

279. Livi L, Buonamici FB, Simontacchi G, et al. Accelerated partial breast irradiation with IMRT: new technical approach and interim analysis of acute toxicity in a phase III randomized clinical trial. *Int J Radiat Oncol Biol Phys.* 2010;77(2):509-515.
280. Dice LR. Measures of the amount of ecologic association between species. *Ecology.* 1945;26(3):297-302.
281. Pinter C, Lasso A, Wang A, Jaffray D, Fichtinger G. SlicerRT: radiation therapy research toolkit for 3D Slicer. *Med Phys.* 2012;39(10):6332-6338.
282. Danielsson P-E. Euclidean distance mapping. *Comput Graph Image Process.* 1980;14(3):227-248.
283. Pitkänen MA, Holli KA, Ojala AT, Laippala P. Quality assurance in radiotherapy of breast cancer variability in planning target volume delineation. *Acta Oncol (Madr).* 2001;40(1):50-55.
284. Sanders KE, Komaki R, Buchholz TA. Target delineation and treatment planning in breast conserving therapy. *Rays.* 2003;28(3):237-245.
285. Llen XALI, Ai ANT, Rthur DOWA, et al. Variability of target and normal structure delineation for breast cancer radiotherapy: An RTOG multi-institutional and multiobserver study. 2009;73(3):944-951. doi:10.1016/j.ijrobp.2008.10.034
286. Offersen B V, Boersma LJ, Kirkove C, et al. ESTRO consensus guideline on target volume delineation for elective radiation therapy of early stage breast cancer. *Radiother Oncol.* 2015;114(1):3-10.
287. Strnad V, Krug D, Sedlmayer F, et al. DEGRO practical guideline for partial-

- breast irradiation. *Strahlentherapie und Onkol Organ der Dtsch Rontgengesellschaft.* [et al]. Published online 2020.
288. Sachs RK, Brenner DJ. Solid tumor risks after high doses of ionizing radiation. *Proc Natl Acad Sci.* 2005;102(37):13040-13045.
289. Li XA, Tai A, Arthur DW, et al. Variability of target and normal structure delineation for breast cancer radiotherapy: an RTOG Multi-Institutional and Multiobserver Study. *Int J Radiat Oncol Biol Phys.* 2009;73(3):944-951.
290. ClinicalTrials.gov. Partial Breast Versus no Irradiation for Women With Early Breast Cancer. Identifier: NCT03646955. Accessed May 7, 2020.
<https://clinicaltrials.gov/ct2/show/NCT03646955>
291. Bosma SCJ, vd Leij F, Vreeswijk S, et al. Five-year results of the Preoperative Accelerated Partial Breast Irradiation (PAPBI) Trial. *Int J Radiat Oncol Biol Phys.* Published online 2020.
292. Yang JD, Lee JW, Cho YK, et al. Surgical techniques for personalized oncoplastic surgery in breast cancer patients with small-to moderate-sized breasts (part 1): volume displacement. *J Breast Cancer.* 2012;15(1):1-6.
293. Yang JD, Lee JW, Cho YK, et al. Surgical techniques for personalized oncoplastic surgery in breast cancer patients with small-to moderate-sized breasts (part 2): volume replacement. *J Breast Cancer.* 2012;15(1):7-14.
294. Rubio IT, Wyld L, Esgueva A, et al. Variability in breast cancer surgery training across Europe: an ESSO-EUSOMA international survey. *Eur J Surg Oncol.* 2019;45(4):567-572.
295. Hamza A, Lohsiriwat V, Rietjens M. Lipofilling in breast cancer surgery. *Gland*

Surg. 2013;2(1):7.

296. Patrick HM, Hijal T, Souhami L, et al. A Canadian Response to the Coronavirus Disease 2019 (COVID-19) Pandemic: Is There a Silver Lining for Radiation Oncology Patients? *Adv Radiat Oncol.* 2020;5(4):774-776.
doi:10.1016/j.adro.2020.06.016
297. Haviland JS, Owen JR, Dewar JA, et al. The UK Standardisation of Breast Radiotherapy (START) trials of radiotherapy hypofractionation for treatment of early breast cancer: 10-year follow-up results of two randomised controlled trials. *Lancet Oncol.* 2013;14(11):1086-1094.
298. Murray Brunt A, Haviland JS, Wheatley DA, et al. Hypofractionated breast radiotherapy for 1 week versus 3 weeks (FAST-Forward): 5-year efficacy and late normal tissue effects results from a multicentre, non-inferiority, randomised, phase 3 trial. *Lancet.* 2020;395(10237):1613-1626. doi:10.1016/S0140-6736(20)30932-6
299. Mitchell S, Lee H, DuPree BB, et al. A novel, adaptable, radiographically opaque, multi-plane continuous filament marker for optimizing tissue identification, radiation planning, and radiographic follow-up. *Gland Surg.* 2019;8(6):609.
300. Brunt AM, Haviland JS, Wheatley DA, et al. Hypofractionated breast radiotherapy for 1 week versus 3 weeks (FAST-Forward): 5-year efficacy and late normal tissue effects results from a multicentre, non-inferiority, randomised, phase 3 trial. *Lancet.* Published online 2020.
301. Yaremko B, Brackstone M, Guidolin K, et al. Results of a Prospective Cohort Trial: Stereotactic Image-Guided Neoadjuvant Ablative Radiation Then Lumpectomy (SIGNAL) for Early-Stage Breast Cancer. *Int J Radiat Oncol.*

2018;102(3):S69. doi:10.1016/j.ijrobp.2018.06.188

302. Whelan T, Levine M, Sussman J. Hypofractionated breast irradiation: what's next?

Published online 2020.